Concentration polarization: Electrodeposition and transport phenomena at overlimiting current

Nielsen, Christoffer Peder

Publication date:
2015

Document Version
Publisher's PDF, also known as Version of record

DTU Physics
Department of Physics

Ph.D. Thesis

Concentration polarization: Electrodeposition and transport phenomena at overlimiting current

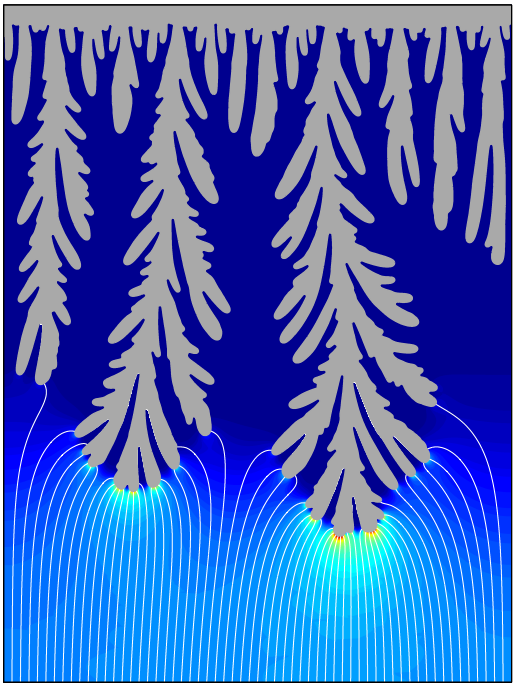

Christoffer P. Nielsen

Advisor: Professor Henrik Bruus

Department of Physics
Technical University of Denmark
August 31, 2015

Cover illustration: Ramified electrodeposit with current streamlines.

Technical University of Denmark
Department of Physics
Building 309, DK-2800 Kongens Lyngby, Denmark
www.staff.dtu.dk/en/bruus/Researchgroup

Abstract

In the present thesis we study different aspects of concentration polarization, with emphasis on nonlinear transport phenomena and ramified electrode growth. We aim at extracting the essential features which characterize the problems, and to that end we employ a variety of numerical and analytical methods.

The initial study concerns a fundamental problem in the study of concentration polarization at overlimiting current, namely the emergence of an extended space-charge region near the ion-selective interface. Based on the so-called quasi-uniform charge density assumption (QCD), we develop an analytical model for the transport in a system with an extended space-charge region. By comparison with numerical simulations, we show that the analytical model captures all of the essential features of the problem. We use the model to derive a range of results characterizing the extended space-charge region.

Secondly, we investigate concentration polarization in a microchannel with charged walls. We provide full numerical solutions to the transport problem, including the effects of advection and surface conduction in the electric double layers. We show that in large areas of the relevant parameter space the transport can be understood in terms of a group of simple analytical models. Some of these are generalizations of a previously published analytical model. In addition to the full numerical model, we employ a numerical boundary layer model with a slip velocity. By carefully comparing the full model and the boundary layer model, we reveal a number of issues, which invalidate most previous attempts at modeling microchannel concentration polarization using a slip model.

Returning to concentration polarization in a bulk system, we study the effects of water splitting at a permselective membrane. We investigate this coupled chemical and transport effect using two simple models of the reaction kinetics. The principal investigations are performed using numerical simulations, but in addition we derive an analytical model for the transport in the system. The analytical model reveals an important link between the current of salt ions and the current of water ions. This link seemingly exists independent of the specific reaction kinetics, and could help in furthering the understanding of the water splitting process. A fit of the model to experimental data from the literature shows quite good agreement, and provides some hints about the reaction kinetics in the given experiment.

In the final part of the thesis we investigate electrodeposition, and specifically the tendency of a cathode to become morphologically unstable and develop ramified growth. Firstly, we consider the stability of a flat metal electrode during electrodeposition. Using linear perturbation theory, we develop numerical and analytical models for the instability

growth rate as a function of the instability wavelength. In contrast to previous work on the stability problem, our models apply at both under- and overlimiting current.

Secondly, we develop a numerical sharp-interface model describing the electrode growth. This model differs from the established phase-field models, in that it is applicable at overlimiting current and implements electrode reactions in a consistent way. Comparison of the sharp-interface model to the results of the stability analysis, provides a validation of the model behavior in the initial stages of the growth. Some preliminary results of the numerical simulations indicate that the electrodeposit morphology might be explainable in terms of a few key parameters.

Resumé

I denne afhandling undersøger vi forskellige aspekter af koncentrationspolarisation, med særligt fokus på ikke-lineære transportfænomener og forgrenet elektrodevækst. Vores mål er at uddrage de essentielle elementer som karakteriserer de undersøgte problemer, og til dette formål anvender vi en række numeriske og analytiske metoder.

Det indledende studie omhandler et fundamentalt problem i studiet af koncentrationspolarisation i det overbegrænsede regime, nemlig udviklingen af en udvidet ladningsregion nær den ion-selektive overflade. Med afsæt i den såkaldte 'quasi-uniform charge density assumption' (QCD) udvikler vi en analytisk model for ion-transporten i et system med en udvidet ladningsregion. Ved sammenligning med numeriske simuleringer viser vi, at den analytiske model inkluderer alle de vigtigste elementer af problemet. Vi anvender modellen til at udvide en række resultater some karakteriserer den udvidede ladningsregion.

Dernæst undersøger vi koncentrationspolarisation i en mikrokanal med ladede vægge. Vi præsenterer fulde numeriske løsninger til transportproblemet, inlusiv effekterne af advektion og overfladestrømme i de elektriske dobbeltlag. Vi viser, at i store områder af det relevante parameterrum kan ion-transporten rationaliseres via en lille gruppe analytiske modeller. Nogle af disse er generaliseringer af en tidligere publiceret analytisk model. Udover den fulde numeriske model anvender vi en numerisk randlagsmodel med en slip-hastighed. Ved omhyggeligt at sammenligne den fulde model og randlagsmodellen, afdækker vi en række forhold, som invaliderer tidligere forsøg på at modellere mikrokanal koncentrationspolarisation med en randlagsmodel.

Det tredje studie omhandler effekterne af koncentrationspolarisation og vandsplitning ved en ion-selektiv membran. Vi undersøger denne koblede kemiske- og transporteffekt ved hjælp af to simple modeller for reaktionskinetikken. Hovedundersøgelserne udføres ved brug af numeriske simuleringer, men derudover udleder vi en analytisk model for transporten i systemet. Den analytiske model afslører et vigtigt bindeled mellem strømmen af salt-ioner of vand-ioner. Dette bindeled eksiterer tilsyneladende uafhængigt af den specifikke reaktionsmodel, og det kunne dermed være en hjælp i arbejdet med at forstå vandsplitningsprocessen. Et fit af modellen til eksperimentelle data fra litteraturen viser en rimelig god overenstemmelse, og giver nogle ledetråde angående reaktionskinetikken i det specifikke eksperiment.

I den sidste del af afhandlingen undersøger vi elektrodeponering, og specifikt en katodes tendens til at blive morfologisk ustabil og udvikle forgrenet vækst. Først betragter vi stabiliteten af en plan metalelektrode under elektrodeponering. Ved brug af lineær perturbationsteori udvikler vi numeriske og analytiske modeller for perturbationsvækstraten som

funktion af perturbationens bølgelængde. I modsætning til tidligere arbejde omhandlende stabilitetsproblemet er vores modeller anvendelige både over og under den begrænsede strøm.

Derefter udvikler vi en numerisk brat-grænseflademodel, som beskriver væksten af elektroden. Denne model afviger fra de etablerede fasefeltsmodeller, i og med at vores model er anvendelig i det overbegrænsede regime og implementerer elektrodereaktioner på en konsistent måde. Ved at sammenligne vores brat-grænseflademodel med resultaterne fra stabilitetsanalysen, opnår vi en validering af modelopførslen i de indledende stadier af væksten. Nogle foreløbige resultater indikerer at elektrodemorfologien muligivs kan forklares ved hjælp af nogle få nøgleparametre.

Preface

This thesis is submitted as partial fulfillment of the prerequisites for obtaining the degree of Doctor of Philosophy (PhD) at the Technical University of Denmark (DTU). The project was financed by a grant from the Technical University of Denmark, and was carried out at the Department of Physics over a three year period from September 2012 to August 2015. The project was supervised by professor Henrik Bruus, leader of the Theoretical Microfluidics Group (TMF) at the Department of Physics. As part of my studies I visited the group of professor Martin Z. Bazant at Massachusetts Institute of Technology from September 1, 2014 to December 21, 2014.

Firstly, I would like to thank my advisor Henrik Bruus for competent supervision and rewarding discussions of physics, language, and notation. I am thankful to Henrik for welcoming me in his group, and for his successful efforts at making the TMF group a place for physics as well as for fun. Likewise, I would like to thank past and present members of the TMF group, in particular Peter Muller Tribler, Jonas Tobias Karlsen, Mikkel Wennemoes Hvitfeld Ley, Rayisa Moiseyenko, Fabio Garofalo, Mathias Bækbo Andersen, Søren Vedel, and Rune Barnkob. They have all contributed to a great working environment over the last three years.

Secondly, I would like to thank professor Martin Z. Bazant and his group at MIT for welcoming me during my visit in the fall 2014. My work on electrodeposition started during my time at MIT, and particularly Martin Z. Bazant and Edwin Khoo provided valuable input to that work.

I would like to thank two groups of friends for support and diversion during my PhD studies. A great thanks go to my former roommates Dea, Daniel, Marie, Nils, and Niels Ole, who have provided a fun and relaxing home and ensured that I occasionally associate with people outside the 3rd quadrant at DTU. I am equally thankful to my former study mates Søren, Nis, Lene, Lasse, Qi, Nikolaj, Nikolai and Anil, who, besides providing social events, have helped with many good discussions about the troubles of being a PhD student.

Finally, I would like to thank my parents Karen and Flemming and my sister Cecilie for providing a safe and loving home, and for having patience with a little curious boy who always had one more question to ask.

Kongens Lyngby, 31 August 2015

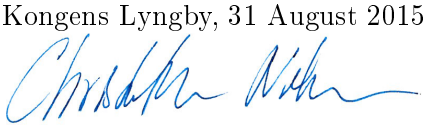

Christoffer P. Nielsen

Table of Contents

List of Figures

List of Tables

List of symbols

Symbol	Description	Unit/value/definition
a	Radius of an atom in a solid metal	m
α_a	Anodic charge-transfer coefficient	
α_c	Cathodic charge-transfer coefficient	
α	Channel aspect ratio	$\frac{R}{L}$
B	Scaling parameter	$\left(\frac{\bar{\lambda}_\mathrm{D}^2}{2(\tilde{J}_+ + \tilde{J}_\mathrm{w})}\right)^{1/3}$
β	Instability driving force	
c_i	Concentration of chemical species i	m^{-3}
$c_\mathrm{H}, [\mathrm{H_3O^+}], [\mathrm{H^+}]$	Hydronium concentration	m^{-3}
$c_\mathrm{OH}, [\mathrm{OH^-}]$	Hydroxide concentration	m^{-3}
C_s	Stern capacitance	$2.9\,\mathrm{F/m^2}$
c_0	Reference salt concentration	m^{-3}
c_i^out	Concentration just outside the EDL	m^{-3}
c_i	Activity of chemical species i	
c_w	Water-ion concentration	$\delta_H c_\mathrm{H} + c_\mathrm{OH}$
c_i^ex	Excess ion concentration	m^{-3}
c_a	Acid concentration	m^{-3}
c_b	Base concentration	m^{-3}
D_i	Diffusivity of chemical species i	$\mathrm{m^2/s}$
δ_H	Diffusivity ratio	$\frac{}{D_\mathrm{OH}}$
δ_inst	Instability length scale	m
δ_char	Characteristic length scale of the electrodeposits	m
η	Dynamic viscosity of water	$1 \times 10^{-3}\,\mathrm{Pas}$
ϵ_0	Vacuum permittivity	$8.85 \times 10^{-12}\,\mathrm{F/m}$
ϵ_w	Permittivity of water	$78\epsilon_0$
ϵ_m	Permittivity in a membrane	F/m
e	Elementary charge	$1.602 \times 10^{-19}\,\mathrm{C}$
ϵ_P	Porosity of membrane	
$\boldsymbol{E}$	Electric field vector	V/m
E	Electric field component	V/m
η	Overpotential	V

Symbol	Description	Unit/value
EDL	Electric double layer	
ESC	Extended space-charge region	
F	Helmholtz Free energy	J
$\boldsymbol{f}$	Body force density	$\mathrm{N/m^3}$
f_0	Normalization body force density	$\frac{c_0 k_\mathrm{B} T}{R}$
GCP	General concentration polarization framework	
γ	Surface energy	$\mathrm{Jm^{-2}}$
Γ	Perturbation growth rate	$\mathrm{s^{-1}}$
Γ_max	Growth rate of the most unstable perturbation	$\mathrm{s^{-1}}$
Δh	Depth of electrode in the z-direction	m
I_+^surf	Surface current density	$\mathrm{m^{-2}s^{-1}}$
$\boldsymbol{J}_i$	Current density of chemical species i	$\mathrm{m^{-2}s^{-1}}$
J_lim	Limiting current density	$\frac{2D_+c_0}{L}$
J_w	Water-ion current	$J_\mathrm{H} - J_\mathrm{OH}$
j	Current fraction	$\frac{\tilde{J}_+ + \tilde{J}_\mathrm{w}}{\tilde{J}_+ - \tilde{J}_\mathrm{w}}$
k_B	Boltzmann constant	$1.38 \times 10^{-23}\,\mathrm{J/K}$
K_w	Self-ionization constant of water	$1 \times 10^{-14}\,\mathrm{M^2}$
k_0	Reaction constant	$\mathrm{m^{-3}s^{-1}}$
K_0	Dimensionless reaction constant	$\frac{k_0}{2D_+c_0/L}$
k	Perturbation wavenumber	$\mathrm{m^{-1}}$
k_c	Critical perturbation wavenumber	$\mathrm{m^{-1}}$
k_max	Most unstable perturbation wavenumber	$\mathrm{m^{-1}}$
λ_D	Debye length	m
L	System dimension	m
$\bar{\lambda}_\mathrm{D}$	Scaled Debye length	$\frac{\lambda_\mathrm{D}}{L}$, $\frac{\lambda_\mathrm{D}}{R}$
l_EDL	Width of the electric double layer	m
l_ESC	Width of the extended space-charge region	m
λ_G	Gouy length	m
λ	Perturbation wavelength	m
λ_max	Most unstable perturbation wavelength	m
λ_c	Critical perturbation wavelength	m
L_Γ	Instability length scale	m
ΔL	Width of deposited layer in a time Δt	m
ΔL_rand	Random electrode growth in a time Δt	m
μ_i	Electrochemical potential of chemical species i	J
μ_i^0	Reference electrochemical potential of species i	J
$\boldsymbol{n}$	Normal vector	
n	Normalized auto-dissociation constant	$\frac{\sqrt{K_\mathrm{w}}}{c_0}$
Ω	Water-ion concentration at the entrance to the EDL	
p	Pressure	Pa
ϕ	Electric potential	V
Pe_i	Péclet number	$\frac{U_0 L}{D_i}$
ϕ_eq	Equilibrium potential	V
ϕ_b	Bulk potential	V
ϕ_d	Diffuse layer potential	V

Symbol	Description	Unit/value
ϕ_e	Electric potential of the electrons inside the metal electrode	V
$\Delta\phi_\mathrm{DL}$	Potential difference over the electric double layer	V
p_0	Microfluidic pressure scale	$\frac{\eta U_0}{R}$
$\langle P_n \rangle$	Average power spectrum of the n'th wavelength component	m^2
QCD	Quasi-uniform charge density distribution	
Q	Mean number of ions arriving in a bin in a time Δt	
ρ	Mass density of water	$1 \times 10^3\,\mathrm{kg/m^3}$
ρ_el	Space-charge density	$\mathrm{C/m^3}$
R_i	Reaction rate of chemical species i	$\mathrm{m^{-3}s^{-1}}$
ρ_m	Space charge density of membrane	$\mathrm{C/m^3}$
R	Radius of microchannel	m
$\boldsymbol{r}$	Position vector	m
r	Radial coordinate	m
ρ_s	Cross-sectionally averaged surface charge density	$-\frac{2\sigma}{ec_0R}$
$\boldsymbol{\sigma'}$	Viscous stress tensor	Pa
σ	Surface charge density	$\mathrm{C/m^2}$
s	Arc length along electrode interface	m
T	Temperature	300 K
τ	Tortuosity of membrane	
t_diff	Diffusive time scale	$\frac{L^2}{2D_+}$
t_ambi	Ambipolar diffusion time	$\frac{L^2}{2}\left(\frac{1}{D_+}+\frac{1}{D_-}\right)$
t_Γ	Instability time scale	s
θ	Tangential angle at electrode interface	
t_tot	Total deposition time	s
$\boldsymbol{u}$	Velocity vector	m/s
u, v	Velocity components	m/s
U_0	Electro-osmotic velocity scale	$\frac{\epsilon_\mathrm{w}V_\mathrm{T}^2}{\eta L}$
u_eo	Electro-osmotic velocity	$-\frac{\epsilon\zeta E}{\eta}$
u_do	Diffusioosmotic velocity	$\mathrm{ms^{-1}}$
$V_\mathrm{T} = \frac{k_\mathrm{B}T}{e}$	Thermal voltage	25.7 mV
V_0	Bias voltage	V
W	Width of system	m
$\boldsymbol{e}_x, \boldsymbol{e}_y, \boldsymbol{e}_r$	Unit vectors	
ξ	Phase-field parameter	
z_i	Valence of chemical species i	
ζ	Potential at the compact layers outer edge	V
Z	Ion valence	
∂_i	Partial derivative	$\mathrm{m^{-1}}$

Chapter 1

Introduction

1.1 Concentration polarization and electrodeposition

Ion transport across an ion-selective interface, such as a nanochannel, a metal electrode or a permselective membrane, has found numerous applications in, e.g., electrodialysis, desalination, electroplating, battery and fuel cell technology, chemical separation, electrochemistry, and microfluidic systems [89, 57, 95, 129, 73, 118, 32, 59, 58, 15, 56, 96, 36, 70, 95, 105, 88]. A characteristic feature of ion transport across ion-selective interfaces is the phenomenon known as concentration polarization, in which the concentration of charge carriers next to the interface depletes, leading to a decrease in conductivity. In the classical linear modeling of the problem, the conductivity goes to zero as the voltage drop over the system is increased, and the current approaches the so-called limiting current. However, when the driving force becomes sufficiently large, the system may enter a nonlinear regime with additional transport phenomena, which give rise to an overlimiting current. Examples of these nonlinear transport phenomena are the development of an extended space-charge region [113, 98, 133, 134, 16, 8], electro-osmotic instabilities [99, 100, 101, 102, 104, 25, 20], water splitting [97, 54, 90, 4], current-induced membrane discharge [5], and surface conduction in microstructures [27, 136, 26, 22]. Understanding these complex transport phenomena is of fundamental scientific interest, but also of great importance to the many applications in which concentration polarization plays a role. Both experimentally and theoretically there are, however, significant obstacles to the development of this understanding. Experimentally, it is difficult to study concentration polarization in a controlled way, due to the small length scales involved and the intermixing of diverse chemical and physical effects. Theoretically, the nonlinearities in the governing equations, the disparate length scales, and the large number of coupled physical effects conspire to create problems which are difficult to treat using standard analytical methods.

In this thesis we use a combination of numerical and analytical methods to study three of the listed nonlinear transport phenomena, namely the development of an extended space-charge region, water splitting, and transport in a microchannel. The two modeling methods complement each other very well, as the full numerical simulations deliver valuable input to the analytical models, which in turn helps structure and interpret the numerical results.

Also, the analytical models provide a generalization of the specific numerical results to a broader class of systems.

In the final two chapters of the thesis we go beyond merely studying the transport in the electrolyte, and extend our treatment to include growth at metal electrodes during electrodeposition. Electrodeposition is a particularly interesting and challenging concentration polarization problem, due to the tendency of the electrode interface to become morphologically unstable and develop ramified growth patterns [39, 91, 122, 51, 86]. It has been pointed out that the nonlinear overlimiting regime is highly relevant for these growth processes [14, 96]. However, due to limitations of the established modeling methods, ramified electrode growth has, so far, primarily been investigated in the linear underlimiting regime [106, 17, 67, 31]. To include the nonlinear effects occurring at overlimiting current, as well as some important effects pertaining to reaction kinetics, we develop a numerical sharp-interface model of electrodeposition and ramified growth. This model, we believe, could aid in the development of a more quantitative understanding of electrodeposits and their morphology.

1.2 Outline of the thesis

This thesis is based on my four research papers listed in Section 1.3.1. Some of the material, in particular from my first paper, has been reworked to create a more cohesive and, I think, readable thesis. The research papers themselves are included in Chapters E to H. Below follows a short outline of the contents of each chapter.

Chapter 2: Basic theory In this chapter we present the basic theory employed in the remainder of the thesis. This includes the field equations governing ion transport, electrostatics, and fluid flow, as well as some simple concepts and results, which follow from the field equations. We also give a basic treatment of concentration polarization and discuss some important classes of ion-selective interfaces.

Chapter 3: Numerical techniques Concentration polarization often involves several nonlinearly coupled physical effects. This makes the typical concentration polarization problem exceedingly difficult to solve by analytical means, and we therefore rely on numerical simulations to solve many of the problems in this thesis. These simulations are made using the commercial finite element method (FEM) software COMSOL MULTIPHYSICS 4.3a. In this chapter we give a brief introduction to the finite element method.

Chapter 4: Concentration polarization: Beyond the local electroneutrality assumption In the most basic treatment of concentration polarization the electrolyte is treated as locally electroneutral. This constrains the concentration of charge carriers to exactly follow the concentration of the stationary ion-species, and it entails that the current can not exceed the limiting current. In this chapter we go beyond the local electroneutrality assumption, and derive an analytical model for concentration polarization valid at both under- and overlimiting current.

Chapter 5: Concentration polarization in a microchannel Due to the importance of surface effects, ion transport in a microchannel differs markedly from transport in a bulk system. Even in the depleted region, a current can run inside the electric double layers, leading to an overlimiting current. The transport properties of the system can be further modified by fluid flow, resulting from the force which the electric field exerts on the electric double layers. In this chapter we set up a full numerical model to study concentration polarization in a microchannel, and we derive analytical models valid in the limit of long and narrow microchannels.

Chapter 6: Water splitting at permselective membranes Besides the salt ions, an aqueous electrolyte contains hydronium and hydroxide ions deriving from the autodissociation of water. Ordinarily, the concentration of these water ions is so low that they do not give a significant contribution to the current in a system. During concentration polarization at a permselective membrane, the concentration of water ions may, however, become so large that they start affecting the transport in the system. In this chapter we provide a combined numerical and analytical analysis of this water splitting problem.

Chapter 7: Electrodeposition: Stability analysis When metal ions are deposited onto a metal electrode the, initially, plane electrode interface may go unstable, resulting in a ramified growth pattern. Just when the initial instabilities develop the problem can be treated in terms of a classical linear stability analysis. In this chapter we provide such an analysis.

Chapter 8: Sharp-interface model of electrodeposition The numerical modeling of electrodeposition and ramified growth is a challenging problem, involving both electrolyte transport, reaction kinetics, and moving interfaces. The conventional phase-field methods include much of the important physics, but they are not suitable at overlimiting current and they have a questionable treatment of the electrode reactions. In this chapter we present a novel method of modeling electrodeposition, which implements electrode reactions in a consistent way and is valid at overlimiting current.

Chapter 9: Conclusion and outlook We summarize our work and provide some directions for future research.

1.3 Publications during the PhD studies

I have, together with my advisor Henrik Bruus, published two peer reviewed journal papers (two more are submitted) and three peer reviewed conference contributions. I have presented my work at five international conferences (four oral, one poster).

1.3.1 Peer reviewed journal papers

- C. P. Nielsen and H. Bruus, *Transport-limited water splitting at ion-selective interfaces during concentration polarization*, Phys Rev E **89** (2014), 042405. Enclosed in Chapter E.
- C. P. Nielsen and H. Bruus, *Concentration polarization, surface currents, and bulk advection in a microchannel*, Phys Rev E **90** (2014), 043020. Enclosed in Chapter F.
- C. P. Nielsen and H. Bruus, *Morphological Instability during steady electrodeposition at overlimiting currents*, (submitted to Phys Rev E). Enclosed in Chapter G.
- C. P. Nielsen and H. Bruus, *A sharp-interface model of electrodeposition and ramified growth*, (submitted to Phys Rev E). Enclosed in Chapter H.

1.3.2 Peer reviewed conference contributions

- C. P. Nielsen and H. Bruus, *Dynamics of surface charges and water splitting in microchannels containing nanoporous ion-selective membranes*, MicroTAS, Conference on microsystems, 27-31 Oct 2013, Freiburg, Germany, **poster presentation**.
- C. P. Nielsen and H. Bruus, *Models of hydrodynamic dispersion in an electrolyte moving through a microchannel during concentration polarization*, ELKIN, International Symposium, 20-23 May 2014, Ghent, Belgium, **oral presentation**.
- C. P. Nielsen and H. Bruus, *Sharp-interface model of electrodeposition and dendritic growth*, ISE 17th topical meeting, 31 May - 3 June 2015, Saint-Malo, France, **oral presentation**.

1.3.3 Other scientific contributions

- C. P. Nielsen and H. Bruus, *Overlimiting current in systems with water splitting and an extended space-charge region*, Complex motion in Fluids, International Summer School, 4-10 Aug 2013, Denmark, **oral presentation**.
- C. P. Nielsen and H. Bruus, *Diffusion-limited current to an ion-selective membrane: The role of water splitting and an extended space-charge region*, APS Division of Fluid Dynamics meeting, 24-26 Nov 2013, Pittsburgh, USA, **oral presentation**.
- C. P. Nielsen and H. Bruus, *Numerical and analytical models of concentration polarization in a microchannel*, APS Division of Fluid Dynamics meeting, 23-25 Nov 2014, San Francisco, USA, **oral presentation**.

Chapter 2

Basic theory

In this chapter we present the basic theory employed in the remainder of the thesis. This includes the field equations governing ion transport, electrostatics, and fluid flow, as well as some simple concepts and results, which follow from the field equations. We also give a basic treatment of concentration polarization and discuss some important classes of ion-selective interfaces.

2.1 Field equations

Throughout the thesis we make use of the continuum hypothesis to describe the motion of the liquid and of dissolved particles. In essence this means that instead of tracking the position of each and every particle in a system, we characterize the state of the system using fields, which represent the average value of a quantity in a small probe volume within a short time interval. For more on the continuum hypothesis see Ref. [13]

2.1.1 Transport equations

Consider a chemical species of concentration $c_i = c_i(\boldsymbol{r}, t)$, which depends on both space and time. The concentration at a given place can change in two ways: either if there is a net particle current to or away from that place, or if a chemical reaction takes place which consumes or produces the chemical species. Thus, the concentration field c_i is governed by the conservation equation

$$\partial_t c_i = -\boldsymbol{\nabla} \cdot \boldsymbol{J}_i + R_i, \tag{2.1}$$

where $\boldsymbol{J}_i$ is the current density of the chemical species and R_i is the reaction rate for the production of the chemical species. Frequently, the reaction rate can be neglected and Eq. (2.1) takes on the simpler form

$$\partial_t c_i = -\boldsymbol{\nabla} \cdot \boldsymbol{J}_i. \tag{2.2}$$

We always assume that dissolved salts dissociate completely, and consequently we model the transport of salt ions using Eq. (2.2). The current density $\boldsymbol{J}_i$ is given as

$$\boldsymbol{J}_i = -\frac{D_i}{k_\mathrm{B}T} c_i \boldsymbol{\nabla} \mu_i + c_i \boldsymbol{u}, \tag{2.3}$$

where D_i is the diffusivity of the i'th chemical species, μ_i is its electrochemical potential, and $\boldsymbol{u}$ is the velocity field of the liquid. For dilute solutions the electrochemical potential is just the sum of an ideal gas entropic term and the electrostatic energy

$$\mu_i = \mu_i^0 + k_\mathrm{B}T \ln(c_i/c_0) + z_i e \phi. \tag{2.4}$$

Here, μ_i^0 is a reference chemical potential, c_0 is a reference concentration, z_i is the valence of the chemical species, e is the unit charge, and ϕ is the electrostatic potential. Since it is mainly differences in electrochemical potential that matter, the reference chemical potential μ_i^0 is often unimportant and simply set to zero. Inserting Eq. (2.4) in Eq. (2.3) yields

$$\boldsymbol{J}_i = -D_i \boldsymbol{\nabla} c_i - D_i \frac{z_i e}{k_\mathrm{B}T} c_i \boldsymbol{\nabla} \phi + c_i \boldsymbol{u}, \tag{2.5}$$

where the diffusive, electromigrative, and advective currents now occur as separate terms. It depends on the given problem which of the two forms Eq. (2.3) and Eq. (2.5) is more convenient.

2.1.2 Electrostatics

In electrokinetics induced magnetic fields are usually negligible. This means that the electric field can be written in terms of the electrostatic potential $\boldsymbol{E} = -\boldsymbol{\nabla}\phi$, which is governed by the Poisson equation,

$$\boldsymbol{\nabla} \cdot (-\epsilon \boldsymbol{\nabla} \phi) = \rho_\mathrm{el}. \tag{2.6}$$

Here, ϵ is the permittivity of the medium, which we will always assume to be constant, and ρ_el is the space charge density

$$\rho_\mathrm{el} = \sum_i z_i e c_i. \tag{2.7}$$

2.1.3 Hydrodynamics

Like the previously introduced field equations, the equations governing the motion of a fluid are continuity equations, expressing the conservation of mass and momentum. The first of these is simply called the continuity equation and reads

$$\partial_t \rho = -\boldsymbol{\nabla} \cdot (\rho \boldsymbol{u}), \tag{2.8}$$

where ρ is the mass density of the fluid. Liquids are only weakly compressible, and for the velocity fields encountered in this thesis they can to a good approximation be treated as incompressible. Eq. (2.8) therefore simplifies to

$$0 = -\boldsymbol{\nabla} \cdot \boldsymbol{u}. \tag{2.9}$$

The momentum density at a given point in a fluid can change by advection of momentum or by application of external forces. The momentum conservation equation therefore has the form

$$\partial_t(\rho \boldsymbol{u}) = \boldsymbol{\nabla} \cdot \left[-\rho \boldsymbol{u}\boldsymbol{u} - p\boldsymbol{I} + \boldsymbol{\sigma}'\right] + \boldsymbol{f}, \tag{2.10}$$

where $\rho\boldsymbol{u}\boldsymbol{u}$ is the advection term, p is the pressure in the fluid, $\boldsymbol{\sigma}'$ is the viscous stress tensor, and $\boldsymbol{f}$ is the sum of any other body force densities. The body forces encountered in this work are gravity $\rho\boldsymbol{g}$ and the electrostatic force density $-\rho_{\mathrm{el}}\boldsymbol{\nabla}\phi$. For an incompressible fluid the viscous stress tensor has the simple form

$$\boldsymbol{\sigma}' = \eta\left[\boldsymbol{\nabla}\boldsymbol{u} + (\boldsymbol{\nabla}\boldsymbol{u})^T\right], \tag{2.11}$$

where η is the dynamic viscosity and $(\cdot)^T$ denotes the transpose of $(\cdot)$. We only investigate systems with small length scales and velocities, meaning that the Reynolds number is much smaller than unity. The nonlinear term in Eq. (2.10) is thus negligible, and the equation reduces to

$$\rho\partial_t \boldsymbol{u} = \boldsymbol{\nabla} \cdot \left[-p\boldsymbol{I} + \boldsymbol{\sigma}'\right] + \boldsymbol{f}. \tag{2.12}$$

Inserting Eq. (2.11) in Eq. (2.12) and applying Eq. (2.9) we finally arrive at the Stokes equation,

$$\rho\partial_t \boldsymbol{u} = -\boldsymbol{\nabla}p + \eta\nabla^2\boldsymbol{u} + \boldsymbol{f}. \tag{2.13}$$

For analytical calculations we generally make use of Eq. (2.13), while Eq. (2.12) is preferable for numerical calculations.

2.2 Nondimensionalization

Throughout this thesis we shall frequently make use of nondimensional variables and equations. This has the dual purpose of putting the equations and expressions in a more succinct form, which at the same time better reveals the important physics of the problem. We denote nondimensional variables by a tilde $\sim$.

Considering the ion current density Eq. (2.5), we see that the thermal voltage $V_{\mathrm{T}} = k_{\mathrm{B}}T/e$ is a natural scale for the electrostatic potential. Likewise, we identify the thermal energy $k_{\mathrm{B}}T$ as the natural scale for the electrochemical potential. There is no intrinsic scale for the ion concentrations, so typically the concentration fields are normalized with a reference concentration c_0. This could for instance be the initial concentration in the studied system or the concentration in a connected reservoir. Typically, we normalize

the spatial coordinates with a characteristic system dimension L. The dimensional and nondimensional variables are thus related as

$$\phi = V_{\mathrm{T}}\tilde{\phi}, \tag{2.14}$$
$$\mu_i = k_{\mathrm{B}}T\tilde{\mu}_i, \tag{2.15}$$
$$c_i = c_0\tilde{c}_i, \tag{2.16}$$
$$\boldsymbol{r} = L\tilde{\boldsymbol{r}}, \tag{2.17}$$
$$\boldsymbol{\nabla} = \frac{1}{L}\tilde{\boldsymbol{\nabla}}. \tag{2.18}$$

Plugging these into Eq. (2.5) and rearranging we find

$$\frac{L}{D_i c_0}\boldsymbol{J}_i = -\tilde{\boldsymbol{\nabla}}\tilde{c}_i - z_i\tilde{c}_i\tilde{\boldsymbol{\nabla}}\tilde{\phi} + \frac{U_0 L}{D_i}\tilde{c}_i\tilde{\boldsymbol{u}}, \tag{2.19}$$

where a velocity scale U_0 was also introduced. This expression suggests the introduction of normalized currents

$$\tilde{\boldsymbol{J}}_i = \frac{L}{2D_+ c_0}\boldsymbol{J}_i, \tag{2.20}$$

where the factor of 2 was included for reasons that will soon become clear. Also, we introduce the Péclet numbers

$$\mathrm{Pe}_i = \frac{U_0 L}{D_i}, \tag{2.21}$$

which measures the strength of advection relative to diffusion. With these definitions Eq. (2.19) becomes

$$2\frac{D_+}{D_i}\tilde{\boldsymbol{J}}_i = -\tilde{\boldsymbol{\nabla}}\tilde{c}_i - z_i\tilde{c}_i\tilde{\boldsymbol{\nabla}}\tilde{\phi} + \mathrm{Pe}_i\tilde{c}_i\tilde{\boldsymbol{u}}. \tag{2.22}$$

The factor of D_+/D_i in front is a result of using the same normalization for all the currents. Inserting the current densities in Eq. (2.2) yields

$$\partial_{\tilde{t}}\tilde{c}_i = -\tilde{\boldsymbol{\nabla}}\cdot\tilde{\boldsymbol{J}}_i, \tag{2.23}$$

where the time was normalized with the diffusive time scale $t_{\mathrm{diff}} = L^2/(2D_+)$.

The remainder of the governing equations can be nondimensionalized in similar fashion. At this point we proceed with the electrostatic problem, and postpone the nondimensionalization of the hydrodynamic problem to Chapter 5.

2.3 The electric double layer

Normalizing the Poisson equation yields some insights into the coupling between concentration fields and the electric potential. It also serves as a good starting point for discussing

the so-called electric double layer. Inserting $\phi = V_{\mathrm{T}}\tilde{\phi}$ and $c_i = c_0\tilde{c}_i$ in Eq. (2.6) and rearranging we find

$$\nabla^2\tilde{\phi} = -\frac{e^2 c_0}{k_{\mathrm{B}}T\epsilon}\sum_i z_i\tilde{c}_i = -\frac{1}{2\lambda_{\mathrm{D}}^2}\sum_i z_i\tilde{c}_i. \tag{2.24}$$

In the last expression we introduced the so-called Debye length

$$\lambda_{\mathrm{D}} = \sqrt{\frac{k_{\mathrm{B}}T\epsilon}{2e^2 c_0}}, \tag{2.25}$$

which is a characteristic length scale for the coupling between electrostatics and the ion concentrations. For most systems the Debye length is tiny. For instance, in the case of a binary monovalent salt (e.g. sodium chloride) of concentration $c_0 = 1$ mM in water at room temperature the Debye length is just 9.6 nm. Because the Debye length is so small, any small deviation from charge neutrality will cause the right hand side in Eq. (2.24) to be huge. This in turn creates a very large electric field, which tends to restore charge neutrality. For this reason, the majority of an electrokinetic system is practically electroneutral in most cases.

One exception to this rule is when the electric potential varies over a distance comparable to the Debye length. In that case the Laplacian in Eq. (2.24) balances the $1/\lambda_{\mathrm{D}}^2$ term, and it is possible to build up a non-negligible charge density. As a concrete example of this, we consider a binary monovalent salt in a quiescent liquid in contact with a planar wall at $y = 0$ with surface charge $\sigma < 0$, as seen in Fig. 2.1. To screen the surface charges, the cations move towards the interface and the anions move away from the interface. The hydration shell of the ions, as well as an adsorbed monolayer of solvent molecules at the wall, prevent the ions from moving closer to the wall than the so-called outer Helmholtz plane (OHP). The region between the wall and the outer Helmholtz plane is called the compact layer, and since it is close to electroneutral it can be modeled as having a constant capacitance, the Stern capacitance C_{S}. In addition to the potential variation in the compact layer, the potential varies outside the OHP in the diffuse layer. Here, the standard transport equations from Section 2.1.1 apply, and since the system is in equilibrium Eq. (2.23) yields a simple Boltzmann distribution of the ions,

$$\tilde{c}_{\pm} = \mathrm{e}^{\mp\tilde{\phi}}. \tag{2.26}$$

Here, $\tilde{c}_+$ is the cation concentration and $\tilde{c}_-$ is the anion concentration. Both are normalized with the concentration far away from the wall, where the electric potential is zero. Inserting in Eq. (2.24) yields the so-called Poisson–Boltzmann equation,

$$\partial_y^2\tilde{\phi} = -\frac{1}{2\lambda_{\mathrm{D}}^2}\left[\mathrm{e}^{-\tilde{\phi}} - \mathrm{e}^{\tilde{\phi}}\right] = \frac{1}{\lambda_{\mathrm{D}}^2}\sinh(\tilde{\phi}). \tag{2.27}$$

In the Debye–Hückel limit $|\tilde{\phi}| \lesssim 1$ Eq. (2.27) simplifies to a simple linear equation,

$$\partial_y^2\tilde{\phi} = \frac{1}{\lambda_{\mathrm{D}}^2}\tilde{\phi}, \tag{2.28}$$

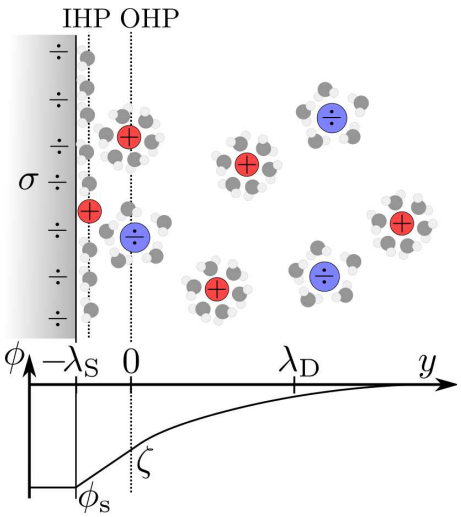

Figure 2.1: Sketch of the electric double layer and potential distribution outside a negatively charged wall. A layer of solvent and ions is directly adsorbed on the wall, and their locus defines the inner Helmholtz plane (IHP). The ions in solution have a distance of closest approach to the wall, due to the adsorbed layer end the hydration shell of the ions. This closest distance of approach defines the outer Helmholtz plane (OHP).

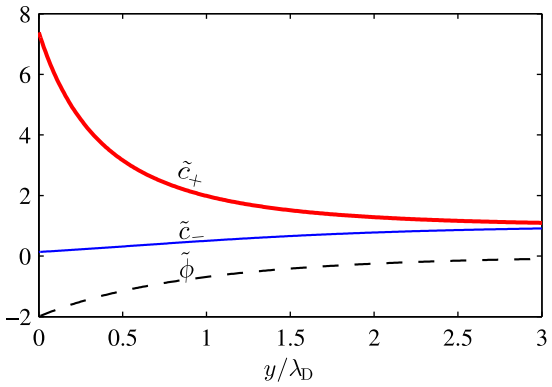

Figure 2.2: Plot of the concentration and potential distribution in the diffuse part of the electric double layer for $\tilde{\zeta} = -2$.

with the solution

$$\phi = \zeta \mathrm{e}^{-y/\lambda_\mathrm{D}}. \tag{2.29}$$

The zeta-potential ζ is the potential at the OHP relative to the bulk liquid. Since the compact layer is charge neutral, the surface charge at the OHP is the same as at the wall. Applying the electrostatic boundary condition $\boldsymbol{n} \cdot \epsilon \boldsymbol{E} = \sigma$, the zeta-potential can therefore be related to the surface charge density,

$$\zeta = \frac{\lambda_\mathrm{D}}{\epsilon}\sigma. \tag{2.30}$$

In the general case, outside the Debye–Hückel limit, a solution to the nonlinear Poisson-Boltzmann equation can also be obtained. This solution is given as

$$\phi = 4V_\mathrm{T}\mathrm{artanh}\left\{\tanh\left(\frac{\zeta}{4V_\mathrm{T}}\right)\mathrm{e}^{-y/\lambda_\mathrm{D}}\right\}, \tag{2.31}$$

and is known as the Gouy-Chapman solution. In Fig. 2.2 the electric potential and the concentration fields are plotted in the diffuse layer for $\tilde{\zeta} = -2$.

Together, the compact layer and the diffuse layer form what is known as the electric double layer (EDL). However, in the systems treated in this thesis it is only necessary to

consider the diffuse part of the electric double layer. Thus, we shall exclusively use EDL and 'electric double layer' to refer to the diffuse part of the electric double layer.

Ostensibly, the above treatment relies on the EDL being in equilibrium. However, even if a current is running in the system the EDL may be well described by an equilibrium model. Considering the normalized cation current density,

$$2\tilde{J}_+ = -\tilde{c}_+\partial_{\tilde{y}}\tilde{\mu}_+ = -\partial_{\tilde{y}}\tilde{c}_+ - \tilde{c}_+\partial_{\tilde{y}}\tilde{\phi}, \tag{2.32}$$

we see that in equilibrium ($\tilde{J}_+ = 0$) the terms $\partial_{\tilde{y}}\tilde{c}_+$ and $\tilde{c}_+\partial_{\tilde{y}}\tilde{\phi}$ cancel each other. Inside the EDL, the fields vary over the Debye length λ_D, and the terms in Eq. (2.32) therefore scale as

$$2\tilde{J}_+ \sim 2, \tag{2.33a}$$

$$\partial_{\tilde{y}}\tilde{c}_+ \sim \frac{L}{\lambda_\mathrm{D}} = \frac{1}{\bar{\lambda}_\mathrm{D}}, \tag{2.33b}$$

$$\tilde{c}_+\partial_{\tilde{y}}\tilde{\phi} \sim \frac{L}{\lambda_\mathrm{D}} = \frac{1}{\bar{\lambda}_\mathrm{D}}, \tag{2.33c}$$

where we introduced the scaled Debye length $\bar{\lambda}_\mathrm{D} = \lambda_\mathrm{D}/L$. For most systems, λ_D is tiny compared to the system dimension L, so each of the terms $\partial_{\tilde{y}}\tilde{c}_+$ and $\tilde{c}_+\partial_{\tilde{y}}\tilde{\phi}$ are very much larger than their difference $2\tilde{J}_+$. Thus, the dominant balance remains $\partial_{\tilde{y}}\tilde{c}_+ + \tilde{c}_+\partial_{\tilde{y}}\tilde{\phi} \approx 0$, and a current only gives a small perturbation to the equilibrium distribution. A similar scaling argument shows that the change in electrochemical potential across the EDL is of order $\Delta\tilde{\mu}_+ \sim 2\tilde{J}_+\bar{\lambda}_\mathrm{D}$, i.e. basically negligible.

2.4 Electro-osmotic flow

The net charge density in the EDL makes a coupling from the ion transport problem to the hydrodynamic problem possible. The flow resulting from this coupling is called an electro-osmotic flow.

Consider the problem from before, where an infinite planar wall is located at $y = 0$. The wall is held at the potential ζ relative to the bulk liquid at infinity. The electrostatic force density will pull the liquid towards the wall, but since the liquid cannot pass through the wall a pressure distribution builds up, which exactly cancels the electrostatic force. The result is that the liquid remains quiescent. Now, we alter the system by applying a constant electric field in the x-direction,

$$\boldsymbol{E} = E\boldsymbol{e}_x. \tag{2.34}$$

In the x-direction there are no obstacles which hinder the flow of the liquid, so there is no pressure build up that can counteract the electric force. For simplicity, we assume that the system has reached a steady state, so that the time derivative in Eq. (2.13) disappears. We have already argued that there is no y-component of the velocity field, so we only consider the x-component of, Eq. (2.13)

$$0 = -\partial_x p + \eta\nabla^2 u + \rho_\mathrm{el}E, \tag{2.35}$$

where u is the x-component of $\boldsymbol{u}$. The x-derivatives vanish since the system is invariant in the x-direction. Using Eq. (2.6) to express ρ_{el} in terms of ϕ we find

$$0 = \eta \partial_y^2 u - \epsilon E \partial_y^2 \phi, \tag{2.36}$$

which upon application of the boundary conditions $u(0) = 0$, $\phi(0) = \zeta$ and $\partial_y u|_\infty = 0$, $\phi(\infty) = 0$ yields

$$u = \frac{\epsilon E}{\eta}(\phi - \zeta). \tag{2.37}$$

We see that far away from the wall, compared to the Debye length, the velocity takes on a constant value,

$$u_{\text{eo}} = -\frac{\epsilon \zeta E}{\eta}. \tag{2.38}$$

This velocity is known as the Helmholtz–Smoluchowski velocity or, simply, the electro-osmotic velocity. In any real system of finite size there will of course be deviations from the idealized behavior outlined above. For more on this see Chapter 5.

2.5 Concentration polarization

All of the phenomena investigated in this thesis have in common that they occur in systems exhibiting concentration polarization. Concentration polarization takes place when an ion current is driven towards an interface, which blocks one ion species and allows the other to pass. Such an interface could for instance be an electrode made of the cation metal, or it could be a permselective membrane which derives its ion-selectivity from charged surface groups in the membrane matrix.

We consider a simple model system composed of a binary monovalent electrolyte, bounded by a reservoir of salt concentration c_0 on one side and an ion-selective interface at the other. At this stage we will not worry about why the interface is ion-selective, but merely state that, for some reason or another, it blocks the negative ions while allowing the positive ions to pass. Also, it is possible to control the electrostatic potential at the ion-selective interface relative to the reservoir. A sketch of the system is shown in Fig. 2.3. In simple terms, what happens during concentration polarization is the following: The anions are transported away from the interface by the electric field, and since the interface blocks the anions, they can not be resupplied from the right. The anion concentration therefore decreases gradually, until a concentration distribution where diffusion compensates electromigration is established. The cations, on the other hand, can freely pass through the interface, but to preserve local electroneutrality their concentration distribution follows that of the anions. The decrease in anion concentration therefore leads to a decrease in cation concentration, and eventually the cation conductivity vanishes entirely and the current saturates at the limiting current. Below we put these notions into more quantitative terms.

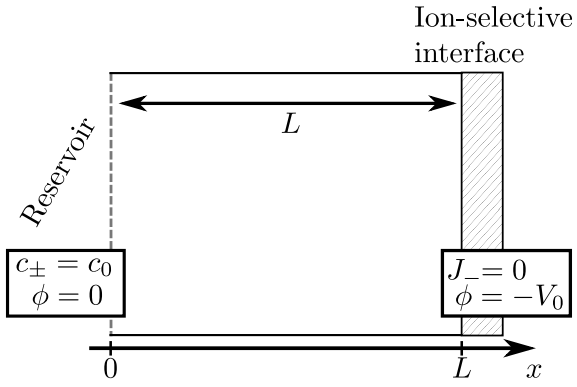

Figure 2.3: Simple concentration polarization model system. To the left is a reservoir of salt concentration c_0 and to the right is an ideal cation selective interface. In between is a compartment of length L.

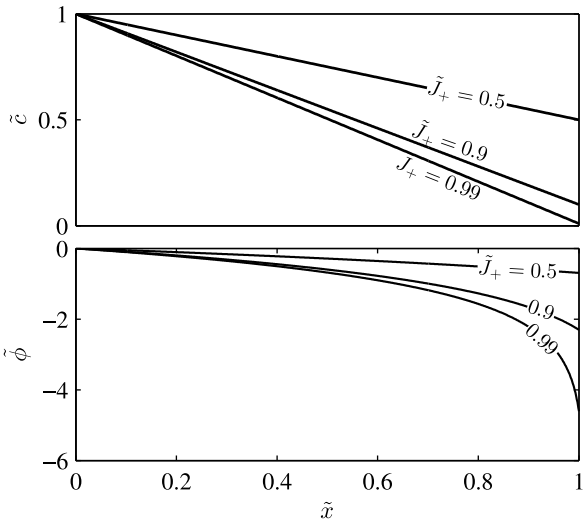

Figure 2.4: Concentration and potential distributions in the simple model system for $\tilde{J}_+ = \{0.5, 0.9, 0.99\}$.

As discussed in Section 2.3 an electrokinetic system tends toward a state of local electroneutrality, so as a first approximation we assume that $\tilde{c}_+ = \tilde{c}_- = \tilde{c}$ everywhere. Local electroneutrality implies a vanishing velocity field, since there is no force to drive a fluid flow. Because the system is translationally invariant in the yz-plane, the problem is effectively one dimensional and the normalized current densities from Eq. (2.22) reduce to

$$2\tilde{J}_+ = -\partial_{\tilde{x}}\tilde{c} - \tilde{c}\partial_{\tilde{x}}\tilde{\phi}, \tag{2.39a}$$

$$2\frac{D_+}{D_-}\tilde{J}_- = -\partial_{\tilde{x}}\tilde{c} + \tilde{c}\partial_{\tilde{x}}\tilde{\phi}. \tag{2.39b}$$

The anions can not pass through the ion-selective interface, so in the simple case of steady-state the anion current J_- is zero everywhere in the system. In that case Eq. (2.39b) yields a Boltzmann distribution of the ions,

$$\tilde{c} = \mathrm{e}^{\tilde{\phi}}. \tag{2.40}$$

Inserting this expression in Eq. (2.39a) we find that

$$2\tilde{J}_+ = -2\partial_{\tilde{x}}\tilde{c} \quad \Rightarrow \quad \tilde{c} = 1 - \tilde{J}_+\tilde{x}, \tag{2.41}$$

where the integration constant is due to the fixed reservoir concentration $\tilde{c}(0) = 1$. The potential in the system follows from Eq. (2.40),

$$\tilde{\phi} = \ln(1 - \tilde{J}_+\tilde{x}). \tag{2.42}$$

In Fig. 2.4 the concentration $\tilde{c}$ and potential $\tilde{\phi}$ are plotted for $\tilde{J}_+ = \{0.5, 0.9, 0.99\}$.

Setting the potential at the ion-selective interface to $-\tilde{V}_0$ we find the current-voltage characteristic

$$\tilde{V}_0 = -\ln(1 - \tilde{J}_+). \tag{2.43}$$

It is seen that as the current approaches unity, the voltage needed to drive the current diverges. Thus, according to this treatment, the dimensional current can not exceed the so-called limiting current

$$J_{\text{lim}} = \frac{2D_+ c_0}{L}. \tag{2.44}$$

The reason for this limitation is that the ion concentration at the interface, and thus also the conductivity, vanishes when $\tilde{J}_+ = 1$. Such a singular behavior is obviously unphysical and indicates that the model assumptions are no longer valid when $\tilde{J}_+$ approaches unity. Specifically, it is the local electroneutrality (LEN) assumption that breaks down at high currents. This is easily seen by evaluating the charge density from the Poisson equation. The nondimensional Poisson equation (2.24) reads

$$2\bar{\lambda}_{\text{D}}^2 \partial_{\tilde{x}}^2 \tilde{\phi} = -(\tilde{c}_+ - \tilde{c}_-), \tag{2.45}$$

where the position was normalized with L. Inserting the potential expression (2.42) in the left hand side of Eq. (2.45) we find

$$2\bar{\lambda}_{\text{D}}^2 \partial_{\tilde{x}}^2 \tilde{\phi} = -2\bar{\lambda}_{\text{D}}^2 \frac{\tilde{J}_+^2}{(1 - \tilde{J}_+ \tilde{x})^2}. \tag{2.46}$$

The charge density at $\tilde{x} = 1$ is comparable to the cation density when

$$2\bar{\lambda}_{\text{D}}^2 \frac{\tilde{J}_+^2}{(1 - \tilde{J}_+)^2} = 1 - \tilde{J}_+ \quad \Rightarrow \quad \tilde{J}_+ \approx 1 - 2^{1/3} \bar{\lambda}_{\text{D}}^{2/3}, \tag{2.47}$$

so when $\tilde{J}_+$ comes within $\bar{\lambda}_{\text{D}}^{2/3}$ of unity, the LEN assumption starts to break down.

In the analysis above, we omitted the transient period after the application of a voltage, in which the system approaches the new steady-state. Adding the currents (2.39) together we find that the electromigrative terms vanish, and we are left with a simple diffusion current,

$$2J_+ + 2\frac{D_+}{D_-} J_- = -2\partial_x \tilde{c}. \tag{2.48}$$

Inserting this current in the conservation equation (2.23) yields the so-called ambipolar diffusion equation for the ions,

$$\Big(1 + \frac{D_+}{D_-}\Big) \partial_{\tilde{t}} \tilde{c} = \partial_x^2 \tilde{c}. \tag{2.49}$$

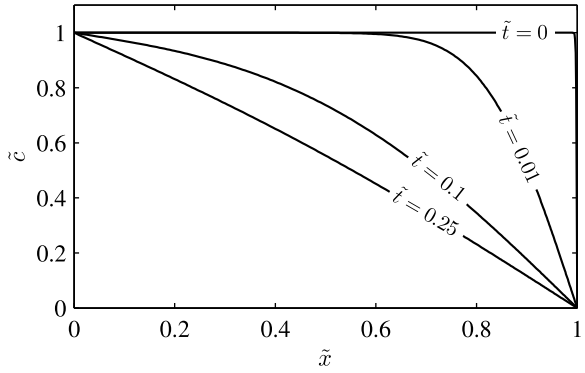

Figure 2.5: Evolution of the concentration distribution in time. At time $\tilde{t}=0$ a bias voltage of $\tilde{V}_0=10$ is applied across the system. The times indicated on the curves are normalized with the ambipolar diffusion time.

Consistent with the previous analysis, the steady-state solution is seen to be a simple linear concentration profile. The characteristic time scale is the ambipolar diffusion time,

$$t_{\text{ambi}}=\frac{L^2}{2}\left(\frac{1}{D_+}+\frac{1}{D_-}\right), \tag{2.50}$$

meaning that the transients will die out on that time scale. In Fig. 2.5 concentration profiles at different times after applying a voltage $\tilde{V}_0=10$ are shown. Just after the voltage is applied only the region close to the ion-selective interface is affected, but as time passes the effect of the applied voltage propagates through the entire system.

2.6 Ion-selective interfaces

In this thesis we consider two types of ion-selective interfaces; permselective membranes and metal electrodes. We begin by describing the permselective membrane, as it is conceptually simpler than the electrode.

2.6.1 Permselective membranes

Permselective membranes come in many forms and are widely applied in industry for filtration and separation purposes [46, 77, 132, 89]. Typically, they consist of a polymer matrix with chemically stable charged surface groups, and large enough pores that water and ions can pass through. The charged surface groups repel ions of like charge, the co-ions, and attract ions of opposite charge, the counter-ions. Here, and in the remainder of the thesis, we assume that the membrane has a negative charge, meaning that the co-ions are anions and the counter-ions are cations. We also assume that the membrane is close to ideal, meaning that the concentration of charged surface groups is much higher than typical ion concentrations.

In a simple model, we can describe an ion-selective membrane as a region with a fixed background charge density $\rho_{\text{m}}<0$, a fixed porosity $0\leq\epsilon_{\text{P}}\leq 1$, and a fixed permittivity

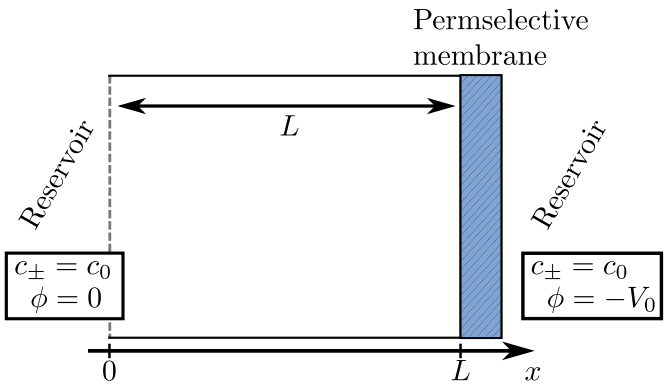

Figure 2.6: Sketch of a simple system exhibiting concentration polarization due to a permselective membrane. To the left and right are reservoirs of salt concentration c_0. In between is a compartment of length L and a permselective membrane.

ϵ_m. To account for the meandering paths taken by the ions inside the membrane the current densities are modified by the so-called tortuosity $\tau \geq 1$,

$$J_\pm = -\frac{\epsilon_\mathrm{P}}{\tau} D_\pm c_\pm \partial_x \mu_\pm. \tag{2.51}$$

Due to the fixed negative background charge the concentration of cations is large inside the membrane and the concentration of anions is small. Outside the membrane the concentration of either ion is roughly the same, and much lower than the cation concentration inside the membrane. The transition between these two concentration distributions happens just around the membrane interface over the characteristic length λ_D. In essence this transition region is simply a variant of the quasi-equilibrium double layer described in Section 2.3. We can therefore relate the ion concentration $c_\pm^\mathrm{in}$ inside the membrane to the concentration $c_\pm^\mathrm{out}$ just outside the membrane via a Boltzmann factor,

$$c_\pm^\mathrm{in} = c_\pm^\mathrm{out} \mathrm{e}^{\mp \Delta\tilde{\phi}}, \tag{2.52}$$

with $\Delta\tilde{\phi}$ being the potential difference from outside to inside the membrane. Using these expressions, the charge density inside the membrane can be written as

$$\rho_\mathrm{el} = \rho_\mathrm{m} + \epsilon_\mathrm{P} e(c_+^\mathrm{in} - c_-^\mathrm{in}) = \rho_\mathrm{m} + \epsilon_\mathrm{P} e(c_+^\mathrm{out} \mathrm{e}^{-\Delta\tilde{\phi}} - c_-^\mathrm{out} \mathrm{e}^{\Delta\tilde{\phi}}). \tag{2.53}$$

Requiring local electroneutrality and using that $c_-^\mathrm{in} \ll c_+^\mathrm{in}$, we find the potential difference over the interface,

$$\Delta\tilde{\phi} = -\ln\left(\frac{|\rho_\mathrm{m}|}{\epsilon_\mathrm{P} e c_+^\mathrm{out}}\right). \tag{2.54}$$

By assumption $|\rho_\mathrm{m}| \gg e c_+^\mathrm{out}$, so this can be a substantial potential difference. Since c_-^in depends exponentially on $\Delta\tilde{\phi}$, the anion concentration, and thus also the anion conductivity, will be tiny inside the membrane. That is, the membrane effectively prevents the anions from passing.

Now, let us consider the role of the permselective membrane in a system undergoing concentration polarization. The system is sketched in Fig. 2.6, and is composed of a reservoir with salt concentration c_0 to the left, a compartment of length L, a permselective membrane, and a reservoir to the right. Using the LEN assumption, the concentration field and electric potential in the compartment are given as Eqs. (2.41) and (2.42),

$$\tilde{c} = 1 - \tilde{J}_+ \tilde{x}, \tag{2.55a}$$

$$\tilde{\phi} = \ln(1 - \tilde{J}_+ \tilde{x}). \tag{2.55b}$$

We normalize the charge density as $\rho_\mathrm{m} = e c_0 \tilde{\rho}_\mathrm{m}$, and write the potential differences over the left and right membrane interface as

$$\Delta\tilde{\phi}_\mathrm{L} = -\ln\left(\frac{|\tilde{\rho}_\mathrm{m}|}{\epsilon_\mathrm{P}\tilde{c}(1)}\right) = -\ln\left(\frac{|\tilde{\rho}_\mathrm{m}|}{\epsilon_\mathrm{P}(1-\tilde{J}_+)}\right), \tag{2.56a}$$

$$\Delta\tilde{\phi}_\mathrm{R} = -\ln\left(\frac{|\tilde{\rho}_\mathrm{m}|}{\epsilon_\mathrm{P}\tilde{c}(2)}\right) = -\ln\left(\frac{|\tilde{\rho}_\mathrm{m}|}{\epsilon_\mathrm{P}}\right). \tag{2.56b}$$

Due to the high cation conductivity inside the membrane, the potential drop over the membrane interior is nearly negligible. The total potential drop $\tilde{V}_0$ over the system is therefore

$$\begin{aligned} -\tilde{V}_0 = \tilde{\phi}(2) &= \tilde{\phi}(1) + \Delta\tilde{\phi}_\mathrm{L} - \Delta\tilde{\phi}_\mathrm{R} \\ &= \ln(1-\tilde{J}_+) - \ln\left(\frac{|\tilde{\rho}_\mathrm{m}|}{\epsilon_\mathrm{P}(1-\tilde{J}_+)}\right) + \ln\left(\frac{|\tilde{\rho}_\mathrm{m}|}{\epsilon_\mathrm{P}}\right) \\ &= 2\ln(1-\tilde{J}_+). \end{aligned} \tag{2.57}$$

In the final result, we notice that the membrane specific parameters $\tilde{\rho}_\mathrm{m}$ and ϵ_P have vanished. Superficially, it thus seems that the membrane does not influence the electric potential drop over the system. While this is not entirely the case, the electric potential at $\tilde{x} = 2$ is actually two times the potential at $\tilde{x} = 1$, it does hint at an important feature of ideal permselective membranes, namely that the electrochemical potential $\tilde{\mu}_+$ is constant across the membrane. This conclusion follows from the vanishing resistivity of the membrane interior and the quasi-equilibrium nature of the interfacial double layers. Eq. (2.57) can therefore be obtained much easier as

$$\begin{aligned} \tilde{\mu}_+(2) &= \tilde{\mu}_+(1) \\ \Rightarrow \ln[\tilde{c}(2)] + \tilde{\phi}(2) &= \ln[\tilde{c}(1)] + \tilde{\phi}(1) \\ \Rightarrow -\tilde{V}_0 &= \ln(1-\tilde{J}_+) + \ln(1-\tilde{J}_+) = 2\ln(1-\tilde{J}_+). \end{aligned} \tag{2.58}$$

It turns out, that in many situations the electrochemical potential is a much more convenient variable than the electric potential. The reason for this, is that the electrochemical potential is the real driving force in the transport equations, whereas the electric potential is only a part of the driving force.

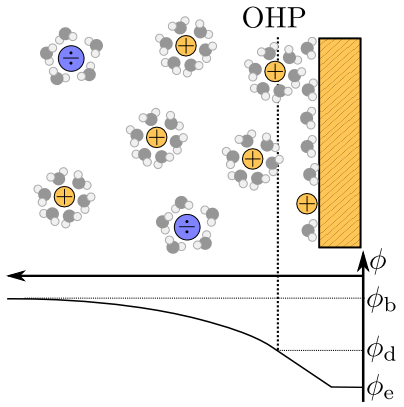

Figure 2.7: Sketch of the electric double layer outside a metal electrode. As we approach the electrode, the potential changes from the bulk potential ϕ_b outside the EDL to the diffuse layer potential ϕ_d at the OHP. The potential changes further over the compact layer to the electrode potential ϕ_e.

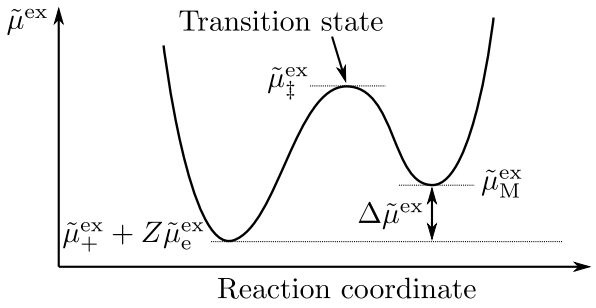

Figure 2.8: Sketch of excess electrochemical potential as a function of reaction coordinate. In the initial and final configuration the excess electrochemical potential has a local minimum. In order to get from one configuration to the other, the reaction complex has to go through the transition state, which is the reaction limiting step.

2.6.2 Metal electrodes

When a metal is brought into contact with an aqueous electrolyte electrochemical reactions can happen at the interface. This either leads to deposition of metal ions from the electrolyte onto the solid metal or dissolution of the solid metal. Exactly how this reaction process proceeds is a matter of much debate, but it is undoubtedly a very complicated process which, among other things, depends on the structure of the interface, the chemical species in solution, and the voltage difference between metal and the aqueous electrolyte [7, 76, 81, 126, 10, 94, 143] . Many of the important features of surface reactions can conveniently be described in the framework of nonequilibrium thermodynamics. The following is based on the account given in Ref. [7].

Consider a system composed of a solid metal electrode in contact with an aqueous electrolyte, which is made by dissolving a salt of the electrode metal. Due to molecules adsorbed onto the electrode surface and the solvation shell of the cations, there is always a small distance which separates the electrode from cations in solution. A sketch of the system is shown in Fig. 2.7. Here, the bulk potential ϕ_b, the diffuse layer potential ϕ_d, and the electrode potential ϕ_e were introduced. The bulk potential is the potential outside the EDL, the diffuse layer potential is the potential at the outer Helmholtz plane, and the electrode potential is the potential in the electrode. The zeta potential ζ, which we encountered in Section 2.3, is related to these potentials as $\zeta = \phi_d - \phi_b$.

The quantities we are interested in are the rate at which cations deposit onto the metal electrode, and the rate at which solid metal dissolves and goes into solution. That is, the rate of the reaction

$$M^{Z+} + Ze^- \leftrightharpoons M, \tag{2.59}$$

where the metal ions M^{Z+} with valence Z react with Z electrons to form a metal atom M in the solid phase. In order for the reaction to occur, the metal ions must shed their solvation shell, move into the adsorbed layer, meet up with electrons coming from the solid metal, and finally deposit onto the metal electrode. While these partial reaction steps are going on, the reaction complex explores a landscape of excess electrochemical potential,

$$\tilde{\mu}_i^{\mathrm{ex}} = \tilde{\mu}_i - \ln(\tilde{c}_i), \tag{2.60}$$

as sketched in Fig. 2.8. The configuration with the highest excess electrochemical potential is rate limiting for the reaction and is denoted the transition state. According to transition state theory, the reaction rate of the forward reaction in Eq. (2.59) depends exponentially on the difference in electrochemical potential between the initial state and the transition state,

$$R_{\rightarrow} \propto \mathrm{e}^{\tilde{\mu}_+ + Z\tilde{\mu}_\mathrm{e} - \tilde{\mu}_\ddagger}. \tag{2.61}$$

Here, $\tilde{\mu}_+$ is the electrochemical potential of cations M^{Z+} in solution, $\tilde{\mu}_\mathrm{e}$ is the electrochemical potential of electrons in the metal electrode, and $\tilde{\mu}_\ddagger$ is the electrochemical potential of the transition state. Similarly, the backwards reaction rate is

$$R_{\leftarrow} \propto \mathrm{e}^{\tilde{\mu}_\mathrm{M} - \tilde{\mu}_\ddagger}, \tag{2.62}$$

with $\tilde{\mu}_\mathrm{M}$ being the electrochemical potential of metal atoms in the solid phase. The total reaction rate of Eq. (2.59) is therefore

$$R = k_0 \left[\mathrm{e}^{\tilde{\mu}_+ + Z\tilde{\mu}_\mathrm{e} - \tilde{\mu}_\ddagger} - \mathrm{e}^{\tilde{\mu}_\mathrm{M} - \tilde{\mu}_\ddagger}\right], \tag{2.63}$$

where k_0 is the rate constant for the reaction. The electrochemical potentials are

$$\tilde{\mu}_+ = \tilde{\mu}_+^0 + \ln(a_+) + Z\tilde{\phi}_\mathrm{d}, \tag{2.64a}$$
$$\tilde{\mu}_\mathrm{M} = \tilde{\mu}_\mathrm{M}^0 + \ln(a_\mathrm{M}), \tag{2.64b}$$
$$\tilde{\mu}_\mathrm{e} = \tilde{\mu}_\mathrm{e}^0 + \ln(a_\mathrm{e}) - \tilde{\phi}_\mathrm{e}, \tag{2.64c}$$

where $\tilde{\mu}_i^0$ are reference electrochemical potentials and a_i are the activities of the chemical species. For an ideal gas $a_i = \tilde{c}_i$.

In equilibrium the electrochemical potential of reactants and product is the same,

$$\tilde{\mu}_+ + Z\tilde{\mu}_\mathrm{e} = \tilde{\mu}_\mathrm{M}, \tag{2.65}$$

and the potential difference over the interface is

$$\Delta\tilde{\phi}_\mathrm{eq} = (\tilde{\phi}_\mathrm{e} - \tilde{\phi}_\mathrm{d})_\mathrm{eq} = \frac{\tilde{\mu}_+^0 + Z\tilde{\mu}_\mathrm{e}^0 - \tilde{\mu}_\mathrm{M}^0}{Z} + \frac{1}{Z}\ln\left(\frac{a_+ a_\mathrm{e}^Z}{a_\mathrm{M}}\right). \tag{2.66}$$

Thus, even when no net reaction is taking place there is a potential drop over the electrode-electrolyte interface. When the system is biased, and a current made to run in the system,

it is therefore natural to express the potential drop across the interface relative to the equilibrium potential. This so-called overpotential $\tilde{\eta}$ is defined as

$$\tilde{\eta} = \Delta\tilde{\phi} - \Delta\tilde{\phi}_{\mathrm{eq}} = \frac{\tilde{\mu}_{\mathrm{M}} - \tilde{\mu}_{+} - Z\tilde{\mu}_{\mathrm{e}}}{Z} = \frac{\Delta\tilde{\mu}}{Z}. \tag{2.67}$$

We model the transition state as an activity term $\ln(a_{\ddagger})$ plus a linear mixing of the excess (i.e. disregarding entropic contributions) electrochemical potentials of initial and final state,

$$\begin{aligned}
\tilde{\mu}_{\ddagger} &= \ln(a_{\ddagger}) + \alpha_{\mathrm{a}}\left[Z\tilde{\phi}_{\mathrm{d}} + \tilde{\mu}^{0}_{+} + Z\tilde{\mu}^{0}_{\mathrm{e}} - Z\tilde{\phi}_{\mathrm{e}}\right] + \alpha_{\mathrm{c}}\tilde{\mu}^{0}_{\mathrm{M}} && (2.68)\\
&= \ln(a_{\ddagger}) + \alpha_{\mathrm{a}}\left[-\Delta\tilde{\mu} - \ln\left(\frac{a_{+}a_{\mathrm{e}}^{Z}}{a_{\mathrm{M}}}\right) + \tilde{\mu}^{0}_{\mathrm{M}}\right] + \alpha_{\mathrm{c}}\tilde{\mu}^{0}_{\mathrm{M}} && (2.69)\\
&= \ln(a_{\ddagger}) - \alpha_{\mathrm{a}}\Delta\tilde{\mu} - \alpha_{\mathrm{a}}\ln\left(\frac{a_{+}a_{\mathrm{e}}^{Z}}{a_{\mathrm{M}}}\right) + \tilde{\mu}^{0}_{\mathrm{M}}. && (2.70)
\end{aligned}$$

Here, the cathodic, α_{c}, and anodic, α_{a}, charge-transfer coefficients measure how close the transition state is to the initial or final state. The charge-transfer coefficients sum to unity, $\alpha_{\mathrm{a}} + \alpha_{\mathrm{c}} = 1$. Inserting the transition state energy in Eq. (2.63) yields

$$R = k_0 \frac{(a_{+}a_{\mathrm{e}}^{Z})^{\alpha_{\mathrm{a}}} a_{\mathrm{M}}^{\alpha_{\mathrm{c}}}}{a_{\ddagger}} \left[\mathrm{e}^{-\alpha_{\mathrm{c}}Z\tilde{\eta}} - \mathrm{e}^{\alpha_{\mathrm{a}}Z\tilde{\eta}}\right]. \tag{2.71}$$

In this thesis, we only consider cases where the cations can be modeled as an ideal gas, $a_{+} = \tilde{c}_{+}$, and where the electron and metal activities are constant, $a_{\mathrm{e}} = 1$, $a_{\mathrm{M}} = 1$. The reaction rate therefore simplifies to

$$R = k_0 \frac{\tilde{c}_{+}^{\alpha_{\mathrm{a}}}}{a_{\ddagger}} \left[\mathrm{e}^{-\alpha_{\mathrm{c}}Z\tilde{\eta}} - \mathrm{e}^{\alpha_{\mathrm{a}}Z\tilde{\eta}}\right], \tag{2.72}$$

known as the Butler–Volmer model of electrode kinetics. By allowing the charge-transfer coefficients to vary with η, this expression could also represent the more elaborate reaction model known as Marcus kinetics [7, 17]. Writing out the overpotentials and introducing the bias voltage $\tilde{V}_0$,

$$\tilde{V}_0 = -\tilde{\phi}_{\mathrm{e}} + \frac{\tilde{\mu}^{0}_{+} + Z\tilde{\mu}^{0}_{\mathrm{e}} - \tilde{\mu}^{0}_{\mathrm{M}}}{Z}, \tag{2.73}$$

Eq. (2.72) can be rewritten as

$$R = k_0 \frac{1}{a_{\ddagger}} \left[\tilde{c}_{+}\mathrm{e}^{\alpha_{\mathrm{c}}Z(\tilde{\phi}_{\mathrm{d}} + \tilde{V}_0)} - \mathrm{e}^{-\alpha_{\mathrm{a}}Z(\tilde{\phi}_{\mathrm{d}} + \tilde{V}_0)}\right]. \tag{2.74}$$

To model the activity $a_{\ddagger}$ of the transition state, we consider the path of the reaction complex during the deposition reaction. Although the detailed path is unknown, it is clear that the reaction complex must in some way adsorb onto the electrode and then merge into the crystal structure. These processes are going on at the metal surface, so the energy

of the reaction complex must be increased by the energy E_{surf} of an atom at the surface. Assuming that the transition state is one of these surface states, we can write the activity of the transition state as

$$a_{\ddagger} = e^{E_{\text{surf}}/k_{\text{B}}T} = e^{\kappa a^3 \gamma / k_{\text{B}}T}. \tag{2.75}$$

Here, we expressed E_{surf} as

$$E_{\text{surf}} = \kappa a^3 \gamma, \tag{2.76}$$

where κ is the surface curvature, γ is the surface energy, and a^3 is the volume of an ion.

Frequently, the Butler–Volmer model (2.74) is applied outside the EDL without distinguishing between $\tilde{\phi}_{\text{b}}$ and $\tilde{\phi}_{\text{d}}$, and without accounting for the variations in $\tilde{c}_+$ in the EDL. The concentration $\tilde{c}_+$ at the interface can be related to the concentration $\tilde{c}_+^{\text{out}}$ outside the double layer as

$$\tilde{c}_+ = \tilde{c}_+^{\text{out}} \mathrm{e}^{-Z\Delta\tilde{\phi}_{\text{EDL}}}, \tag{2.77}$$

where $\Delta\tilde{\phi}_{\text{EDL}} = \tilde{\phi}_{\text{d}} - \tilde{\phi}_{\text{b}}$ is the potential difference over the EDL. The total potential difference $\Delta\tilde{\phi}_{\text{tot}} = -(\tilde{\phi}_{\text{b}} + \tilde{V}_0)$ is the sum of the potential differences over the EDL $\Delta\tilde{\phi}_{\text{EDL}}$ and the electrode $\Delta\tilde{\phi}_{\text{el}} = -\tilde{V}_0 - \tilde{\phi}_{\text{d}}$,

$$\Delta\tilde{\phi}_{\text{tot}} = \Delta\tilde{\phi}_{\text{EDL}} + \Delta\tilde{\phi}_{\text{el}}. \tag{2.78}$$

Since $\Delta\tilde{\phi}_{\text{EDL}}$ is smaller than $\Delta\tilde{\phi}_{\text{tot}}$, there exists some function $0 \leq f(\Delta\tilde{\phi}_{\text{tot}}, \tilde{c}_+^{\text{out}}) \leq 1$ which allows us to write

$$\Delta\tilde{\phi}_{\text{EDL}} = f(\Delta\tilde{\phi}_{\text{tot}}, \tilde{c}_+^{\text{out}}) \Delta\tilde{\phi}_{\text{tot}}. \tag{2.79}$$

Inserting these definitions in Eq. (2.74) and rewriting a bit we obtain the Butler–Volmer–Frumkin model,

$$R = k_0 e^{-\kappa a^3 \gamma / k_{\text{B}}T} \left[\tilde{c}_+^{\text{out}} \mathrm{e}^{\alpha_{\text{c}}^* Z(\tilde{\phi}_{\text{b}} + \tilde{V}_0)} - \mathrm{e}^{-\alpha_{\text{a}}^* Z(\tilde{\phi}_{\text{b}} + \tilde{V}_0)} \right], \tag{2.80}$$

which depends on quantities evaluated outside the EDL. The modified charge transfer coefficients α_{c}^* and α_{a}^* are defined as

$$\alpha_{\text{c}}^* = \alpha_{\text{c}} + \alpha_{\text{a}} f(\Delta\tilde{\phi}_{\text{tot}}, \tilde{c}_+^{\text{out}}), \tag{2.81a}$$

$$\alpha_{\text{a}}^* = \alpha_{\text{a}} \left[1 - f(\Delta\tilde{\phi}_{\text{tot}}, \tilde{c}_+^{\text{out}}) \right]. \tag{2.81b}$$

The modified coefficients still satisfy $0 \leq \alpha^* \leq 1$, but their sum is no longer unity,

$$\alpha_{\text{c}}^* + \alpha_{\text{a}}^* = 1 - \alpha_{\text{c}} f(\Delta\tilde{\phi}_{\text{tot}}, \tilde{c}_+^{\text{out}}) \leq 1. \tag{2.82}$$

Obviously, in order to use the Butler–Volmer–Frumkin model a supplementary model is needed to determine the function f, see for instance Refs. [126, 16, 10]. The main thing we want to stress is that although f does influence the reaction rate, the fundamental exponential behavior is retained after applying the Frumkin correction to the Butler–Volmer model.

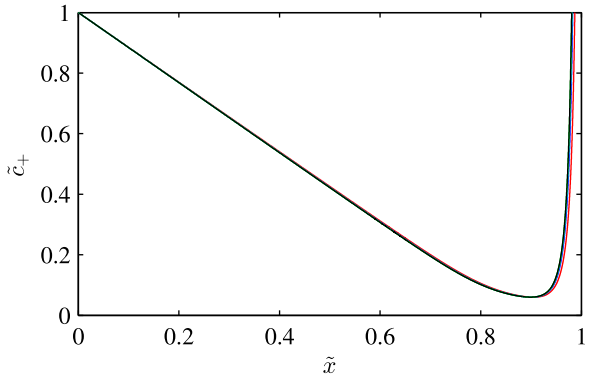

Figure 2.9: Concentration distribution outside an ion-selective interface during concentration polarization with $\bar{\lambda}_D = 0.01$. At the interface the cation concentration is varied between $\tilde{c}_+ = \{20, 10^2, 10^3, 10^5, 10^8\}$, while the difference in electrochemical potential across the system is kept constant $\tilde{\mu}_+ = 10$. The five different concentration distributions nearly collapse on one line.

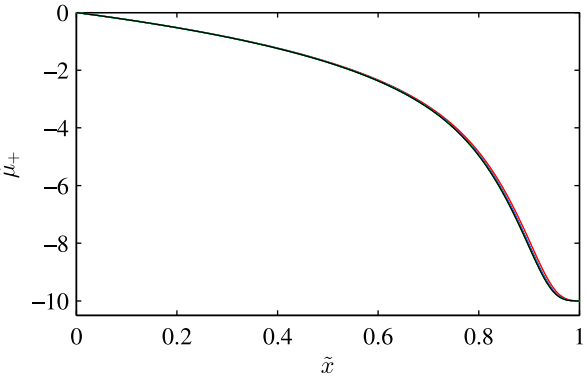

Figure 2.10: Electrochemical potential outside an ion-selective interface during concentration polarization with $\bar{\lambda}_D = 0.01$. At the interface the cation concentration is varied between $\tilde{c}_+ = \{20, 10^2, 10^3, 10^5, 10^8\}$, while the difference in electrochemical potential across the system is kept constant $\tilde{\mu}_+ = 10$. The five different distributions of electrochemical potential nearly collapse on one line.

2.7 Framework for modeling concentration polarization

Both of the ideal ion-selective interfaces treated above put specific demands on the concentration fields and the electric potential just at the interface. In order to meet these demands, a quasi-equilibrium electric double layer forms near the interface, in which the concentration and electric potential vary rapidly over a few Debye lengths. The electrochemical potential is, however, almost constant through the double layer. It turns out, that because the adaptation to the interface boundary conditions happen in this particular way, it is possible to solve the transport problem in the remainder of the domain, without reference to the specific interface boundary conditions. The only requirement is that the cation concentration at the interface is larger than the bulk cation concentration.

In Fig. 2.9 we plot the cation concentration in a domain bounded by a reservoir at $\tilde{x} = 0$ and an ion-selective interface at $\tilde{x} = 1$. An electrochemical potential difference of $\Delta\tilde{\mu}_+ = 10$ is applied across the system, and the cation concentration at the interface is varied between $\tilde{c}_+ = \{20, 10^2, 10^3, 10^5, 10^8\}$. It is seen, that despite the huge differences in concentration inside the EDL, the concentration distributions are nearly identical outside the EDL. In Fig. 2.10 the electrochemical potentials are plotted, and we see that the graphs nearly coincide. Thus, the behavior outside the EDL is very nearly independent of the interface values of $\tilde{c}_+$ and $\tilde{\phi}$. Only the value of $\tilde{\mu}_+$ is important.

This observation leads us to suggest a general concentration polarization framework (GCP) for modeling concentration polarization problems: We cut the EDL out of the problem and only solve the transport equations in the remaining parts of the system. Then, if we are interested in the current-voltage curve of a specific ion-selective interface, we can just add an interface specific correction to the general result. To uniquely specify

the boundary conditions of the trimmed system, we make use of the fact that the cation concentration has a local minimum at the entrance to the EDL. The boundary conditions therefore are

$$\boldsymbol{n} \cdot \tilde{\boldsymbol{\nabla}} \tilde{c}_+ = 0, \quad \boldsymbol{n} \cdot \tilde{\boldsymbol{J}}_- = 0, \quad \tilde{\mu}_+ = -\tilde{V}_0. \tag{2.83}$$

As an example, let us assume that we have used the GCP framework to solve the 1D transport problem from a reservoir to a general ion-selective interface. As input to the problem we have given the difference in electrochemical potential $\Delta\tilde{\mu}_+$ over the system, and as output we have found the current $\tilde{J}_+$ in the system and the concentration distribution $\tilde{c}_+$. We are now told, that the ion-selective interface is in fact an electrode obeying the Butler–Volmer–Frumkin model (2.80), with some auxiliary model for the function $f(\Delta\tilde{\phi}_{\text{tot}}, \tilde{c}_+^{\text{out}})$,

$$R = k_0 e^{-\kappa a^3 \gamma / k_{\text{B}} T} \left[\tilde{c}_+^{\text{out}} \mathrm{e}^{-\alpha_{\text{c}}^* Z \Delta\tilde{\phi}_{\text{tot}}} - \mathrm{e}^{\alpha_{\text{a}}^* Z \Delta\tilde{\phi}_{\text{tot}}} \right] = F(\tilde{c}_+^{\text{out}}, \Delta\tilde{\phi}_{\text{tot}}). \tag{2.84}$$

The function F may be fairly complicated, but the main point is that it allows us to express $\Delta\tilde{\phi}_{\text{tot}}$ in terms of the quantities $\tilde{c}_+^{\text{out}}$ and $\tilde{J}_+$ known from the general problem,

$$\Delta\tilde{\phi}_{\text{tot}} = F^{-1}(\tilde{c}_+^{\text{out}}, R) = F^{-1}(\tilde{c}_+^{\text{out}}, \tilde{J}_+). \tag{2.85}$$

Thus, the total voltage drop over a specific system has, at least in principle, been recovered from the solution to the general concentration polarization problem.

Chapter 3

Numerical techniques

As we have seen in Chapter 2, a proper model of concentration polarization involves several nonlinearly coupled partial differential equations. This makes the typical concentration polarization problem exceedingly difficult to solve by analytical means, and we therefore rely on numerical simulations to provide solutions to many of the problems in this thesis. Often, these numerical solutions provide some insight into the behavior of a system, which then enables us to derive analytical results in some important limits.

In the numerical simulations we use the commercial finite element model (FEM) software COMSOL Multiphysics 4.3a. Below we give a brief introduction to numerical modeling using the finite element method [93, 18, 12].

3.1 The finite element method

The core idea in the finite element method is to discretize the problem by expanding the physical fields in a set of localized basis functions. In COMSOL these basis functions are called test functions. The concept of using basis functions in the study of boundary value problems is familiar from Fourier analysis, where harmonic functions are used as a basis on high symmetry geometries like rectangles, cylinders, and spheres.

In the finite element method, the basis functions are constructed by placing a grid over the computational domain and associating a localized function with each grid node. The value of each basis function varies in some specified (usually polynomial) way between 1 at its own node and 0 on the neighboring nodes. See Fig. 3.1 for a sketch of a test function on the domain Ω.

We consider an inhomogeneous boundary value problem for the dependent variable $g(\boldsymbol{r})$, defined by a set of boundary conditions plus the PDE

$$\mathcal{L}\{g(\boldsymbol{r})\} = F(\boldsymbol{r}). \tag{3.1}$$

Here $\mathcal{L}$ is a differential operator and F is a forcing term. We also define the defect

$$d(\boldsymbol{r}) \equiv \mathcal{L}\{g(\boldsymbol{r})\} - F(\boldsymbol{r}), \tag{3.2}$$

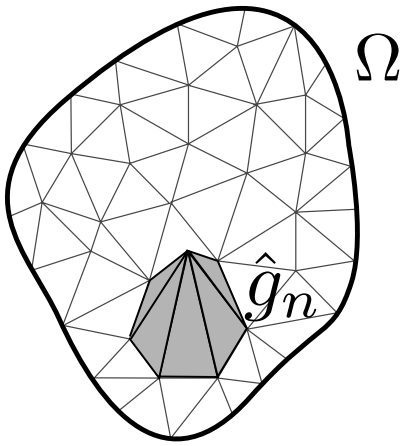

Figure 3.1: Sketch of the test function $\hat{g}_n$ on the domain Ω.

which is zero when Eq. (3.1) is satisfied. It is assumed that g can be approximately expressed in terms of a finite basis $\{\hat{g}_n\}$

$$g(\boldsymbol{r}) = \sum_n c_n \hat{g}_n(\boldsymbol{r}), \tag{3.3}$$

where c_n are the expansion coefficients. Since the basis functions nearly span the function space, Eq. (3.1) is approximately satisfied if the projection of the defect $d(\boldsymbol{r})$ on every basis function vanishes,

$$\langle \hat{g}_m, d \rangle = 0, \quad \text{for all } m. \tag{3.4}$$

Here, the inner product is defined as $\langle a(\boldsymbol{r}), b(\boldsymbol{r}) \rangle = \int_\Omega a(\boldsymbol{r}) b(\boldsymbol{r}) \, \mathrm{d}V$ for real functions. A solution satisfying Eq. (3.4) is called a weak solution of the boundary value problem. In contrast a solution satisfying Eq. (3.1) is called a strong solution of the boundary value problem. An important feature of this weak formulation of the problem is that the smoothness of g is not of critical importance. The reason for this is that any singularities in the defect, resulting from kinks in g, are immediately integrated away. Inserting the defect in Eq. (3.4) we obtain

$$\left\langle \hat{g}_m, \mathcal{L} \sum_n c_n \hat{g}_n \right\rangle = \langle \hat{g}_m, F \rangle, \quad \text{for all } m, \tag{3.5}$$

which, in the important case where $\mathcal{L}$ is linear, reduces to

$$\sum_n c_n \langle \hat{g}_m, \mathcal{L} \hat{g}_n \rangle = \langle \hat{g}_m, F \rangle, \quad \text{for all } m. \tag{3.6}$$

This system of equations can be written as a matrix problem,

$$\boldsymbol{K}\boldsymbol{c} = \boldsymbol{f}, \tag{3.7}$$

where the so-called stiffness matrix $\boldsymbol{K}$ has elements $K_{mn} = \langle \hat{g}_m, \mathcal{L}\hat{g}_n \rangle$, the vector $\boldsymbol{c}$ contains the coefficients c_n and the elements in $\boldsymbol{f}$ are given as $\langle \hat{g}_m, F \rangle$. Obtaining the weak solution to Eq. (3.1) is thus just a matter of solving the matrix equation Eq. (3.7) for the coefficient vector $\boldsymbol{c}$.

So far we made no mention of the boundary conditions, although they are an essential part of a boundary value problem. A quite natural way of implementing the boundary conditions is provided by rewriting Eq. (3.4) a bit. To do this we will assume that Eq. (3.1) can be written as a continuity equation

$$\boldsymbol{\nabla} \cdot \boldsymbol{\Gamma} = F, \tag{3.8}$$

where $\boldsymbol{\Gamma}$ is a generalized flux. This may seem restrictive, but in reality most governing equations encountered in field theories of physics can be formulated as continuity equations. Inserting Eq. (3.8) in Eq. (3.4) and integrating by parts, we obtain

$$\langle \hat{g}_m, \boldsymbol{\nabla} \cdot \boldsymbol{\Gamma} - F \rangle = \int_\Omega \left[\hat{g}_m \boldsymbol{\nabla} \cdot \boldsymbol{\Gamma} - \hat{g}_m F \right] \mathrm{d}V = 0 \tag{3.9a}$$

$$\Rightarrow \int_{\partial\Omega} \hat{g}_m \boldsymbol{n} \cdot \boldsymbol{\Gamma} \, \mathrm{d}A + \int_\Omega \left[-\boldsymbol{\nabla}\hat{g}_m \cdot \boldsymbol{\Gamma} - \hat{g}_m F \right] \mathrm{d}V = 0. \tag{3.9b}$$

In Eq. (3.9b) Neumann boundary conditions can be implemented by simply replacing $\boldsymbol{n} \cdot \boldsymbol{\Gamma}$ in the surface integral with the appropriate condition. Another advantage of the formulation in Eq. (3.9b) is that it does not include derivatives of $\boldsymbol{\Gamma}$, and as a consequence shape functions of a lower order can be used to construct the basis functions.

Dirichlet boundary conditions are not as straight-forward to implement, and requires the introduction of a Lagrange multiplier field $\lambda(\boldsymbol{r})$ on the domain boundary. The Lagrange multiplier can be expanded in a set of basis functions $\{\hat{\lambda}_m\}$. A given boundary constraint,

$$g(\boldsymbol{r}) - D(\boldsymbol{r}) = 0, \tag{3.10}$$

is then satisfied if its projection on all the basis functions $\hat{\lambda}_m$ vanishes,

$$\left\langle \hat{\lambda}_m, g(\boldsymbol{r}) - D(\boldsymbol{r}) \right\rangle = 0, \quad \text{for all } m. \tag{3.11}$$

We add this term to the surface integral in Eq. (3.9b). To allow the Dirichlet condition to affect the bulk problem, we also substitute the term $\boldsymbol{n} \cdot \boldsymbol{\Gamma}$ with the Lagrange multiplier,

$$\int_{\partial\Omega} \hat{g}_m \lambda(\boldsymbol{r}) + \hat{\lambda}_m [g(\boldsymbol{r}) - D(\boldsymbol{r})] \, \mathrm{d}A + \int_\Omega \left[-\boldsymbol{\nabla}\hat{g}_m \cdot \boldsymbol{\Gamma} - \hat{g}_m F \right] \mathrm{d}V = 0. \tag{3.12}$$

This formulation of the problem ensures that the boundary flux $\boldsymbol{n} \cdot \boldsymbol{\Gamma} = \lambda(\boldsymbol{r})$ varies until the Dirichlet condition $g(\boldsymbol{r}) - D(\boldsymbol{r})$ is satisfied.

In COMSOL the construction of the stiffness matrix $\boldsymbol{K}$ and inversion of the matrix problem Eq. (3.7) is all handled automatically. As users, we only have to provide the weak form of the governing equations and boundary conditions Eqs. (3.9b) and (3.12). In addition, we have to choose a mesh on which to discretize the boundary value problem. This is an important part in setting up the problem, as the numerical solution is only reliable if the important physics is well-resolved by the mesh. To ascertain that the mesh does indeed resolve the relevant physics, we test the model in a variety of ways, including mesh convergence tests and visual inspection of the fields.

Chapter 4

Concentration polarization: Beyond the local electroneutrality assumption

The possible mechanisms behind overlimiting current are many and diverse in nature, including both symmetry breaking and chemical effects. However, as Smyrl and Newman realized as early as 1967 [113], even the simple one-dimensional model of concentration polarization admits an overlimiting current. A careful analysis shows that as the current approaches the limiting current, the LEN model outlined in Section 2.5 breaks down, and a non-equilibrium extended space charge region (ESC) develops near the ion-selective interface. The extended space-charge region has a finite, albeit small, conductivity, enabling an overlimiting current to run in the system.

The standard approach to solving the 1D transport problem is to employ the method of matched asymptotic expansions [113, 16, 8, 134, 98, 94, 80]. While this method gives important insight into the structure of the expanded double layer, it has the quite serious issue that both the inner and outer expansions diverge at the matching point. Consequently, a proper matching of the expansions is not possible, and an analytical I-V curve can not be obtained.

In this chapter we use an alternate method to derive a uniformly valid solution to the transport problem. Besides being free from any divergences our solution has the advantage of having a comparatively simple form. This chapter is based on work from our paper Ref. [83], which can be found in Appendix E.

4.1 Model

We consider one-dimensional transport of a binary symmetric electrolyte from a reservoir at $x = 0$ to an ion-selective interface at $x = L$. The ions are assumed monovalent and their reservoir concentration is c_0. A sketch of the system is shown in Fig. 4.1. Using the

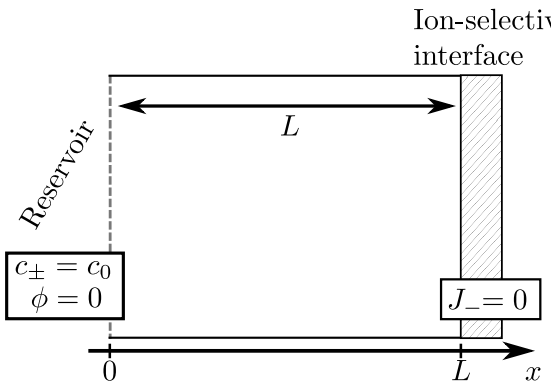

Figure 4.1: The simple concentration polarization model system used in this chapter. To the left is a reservoir of salt concentration c_0 and to the right is a cation selective interface. In between is a compartment of length L.

standard normalization from Section 2.2 the currents become

$$2\tilde{J}_+ = -\partial_{\tilde{x}}\tilde{c}_+ - \tilde{c}_+\partial_{\tilde{x}}\tilde{\phi}, \tag{4.1a}$$

$$2\frac{D_+}{D_-}\tilde{J}_- = -\partial_{\tilde{x}}\tilde{c}_- + \tilde{c}_-\partial_{\tilde{x}}\tilde{\phi}. \tag{4.1b}$$

Similarly, the Poisson equation becomes

$$2\bar{\lambda}_{\mathrm{D}}^2\partial_{\tilde{x}}^2\tilde{\phi} = \tilde{c}_- - \tilde{c}_+. \tag{4.2}$$

In the numerical simulations we model the ion-selective interface using two different approaches. In one approach we model the interface as a membrane with $\tilde{\rho}_{\mathrm{m}} = 1000$, and in another we employ the GCP framework from Section 2.7 and apply the boundary condition

$$\partial_{\tilde{x}}\tilde{c}_+ = 0, \tag{4.3}$$

at the interface.

4.2 Analysis

In steady state the anion current vanishes and the cation current is a constant. Adding Eq. (4.1b) to Eq. (4.1a) and subtracting Eq. (4.1b) from Eq. (4.1a) thus yields

$$2\tilde{J}_+ = -\partial_{\tilde{x}}(\tilde{c}_+ + \tilde{c}_-) - (\tilde{c}_+ - \tilde{c}_-)\partial_{\tilde{x}}\tilde{\phi}, \tag{4.4a}$$

$$2\tilde{J}_+ = -\partial_{\tilde{x}}(\tilde{c}_+ - \tilde{c}_-) - (\tilde{c}_+ + \tilde{c}_-)\partial_{\tilde{x}}\tilde{\phi}, \tag{4.4b}$$

which upon insertion of Eq. (4.2) becomes

$$2\tilde{J}_+ = -2\partial_{\tilde{x}}\tilde{c}_+ - 2\bar{\lambda}_{\mathrm{D}}^2\partial_{\tilde{x}}^3\tilde{\phi} + 2\bar{\lambda}_{\mathrm{D}}^2\partial_{\tilde{x}}^2\tilde{\phi}\partial_{\tilde{x}}\tilde{\phi}, \tag{4.5a}$$

$$2\tilde{J}_+ = 2\bar{\lambda}_{\mathrm{D}}^2\partial_{\tilde{x}}^3\tilde{\phi} - 2\bar{\lambda}_{\mathrm{D}}^2\partial_{\tilde{x}}^2\tilde{\phi}\partial_{\tilde{x}}\tilde{\phi} - 2\tilde{c}_+\partial_{\tilde{x}}\tilde{\phi}. \tag{4.5b}$$

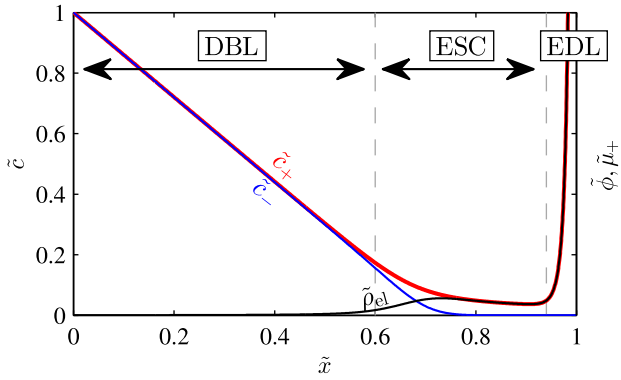

Figure 4.2: Numerically obtained concentration distributions for a system with $\bar{\lambda}_{\mathrm{D}} = 0.01$ and $\tilde{\rho}_{\mathrm{m}} = 1000$. The system can be divided into three regions: a locally electroneutral diffusion boundary layer (DBL), a nonequilibrium extended space-charge region (ESC), and a quasi-equilibrium electric double layer (EDL).

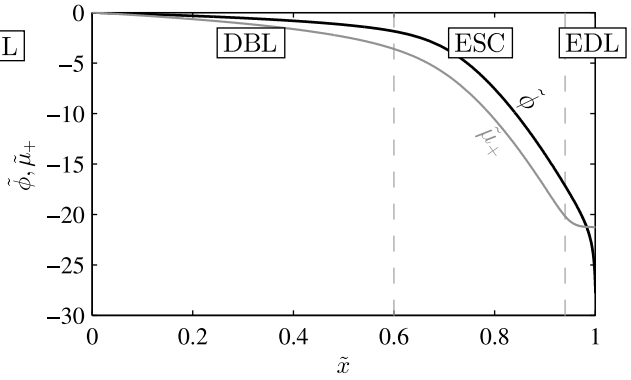

Figure 4.3: Numerically obtained electric and electrochemical potentials for a system with $\bar{\lambda}_{\mathrm{D}} = 0.01$ and $\tilde{\rho}_{\mathrm{m}} = 1000$. The electrochemical potential only varies little inside the EDL.

The first of these equations is easily integrated,

$$\tilde{J}_+\tilde{x} - 1 = -\tilde{c}_+ - \bar{\lambda}_{\mathrm{D}}^2\partial_{\tilde{x}}^2\tilde{\phi} + \frac{\bar{\lambda}_{\mathrm{D}}^2}{2}\left(\partial_{\tilde{x}}\tilde{\phi}\right)^2, \tag{4.6}$$

where the integration constant was set to unity, since the terms involving $\tilde{\phi}$ are very small at the reservoir $\tilde{x} = 0$. Multiplying Eq. (4.6) by $\partial_{\tilde{x}}\tilde{\phi}$ and subtracting it from Eq. (4.5b) yields an ordinary differential equation for the potential $\tilde{\phi}$,

$$\tilde{J}_+ - [\tilde{J}_+x - 1]\partial_{\tilde{x}}\tilde{\phi} = \bar{\lambda}_{\mathrm{D}}^2\partial_{\tilde{x}}^3\tilde{\phi} - \frac{\bar{\lambda}_{\mathrm{D}}^2}{2}\left(\partial_{\tilde{x}}\tilde{\phi}\right)^3. \tag{4.7}$$

This equation, sometimes referred to as the master equation for the electric field, has previously been derived in various forms, see for instance Refs. [113, 16, 125].

Before trying to derive analytical solutions to Eq. (4.7) we solve the problem numerically to get an impression of the important features in the solution. In Fig. 4.2 we plot $\tilde{c}_+$, $\tilde{c}_-$, and $\tilde{\rho}_{\mathrm{el}}$ for a system with $\bar{\lambda}_{\mathrm{D}} = 0.01$, where the ion-selective interface is a permselective membrane with $\tilde{\rho}_{\mathrm{m}} = 1000$. In Fig. 4.3 we plot $\tilde{\phi}$ and $\tilde{\mu}_+$ in the same system. Starting with Fig. 4.2 it is seen that the system can be divided into three regions: a locally electroneutral diffusive boundary layer (DBL) to the left, a quasi-equilibrium electric double layer (EDL) to the right, and a nonequilibrium extended space-charge region (ESC) in between. The same three regions are marked in Fig. 4.3, and it is seen that the electric potential $\tilde{\phi}$ varies significantly in all three regions. The electrochemical potential, on the other hand, has a quite small variation inside the electric double layer, as indeed we would expect from the considerations in Section 2.6.1. Since the electrochemical potential is the relevant driving force in the transport problem, this means that we can choose to disregard the electric double layer in the solution of Eq. (4.7). That is, we apply the GCP framework outlined in Section 2.7.

In order to simplify Eq. (4.7) we look for terms which are negligible in the two relevant regions. The terms on the left-hand side represent the simple LEN solution to the problem, so they are obviously non-negligible. The terms on the right-hand side derive from the Poisson equation, and as such they are associated with the charge in the system. We therefore expect these terms to only matter in the ESC. Inside the ESC the right-hand side terms scale as

$$\bar{\lambda}_{\mathrm{D}}^2 \partial_{\tilde{x}}^3 \tilde{\phi} \sim \bar{\lambda}_{\mathrm{D}}^2 \frac{\Delta\tilde{\phi}}{\Delta\tilde{x}^3}, \tag{4.8a}$$

$$\frac{\bar{\lambda}_{\mathrm{D}}^2}{2} \left(\partial_{\tilde{x}} \tilde{\phi}\right)^3 \sim \frac{\bar{\lambda}_{\mathrm{D}}^2}{2} \frac{\Delta\tilde{\phi}^3}{\Delta\tilde{x}^3}, \tag{4.8b}$$

where $\Delta\tilde{\phi}$ is the potential drop over the ESC and $\Delta\tilde{x}$ is the width of the ESC. The amount of charge carriers is small in the ESC, so the potential drop $\Delta\tilde{\phi}$ over the ESC is large. Consequently, Eq. (4.8b) will dominate over Eq. (4.8a) and it is reasonable to neglect $\bar{\lambda}_{\mathrm{D}}^2 \partial_{\tilde{x}}^3 \tilde{\phi}$ in Eq. (4.7),

$$\tilde{J}_+ - [\tilde{J}_+ x - 1] \partial_{\tilde{x}} \tilde{\phi} = -\frac{\bar{\lambda}_{\mathrm{D}}^2}{2} \left(\partial_{\tilde{x}} \tilde{\phi}\right)^3. \tag{4.9}$$

Since $2\bar{\lambda}_{\mathrm{D}}^2 \partial_{\tilde{x}}^3 \tilde{\phi} = -\partial_{\tilde{x}} \tilde{\rho}_{\mathrm{el}}$ the above assumption corresponds to assuming a quasi-uniform distribution of the charge density. As seen by the smooth variation of $\tilde{\rho}_{\mathrm{el}}$ in Fig. 4.2 this is indeed a reasonable way of characterizing the charge density in the ESC. Inside the EDL, on the other hand, the charge density is far from uniform, so the fact that we can disregard the EDL is crucial for this solution approach.

We are not the first to come up with this way of simplifying Eq. (4.7). It has previously been used by Urtenov *et al.* [125] and dubbed the assumption of quasi-uniform charge density distribution (QCD). In their work they are, however, only using the QCD assumption as a means of simplifying numerical simulations. While this is certainly worthwhile in itself, it seems to us that they are missing out on the biggest incentive for using the QCD assumption, namely the abundance of useful analytical results which can be derived from Eq. (4.9).

To simplify the analysis we introduce a scaled electric field $\hat{E}$ and a scaled position $\hat{x}$, defined by

$$\hat{E} = -B \partial_{\tilde{x}} \tilde{\phi}, \quad \text{with} \quad B = \left(\frac{\bar{\lambda}_{\mathrm{D}}^2}{2\tilde{J}_+}\right)^{1/3}, \tag{4.10}$$

and

$$\hat{x} = \frac{1}{B}\left[\tilde{x} - \frac{1}{\tilde{J}_+}\right]. \tag{4.11}$$

We can then rewrite Eq. (4.9) as

$$1 + \hat{x}\hat{E} = \hat{E}^3. \tag{4.12}$$

Before actually solving this equation we can use it to derive some results characterizing the ESC. The scaled charge density $\hat{\rho}_{\mathrm{el}} = \partial_{\hat{x}}\hat{E}$ is found by implicit differentiation of Eq. (4.12)

$$\hat{E} + \hat{x}\partial_{\hat{x}}\hat{E} = 3\hat{E}^2\partial_{\hat{x}}\hat{E} \quad \Rightarrow \quad \hat{\rho}_{\mathrm{el}} = \partial_{\hat{x}}\hat{E} = \frac{\hat{E}}{3\hat{E}^2 - \hat{x}} = \frac{\hat{E}^2}{2\hat{E}^3 + 1}. \tag{4.13}$$

Differentiating $\hat{\rho}_{\mathrm{el}}$ again, it is found that the point of maximum charge density is at $\hat{x} = 0$ and that

$$\max(\hat{\rho}_{\mathrm{el}}) = \hat{\rho}_{\mathrm{el}}(0) = \frac{1}{3}. \tag{4.14}$$

The simple form of this result is due to Eq. (4.12) being trivial for $\hat{x} = 0$. From the scaled charge density $\hat{\rho}_{\mathrm{el}}$ we can easily recover the unscaled charge density $\tilde{\rho}_{\mathrm{el}}$,

$$\tilde{\rho}_{\mathrm{el}} = -2\bar{\lambda}_{\mathrm{D}}^2\partial_{\tilde{x}}^2\tilde{\phi} = \frac{2\bar{\lambda}_{\mathrm{D}}^2}{B}\partial_{\tilde{x}}\hat{x}\partial_{\hat{x}}\hat{E} = \left(32\bar{\lambda}_{\mathrm{D}}^2\tilde{J}_+^2\right)^{1/3}\hat{\rho}_{\mathrm{el}}. \tag{4.15}$$

In Fig. 4.2 it is seen that the point of maximum charge density roughly marks the left edge of the ESC. Inserting $\hat{x} = 0$ in Eq. (4.11) we find that the beginning of the ESC is at $\tilde{x}_\rho = 1/\tilde{J}_+$, so the width of the ESC is $\tilde{l}_{\mathrm{ESC}} = 1 - 1/\tilde{J}_+$.

To proceed beyond this point, we write up the general solution to Eq. (4.12)

$$\begin{aligned}\hat{E} = &-\frac{1}{2^{1/3}}\left(-1 + \sqrt{1 - \frac{4}{27}\hat{x}^3}\right)^{1/3} \mathrm{e}^{i\omega} \\ &- \frac{2^{1/3}}{3}\hat{x}\left(-1 + \sqrt{1 - \frac{4}{27}\hat{x}^3}\right)^{-1/3} \mathrm{e}^{-i\omega},\end{aligned} \tag{4.16}$$

where $\omega = 0, \frac{2\pi}{3}$ or $\frac{4\pi}{3}$. We require that the solution is real and find

$$\hat{E} = \begin{cases} \hat{E}_-, & \text{for } \hat{x} \leq 0, \\ \hat{E}_+, & \text{for } \hat{x} \geq 0, \end{cases} \tag{4.17a}$$

which is continuous and differentiable at $\hat{x} = 0$ and where

$$\begin{aligned}\hat{E}_\pm = &\pm\frac{1}{2^{1/3}}\left(\pm 1 \mp \sqrt{1 - \frac{4}{27}\hat{x}^3}\right)^{1/3} \\ &\pm\frac{2^{1/3}}{3}\hat{x}\left(\pm 1 \mp \sqrt{1 - \frac{4}{27}\hat{x}^3}\right)^{-1/3}.\end{aligned} \tag{4.17b}$$

In Fig. 4.4 the scaled electric field $\hat{E}$ is plotted for $-10 < \hat{x} < 10$ along with the asymptotic expressions. It is seen that both of the far field asymptotics diverge at $\hat{x} = 0$, whereas $\hat{E}$ itself is well behaved for all values of $\hat{x}$. We note that although this approach, like the method of matched asymptotic expansions [8, 16, 53], deals with different expressions inside and outside the ESC, the expressions used here are different branches of the same

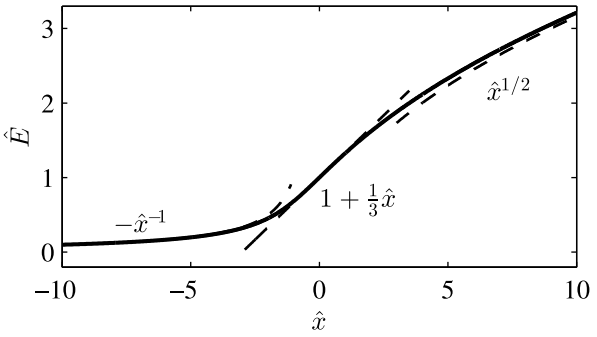

Figure 4.4: Plot of the scaled electric field $\hat{E}$ versus $\hat{x}$. The dashed lines show the asymptotic behavior for $\hat{x} \to -\infty$, $\hat{x} \to 0$, and $\hat{x} \to \infty$

solution and as such they are matched by construction. This is a distinct advantage of the present approach, and it allows for an integration of the electric field to find the potential drop over the system.

Looking at the rather unpleasant form of Eq. (4.17), one might easily conclude that it is simply to cumbersome to work with to be worth the effort. For instance, how are we ever going to integrate $\hat{E}$ given on this form? Indeed, mathematical software packages like MAPLE and MATHEMATICA come up short when tasked with integrating Eq. (4.17b). Luckily, there is a work around. Because the QCD master equation (4.12) is a simple algebraic equation for $\hat{E}$, we can derive all the results we need without ever having to perform explicit operations on Eq. (4.17). The explicit form Eq. (4.17) is only needed for evaluating the end results.

In order to find the potential $\tilde{\phi}$ we use Eq. (4.13) to make a change of variable,

$$\begin{aligned}\tilde{\phi} &= \int \partial_{\tilde{x}}\tilde{\phi}\,\mathrm{d}\tilde{x} = -\frac{1}{B}\frac{1}{\partial_{\tilde{x}}\hat{x}}\int \hat{E}\,\mathrm{d}\hat{x} = -\int \hat{E}\,\mathrm{d}\hat{x} \\ &= -\int \hat{E}\frac{1}{\partial_{\hat{x}}\hat{E}}\,\mathrm{d}\hat{E} = -\int 2\hat{E}^2 + \frac{1}{\hat{E}}\,\mathrm{d}\hat{E} \\ &= -\frac{2}{3}\left[\hat{E}^3 - \hat{E}^3(\hat{x}_0)\right] - \ln\left(\frac{\hat{E}}{\hat{E}(\hat{x}_0)}\right),\end{aligned} \tag{4.18}$$

with $\hat{x}_0 = -1/(B\tilde{J}_+)$ (Eq. (4.11) with $\tilde{x} = 0$). Equivalently, we define $\hat{x}_1 = (\tilde{J}_+ - 1)/(B\tilde{J}_+)$ (Eq. (4.11) with $\tilde{x} = 1$). At the reservoir $\hat{E}$ is small, so we can make the approximations $\hat{E}^3(\hat{x}_0) \approx 0$ and $\hat{E}(\hat{x}_0) \approx -\frac{1}{\hat{x}_0}$,

$$\tilde{\phi} \approx -\frac{2}{3}\hat{E}^3 - \ln(-\hat{E}\hat{x}_0). \tag{4.19}$$

The cation concentration is obtained from Eq. (4.6),

$$\tilde{c}_+ = \frac{\bar{\lambda}_\mathrm{D}^2}{B^2}\left[\frac{1}{2\hat{E}} + \partial_{\hat{x}}\hat{E}\right] = \frac{\bar{\lambda}_\mathrm{D}^2}{B^2}\left[\frac{1}{2\hat{E}} + \frac{\hat{E}^2}{2\hat{E}^3+1}\right] = \frac{\bar{\lambda}_\mathrm{D}^2}{B^2}\frac{4\hat{E}^3+1}{4\hat{E}^3+2}\frac{1}{\hat{E}}, \tag{4.20}$$

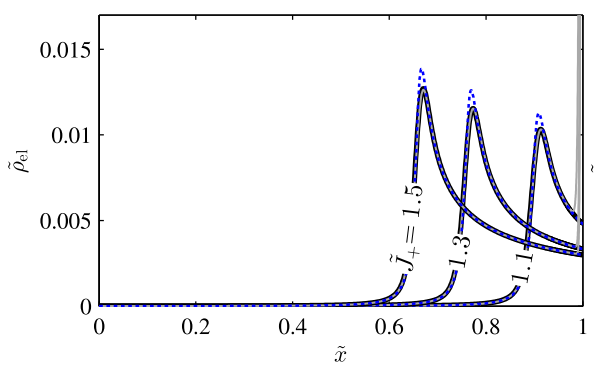

Figure 4.5: The space-charge density in a system with $\bar{\lambda}_{\mathrm{D}} = 0.001$ and $\tilde{J}_+ = \{1.1, 1.3, 1.5\}$. The gray lines show the results from numerical simulations with a membrane, the black lines show the results from a numerical simulation with GCP boundary conditions, and the blue dashed lines show the analytical results.

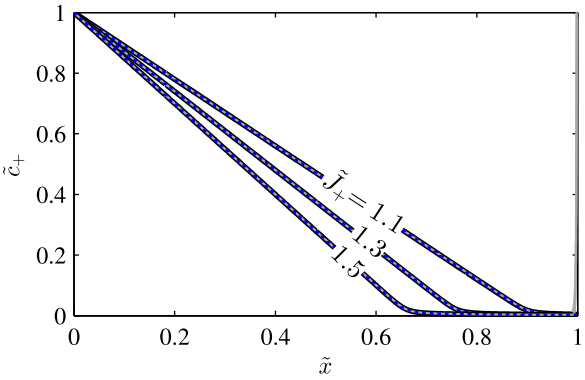

Figure 4.6: The cation concentration in a system with $\bar{\lambda}_{\mathrm{D}} = 0.001$ and $\tilde{J}_+ = \{1.1, 1.3, 1.5\}$. The gray lines show the results from numerical simulations with a membrane, the black lines show the results from a numerical simulation with GCP boundary conditions, and the blue dashed lines show the analytical results.

and since the anions are Boltzmann distributed,

$$\tilde{c}_- = \mathrm{e}^{\tilde{\phi}}. \tag{4.21}$$

In Fig. 4.5 we plot the charge density for $\bar{\lambda}_{\mathrm{D}} = 0.001$ and $\tilde{J}_+ = \{1.1, 1.3, 1.5\}$. The analytical result (4.15) is shown with a blue dashed line and the numerical results are shown in gray for the membrane boundary condition and in black for the GCP boundary condition. Comparing the analytical results with those from the numerical membrane model, we see that they differ markedly in the EDL. Here, the numerically obtained charge density increases rapidly, while the analytical charge density is unaffected. This is as expected, since the EDL was intentionally removed from the analytical treatment. In the ESC there are also slight deviations between the results, but both models agree on the essential behavior. In Fig. 4.6 we plot the ion concentrations for the same set of parameter values. Also here, there is excellent agreement between the analytical and numerical models.

To find the current-voltage characteristic of the system, we need an expression for the electrochemical potential. Such an expression is easily obtained from Eqs. (4.19) and (4.20),

$$\tilde{\mu}_+ = \ln(\tilde{c}_+) + \tilde{\phi} = -\frac{2}{3}\hat{E}^3 - \ln\left(-\frac{B^2}{\bar{\lambda}_{\mathrm{D}}^2}\frac{4\hat{E}^3 + 2}{4\hat{E}^3 + 1}\hat{E}^2\hat{x}_0\right). \tag{4.22}$$

In Fig. 4.7 we plot the electrochemical potential in the system for $\bar{\lambda}_{\mathrm{D}} = 0.001$ and $\tilde{J}_+ = 1.5$. Both the analytical and numerical results are shown. The numerical and analytical models are seen to be in good agreement except inside the EDL. Here, $\tilde{\mu}_+$ from the numerical membrane model levels off, while $\tilde{\mu}_+$ continues with an approximately constant slope through the EDL in the two other models. Thus, if we base the analytical I-V curve on

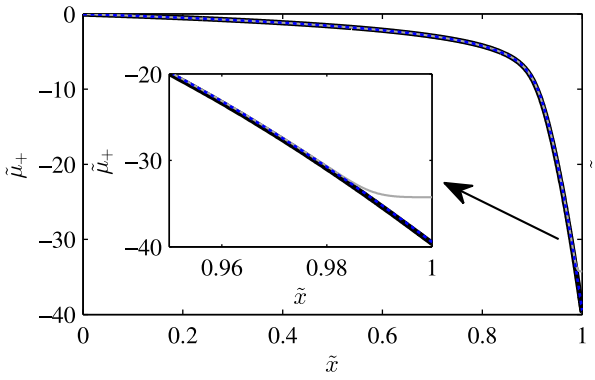

Figure 4.7: The electrochemical potential $\tilde{\mu}_+$ in a system with $\bar{\lambda}_\mathrm{D} = 0.001$ and $\tilde{J}_+ = 1.5$. The gray line shows the result from a numerical simulation with a membrane, the black line shows the result from a numerical simulation with GCP boundary conditions, and the blue dashed line shows the analytical result.

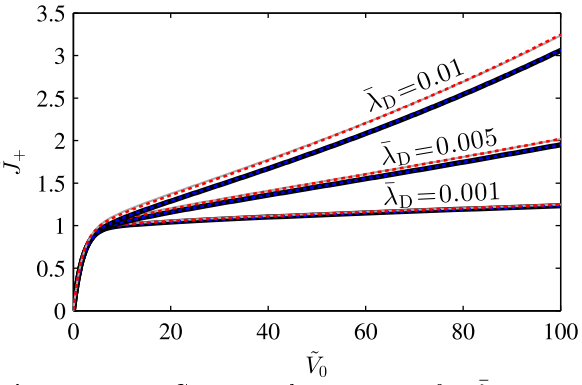

Figure 4.8: Current-voltage curves for $\bar{\lambda}_\mathrm{D} = \{0.001, 0.005, 0.01\}$. The gray lines show the results from numerical simulations with a membrane, the black lines show the results from a numerical simulation with GCP boundary conditions, the blue dashed lines show the analytical results, and the red dashed lines show the corrected analytical results.

the electrochemical potential at $\tilde{x} = 1$, we will slightly overestimate the voltage required to drive a given current. Alternatively, we can evaluate the analytical $\tilde{\mu}_+$ at the beginning of the EDL, to avoid part of the spurious potential drop inside the EDL. i.e. rather than evaluating $\tilde{\mu}_+$ at $\tilde{x} = 1$, we evaluate it at $\tilde{x} = 1 - \tilde{l}_\mathrm{EDL}$. Assuming that $\tilde{l}_\mathrm{EDL}$ corresponds to the local Debye length we have

$$\tilde{l}_\mathrm{EDL} \approx \frac{\bar{\lambda}_\mathrm{D}}{\sqrt{\tilde{c}_+}}. \tag{4.23}$$

In the overlimiting regime the cation concentration in the ESC almost equals the charge density. The scale of the charge density is set by the peak charge density $\tilde{\rho}_\mathrm{el}(\tilde{x}_\rho)$, so we can express the width of the EDL as

$$\tilde{l}_\mathrm{EDL} \approx \frac{\bar{\lambda}_\mathrm{D}}{\sqrt{\tilde{\rho}_\mathrm{el}(\tilde{x}_\rho)}} = 3^{1/2} 2^{-5/6} \bar{\lambda}_\mathrm{D}^{2/3} \tilde{J}_+^{-1/3}. \tag{4.24}$$

In Fig. 4.8 we plot analytical and numerical I-V curves for $\bar{\lambda}_\mathrm{D} = \{0.001, 0.005, 0.01\}$. The numerical results are shown in full gray lines for the membrane boundary condition and in full black lines for the GCP boundary condition. The dashed blue lines denote analytical results evaluated at $\tilde{x} = 1$ and the dashed red lines denote the corrected analytical results evaluated at $\tilde{x} = 1 - \tilde{l}_\mathrm{EDL}$. Both of the analytical models are seen to capture the essential behavior of the I-V curve, with the results evaluated at $\tilde{x} = 1 - \tilde{l}_\mathrm{EDL}$ doing slightly better than those evaluated at $\tilde{x} = 1$.

4.3 Characterizing the extended space charge region

The accurate I-V curve is a key result of the analytical model. However, the true strength of the model lies in its ability to predict quantities which are inaccessible to experimental measurements. For instance, results characterizing the ESC are of great theoretical and practical interest. We already derived one such result, namely the value of the peak charge density,

$$\max(\tilde{\rho}_{\mathrm{el}}) = \frac{1}{3}\left(32\bar{\lambda}_{\mathrm{D}}^2\tilde{J}_+^2\right)^{1/3}. \tag{4.25}$$

Likewise, the total charge $\tilde{Q}$ in the system is easily obtained from Eq. (4.15)

$$\tilde{Q} = \int_0^1 \tilde{\rho}_{\mathrm{el}}\,\mathrm{d}\tilde{x} = \left(32\bar{\lambda}_{\mathrm{D}}^2\tilde{J}_+^2\right)^{1/3}\int_{\hat{x}_0}^{\hat{x}_1}\hat{\rho}_{\mathrm{el}}\frac{1}{\partial_{\tilde{x}}\hat{x}}\,\mathrm{d}\hat{x} = \left(16\bar{\lambda}_{\mathrm{D}}^4\tilde{J}_+\right)^{1/3}\left[\hat{E}(\hat{x}_1) - \hat{E}(\hat{x}_0)\right] \tag{4.26}$$

$$\approx \left(16\bar{\lambda}_{\mathrm{D}}^4\tilde{J}_+\right)^{1/3}\hat{E}(\hat{x}_1), \tag{4.27}$$

since $\hat{E}(x_0) \ll \hat{E}(x_1)$. The charge is only significant in the overlimiting regime, and in this regime we can approximate $\hat{E} \approx \sqrt{\hat{x}}$,

$$\tilde{Q} \approx \left(16\bar{\lambda}_{\mathrm{D}}^4\tilde{J}_+\right)^{1/3}\sqrt{\frac{1}{B}\left(1 - \frac{1}{\tilde{J}_+}\right)} = 2^{3/2}\bar{\lambda}_{\mathrm{D}}\sqrt{\tilde{J}_+ - 1}. \tag{4.28}$$

Surprisingly, the total charge $\tilde{Q}$ has a different scaling with $\bar{\lambda}_{\mathrm{D}}$ than the peak charge density $\max(\tilde{\rho}_{\mathrm{el}})$.

In the last 15 years the so-called electro-osmotic instability of the second kind has attracted considerable attention. Rubinstein and Zaltzman showed that under certain conditions the ESC can go unstable leading to periodic flow patterns in the liquid [99, 100, 101, 102, 104]. A key step in their analysis is the derivation of an effective slip velocity, applicable just outside the ESC. However, this is a fairly laborious derivation requiring quite a few approximations along the way. In the following we re-derive the effective slip velocity using our much simpler, and more accurate, model of the extended space-charge region.

We investigate the geometry shown in Fig. 4.9, in which current runs in the $\tilde{x}$ direction from a reservoir to a planar ion-selective interface lying in the $\tilde{y}\tilde{z}$ plane. Due to the symmetry breaking electro-osmotic instability, our analytical QCD model is not applicable in the entire geometry. However, close to the interface advection plays a comparatively small role, and we expect the QCD model to give a reasonable description of the transport. We define a slip plane at the transition point $\tilde{x} = \tilde{x}_{\mathrm{s}}$ between the ESC and the locally electroneutral, partially advection driven bulk system. By applying the QCD model in the region between $\tilde{x} = \tilde{x}_{\mathrm{s}}$ and $\tilde{x} = 1$, we can then derive a slip velocity for the bulk part of the system. To simplify matters, we only consider transverse variations along the $\tilde{y}$ direction.

The starting point for deriving an effective slip velocity is the normalized Stokes equation

$$0 = -\tilde{\boldsymbol{\nabla}}\tilde{p} + \tilde{\nabla}^2\tilde{\boldsymbol{u}} + \tilde{\nabla}^2\tilde{\phi}\tilde{\boldsymbol{\nabla}}\tilde{\phi}, \tag{4.29}$$

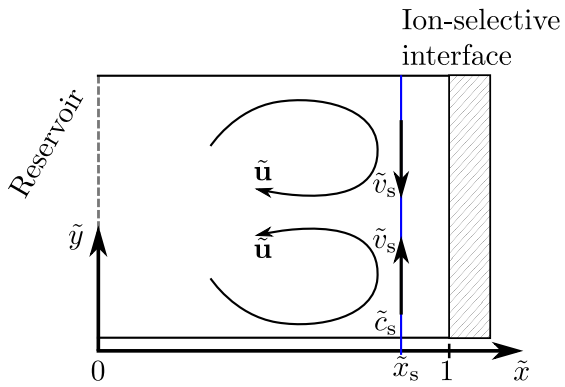

Figure 4.9: Sketch of a system with electro-osmotic instability. To the left is a reservoir and to the right is an ion-selective interface. The blue line shows the slip plane at the transition point between the electroneutral, partially advection driven bulk system and the ESC. The position $\tilde{x}_s$ of the slip plane, the concentration $\tilde{c}_s$ at the slip plane, and the slip velocity $\tilde{v}_s$ are indicated.

where the velocity was normalized by $U_0 = \epsilon_w V_T^2/(\eta L)$ and the pressure was normalized by $p_0 = \eta U_0/L$. The potential variations are much larger in the $\tilde{x}$-direction than in the $\tilde{y}$-direction, so we can approximate $\tilde{\nabla}^2\tilde{\phi} \approx \partial_{\tilde{x}}^2\tilde{\phi}$. Since the ion-selective interface blocks the fluid flow, the $\tilde{x}$ component of Eq. (4.29) yields

$$0 = -\partial_{\tilde{x}}\tilde{p} + \partial_{\tilde{x}}^2\tilde{\phi}\partial_{\tilde{x}}\tilde{\phi} \quad \Rightarrow \quad \tilde{p} = \frac{1}{2}(\partial_{\tilde{x}}\tilde{\phi})^2 + \text{constant}. \tag{4.30}$$

Inserting this in the $\tilde{y}$ component of Eq. (4.29) we find

$$0 = -\frac{1}{2}\partial_{\tilde{y}}\left\{(\partial_{\tilde{x}}\tilde{\phi})^2\right\} + \partial_{\tilde{x}}^2\tilde{v} + \partial_{\tilde{x}}^2\tilde{\phi}\partial_{\tilde{y}}\tilde{\phi}. \tag{4.31}$$

Because we only apply the QCD model between $\tilde{x} = \tilde{x}_s$ and $\tilde{x} = 1$ the scaled coordinate $\hat{x}$ takes the form

$$\hat{x} = \frac{1}{B}\left[\tilde{x} - \tilde{x}_s - \frac{\tilde{c}_s}{\tilde{J}_+}\right] \tag{4.32}$$

where $\tilde{c}_s$ is the ion concentration at $\tilde{x}_s$. We note that since the symmetry is broken both $\tilde{c}_s$, $\tilde{J}_+$, and B depend on the $\tilde{y}$ coordinate. Evaluating the pressure term in Eq. (4.31) we find

$$\frac{1}{2}\partial_{\tilde{y}}\left\{(\partial_{\tilde{x}}\tilde{\phi})^2\right\} = \frac{1}{2}\partial_{\tilde{y}}\left\{\frac{\hat{E}^2}{B^2}\right\} = -\frac{1}{B^2}\hat{E}^2\partial_{\tilde{y}}\ln(B) + \frac{1}{B^2}\hat{E}\partial_{\tilde{y}}\hat{x}\partial_{\hat{x}}\hat{E}, \tag{4.33}$$

and from the electrostatic force term,

$$\partial_{\tilde{x}}^2\tilde{\phi}\partial_{\tilde{y}}\tilde{\phi} = -\frac{1}{B^2}\partial_{\hat{x}}\hat{E}\partial_{\tilde{y}}\hat{x}\partial_{\hat{x}}\tilde{\phi} = \frac{1}{B^2}\partial_{\tilde{y}}\hat{x}\hat{E}\partial_{\hat{x}}\hat{E}. \tag{4.34}$$

Inserting these expressions in Eq. (4.31) the electrostatic terms cancel and we are left with

$$\partial_{\tilde{x}}^2 \tilde{v} = -\frac{1}{B^2}\hat{E}^2 \partial_{\tilde{y}} \ln(B) = -\frac{1}{B^2}\hat{E}^2 \partial_{\tilde{y}} \ln\left(\left[\frac{\bar{\lambda}_{\mathrm{D}}^2}{2\tilde{J}_+}\right]^{1/3}\right) = \frac{1}{3}\frac{\hat{E}^2}{B^2}\partial_{\tilde{y}} \ln(\tilde{J}_+). \tag{4.35}$$

Integrating this result twice with $\partial_{\tilde{x}}\tilde{v}(\tilde{x}_{\mathrm{s}}) = 0$ and $\tilde{v}(1) = 0$ we find

$$\tilde{v}_{\mathrm{s}} = \tilde{v}(\tilde{x}_{\mathrm{s}}) \approx -\frac{1}{3}\partial_{\tilde{y}} \ln(\tilde{J}_+)\left[\frac{1}{6}\hat{E}^6 + \frac{5}{6}\hat{E}^3\right], \tag{4.36}$$

where $\hat{E}$ should be evaluated at $\tilde{x} = 1$. For clarity some lower order terms have been omitted from this result. From Eq. (4.19) we see that to leading order the potential is given as $\tilde{\phi} \approx -\frac{2}{3}\hat{E}^3$. Inserting this in Eq. (4.36) we find

$$\tilde{v}_{\mathrm{s}} \approx -\partial_{\tilde{y}} \ln(\tilde{J}_+)\left[\frac{1}{8}\tilde{\phi}^2 - \frac{5}{12}\tilde{\phi}\right]. \tag{4.37}$$

If the velocity field in the $\tilde{x}$-direction vanishes at the slip plane, the current at the slip plane is given as $\tilde{J}_+ = -\partial_{\tilde{x}}\tilde{c}$, and the leading order behavior of Eq. (4.37) is identical to the slip model in Ref. [100]. The correction $\frac{5}{12}\tilde{\phi}$ is new, and for the voltages $|\tilde{\phi}| \lesssim 10$ investigated in Ref. [100], it does give a significant contribution to the slip velocity.

In Ref. [100] the ESC is treated as being decoupled from the bulk system. That is, the voltage over the ESC is treated as an independent tunable variable. In reality, the voltage over the ESC is, however, determined by the current into the ESC and the salt concentration at the edge of the ESC. This coupling is apparent in our model, and the inclusion of this effect might help to provide a better understanding of the electro-osmotic instability and maybe even the transition to chaotic behavior [25, 20].

4.4 Conclusion

Based on an assumption of a quasi-uniform distribution of the charge density, we have derived an analytical model (QCD) for concentration polarization in 1D. The QCD model improves on existing analytical models both in predictive power and in ease of use, cf. Refs. [113, 98, 133, 134]. The main limitation of the presented model is that it does not consider the role of the EDL. However, as discussed in Section 2.7, the quasi-equilibrium EDL usually does not affect the transport problem in a decisive way. For instance, in the case of a membrane boundary condition, the EDL only affects the problem by a slight modification of the effective compartment length. As an example of the versatility of the analytical model, we rederive an important result in the study of the electro-osmotic instability [100], namely the effective slip velocity outside the ESC. To leading order our result agrees with Ref. [100], but we also find significant corrections to the slip model. These corrections may help to improve the understanding of electro-osmotic instabilities.

The extended space-charge region is a fundamental feature of problems involving concentration polarization, and it is a feature which we encounter in all of the remaining chapters. We shall therefore make frequent use of the QCD model to rationalize results, and as a part in analytical models applicable to the physics studied in those chapters.

Chapter 5

Concentration polarization in a microchannel

In recent years, concentration polarization in the context of microsystems has gathered increasing interest [59, 58, 74, 75, 142, 15, 56]. This interest has been spurred both by the implications for battery [71] and fuel cell technology [119, 127, 30] and by the potential applications in water desalination [57] and solute preconcentration [128, 63, 60]. In microsystems, surface effects are comparatively important, and for this reason their behavior is fundamentally different from bulk systems [135, 137]. For instance, an entirely new mode of overlimiting current enabled by surface conduction, has been predicted by Dydek *et al.* [27, 26]. In this mode, the current exceeding the diffusion-limited current runs through the depletion region inside the electric double layers, which screen the surface charges. This gives rise to an overlimiting current depending linearly on the surface charge, the surface-to-bulk ratio, and the applied potential. In addition to carrying a current, the moving ions in the electric double layers exert a force on the liquid medium, and thereby they create an electro-diffusio-osmotic flow in the channel. This fluid flow does in turn affect the transport of ions, and the resulting Poisson–Nernst–Planck–Stokes problem has strong nonlinear couplings between diffusion, electromigration, electrostatics, and advection. While different aspects of the problem can be, and has been, treated analytically [27, 135, 139, 103], the fully coupled system is in general too complex to allow for a simple analytical description.

In this chapter we investigate concentration polarization in a microchannel using three complementary approaches. Firstly, we carry out full numerical simulations of the coupled Poisson–Nernst–Planck–Stokes problem. Secondly, we derive an accurate boundary layer model for the transport in the system. Thirdly, in the limit of low aspect ratio, we derive simple analytical expressions for the current-voltage characteristic, which includes electromigration, diffusion, and advection in the electric double layers. The latter two models include some important effects which are absent from similar models published in the literature, and which we were able to identify by comparison with the full numerical model. For instance, the overlimiting conductance in our analytical model is $2 + 4\mathrm{Pe}_+^0$ times larger than the conductance found in Ref. [27], where diffusion and advection in the

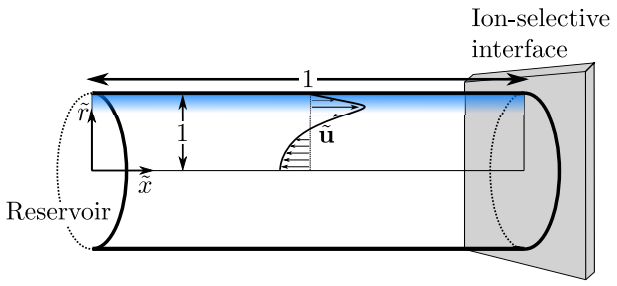

Figure 5.1: A sketch of the axisymmetric 2D system studied in this chapter. A microchannel of normalized length and radius unity connects a reservoir to the left to an ion-selective interface. The electric double layer adjoining the wall is shown as a shaded blue area, and the arrows indicate a velocity field deriving from electro-diffusio-osmosis with back-pressure.

double layers is neglected.

The content in this chapter is based on work from our paper Ref. [82], which can be found in Appendix F.

5.1 Model system

Our model system consists of a straight cylindrical microchannel of radius R and length L, which is filled with a binary and symmetric monovalent electrolyte. To the left the channel is attached to a reservoir with fixed electrolyte concentration c_0 and to the right the channel is attached to an ion-selective interface. The channel walls have a uniform negative surface charge density σ, which is screened by ions in the liquid over the characteristic distance λ_{D}. In Fig. 5.1 a sketch of the system is shown. The electric double layer adjoining the wall is shown as a shaded blue area, and the arrows indicate a velocity field deriving from electro-diffusio-osmosis with back-pressure. We assume cylindrical symmetry and we can therefore reduce the full three-dimensional problem to a two-dimensional problem.

5.2 Governing equations

Due to the presence of two different length scales in the geometry, R and L, the normalization in this chapter differs slightly from the normalization in previous chapters. We normalize the radial coordinate by R and the axial coordinate by L, and introduce the aspect ratio α and the nondimensional gradient operator $\tilde{\boldsymbol{\nabla}}$,

$$\alpha = \frac{R}{L}, \tag{5.1a}$$

$$\tilde{\boldsymbol{\nabla}} = \alpha \boldsymbol{e}_x \partial_{\tilde{x}} + \boldsymbol{e}_r \partial_{\tilde{r}}. \tag{5.1b}$$

Since the double layers vary in the transverse direction, we define the normalized Debye length as

$$\bar{\lambda}_{\mathrm{D}} = \frac{\lambda_{\mathrm{D}}}{R}. \tag{5.2}$$

We normalize the fluid velocity $\boldsymbol{u}$ by the electro-osmotic velocity scale U_0, the pressure by the corresponding microfluidic pressure scale p_0, and the body force density by f_0,

$$U_0 = \frac{\epsilon_\mathrm{w} V_\mathrm{T}^2}{\eta L}, \qquad p_0 = \frac{\eta U_0}{R}, \qquad f_0 = \frac{c_0 k_\mathrm{B} T}{R}. \tag{5.3a}$$

The remaining normalizations are as in Section 2.2. The steady-state transport equations for the ions then are

$$0 = -\tilde{\boldsymbol{\nabla}} \cdot \tilde{\boldsymbol{J}}_\pm, \tag{5.4a}$$

$$2\alpha \frac{D_+}{D_\pm} \tilde{\boldsymbol{J}}_\pm = -\tilde{c}_\pm \tilde{\boldsymbol{\nabla}} \tilde{\mu}_\pm + \alpha \mathrm{Pe}_\pm^0 \tilde{c}_\pm \tilde{\boldsymbol{u}}, \tag{5.4b}$$

$$\mathrm{Pe}_\pm^0 = \frac{L U_0}{D_\pm} = \frac{\epsilon_\mathrm{w} V_\mathrm{T}^2}{\eta D_\pm}. \tag{5.4c}$$

The Poisson equation takes the form

$$2\bar{\lambda}_\mathrm{D}^2 \tilde{\nabla}^2 \tilde{\phi} = -(\tilde{c}_+ - \tilde{c}_-), \tag{5.5}$$

and the Stokes and continuity equations become

$$0 = -\tilde{\boldsymbol{\nabla}} \tilde{p} + \tilde{\nabla}^2 \tilde{\boldsymbol{u}} + \frac{1}{2\alpha \bar{\lambda}_\mathrm{D}^2} \tilde{\boldsymbol{f}}, \tag{5.6a}$$

$$0 = \tilde{\boldsymbol{\nabla}} \cdot \tilde{\boldsymbol{u}}. \tag{5.6b}$$

5.2.1 The thermodynamic driving force

In Section 2.7 we made the case that it is more convenient to use the electrochemical potential $\tilde{\mu}_+$ as control variable than the electric potential $\tilde{\phi}$. The main reason that $\tilde{\mu}_+$ is the preferable variable is that it does not vary significantly across electric double layers. We can apply a similar reasoning to the body force density $\tilde{\boldsymbol{f}}$ occurring in the Stokes equation (5.6a).

Conventionally, the body force density is set to be the electrostatic force density $-\tilde{\rho}_\mathrm{el} \tilde{\boldsymbol{\nabla}} \tilde{\phi} = -(\tilde{c}_+ - \tilde{c}_-) \tilde{\boldsymbol{\nabla}} \tilde{\phi}$. By considering the forces on each constituent we can, however, formulate the problem in a way that is more convenient and better reveals the physics of the problem. The force acting on each particle is minus the gradient of its electrochemical potential. The force density can therefore be written as

$$\tilde{\boldsymbol{f}} = -\tilde{c}_+ \tilde{\boldsymbol{\nabla}} \tilde{\mu}_+ - \tilde{c}_- \tilde{\boldsymbol{\nabla}} \tilde{\mu}_- - \tilde{c}_{\mathrm{H_2O}} \tilde{\boldsymbol{\nabla}} \tilde{\mu}_{\mathrm{H_2O}}, \tag{5.7}$$

where $\tilde{c}_{\mathrm{H_2O}} \gg \tilde{c}_\pm$ and $\tilde{\mu}_{\mathrm{H_2O}}$ is the concentration and chemical potential of water, respectively. As opposed to $\tilde{\mu}_\pm$ given by the ideal gas expression $\tilde{\mu}_\pm = \ln(\tilde{c}_\pm) \pm \tilde{\phi}$, $\tilde{\mu}_{\mathrm{H_2O}}$ depends linearly on $\tilde{c}_\pm$ [64],

$$\tilde{\mu}_{\mathrm{H_2O}} = -\frac{\tilde{c}_+ + \tilde{c}_-}{\tilde{c}_{\mathrm{H_2O}}}, \tag{5.8a}$$

$$\tilde{\boldsymbol{f}} = -\tilde{c}_+ \tilde{\boldsymbol{\nabla}} \tilde{\mu}_+ - \tilde{c}_- \tilde{\boldsymbol{\nabla}} \tilde{\mu}_- + \tilde{\boldsymbol{\nabla}} (\tilde{c}_+ + \tilde{c}_-). \tag{5.8b}$$

If we insert the expressions for $\tilde{\mu}_\pm$, the force density reduces, as it should, to the usual electrostatic force density. It is, however, advantageous to keep the force density on this form, because it reveals the origin of each part of the force. For instance, if we insert a membrane which is impenetrable to ions, only the last term $\tilde{\boldsymbol{\nabla}}(\tilde{c}_+ + \tilde{c}_-)$ in the force, can drive a flow across the membrane, because the other forces are transmitted to the liquid via the motion of the ions. It is thus easy to identify $-(\tilde{c}_+ + \tilde{c}_-)$ as the osmotic pressure in the solution. Inserting Eq. (5.8b) for the force $\tilde{\boldsymbol{f}}$ in Eq. (5.6a) and absorbing the osmotic pressure into the new pressure $\tilde{p}' = \tilde{p} - (\tilde{c}_+ + \tilde{c}_-)$, we obtain

$$0 = -\tilde{\boldsymbol{\nabla}}\tilde{p}' + \tilde{\nabla}^2\tilde{\boldsymbol{u}} - \frac{1}{2\alpha\bar{\lambda}_\mathrm{D}^2}\left[\tilde{c}_+\tilde{\boldsymbol{\nabla}}\tilde{\mu}_+ + \tilde{c}_-\tilde{\boldsymbol{\nabla}}\tilde{\mu}_-\right]. \tag{5.9}$$

It is seen, that when the Stokes equation is given in this form, the body force density is guaranteed to vanish in equilibrium. This is in stark contrast to the conventional electrostatic body force $-\tilde{\rho}_\mathrm{el}\tilde{\boldsymbol{\nabla}}\tilde{\phi}$, which can be very large in the electric double layers, even in equilibrium. This feature of Eq. (5.9) simplifies both the numerical and analytical treatment of the problem.

5.2.2 Boundary conditions

To supplement the field equations (5.4a), (5.5), (5.6b), and (5.9) we specify boundary conditions on the channel walls, at the reservoir, and at the ion-selective interface. At the reservoir $\tilde{x} = 0$ we require that the flow is unidirectional along the $\tilde{x}$ axis. At the channel wall $\tilde{r} = 1$ and at the ion-selective interface $\tilde{x} = 1$ we impose a no-slip boundary condition,

$$\tilde{\boldsymbol{u}} = \tilde{u}\boldsymbol{e}_x, \quad \text{at } \tilde{x} = 0, \tag{5.10a}$$
$$\tilde{\boldsymbol{u}} = \boldsymbol{0}, \qquad \text{at } \tilde{r} = 1 \text{ or } \tilde{x} = 1. \tag{5.10b}$$

We assume that the ions are in local transverse equilibrium at the reservoir, so that the electric potential is determined by the Poisson–Boltzmann equation

$$\bar{\lambda}_\mathrm{D}^2 \frac{1}{\tilde{r}}\partial_{\tilde{r}}(\tilde{r}\partial_{\tilde{r}}\tilde{\phi}) = \sinh(\tilde{\phi}), \quad \text{at } \tilde{x} = 0. \tag{5.11a}$$

The boundary conditions for $\tilde{\phi}$ are a symmetry condition on the cylinder axis $\tilde{r} = 0$, and a surface charge boundary condition at the wall $\tilde{r} = 1$,

$$\partial_{\tilde{r}}\tilde{\phi} = 0, \qquad \text{at } \tilde{r} = 0, \tag{5.11b}$$
$$\boldsymbol{e}_r \cdot \tilde{\boldsymbol{\nabla}}\tilde{\phi} = -\frac{R\sigma}{V_\mathrm{T}\epsilon_\mathrm{w}} = \frac{\rho_\mathrm{s}}{4}\frac{1}{\bar{\lambda}_\mathrm{D}^2}, \quad \text{at } \tilde{r} = 1. \tag{5.11c}$$

The parameter ρ_s is defined as

$$\rho_\mathrm{s} = -\frac{2\sigma}{ec_0R}, \tag{5.11d}$$

and physically it is the average charge density in a channel cross-section, which is required to compensate the surface charge density. As explained in Ref. [27], ρ_s is closely related to the overlimiting conductance in the limit of negligible advection.

The boundary conditions for the ions are impenetrable channel walls at $\tilde{r} = 1$, and the ion-selective interface at $\tilde{x} = 1$ is impenetrable to anions while it allows cations to pass,

$$\boldsymbol{e}_r \cdot \tilde{\boldsymbol{J}}_\pm = 0, \quad \text{at } \tilde{r} = 1, \tag{5.12a}$$

$$\boldsymbol{e}_x \cdot \tilde{\boldsymbol{J}}_- = 0, \quad \text{at } \tilde{x} = 1. \tag{5.12b}$$

The assumption of transverse equilibrium at the reservoir entail that both the electrochemical potentials $\tilde{\mu}_\pm$ and the pressure $\tilde{p}'$ are constant here,

$$\tilde{\mu}_\pm = 0, \quad \text{at } \tilde{x} = 0, \tag{5.13a}$$

$$\tilde{p}' = 0, \quad \text{at } \tilde{x} = 0. \tag{5.13b}$$

In order to keep the analysis as general as possible, we use the GCP framework outlined in Section 2.7 to model the ion-selective interface. The remaining boundary conditions at $\tilde{x} = 1$ therefore are

$$\boldsymbol{e}_x \cdot \tilde{\boldsymbol{\nabla}} \tilde{c}_+ = 0, \qquad \text{at } \tilde{x} = 1, \tag{5.14a}$$

$$\tilde{\mu}_+ = -\tilde{V}_0, \quad \text{at } \tilde{x} = 1. \tag{5.14b}$$

The above governing equations and boundary conditions completely specify the problem and enable a numerical solution of the full Poisson–Nernst–Planck–Stokes problem with couplings between advection, electrostatics, and ion transport. In the remainder of this text we refer to the model specified above as the full model (FULL). See Table 5.1 for a list of all numerical and analytical models employed in this chapter. While the full numerical model provides an excellent tool to study the microchannel system, it may not be sufficient to give us the desired insight into the transport properties of the system. To obtain that insight, we develop a number of simplified models which separate the various transport mechanisms from each other.

5.3 Boundary layer models

To simplify the problem, we divide the system into a locally electroneutral bulk system and a thin region near the walls, comprising the electric double layer. The influence of the double layers on the bulk system is included via a surface current inside the boundary layer and an electro-diffusio-osmotic slip velocity.

5.3.1 Ion transport

To properly divide the variables into surface and bulk variables, we again consider the electrochemical potentials. In the limit of long and narrow channels the electrolyte is in transverse equilibrium, and the electrochemical potentials vary only along the $\tilde{x}$ direction,

Table 5.1: The numerical and analytical models employed in this chapter.

Abbreviation	Name	Described in
FULL	Full model (numerical)	Section 5.2
BNDF	Boundary layer model, full (numerical)	Section 5.3
BNDS	Boundary layer model, slip (numerical)	Section 5.3
ASCA	Analytical model, surface conduction-advection	Section 5.4.2
ASC	Analytical model, surface conduction	Section 5.4.2
QCD	Analytical model, bulk conduction through the ESC	Section 5.4.3

$$\tilde{\mu}_{\pm}(\tilde{x}) = \ln[\tilde{c}_{\pm}(\tilde{x},\tilde{r})] \pm \tilde{\phi}(\tilde{x},\tilde{r}). \tag{5.15}$$

Since the left hand side is independent of $\tilde{r}$, it must be possible to pull out the $\tilde{x}$ dependent parts of $\tilde{c}_{\pm}$ and $\tilde{\phi}$. We denote these parts $\bar{c}_{\pm}(\tilde{x})$ and $\tilde{\phi}_{\mathrm{b}}(\tilde{x})$,

$$\tilde{\mu}_{\pm}(\tilde{x}) = \ln[\bar{c}_{\pm}(\tilde{x})] + \ln\left[\frac{\tilde{c}_{\pm}(\tilde{x},\tilde{r})}{\bar{c}_{\pm}(\tilde{x})}\right] \pm \tilde{\phi}_{\mathrm{b}}(\tilde{x}) \pm \tilde{\phi}_{\mathrm{eq}}(\tilde{x},\tilde{r}), \tag{5.16}$$

where the equilibrium potential $\tilde{\phi}_{\mathrm{eq}}(\tilde{x},\tilde{r})$ is the remainder of the electric potential, $\tilde{\phi}_{\mathrm{eq}} = \tilde{\phi} - \tilde{\phi}_{\mathrm{b}}$. The $\tilde{r}$ dependent parts must compensate each other, and this implies a Boltzmann distribution of the ions in the $\tilde{r}$-direction,

$$\tilde{c}_{\pm}(\tilde{x},\tilde{r}) = \bar{c}_{\pm}(\tilde{x})\mathrm{e}^{\mp\tilde{\phi}_{\mathrm{eq}}(\tilde{x},\tilde{r})}. \tag{5.17}$$

The electrochemical potentials can then be written

$$\tilde{\mu}_{\pm}(\tilde{x}) = \ln[\bar{c}_{\pm}(\tilde{x})] \pm \tilde{\phi}_{\mathrm{b}}(\tilde{x}). \tag{5.18}$$

For further simplification, we assume that electroneutrality is only violated to compensate the surface charges, i.e. $\bar{c}_{+} = \bar{c}_{-} = \bar{c}$. As long as surface conduction or electro-diffusio-osmosis causes some overlimiting current this is a quite good assumption, because in that case the bulk system is not driven hard enough to cause any significant deviation from charge neutrality. For thin double layers, $\bar{c}$ corresponds to the ion concentration at $\tilde{r} = 0$. However, if the Debye length is larger than the radius, $\bar{c}$ does not actually correspond to a concentration which can be found anywhere in the cross-section, and for this reason $\bar{c}$ is often called the virtual salt concentration [135, 138].

To describe the general case, where transverse equilibrium is not satisfied in each cross-section, we allow the bulk potential $\tilde{\phi}_{\mathrm{b}}$ to vary in both $\tilde{x}$ and $\tilde{r}$ direction. Then, however,

the simple picture outlined above fails partially, and consequently, we make the ansatz

$$\tilde{c}_{\pm}(\tilde{x},\tilde{r}) = \bar{c}(\tilde{x})\mathrm{e}^{\mp\tilde{\phi}_{\mathrm{eq}}(\tilde{x},\tilde{r})} + \tilde{c}'(\tilde{x},\tilde{r}), \tag{5.19}$$

where $\tilde{c}'(\tilde{x},\tilde{r})$ accounts for the deviations from transverse equilibrium. Close to the walls, i.e. in or near the double layer, we therefore have $\tilde{c}'(\tilde{x},\tilde{r}) \approx 0$. Rearranging Eq. (5.19) we find

$$\begin{aligned}\tilde{c}_{\pm}(\tilde{x},\tilde{r}) &= \bar{c}(\tilde{x}) + \tilde{c}'(\tilde{x},\tilde{r}) + \bar{c}(\tilde{x})\left[\mathrm{e}^{\mp\tilde{\phi}_{\mathrm{eq}}(\tilde{x},\tilde{r})} - 1\right] \\ &= \tilde{c}(\tilde{x},\tilde{r}) + \tilde{c}^{\mathrm{ex}}_{\pm}(\tilde{x},\tilde{r}),\end{aligned} \tag{5.20}$$

where we have introduced the bulk salt concentration $\tilde{c}$ and the excess ion concentration $\tilde{c}^{\mathrm{ex}}_{\pm}$,

$$\tilde{c}(\tilde{x},\tilde{r}) = \bar{c}(\tilde{x}) + \tilde{c}'(\tilde{x},\tilde{r}), \tag{5.21}$$

$$\tilde{c}^{\mathrm{ex}}_{\pm}(\tilde{x},\tilde{r}) = \bar{c}(\tilde{x})\left[\mathrm{e}^{\mp\tilde{\phi}_{\mathrm{eq}}(\tilde{x},\tilde{r})} - 1\right]. \tag{5.22}$$

In the ion transport problem, the main significance of the excess ion concentration is that it allows an extra cation current to run inside the double layers. The excess anion concentration $\tilde{c}^{\mathrm{ex}}_{-}$, on the other hand, is largely unimportant.

Inserting Eq. (5.20) in Eq. (5.4b) we find

$$\begin{aligned}2\alpha\tilde{\boldsymbol{J}}_{+} = &-\tilde{\boldsymbol{\nabla}}\tilde{c} - \tilde{c}\tilde{\boldsymbol{\nabla}}\tilde{\phi}_{\mathrm{b}} + \alpha\mathrm{Pe}^0_{+}\tilde{c}\tilde{\boldsymbol{u}} - \tilde{c}'\tilde{\boldsymbol{\nabla}}\tilde{\phi}_{\mathrm{eq}} \\ &- \tilde{c}^{\mathrm{ex}}_{+}\tilde{\boldsymbol{\nabla}}\{\ln(\bar{c}) + \tilde{\phi}_{\mathrm{b}}\} + \alpha\mathrm{Pe}^0_{+}\tilde{c}^{\mathrm{ex}}_{+}\tilde{\boldsymbol{u}},\end{aligned} \tag{5.23}$$

where $\tilde{c}'\tilde{\boldsymbol{\nabla}}\tilde{\phi}_{\mathrm{eq}}$ can be neglected, since $\tilde{\phi}_{\mathrm{eq}}$ is only significant in the double layer where $\tilde{c}' \approx 0$. The terms involving $\tilde{c}^{\mathrm{ex}}_{+}$ are only significant near the walls, so it is natural to divide Eq. (5.23) into a bulk current and a surface current,

$$2\alpha\tilde{\boldsymbol{J}}^{\mathrm{bulk}}_{+} = -\tilde{\boldsymbol{\nabla}}\tilde{c} - \tilde{c}\tilde{\boldsymbol{\nabla}}\tilde{\phi}_{\mathrm{b}} + \alpha\mathrm{Pe}^0_{+}\tilde{c}\tilde{\boldsymbol{u}}, \tag{5.24a}$$

$$2\alpha\tilde{\boldsymbol{J}}^{\mathrm{surf}}_{+} = -\tilde{c}^{\mathrm{ex}}_{+}\tilde{\boldsymbol{\nabla}}\{\ln(\bar{c}) + \tilde{\phi}_{\mathrm{b}}\} + \alpha\mathrm{Pe}^0_{+}\tilde{c}^{\mathrm{ex}}_{+}\tilde{\boldsymbol{u}}. \tag{5.24b}$$

For the anions we only define a bulk current, since the excess anion concentration $\tilde{c}^{\mathrm{ex}}_{-}$ plays a minor role for the transport problem,

$$2\alpha\frac{D_+}{D_-}\tilde{\boldsymbol{J}}^{\mathrm{bulk}}_{-} = -\tilde{\boldsymbol{\nabla}}\tilde{c} + \tilde{c}\tilde{\boldsymbol{\nabla}}\tilde{\phi}_{\mathrm{b}} + \alpha\mathrm{Pe}^0_{-}\tilde{c}\tilde{\boldsymbol{u}}. \tag{5.25}$$

From the bulk currents Eq. (5.24a) and Eq. (5.25) we construct the linear combinations $\tilde{\boldsymbol{J}}^{\mathrm{bulk}}_{\mathrm{sum}}$ and $\tilde{\boldsymbol{J}}^{\mathrm{bulk}}_{\mathrm{dif}}$,

$$\alpha\tilde{\boldsymbol{J}}^{\mathrm{bulk}}_{\mathrm{sum}} = \alpha\left(\tilde{\boldsymbol{J}}^{\mathrm{bulk}}_{+} + \frac{D_+}{D_-}\tilde{\boldsymbol{J}}^{\mathrm{bulk}}_{-}\right) = -\tilde{\boldsymbol{\nabla}}\tilde{c} + \alpha\mathrm{Pe}^0\tilde{c}\tilde{\boldsymbol{u}}, \tag{5.26a}$$

$$\alpha\tilde{\boldsymbol{J}}^{\mathrm{bulk}}_{\mathrm{dif}} = \alpha\left(\tilde{\boldsymbol{J}}^{\mathrm{bulk}}_{+} - \frac{D_+}{D_-}\tilde{\boldsymbol{J}}^{\mathrm{bulk}}_{-}\right) = -\tilde{c}\tilde{\boldsymbol{\nabla}}\tilde{\phi}_{\mathrm{b}} + \alpha\frac{D_- - D_+}{D_- + D_+}\mathrm{Pe}^0\tilde{c}\tilde{\boldsymbol{u}}, \tag{5.26b}$$

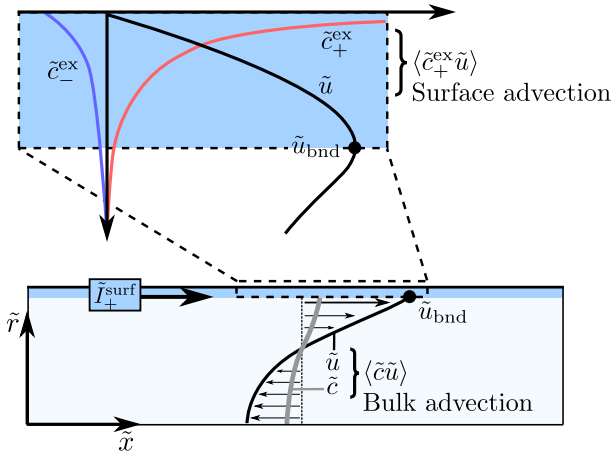

Figure 5.2: Sketch indicating the two regions in the boundary layer model. In the bulk region (lightly shaded) the boundary driven velocity field u (black line), the salt concentration profile c (gray line), and the bulk advection $\langle cu \rangle$ is shown. In the boundary region (shaded and top zoom-in) the excess ion concentrations $\tilde{c}_\pm^{\mathrm{ex}}$, the velocity field u, and the surface advection $\langle \tilde{c}_+^{\mathrm{ex}} u \rangle$ is shown.

with $\mathrm{Pe}^0 = \big(\mathrm{Pe}_+^0 + \mathrm{Pe}_-^0\big)/2$. Like the constituent currents, both of the currents $\tilde{\boldsymbol{J}}_{\mathrm{sum}}^{\mathrm{bulk}}$ and $\tilde{\boldsymbol{J}}_{\mathrm{dif}}^{\mathrm{bulk}}$ obey a continuity equation,

$$0 = \tilde{\boldsymbol{\nabla}} \cdot \tilde{\boldsymbol{J}}_{\mathrm{sum}}^{\mathrm{bulk}}, \quad 0 = \tilde{\boldsymbol{\nabla}} \cdot \tilde{\boldsymbol{J}}_{\mathrm{dif}}^{\mathrm{bulk}}. \tag{5.26c}$$

The surface current in Eq. (5.24b) is tightly bound to the wall, so we can describe it as a scalar current,

$$\begin{aligned} 2\tilde{I}_+^{\mathrm{surf}} &= 2\langle \boldsymbol{e}_x \cdot \tilde{\boldsymbol{J}}_+^{\mathrm{surf}} \rangle \\ &= -\langle \tilde{c}_+^{\mathrm{ex}} \rangle \big[\partial_{\tilde{x}} \ln(\bar{c}) + \partial_{\tilde{x}} \tilde{\phi}_{\mathrm{b}}\big] + \mathrm{Pe}_+^0 \langle \tilde{c}_+^{\mathrm{ex}} \tilde{u} \rangle \\ &= -\big(\rho_{\mathrm{s}} + \langle \tilde{c}_-^{\mathrm{ex}} \rangle\big) \big[\partial_{\tilde{x}} \ln(\bar{c}) + \partial_{\tilde{x}} \tilde{\phi}_{\mathrm{b}}\big] + \mathrm{Pe}_+^0 \langle \tilde{c}_+^{\mathrm{ex}} \tilde{u} \rangle, \end{aligned} \tag{5.27}$$

where the cross-sectional average is given as $\big\langle f(\tilde{r}) \big\rangle = \int_0^1 f(\tilde{r}) 2\tilde{r}\ \mathrm{d}\tilde{r}$, and we used that $\rho_{\mathrm{s}} = \big\langle \tilde{c}_+^{\mathrm{ex}} - \tilde{c}_-^{\mathrm{ex}} \big\rangle$. The first term in Eq. (5.27) we denote the surface conduction and the second term the surface advection. Equivalently, we call the terms proportional to Pe^0 in Eqs. (5.26a) and (5.26b) the bulk advection. In Fig. 5.2 the division of the system into a bulk region and a surface region is illustrated. The sketch also highlights the distinction between bulk and surface advection.

The surface current couples to the bulk problem through a boundary condition at $\tilde{r} = 1$,

$$\boldsymbol{n} \cdot \tilde{\boldsymbol{J}}_{\mathrm{sum}}^{\mathrm{bulk}} = \boldsymbol{n} \cdot \tilde{\boldsymbol{J}}_{\mathrm{dif}}^{\mathrm{bulk}} = \frac{1}{2} \alpha \partial_{\tilde{x}} \tilde{I}_+^{\mathrm{surf}}, \tag{5.28}$$

where the factor of a half comes from the channel cross section divided by the circumference. Rather than resolve the double layers, we can therefore include their approximate influence through the boundary condition Eq. (5.28).

Before we proceed with the analysis there is an issue we need to address: Several steps in the above derivations rely on the double layers being thin compared to the channel

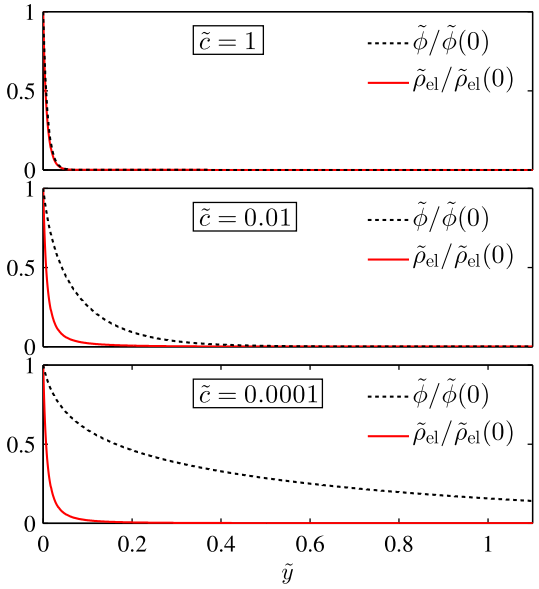

Figure 5.3: Plot of the charge density $\tilde{\rho}_{\mathrm{el}}$ and the potential $\tilde{\phi}$ near the channel wall for a system with $\bar{\lambda}_{\mathrm{D}} = 0.01$, $\rho_{\mathrm{s}} = 1$, and $\tilde{c} = \{1, 0.01, 0.0001\}$. At low values of $\tilde{c}$ the EDL extends across the channel, but the charge density is still confined to a small region near the wall.

radius. For typical system parameters this is a reasonable assumption in much of the system, but due to the low ion concentration in the depletion region, the double layers are in general not thin in that region. However, the method is saved by the structure of the double layer. Since the Debye length $\bar{\lambda}_{\mathrm{D}}$ is large in the depletion region the negative zeta potential is also large, $-\tilde{\zeta} \gg 1$. The majority of the screening charge is therefore located within the Gouy length $\bar{\lambda}_{\mathrm{G}}$, which can be considerably smaller than the Debye length [6, 92]. In Fig. 5.3, the charge density and the potential are plotted near the channel wall for a system with $\bar{\lambda}_{\mathrm{D}} = 0.01$, $\rho_{\mathrm{s}} = 1$, and $\tilde{c} = \{1, 0.01, 0.0001\}$. For $\tilde{c} = 1$ the charge density and the electric potential both decay at the same length scale. For lower values of $\tilde{c}$, the electric potential decays on a much longer length scale than the charge density. The normalized Gouy-length is given as

$$\bar{\lambda}_{\mathrm{G}} = \frac{\bar{\lambda}_{\mathrm{D}}}{\sqrt{\tilde{c}}} \operatorname{asinh}\left(8\frac{\bar{\lambda}_{\mathrm{D}}\sqrt{\tilde{c}}}{\rho_{\mathrm{s}}}\right) \leq 8\frac{\bar{\lambda}_{\mathrm{D}}^2}{\rho_{\mathrm{s}}}, \tag{5.29}$$

where the upper limit is a good approximation when $\sqrt{\tilde{c}} \ll \rho_{\mathrm{s}}/\bar{\lambda}_{\mathrm{D}}$. The boundary layer method is therefore justified provided that

$$\bar{\lambda}_{\mathrm{D}} \ll 1 \quad \text{or} \quad 8\frac{\bar{\lambda}_{\mathrm{D}}^2}{\rho_{\mathrm{s}}} \ll 1. \tag{5.30}$$

5.3.2 Flow problem

Using a procedure similar to the one used above, the flow problem is decomposed into bulk and surface contributions

$$0 = -\tilde{\boldsymbol{\nabla}}\tilde{p}' + \tilde{\nabla}^2\tilde{\boldsymbol{u}}, \qquad \text{bulk}, \tag{5.31a}$$

$$0 = \tilde{\boldsymbol{\nabla}}\cdot\tilde{\boldsymbol{u}}, \qquad \text{bulk}, \tag{5.31b}$$

$$0 = -\alpha\partial_{\tilde{x}}\tilde{p}' + \frac{1}{\tilde{r}}\partial_{\tilde{r}}\big(\tilde{r}\partial_{\tilde{r}}\tilde{u}\big) - \frac{1}{2}\frac{1}{\bar{\lambda}_{\mathrm{D}}^2}\big(\bar{c}\mathrm{e}^{-\tilde{\phi}_{\mathrm{eq}}}\partial_{\tilde{x}}\tilde{\mu}_+ + \bar{c}\mathrm{e}^{\tilde{\phi}_{\mathrm{eq}}}\partial_{\tilde{x}}\tilde{\mu}_-\big), \qquad \text{surface}. \tag{5.31c}$$

Since Eq. (5.31c) is linear in $\tilde{u}$ we can calculate the electro-osmotic velocity $\tilde{u}_{\mathrm{eo}}$, the diffusio-osmotic velocity $\tilde{u}_{\mathrm{do}}$, and the pressure-driven velocity $\tilde{u}_{\mathrm{p}}$ individually,

$$\begin{aligned}\tilde{u} &= \tilde{u}_{\mathrm{eo}} + \tilde{u}_{\mathrm{do}} + \tilde{u}_{\mathrm{p}}\\ &= \big[\tilde{u}_{\mathrm{eo}}^{\mathrm{u}} - 2\big\langle\tilde{u}_{\mathrm{eo}}^{\mathrm{u}}\big\rangle(1-\tilde{r}^2)\big]\,\partial_{\tilde{x}}\tilde{\phi}_{\mathrm{b}} + \big[\tilde{u}_{\mathrm{do}}^{\mathrm{u}} - 2\big\langle\tilde{u}_{\mathrm{do}}^{\mathrm{u}}\big\rangle(1-\tilde{r}^2)\big]\,\partial_{\tilde{x}}\ln(\bar{c})\\ &= \tilde{u}_{\mathrm{eo}}^{\mathrm{up}}\partial_{\tilde{x}}\tilde{\phi}_{\mathrm{b}} + \tilde{u}_{\mathrm{do}}^{\mathrm{up}}\partial_{\tilde{x}}\ln(\bar{c}),\end{aligned} \tag{5.32a}$$

$$\frac{1}{\tilde{r}}\partial_{\tilde{r}}\big(\tilde{r}\partial_{\tilde{r}}\tilde{u}_{\mathrm{eo}}^{\mathrm{u}}\big) = -\frac{\bar{c}}{\bar{\lambda}_{\mathrm{D}}^2}\sinh(\tilde{\phi}_{\mathrm{eq}}), \tag{5.32b}$$

$$\frac{1}{\tilde{r}}\partial_{\tilde{r}}\big(\tilde{r}\partial_{\tilde{r}}\tilde{u}_{\mathrm{do}}^{\mathrm{u}}\big) = \frac{\bar{c}}{\bar{\lambda}_{\mathrm{D}}^2}\cosh(\tilde{\phi}_{\mathrm{eq}}). \tag{5.32c}$$

Here, we introduced the unit velocity fields $\tilde{u}_{\mathrm{eo}}^{\mathrm{u}}$ and $\tilde{u}_{\mathrm{do}}^{\mathrm{u}}$, which both have driving forces of unity. We also introduced the unit velocities $\tilde{u}_{\mathrm{eo}}^{\mathrm{up}}$ and $\tilde{u}_{\mathrm{do}}^{\mathrm{up}}$, which include back-pressure driven flow. The surface advection term in Eq. (5.27) can therefore be written

$$\big\langle\tilde{c}_+^{\mathrm{ex}}\tilde{u}\big\rangle = I_2\partial_{\tilde{x}}\tilde{\phi}_{\mathrm{b}} + I_3\partial_{\tilde{x}}\ln(\bar{c}), \tag{5.33a}$$

$$I_2 = \big\langle\tilde{c}_+^{\mathrm{ex}}\tilde{u}_{\mathrm{eo}}^{\mathrm{up}}\big\rangle, \tag{5.33b}$$

$$I_3 = \big\langle\tilde{c}_+^{\mathrm{ex}}\tilde{u}_{\mathrm{do}}^{\mathrm{up}}\big\rangle. \tag{5.33c}$$

Equivalently, we define

$$I_1 = \big\langle\tilde{c}_-^{\mathrm{ex}}\big\rangle, \tag{5.33d}$$

so that we can write Eq. (5.27) as

$$2\tilde{I}_+^{\mathrm{surf}} = -(\rho_{\mathrm{s}} + I_1)\left[\partial_{\tilde{x}}\tilde{\phi}_{\mathrm{b}} + \partial_{\tilde{x}}\ln(\bar{c})\right] + \mathrm{Pe}_+^0\left[I_2\partial_{\tilde{x}}\tilde{\phi}_{\mathrm{b}} + I_3\partial_{\tilde{x}}\ln(\bar{c})\right], \tag{5.34}$$

in close analogy with the surface part of the current in Ref. [135].

The velocity field Eq. (5.32a) is also used to define a slip velocity for the bulk flow problem. In similar boundary layer models, the slip velocity is frequently taken to be the velocity outside the double layer, meaning that the slip velocity is proportional to the zeta potential [145, 144, 135, 27]. However, in the depletion region this approach often yields a slip velocity which significantly overestimates the actual velocity fields. The issue is that,

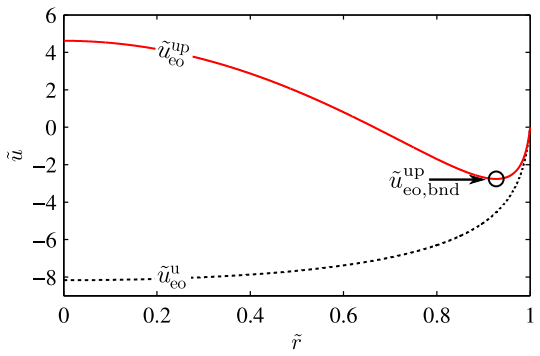

Figure 5.4: Plot of the transverse electro-osmotic unit velocity in a microchannel for $\bar{\lambda}_D = 0.01$, $\rho_s = 0.1$, and $\bar{c} = 0.001$. The black dashed line indicates the velocity field $\tilde{u}^{u}_{eo}$ without backpressure and the red line indicates the velocity field $\tilde{u}^{up}_{eo}$ with backpressure. The effective boundary velocity $\tilde{u}^{up}_{eo,bnd}$ is also indicated.

unlike the charge density, the electric potential always decays on the Debye length scale. In the depletion region the Debye length typically exceeds the channel width, so there is no place in the channel cross section which is truly outside the double layer. Also, since the electro-diffusio-osmotic velocity can vary across the entire channel width, the back-pressure driven flow enters into the definition of the slip velocity. In Fig. 5.4 we show the electro-osmotic unit velocity with and without back-pressure for $\bar{\lambda}_D = 0.01$, $\rho_s = 0.1$, and $\bar{c} = 0.001$.

It is seen from Fig. 5.4, that even when the Debye length is large the peak velocity is found pretty close to the wall at $\tilde{r} = 1$. We use this peak velocity as the effective slip velocity, meaning that the bulk flow problem Eqs. (5.31a) and (5.31b) is subject to the boundary condition

$$\tilde{\boldsymbol{u}} = \left[\tilde{u}^{up}_{eo,bnd}\partial_{\tilde{x}}\tilde{\phi}_b + \tilde{u}^{up}_{do,bnd}\partial_{\tilde{x}}\ln(\bar{c})\right]\boldsymbol{e}_x, \quad \text{at } \tilde{r} = 1, \tag{5.35}$$

where $\tilde{u}^{up}_{eo,bnd}$ and $\tilde{u}^{up}_{do,bnd}$ are the minimum values of $\tilde{u}^{up}_{eo}$ and $\tilde{u}^{up}_{do}$. The model developed in this section we refer to as the full boundary layer model (BNDF). We also introduce the slip boundary layer (BNDS) model, in which the bulk couples to the boundary layers only through a slip velocity, while the boundary condition (5.28) for the normal current is substituted by $\boldsymbol{n}\cdot\boldsymbol{J}_+ = 0$. In other words, the BNDS and BNDF models are identical, except the BNDS model does not include the surface current. These models are listed in Table 5.1 along with the other models used in this chapter.

5.4 Analysis

5.4.1 Scaling of bulk advection

To estimate the influence of bulk advection we consider the cross-sectional average of the bulk current $\tilde{\boldsymbol{J}}^{bulk}_{sum}$,

$$\tilde{J}^{bulk}_{sum} = \langle \boldsymbol{e}_x \cdot \tilde{\boldsymbol{J}}^{bulk}_{sum}\rangle = -\partial_{\tilde{x}}\langle\tilde{c}\rangle + \mathrm{Pe}^0\langle\tilde{c}\tilde{u}\rangle. \tag{5.36}$$

Since the ion-selective interface blocks the flow in one end, the net flow in a channel cross section is zero. This means that

$$\langle \tilde{c}\tilde{u} \rangle = \langle [\bar{c}(\tilde{x}) + \tilde{c}'(\tilde{x},\tilde{r})]\tilde{u} \rangle = \langle \tilde{c}'(\tilde{x},\tilde{r})\tilde{u} \rangle. \tag{5.37}$$

Now, the source of the deviation $\tilde{c}'$ between $\bar{c}$ and $\tilde{c}$ is the flow itself. Considering the dominant balance in $0 = \tilde{\boldsymbol{\nabla}} \cdot \tilde{\boldsymbol{J}}_{\mathrm{sum}}^{\mathrm{bulk}}$,

$$\frac{1}{\tilde{r}} \partial_{\tilde{r}} \big(\tilde{r} \partial_{\tilde{r}} \tilde{c} \big) \approx \alpha^2 \mathrm{Pe}^0 \partial_{\tilde{x}} \big(\tilde{c}\tilde{u} \big), \tag{5.38}$$

we find that $\tilde{c}'$ must scale as

$$\tilde{c}' \sim \alpha^2 \mathrm{Pe}^0 \partial_{\tilde{x}} \big(\bar{c}\tilde{u} \big). \tag{5.39}$$

Inserting this expression in Eq. (5.36) we find the following scaling of $\tilde{J}_{\mathrm{sum}}^{\mathrm{bulk}}$

$$\tilde{J}_{\mathrm{sum}}^{\mathrm{bulk}} \sim -\partial_{\tilde{x}} \langle \tilde{c} \rangle + \big(\alpha \mathrm{Pe}^0 \big)^2 \langle \partial_{\tilde{x}} \big(\bar{c}\tilde{u} \big) \tilde{u} \rangle. \tag{5.40}$$

This approximate expression reveals an essential aspect of the transport problem: With the chosen normalization neither the velocity, the diffusive current, the electromigration current, nor the surface current depend on the aspect ratio α. The only term that depends on α, is the bulk advection, and we see that for long slender channels ($\alpha \ll 1$) bulk advection vanishes, whereas it can be significant for short broad channels ($\alpha \sim 1$).

5.4.2 Local equilibrium models for small aspect ratio α

In the limit $\alpha \ll 1$, where bulk advection has a negligible effect, the system is nearly in local equilibrium in each cross section. The bulk concentration $\tilde{c}(\tilde{x},\tilde{r})$ therefore equals the virtual concentration $\bar{c}(\tilde{x})$, and the area averaged bulk currents are

$$\tilde{J}_{\mathrm{sum}}^{\mathrm{bulk}} = -\partial_{\tilde{x}} \bar{c}(\tilde{x}), \tag{5.41a}$$

$$\tilde{J}_{\mathrm{dif}}^{\mathrm{bulk}} = -\bar{c}(\tilde{x}) \partial_{\tilde{x}} \tilde{\phi}_{\mathrm{b}}(\tilde{x}). \tag{5.41b}$$

In steady state these currents are equal and can only change if there is a current into or out of the boundary layer. The conserved current $\tilde{J}_+$ is therefore

$$\tilde{J}_+ = -\partial_{\tilde{x}} \bar{c}(\tilde{x}) + \tilde{I}_+^{\mathrm{surf}} = -\bar{c}(\tilde{x}) \partial_{\tilde{x}} \tilde{\phi}_{\mathrm{b}}(\tilde{x}) + \tilde{I}_+^{\mathrm{surf}}. \tag{5.42}$$

It is readily seen that $\bar{c} = \mathrm{e}^{\tilde{\phi}_{\mathrm{b}}} = \mathrm{e}^{\tilde{\mu}_+/2}$ is a solution to this equation. To proceed we need expressions for the integrals I_1, I_2, and I_3 occurring in $\tilde{I}_+^{\mathrm{surf}}$.

First, let us consider $I_1 = \langle \tilde{c}_-^{\mathrm{ex}} \rangle$. Outside the depletion region the Debye length is small, so in most of the channel cross section $\tilde{c}_-^{\mathrm{ex}} = \bar{c}\big(\mathrm{e}^{\tilde{\phi}_{\mathrm{eq}}} - 1 \big) \approx 0$. Inside the depletion region the negative zeta potential is large $-\tilde{\zeta} \gg 1$. This means that most of the charge density is due to excess cations $\rho_{\mathrm{s}} \approx \tilde{c}_+^{\mathrm{ex}} \gg \tilde{c}_-^{\mathrm{ex}}$, and I_1 is therefore also negligible in this region. To a good approximation we thus have

$$I_1 \approx 0. \tag{5.43}$$

For the surface advection we consider first the electro-osmotic unit velocity without any pressure contributions,

$$\frac{1}{\tilde{r}}\partial_{\tilde{r}}\left(\tilde{r}\partial_{\tilde{r}}\tilde{u}^{\mathrm{u}}_{\mathrm{eo}}\right) = -\frac{\bar{c}}{\bar{\lambda}_{\mathrm{D}}^2}\sinh(\tilde{\phi}_{\mathrm{eq}}). \tag{5.44}$$

Integrating twice and employing the boundary conditions $\tilde{\phi}_{\mathrm{eq}}(1) = \tilde{\zeta}$ and $\tilde{u}^{\mathrm{u}}_{\mathrm{eo}}(1) = 0$ we find,

$$\tilde{u}^{\mathrm{u}}_{\mathrm{eo}} = (\tilde{\zeta} - \tilde{\phi}_{\mathrm{eq}}). \tag{5.45}$$

Because the excess cation concentration $\tilde{c}^{\mathrm{ex}}_{+}$ is located within the Gouy length $\bar{\lambda}_{\mathrm{G}} \ll 1$ from the wall, the back-pressure driven flow is not an important factor for the surface advection. When calculating I_2 we can therefore neglect the pressure driven velocity field,

$$I_2 = \left\langle \tilde{c}^{\mathrm{ex}}_{+}\tilde{u}^{\mathrm{up}}_{\mathrm{eo}}\right\rangle \approx \left\langle \tilde{c}^{\mathrm{ex}}_{+}\tilde{u}^{\mathrm{u}}_{\mathrm{eo}}\right\rangle = \left\langle \tilde{c}^{\mathrm{ex}}_{+}(\tilde{\zeta} - \tilde{\phi}_{\mathrm{eq}})\right\rangle. \tag{5.46}$$

Furthermore, since $\tilde{r} \approx 1$ whenever the integrand is nonnegligible,

$$I_2 \approx \int_0^1 \tilde{c}^{\mathrm{ex}}_{+}(\tilde{\zeta} - \tilde{\phi}_{\mathrm{eq}})2\tilde{r}\ \mathrm{d}\tilde{r} \approx \int_0^1 \tilde{c}^{\mathrm{ex}}_{+}(\tilde{\zeta} - \tilde{\phi}_{\mathrm{eq}})2\ \mathrm{d}\tilde{r}, \tag{5.47}$$

and we can approximate the equilibrium potential with the Gouy–Chapman solutionn Eq. (2.31),

$$\tilde{\phi}_{\mathrm{eq}} \approx 4\,\mathrm{artanh}\left\{\tanh\left[\frac{\tilde{\zeta}}{4}\right]\exp\left[-\frac{\tilde{y}}{\bar{\lambda}_{\mathrm{D}}/\sqrt{\bar{c}}}\right]\right\}, \tag{5.48}$$

$$\tilde{\zeta} = -2\,\mathrm{arsinh}\left[\frac{\rho_{\mathrm{s}}}{8\bar{\lambda}_{\mathrm{D}}\sqrt{\bar{c}}}\right] \approx -2\ln\left[\frac{\rho_{\mathrm{s}}}{4\bar{\lambda}_{\mathrm{D}}\sqrt{\bar{c}}}\right]. \tag{5.49}$$

Here, $\tilde{y}$ is the distance from the wall, and the last approximation is valid when $-\tilde{\zeta} \gtrsim 2$. We then find

$$\begin{aligned} I_2 &\approx \bar{c}\int_0^1 (\mathrm{e}^{-\tilde{\phi}_{\mathrm{eq}}} - 1)(\tilde{\zeta} - \tilde{\phi}_{\mathrm{eq}})2\ \mathrm{d}\tilde{y} \\ &\approx \bar{c}\int_0^\infty (\mathrm{e}^{-\tilde{\phi}_{\mathrm{eq}}} - 1)(\tilde{\zeta} - \tilde{\phi}_{\mathrm{eq}})2\ \mathrm{d}\tilde{y} \\ &= 8\bar{\lambda}_{\mathrm{D}}\sqrt{\bar{c}}\left(1 - \frac{1}{2}\tilde{\zeta} - \mathrm{e}^{-\frac{1}{2}\tilde{\zeta}}\right) \\ &\approx -8\bar{\lambda}_{\mathrm{D}}\sqrt{\bar{c}}\mathrm{e}^{-\frac{1}{2}\tilde{\zeta}} \approx -2\rho_{\mathrm{s}}, \end{aligned} \tag{5.50}$$

where we used that $-\tilde{\zeta} \gg 1$. Since the zeta potential is large and negative the factor $\cosh(\tilde{\phi}_{\mathrm{eq}})$, appearing in the diffusioosmotic velocity, is nearly identical to the factor $-\sinh(\tilde{\phi}_{\mathrm{eq}})$, appearing in the electro-osmotic velocity. We therefore have

$$I_3 \approx I_2 \approx -2\rho_{\mathrm{s}}, \tag{5.51}$$

and the current in the system Eq. (5.42) becomes

$$\tilde{J}_+ = -\partial_{\tilde{x}}\bar{c}(\tilde{x}) - \frac{\rho_s}{2}\partial_{\tilde{x}}\tilde{\mu}_+ - \rho_s \mathrm{Pe}_+^0 \partial_{\tilde{x}}\tilde{\mu}_+ \tag{5.52}$$

$$\Rightarrow \tilde{J}_+\tilde{x} = 1 - \mathrm{e}^{-\tilde{\mu}_+/2} - \left(\frac{1}{2} + \mathrm{Pe}_+^0\right)\rho_s\tilde{\mu}_+. \tag{5.53}$$

Applying the boundary condition $\tilde{\mu}_+(1) = -\tilde{V}_0$, we obtain the current-voltage relation

$$\tilde{J}_+ = 1 - \mathrm{e}^{-\frac{1}{2}\tilde{V}_0} + \left(\frac{1}{2} + \mathrm{Pe}_+^0\right)\rho_s\tilde{V}_0. \tag{5.54}$$

While this expression was derived with a cylindrical geometry in mind, it applies to most channel geometries. The only requirement is that the local radius of curvature of the channel wall is much larger than the Gouy length $\bar{\lambda}_G$, so that the potential is well approximated by the Gouy-Chapman solution. We call this analytical model the surface conduction-advection (ASCA) model. As shown in Section 5.5, it is very accurate in the limit of long slender channels, $\alpha \ll 1$.

For a system with a Gouy length on the order of unity, the screening charges are distributed across the channel in the depletion region. Advection therefore transports approximately as many cations towards the ion-selective interface as away from the interface, and there is no net effect of surface advection. In this limit, Eq. (5.54) reduces to the pure surface conduction expression

$$\tilde{J}_+ = 1 - \mathrm{e}^{-\frac{1}{2}\tilde{V}_0} + \frac{\rho_s}{2}\tilde{V}_0, \tag{5.55}$$

which we refer to as the analytical surface conduction (ASC) model. See Table 5.1 for a list of the models employed in this chapter.

Both of the models Eq. (5.54) and Eq. (5.55) have a constant overlimiting conductivity, and in this respect they agree with the Dydek model of surface conduction in a microchannel [27]. However, because we consistently apply the local equilibrium condition we find an overlimiting conductivity that is either 2 times larger (ASC) or $2 + 4\mathrm{Pe}_+^0$ times larger (ASCA) than the Dydek conductivity.

5.4.3 Bulk conduction through the extended space-charge region

In the limit of low surface charge and high $\bar{\lambda}_D$, neither surface conduction nor advection matter much. However, this does not mean that there can not be an overlimiting current. As described in Chapter 4 an extended space-charge region (ESC) can develop under these conditions, in which an overlimiting current can run in the bulk of the microchannel. This effect is not captured by the numerical boundary layer model (BNDF), since it assumes local electroneutrality, but it is captured in the FULL numerical model. The analytical QCD model from Chapter 4 describes the transport in the bulk of the microchannel and the influence of the ESC. From Eq. (4.22) we find the leading order behavior of the QCD model at overlimiting current,

$$-\tilde{V}_0 = \tilde{\mu}_+(1) \approx -\frac{2\sqrt{2}}{3}\frac{(\tilde{J}_+ - 1)^{3/2}}{\alpha\bar{\lambda}_D\tilde{J}_+} + 2\ln(\alpha\bar{\lambda}_D), \tag{5.56}$$

Table 5.2: Parameters and their values or range of values. To simplify the analysis, Pe^0 and D_+/D_- are fixed.

Parameter	Symbol	Value/Range
Normalization Péclet number	Pe^0	0.235
Diffusivity ratio	D_+/D_-	1
Aspect ratio	α	0.01–0.2
Normalized Debye length	$\bar{\lambda}_\mathrm{D}$	0.0001–0.1
Average surface charge density	ρ_s	0.001–1
Bias voltage	$\tilde{V}_0$	0–100

where the factors of α enter the expression due to the different definition of $\bar{\lambda}_\mathrm{D}$ in Chapter 4. The QCD model is listed in Table 5.1 along with the other models employed in this chapter.

5.5 Numerical analysis

5.5.1 Numerical implementation

Following the methods outlined in Section 3.1 the governing equations of the FULL model and the BNDF model are written in weak form and implemented in COMSOL. The cross-sectional averages I_1, I_2, and I_3 [Eq. (5.33)] as well as the slip velocity [Eq. (5.35)] are calculated and tabulated in a separate model.

In the theoretical treatment we found seven dimensionless numbers, which govern the behaviour of the system. These are the normalization Péclet number Pe^0, the diffusivity ratio D_+/D_-, the aspect ratio α, the normalized Debye length $\bar{\lambda}_\mathrm{D}$, the cross-sectionally averaged charge density ρ_s, and the applied bias voltage $\tilde{V}_0$. To further limit the parameter space, we have chosen fixed and physically reasonable values for a few of the parameters. The ionic diffusivities are assumed to be equal. For a solution of potassium chloride with $D_{\mathrm{K}^+} = 1.96\ \mathrm{m}^2/\mathrm{s}$ and $D_{\mathrm{Cl}^-} = 2.03\ \mathrm{m}^2/\mathrm{s}$, this is actually nearly the case. The normalization Péclet number is set to $\mathrm{Pe}^0 = 0.235$, which is a realistic number for potassium ions in water at room temperature. This leaves us with four parameters, α, $\bar{\lambda}_\mathrm{D}$, ρ_s and $\tilde{V}_0$, which govern the system behavior. We mainly present our results in the form of I-V characteristics, i.e. sweeps in $\tilde{V}_0$, since the important features of the transport mechanisms can most often be inferred from these. We vary the other parameters as follows: the aspect ratio α takes on the values $\{0.01, 0.05, 0.1, 0.2\}$, the normalized Debye length $\bar{\lambda}_\mathrm{D}$ takes the values $\{0.0001, 0.001, 0.01, 0.1\}$, and the averaged charge density ρ_s takes the values $\{0.001, 0.01, 0.1, 1\}$. The parameters and their values or range of values are listed in Table 5.2. The $\bar{\lambda}_\mathrm{D} = 0.0001$ systems are only solved in the BNDF model, since a full numerical solution with resolved electric double layers is computationally costly in this limit $\bar{\lambda}_\mathrm{D} \ll 1$. The boundary layer model is quite accurate in the small $\bar{\lambda}_\mathrm{D}$ limit, so the lack of a full numerical solution for $\bar{\lambda}_\mathrm{D} = 0.0001$ is not a concern.

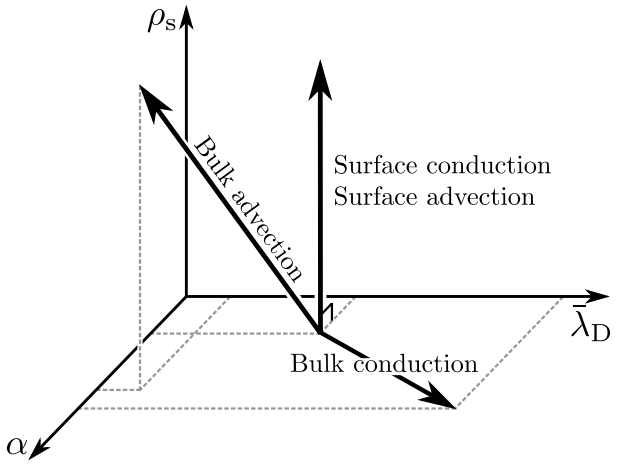

Figure 5.5: Directions of increase of the various mechanisms of overlimiting current. Bulk advection increases with α and ρ_s and decreases with $\bar{\lambda}_D$. Surface conduction and surface advection increases with ρ_s, and bulk conduction through the ESC increases with $\alpha\bar{\lambda}_D$.

5.5.2 Parameter dependence of I-V characteristics

The results of the simulations are presented in the following way: For each α value a $(\bar{\lambda}_D, \rho_s)$ grid is made, and in each grid point the corresponding I-V characteristic is shown. The I-V characteristics obtained from the simulations are supplemented with relevant analytical results. To aid in the interpretation of the results, Fig. 5.5 shows the trends we expect on the basis of the governing equations and our analysis. Based on Eq. (5.54) we expect surface conduction and surface advection to increase with ρ_s. Based on the simple expression (5.49) for the zeta potential and the scaling result in Eq. (5.40), we expect bulk advection to increase with ρ_s and α and decrease with $\bar{\lambda}_D$. As outlined in Section 5.4.3 the bulk conduction through the extended space-charge region is expected to increase with $\alpha\bar{\lambda}_D$.

In Figs. 5.6 and 5.7 the numerically calculated I-V characteristics are plotted for a long slender channel ($\alpha = 0.05$) and a short broad channel ($\alpha = 0.2$), respectively. In Appendix A additional results for $\alpha = 0.01$ and $\alpha = 0.1$ are given. The results for the FULL model with resolved double layers (defined in Section 5.2) are shown in a full black line. The results for the BNDF model (defined in Section 5.3) are shown in a dashed red line. The gray long-dash-short-dash line is obtained from the QCD model specified in Chapter 4. The blue dash-dot line is the analytical curve from the ASC model, and the green dash-diamond line is the analytical curve from the ASCA model. To help structure the results the I-V characteristics have been given a colored background pattern, which indicate the dominant conduction mechanisms. A green cross-hatched background indicates that the dominant mechanisms are surface conduction and surface advection. A red horizontally-hatched background indicates that bulk advection is the dominant mechanism. Blue with vertical hatches indicates that surface conduction without surface advection is the dominant mechanism and gray with skewed hatches indicates that the dominant mechanism is bulk conduction through the extended space-charge region.

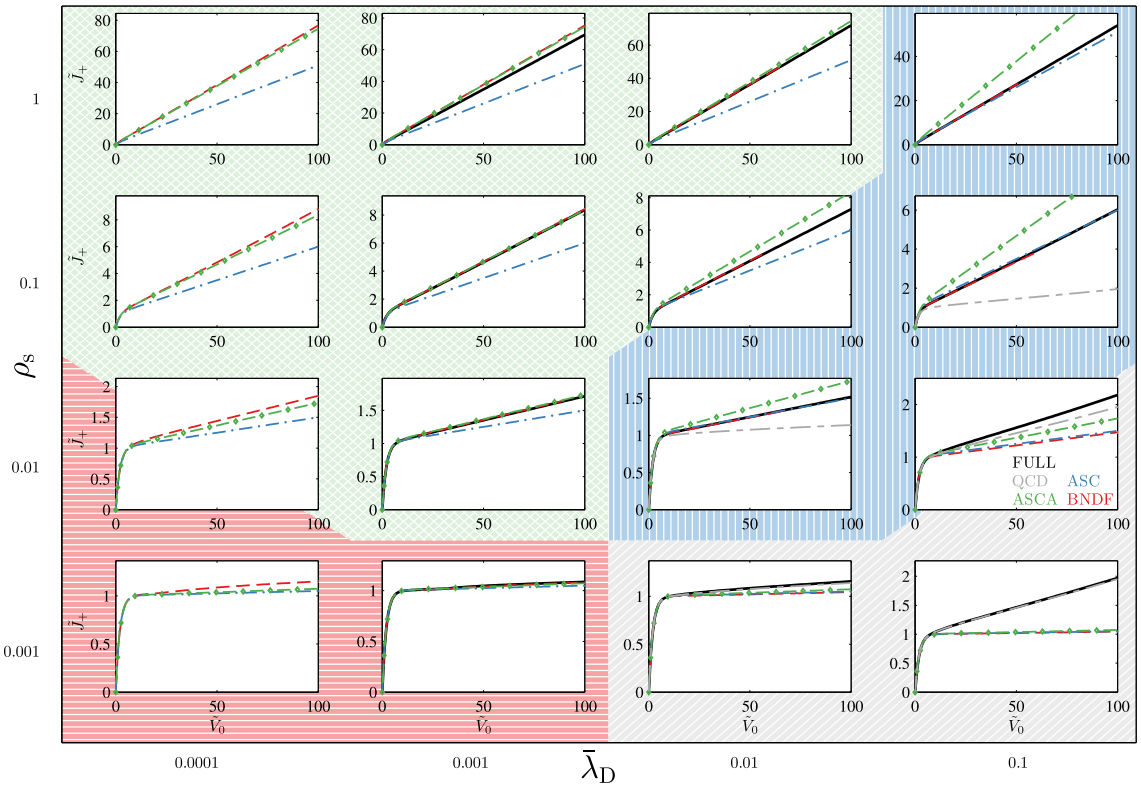

Figure 5.6: *I-V* characteristics for $\alpha = 0.05$, $\bar{\lambda}_D = \{0.0001, 0.001, 0.01, 0.1\}$, and $\rho_s = \{0.001, 0.01, 0.1, 1\}$. The full black lines show the characteristics obtained from the FULL model. The dashed red curves are obtained from the BNDF model. The blue dash-dot curves are from the ASC model, and the green dash-diamond curves are from the ASCA model. The gray long-dash-short-dash curves are obtained from the QCD model. The background patterns indicate the dominant overlimiting conduction mechanism. The green cross-hatched pattern indicates that surface advection and surface conduction are the dominant mechanisms. The blue vertically hatched pattern indicates that surface conduction without surface advection is the dominant mechanism. The red horizontally hatched pattern indicates that bulk advection is the dominant mechanism. The gray skew-hatched pattern indicates that bulk conduction through the ESC is the dominant mechanism. Intermediate cases are indicated with mixed background patterns.

A split background indicates that the overlimiting current is the result of two different mechanisms. In the case of a split cross-hatched/vertically-hatched background, the split indicates that surface conduction is important, and that surface advection plays a role, but that this role is somewhat reduced due to backflow along the channel axis.

We first consider the case $\alpha = 0.05$ shown in Fig. 5.6. Here, the aspect ratio α is so low that the effects of bulk advection are nearly negligible. As a consequence the numerical (red dashed and full black lines) and analytical (green dash-diamond line) curves nearly match each other in a large portion of the parameter space (green cross-hatched region). Although there is a small region in which bulk advection does play a role (red horizontally-hatched region), the overlimiting current due to bulk advection is small for all of the investigated $\bar{\lambda}_D$ and ρ_s values. In the right part (high $\bar{\lambda}_D$) of Fig. 5.6 the effects of bulk and surface advection are negligible. For high ρ_s values surface conduction dominates (blue

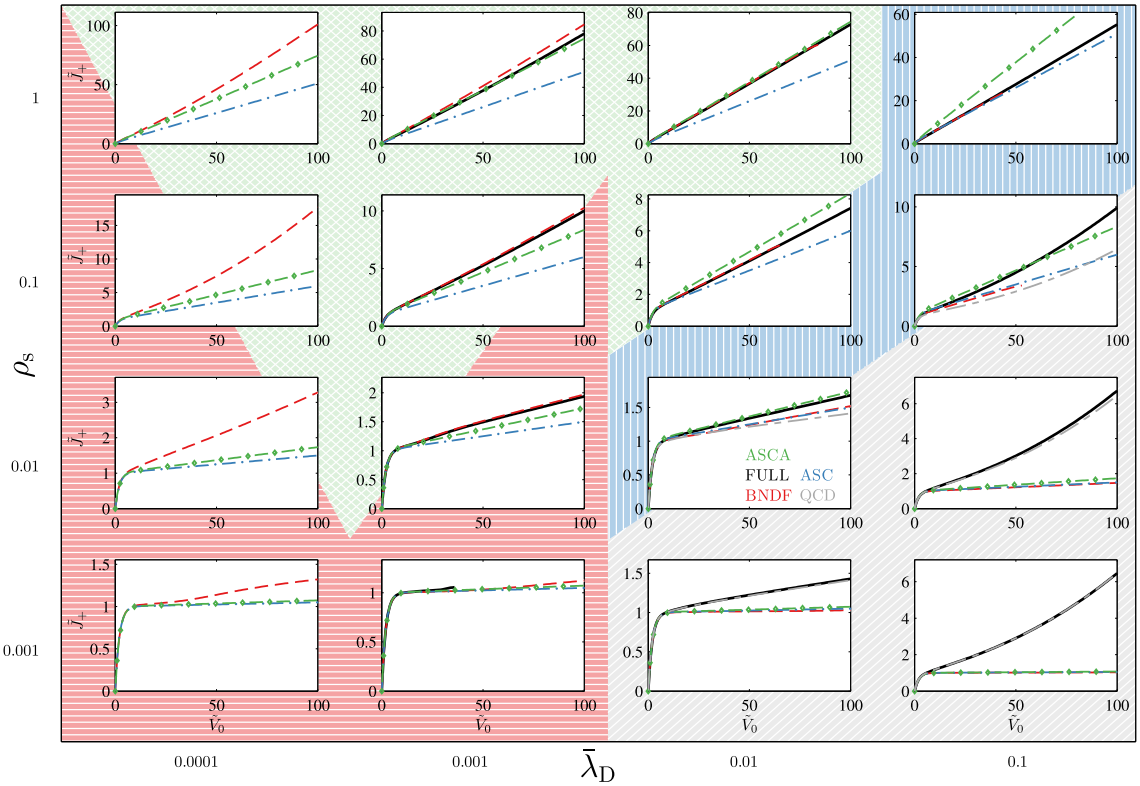

Figure 5.7: Same I-V characteristics as Fig. 5.6, except that here $\alpha = 0.2$ instead of 0.05.

vertically-hatched region) and for low ρ_s bulk conduction through the ESC dominates (gray skew-hatched region).

The case of $\alpha = 0.2$, shown in Fig. 5.7, follows the same basic pattern as the $\alpha = 0.05$ case. As expected from Fig. 5.5, the regions where bulk advection (red horizontal hatches) or bulk conduction (gray skewed hatches) dominates grow as α is increased. Inside the regions an increase in magnitude of both effects is also seen. The picture that emerges, is that in the long channel limit $\alpha \lesssim 0.05$ the effects of bulk advection are negligible, and for small $\bar{\lambda}_D$ the overlimiting current is entirely due to surface conduction and surface advection. For bulk advection to cause a significant overlimiting current the channel has to be relatively short, $\alpha \gtrsim 0.1$, and the normalized Debye length has to be small, $\bar{\lambda}_D \lesssim 0.001$.

5.5.3 Field distributions

In Fig. 5.8 some of the important fields are plotted for two different sets of parameter values. The fields are obtained from the BNDF model. To the left, in panel (a), (b), and (c), the fields are given for a system with $\bar{\lambda}_D = 0.0001$, $\rho_s = 0.01$, $\alpha = 0.2$, $\tilde{V}_0 = 60$, and to the right, in panel (d), (e), and (f), the fields are given for a system with $\bar{\lambda}_D = 0.001$, $\rho_s = 0.1$, $\alpha = 0.05$, $\tilde{V}_0 = 60$. The colors indicate the relative magnitude (blue low value, red high value) of the fields within each panel. Comparing panel (c) and (f) we see that

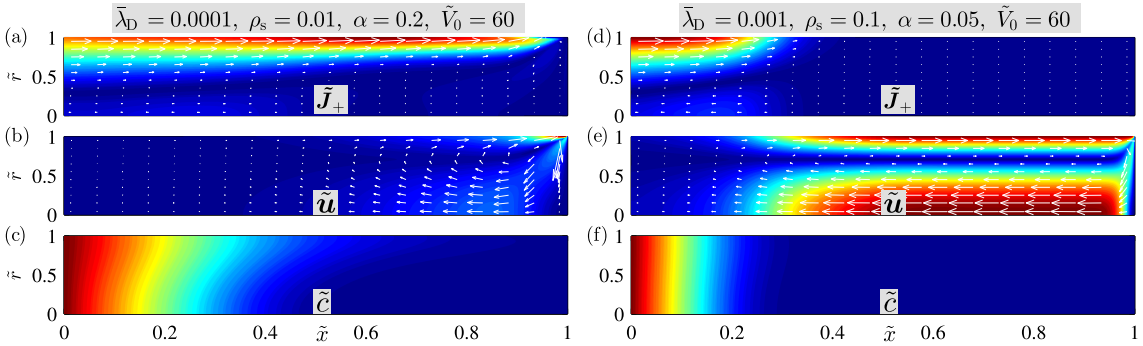

Figure 5.8: For a system with $\bar{\lambda}_D = 0.0001$, $\rho_s = 0.01$, $\alpha = 0.2$, and $\tilde{V}_0 = 60$ is plotted (a) the cation current $\tilde{\boldsymbol{J}}_+$, (b) the velocity $\tilde{\boldsymbol{u}}$, and (c) the salt concentration $\tilde{c}$. For a system with $\bar{\lambda}_D = 0.001$, $\rho_s = 0.1$, $\alpha = 0.05$, and $\tilde{V}_0 = 60$ is plotted (d) the cation current $\tilde{\boldsymbol{J}}_+$, (e) the velocity $\tilde{\boldsymbol{u}}$, and (f) the salt concentration $\tilde{c}$. The fields are obtained from the BNDF model, and the colors indicate the relative magnitude (blue low and red high) of the fields within each panel, while arrows represent vector fields.

the depletion region is bigger in panel (f) than panel (c), which is as expected since the current in panel (f) is larger than in panel (c) (cf. Figs. 5.6 and 5.7). It is also noted that the transverse distribution of the concentration is much less uniform in the (c) panel than in the (f) panel. Due to this nonuniformity (see Section 5.4.1), system (a)-(b)-(c) has a net current contribution from bulk advection, whereas bulk advection contributes negligibly to the current in the transversally uniform system (d)-(e)-(f).

5.5.4 Coupling between bulk advection and the surface current

As seen in Figs. 5.6 and 5.7, the limits where the overlimiting current is due to either surface advection and surface conduction, surface conduction alone, or bulk conduction through the ESC, are well described by our analytical models. The analytical models do not describe the transitions between the limiting behaviours, but the essentials of the involved mechanisms are well understood. It is thus mainly the bulk advection which requires a more thorough investigation. As pointed out in Refs. [145, 144, 40, 139], the effects of bulk advection can to some extent be understood in terms of a Taylor–Aris-like model of hydrodynamic dispersion. However, in those papers surface conduction and surface advection is neglected on account of their small contribution to the total current in the investigated limits. It turns out that in the context of concentration polarization, the surface currents do in fact play a crucial role for the bulk advection, even when the surface currents themselves only give a minute contribution to the total current. Our boundary layer model is ideally suited to demonstrate just that point, since it allows us to artificially turn off the surface currents while keeping the electro-diffusio-osmotic flow.

In Fig. 5.9 I-V characteristics obtained from the BNDF (dashed red line) and BNDS (dotted purple line) models are plotted for $\alpha = 0.2$, $\bar{\lambda}_D = 0.0001$, and $\rho_s = 0.001$. For comparison the I-V characteristic from the ASCA model, which includes surface conduction and surface advection but excludes bulk advection, is also plotted. In Fig. 5.10 the same curves are plotted with $\rho_s = 0.1$ instead of 0.001. Comparing the BNDF model (dashed

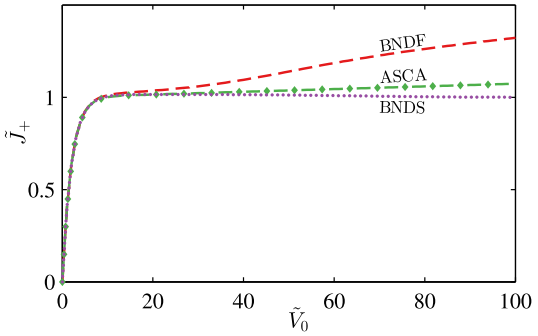

Figure 5.9: *I-V* characteristics highlighting the role of the surface current for bulk advection. $\alpha = 0.2$, $\bar{\lambda}_D = 0.0001$, and $\rho_s = 0.001$. The dashed red curve is obtained from the BNDF model and the green dash-diamond curve is from the ASCA model. The dotted purple curve is obtained from the BNDS model, in which the surface current has been artificially removed while the electro-diffusio-osmotic slip velocity is kept.

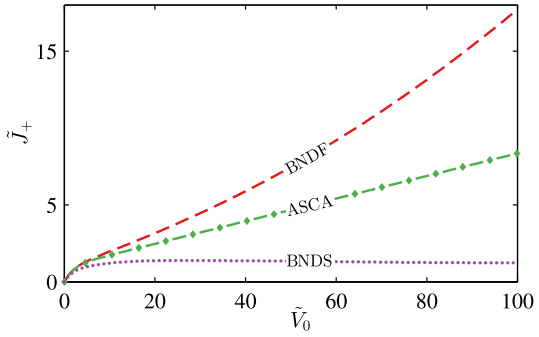

Figure 5.10: Same as Fig. 5.9 but with $\rho_s = 0.1$.

red) with the ASCA model (green dash-diamond), it is seen that bulk advection plays a significant role in these regimes. In light of this it is remarkable that the BNDS model, which includes bulk advection but excludes surface currents, (dotted purple line) exhibits no overlimiting current at all. We conclude that the surface current is, in some way, a prerequisite for significant bulk advection.

Our investigations suggest that the reason for this highly nonlinear coupling between bulk advection and the surface current is that the surface current sets the length of the depletion region before bulk advection sets in. The large gradients in electrochemical potentials, and thereby the large electro-diffusio-osmotic velocities, exist in the depletion region, so a wide depletion region implies a wide region with significant advection. In the limit of zero surface current, the depletion region only extends over a tiny region next to the ion-selective interface. In this region there is a huge electro-diffusio-osmotic flow towards the interface, but the effects of that flow are not felt very far away, because it is compensated by the back-pressure driven flow over a quite small distance. When there is a surface current, the depletion region will eventually, as the driving potential is increased, extend so far away from the ion-selective interface that back-pressure does not immediately compensate the electro-diffusio-osmotic flow. In that situation, bulk advection may begin to play a role. The need for a sufficiently large depletion region is seen by the plateau in the BNDF *I-V* characteristic in Fig. 5.9. What happens is that as a function of voltage, the current increases to the limiting current, remains there for a while, and then, once the depletion region is sufficiently developed, increases further due to bulk advection.

5.6 Conclusion

In this chapter, we have presented a thorough combined numerical and analytical study of the transport mechanisms in a microchannel undergoing concentration polarization. We have rationalized the behavior of the system and identified four mechanisms of overlimiting current: surface conduction, surface advection, bulk advection, and bulk conduction through the extended space-charge region. In the limits where surface conduction, surface advection, or bulk conduction through the ESC dominates we have derived accurate analytical models for the ion transport and verified them numerically. In the limit of long, narrow channels these models are in excellent agreement with the numerical results. We have found that bulk advection is mainly important for short, broad channels, and using numerical simulations we have quantified this notion and outlined the parameter regions with significant bulk advection. A noteworthy discovery is that the development of bulk advection is strongly dependent on the surface current, even in cases where the surface current contributes much less to the total current than bulk advection.

Our treatment confirms the basics of the analytical surface conduction model from Ref. [27], while providing a significant correction to the overlimiting conductivity. Regarding the treatment of electro-osmosis in Ref. [27], we have, as discussed in Section 5.3, identified some issues with the employed slip model. We are therefore skeptical about the detailed scaling relation for electro-osmosis presented in that paper. Nevertheless, there is little doubt that the essential feature predicted in Ref. [27], the existence of a conductance minimum as a function of channel height, is a real effect. Indeed, this has recently been confirmed in an experimental study [79].

Recently, so-called shock electrodialysis in microporous media has been proposed as a method of water desalination and electrochemical separation [26, 22, 21, 88]. These systems are typically analyzed in terms of a volume averaged leaky membrane model, where the surface-charge density on the microchannel walls provide an average background space-charge density [136, 26, 22]. However, as pointed out in Ref. [22], the volume averaged models fail to take flow loops forming among the irregular microstructures into account. These loops provide increased hydrodynamic dispersion in the system, and presumably affect the transport quite significantly. It seems, that to include these loop effects, an explicit model of the microporous geometry is required. This approach has been tentatively explored in Ref. [1], where the transport through a network of microchannels was considered. Our simple analytical models could simplify such network models considerably, as they would remove the need for solving a set of ODE's on each of the many individual microchannels.

Chapter 6

Water splitting at permselective membranes

As seen in the preceding chapters, there are a variety of physical effects, which can influence the transport properties of a system exhibiting concentration polarization. However, for many types of systems chemical reactions may play an important role as well. For instance, the autoprotolytic reaction of water can either produce or consume hydronium and hydroxide in the system. Since hydronium and hydroxide are charged species, they influence the transport of salt ions by affecting the electric field. Also, in the context of microchannels or microporous systems, reactions between hydronium ions and surface groups can alter the local surface-charge density, and thereby modify the transport in the system [49, 5, 3, 2, 9, 48].

In bulk systems containing permselective membranes, water splitting has long been investigated as a possible cause of overlimiting current [97, 11, 114, 54, 55, 111, 90, 141, 117, 78, 110, 111]. A central result is the prediction by Kharkats, that besides adding to the total current, a water-ion current is also able to increase, or exalt, the current of salt ions above the limiting current [54]. It is reasonably well understood that the origin of the water-ion current is water dissociation taking place in a region close to the permselective membrane. In many experiments, the magnitude of the water-ion current does, however, indicate a reaction rate much larger than what should be possible, considering only the bulk dissociation rates [108, 110, 89, 116]. A number of models have been suggested to explain this remarkable feature. Some of these ascribe the increased reaction rate to catalytic interactions with membrane surface groups [108, 111, 50], while others use that the dissociation rate is increased in strong electric fields, and employ a phenomenological function with one or more fitting parameters to describe this dependence [110, 19, 90, 116].

In this work we attempt to avoid the subject of the detailed reaction kinetics, by focusing on the transport mechanisms rather than the reaction. Initially, we assume that, for one reason or another, the rate constant for the reaction is so large that the water-ion current is transport limited rather than reaction limited. Put in another way, we assume local equilibrium of the water ions everywhere in the system as done in Refs. [140, 5]. This simple view of the reaction process allow us to derive an accurate analytical model for the

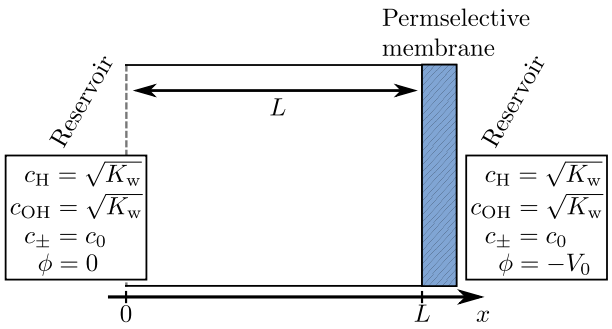

Figure 6.1: Sketch of the simple model system used in the problem. Two reservoirs with identical salt concentrations c_0 and neutral pH are connected by a compartment of length L and a cation-selective membrane.

transport in the system.

Going beyond the assumption of transport-limitation, we investigate the behavior of the system with finite values of the reaction constant. Surprisingly, we find that the analytical model derived in the transport-limited case still captures some essential features of the problem. To test these universal features of the analytical model, we compare the experimental results of Ref. [90] with the predictions of our model.

This chapter includes material from our paper Ref. [83], which can be found in Appendix E. In addition, the chapter contains some unpublished work about water splitting at finite reaction rates.

6.1 Model

As in Chapter 4 we consider one-dimensional transport of a monovalent and binary symmetric electrolyte. However, due to the need for well defined boundary conditions on the water ions, we can not use the GCP framework from Section 2.7. Instead, we have to explicitly include a permselective membrane in the modeling domain, which is therefore composed of two reservoirs connected by a compartment and a permselective membrane, see Fig. 6.1. The permselective membrane is modeled as outlined in Section 2.6.1, using the parameter values $\tilde{\rho}_m = 1000$, $\epsilon_P = 0.4$ [28], $\tau = (2-\epsilon_P)^2/\epsilon_P$ [72], and $\epsilon_m = 33\epsilon_0$. Since $\tilde{\rho}_m \gg 1$, the exact values taken by these parameters is unimportant.

6.2 Governing equations

As in Chapter 4 the cation and anion currents are given as

$$2\tilde{J}_+ = -\partial_{\tilde{x}}\tilde{c}_+ - \tilde{c}_+\partial_{\tilde{x}}\tilde{\phi}, \tag{6.1a}$$

$$2\frac{D_+}{D_-}\tilde{J}_- = -\partial_{\tilde{x}}\tilde{c}_- + \tilde{c}_-\partial_{\tilde{x}}\tilde{\phi}. \tag{6.1b}$$

The concentration of hydronium and hydroxide ions are normalized by the reservoir salt concentration c_0,

$$c_{\mathrm{H}} = c_0 \tilde{c}_{\mathrm{H}}, \qquad c_{\mathrm{OH}} = c_0 \tilde{c}_{\mathrm{OH}}, \tag{6.2}$$

and the current densities are normalized by $2D_{\mathrm{OH}}c_0/L$. The normalized current densities of hydronium $\tilde{c}_{\mathrm{H}}$ and hydroxide c_{OH} can then be written

$$2\tilde{J}_{\mathrm{H}} = -\delta_H \partial_{\tilde{x}} \tilde{c}_{\mathrm{H}} - \delta_H \tilde{c}_{\mathrm{H}} \partial_{\tilde{x}} \tilde{\phi}, \tag{6.3a}$$

$$2\tilde{J}_{\mathrm{OH}} = -\partial_{\tilde{x}} \tilde{c}_{\mathrm{OH}} + \tilde{c}_{\mathrm{OH}} \partial_{\tilde{x}} \tilde{\phi}, \tag{6.3b}$$

where we have introduced the diffusivity ratio $\delta_H = D_{\mathrm{H}}/D_{\mathrm{OH}} = 1.75$. In steady-state the conservation equations for the water ions read

$$0 = -\partial_{\tilde{x}} \tilde{J}_{\mathrm{H}} + \tilde{R}, \tag{6.4}$$

$$0 = -\partial_{\tilde{x}} \tilde{J}_{\mathrm{OH}} + \tilde{R}, \tag{6.5}$$

where the reaction term $\tilde{R}$ derives from the autoprotolytic reaction of water. The reaction rates are identical in both conservation equations, since the reaction

$$\mathrm{H_3O^+ + OH^- \rightleftharpoons 2\,H_2O}, \tag{6.6}$$

produces or consumes one unit of each species. Introducing the water-ion current $\tilde{J}_{\mathrm{w}} = \tilde{J}_{\mathrm{H}} - \tilde{J}_{\mathrm{OH}}$ we obtain a single transport equation for the water ions,

$$\partial_{\tilde{x}} \tilde{J}_{\mathrm{w}} = 0. \tag{6.7}$$

When the reaction Eq. (6.6) is in equilibrium, the concentrations of hydronium and hydroxide are simply related via the equilibrium constant $K_{\mathrm{w}} = c_{\mathrm{H}} c_{\mathrm{OH}}$. Deviations from equilibrium leads to a reaction rate given as [89]

$$\tilde{R} = \tilde{k}_{\mathrm{w}} \left[1 - \frac{\tilde{c}_{\mathrm{H}} \tilde{c}_{\mathrm{OH}}}{n^2} \right]. \tag{6.8}$$

Here, we introduced the parameter $n = \sqrt{K_{\mathrm{w}}}/c_0$ and the nondimensional reaction constant $\tilde{k}_{\mathrm{w}}$, which is related to the dimensional reaction constant k_{w} as

$$\tilde{k}_{\mathrm{w}} = \frac{L^2}{2D_{\mathrm{H}}c_0} k_{\mathrm{w}}. \tag{6.9}$$

In bulk the reaction constant k_{w} has the approximate value $k_{\mathrm{w}} \approx 1$ mM/s [89]. It has however been reported that the value of the reaction constant can increase several orders of magnitude in a thin reaction layer next to the membrane [108, 109, 110, 50]. Initially, we shall assume that for whatever reason, the reaction rate is so large that the autoprotolytic

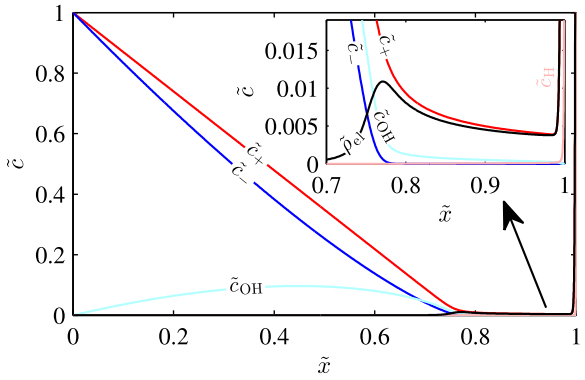

Figure 6.2: Numerically calculated concentration distributions for $\tilde{J}_+ = 1.5$, $\bar{\lambda}_{\mathrm{D}} = 0.001$, and $n = 0.0002$, assuming local equilibrium of the water dissociation reaction. The inset shows the behavior in the ESC.

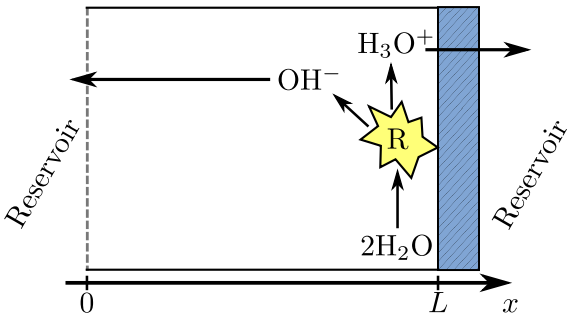

Figure 6.3: Sketch of the water-splitting reaction in the system. In a region to the left of the membrane water splits into hydronium and hydroxide. The hydroxide generated near the membrane is swept left by the electric field and the hydronium is swept right.

reaction (6.6) can be considered to be in equilibrium at all times. The concentrations of $\tilde{c}_{\mathrm{H}}$ and $\tilde{c}_{\mathrm{OH}}$ are then related as

$$\tilde{c}_{\mathrm{H}}\tilde{c}_{\mathrm{OH}} = n^2. \tag{6.10}$$

More elaborate time-dependent simulations have recently shown that this is a relevant limit, at least for some systems [4]. The Poisson equation takes the form

$$2\bar{\lambda}_{\mathrm{D}}^2\partial_{\tilde{x}}^2\tilde{\phi} = -\tilde{\rho}_{\mathrm{el}} = -\tilde{c}_+ + \tilde{c}_- - \tilde{c}_{\mathrm{H}} + \tilde{c}_{\mathrm{OH}}, \tag{6.11}$$

with appropriate modifications inside the membrane. Both reservoirs are taken to have the same salt concentration,

$$\tilde{c}_\pm(0) = \tilde{c}_\pm(2) = 1, \tag{6.12}$$

and they are assumed to be in equilibrium, so that

$$\tilde{c}_{\mathrm{H}}(0) = \tilde{c}_{\mathrm{H}}(2) = \tilde{c}_{\mathrm{OH}}(0) = \tilde{c}_{\mathrm{OH}}(2) = n. \tag{6.13}$$

6.3 Analysis

As a starting point for the analysis, we show numerically obtained concentration distributions in Fig. 6.2. The results are obtained for $\tilde{J}_+ = 1.5$, $\bar{\lambda}_{\mathrm{D}} = 0.001$, and $n = 0.0002$, assuming local equilibrium of the water dissociation reaction. The charge density in the system is seen to resemble the one in Chapter 4, with both a visible ESC and an EDL. The behavior of the concentration fields outside the ESC is, however, markedly changed due to the presence of a rather large concentration of hydroxide in this region. This large hydroxide concentration is tied to a significant current of hydroxide ions in the compartment.

Thus, even though the permselective membrane blocks the passage of hydroxide ions, it is possible to sustain a hydroxide current in the system. The reason for this, is that the autoprotolytic reaction at the membrane interfaces allow the hydroxide ions to run in the system without actually passing the permselective membrane. A sketch of this is shown in Fig. 6.3.

Obviously, the present system has many similarities with the system studied in Chapter 4. We will therefore try a similar solution approach, in which we only consider the LEN region and the ESC region. A major difficulty in dealing with the water splitting problem comes from the nonlinear coupling Eq. (6.8) or Eq. (6.10) between $\tilde{c}_{\mathrm{H}}$ and $\tilde{c}_{\mathrm{OH}}$. However, because we are disregarding the EDL we can get around this nonlinearity by introducing the effective water-ion concentration $\tilde{c}_{\mathrm{w}}$,

$$\tilde{c}_{\mathrm{w}} = \delta_H \tilde{c}_{\mathrm{H}} + \tilde{c}_{\mathrm{OH}}, \tag{6.14a}$$

$$2\tilde{J}_{\mathrm{w}} = \partial_{\tilde{x}}\tilde{c}_{\mathrm{w}} - \tilde{c}_{\mathrm{w}}\partial_{\tilde{x}}\tilde{\phi} - 2\delta_H\partial_{\tilde{x}}\tilde{c}_{\mathrm{H}} \approx \partial_{\tilde{x}}\tilde{c}_{\mathrm{w}} - \tilde{c}_{\mathrm{w}}\partial_{\tilde{x}}\tilde{\phi}. \tag{6.14b}$$

Here, we can discard the $2\delta_H\partial_{\tilde{x}}\tilde{c}_{\mathrm{H}}$ term because the hydroxide concentration is very much larger than the hydronium concentration in the entire LEN region, and in the ESC region, where this may not be the case, diffusion plays a negligible role compared to electromigration. Since the membrane is impenetrable to anions $\tilde{J}_- = 0$, and we find

$$2\tilde{J}_{\mathrm{w}} = 2\tilde{J}_{\mathrm{w}} - 2\frac{D_+}{D_-}\tilde{J}_- = \partial_{\tilde{x}}(\tilde{c}_{\mathrm{w}} + \tilde{c}_-) - (\tilde{c}_{\mathrm{w}} + \tilde{c}_-)\partial_{\tilde{x}}\tilde{\phi} \tag{6.15}$$

$$= \partial_{\tilde{x}}\left[c_+ + 2\bar{\lambda}_{\mathrm{D}}^2\partial_{\tilde{x}}^2\tilde{\phi} + (1+\delta_H)\tilde{c}_{\mathrm{H}}\right] - \left[c_+ + 2\bar{\lambda}_{\mathrm{D}}^2\partial_{\tilde{x}}^2\tilde{\phi} + (1+\delta_H)\tilde{c}_{\mathrm{H}}\right]\partial_{\tilde{x}}\tilde{\phi} \tag{6.16}$$

$$\approx \partial_{\tilde{x}}\tilde{c}_+ - \tilde{c}_+\partial_{\tilde{x}}\tilde{\phi} + 2\bar{\lambda}_{\mathrm{D}}^2\partial_{\tilde{x}}^3\tilde{\phi} - 2\bar{\lambda}_{\mathrm{D}}^2\partial_{\tilde{x}}^2\tilde{\phi}\partial_{\tilde{x}}\tilde{\phi}, \tag{6.17}$$

where we used Eq. (6.11) and approximated $(1+\delta_H)\tilde{c}_{\mathrm{H}} \approx 0$. This might introduce an error as $c_{\mathrm{w}} \gg c_{\mathrm{H}}$ does not necessarily hold in the ESC. The majority of the charge density in the ESC does however derive from the salt ions, so reasonable results can still be obtained with this approximation. In analogy with Eq. (4.5) we construct the two linear combinations $\tilde{J}_+ - \tilde{J}_{\mathrm{w}}$ and $\tilde{J}_+ + \tilde{J}_{\mathrm{w}}$,

$$\tilde{J}_+ - \tilde{J}_{\mathrm{w}} = -\partial_{\tilde{x}}\tilde{c}_+ - \bar{\lambda}_{\mathrm{D}}^2\partial_{\tilde{x}}^3\tilde{\phi} + \bar{\lambda}_{\mathrm{D}}^2\partial_{\tilde{x}}^2\tilde{\phi}\partial_{\tilde{x}}\tilde{\phi}, \tag{6.18a}$$

$$\tilde{J}_+ + \tilde{J}_{\mathrm{w}} = \bar{\lambda}_{\mathrm{D}}^2\partial_{\tilde{x}}^3\tilde{\phi} - \bar{\lambda}_{\mathrm{D}}^2\partial_{\tilde{x}}^2\tilde{\phi}\partial_{\tilde{x}}\tilde{\phi} - \tilde{c}_+\partial_{\tilde{x}}\tilde{\phi}. \tag{6.18b}$$

Using the same arguments which lead to Eq. (4.9), we then arrive at the following equation governing the electric field

$$1 + \frac{\bar{\lambda}_{\mathrm{D}}^2(\partial_{\tilde{x}}\tilde{\phi})^3}{2(\tilde{J}_+ + \tilde{J}_{\mathrm{w}})} = \left[\frac{\tilde{J}_+ - \tilde{J}_{\mathrm{w}}}{\tilde{J}_+ + \tilde{J}_{\mathrm{w}}}\tilde{x} - \frac{1}{\tilde{J}_+ + \tilde{J}_{\mathrm{w}}}\right]\partial_{\tilde{x}}\tilde{\phi}. \tag{6.19}$$

Rescaling the variables in this equation we find

$$1 + \hat{x}\hat{E} = \hat{E}^3, \tag{6.20}$$

where the only difference to the treatment in Chapter 4 is that the definitions of $\hat{x}$ and B are slightly altered,

$$\hat{E} = -B\partial_{\tilde{x}}\tilde{\phi}, \quad \text{with} \quad B = \left[\frac{\bar{\lambda}_{\mathrm{D}}^2}{2(\tilde{J}_+ + \tilde{J}_{\mathrm{w}})}\right]^{1/3}, \tag{6.21}$$

and

$$\hat{x} = \frac{1}{B}\left[\frac{\tilde{x}}{j} - \frac{1}{\tilde{J}_+ + \tilde{J}_{\mathrm{w}}}\right], \quad \text{with} \quad j = \frac{\tilde{J}_+ + \tilde{J}_{\mathrm{w}}}{\tilde{J}_+ - \tilde{J}_{\mathrm{w}}}. \tag{6.22}$$

The water-ion current $\tilde{J}_{\mathrm{w}}$ changes the expressions for the potential and concentration distributions slightly,

$$\tilde{\phi} \approx -\frac{2}{3}j\hat{E}^3 - j\ln\big(-\hat{E}\hat{x}_0\big), \tag{6.23a}$$

$$\tilde{\rho}_{\mathrm{el}} = \frac{2\bar{\lambda}_{\mathrm{D}}^2}{jB^2}\hat{\rho}_{\mathrm{el}} = \left[32\bar{\lambda}_{\mathrm{D}}^2\frac{\big(\tilde{J}_+ - \tilde{J}_{\mathrm{w}}\big)^3}{\tilde{J}_+ + \tilde{J}_{\mathrm{w}}}\right]^{1/3}\hat{\rho}_{\mathrm{el}}, \tag{6.23b}$$

$$\tilde{c}_+ = \frac{\bar{\lambda}_{\mathrm{D}}^2}{jB^2}\frac{2(1+j)\hat{E}^3 + j}{4\hat{E}^3 + 2}\frac{1}{\hat{E}}, \tag{6.23c}$$

$$\tilde{c}_- = \mathrm{e}^{\tilde{\phi}}. \tag{6.23d}$$

The effective water-ion concentration $\tilde{c}_{\mathrm{w}}$ can be found from the Poisson equation. To make the calculations internally consistent, we again use $(1+\delta_H)\tilde{c}_{\mathrm{H}} \approx 0$, and find

$$\tilde{c}_{\mathrm{w}} = \tilde{c}_+ - \tilde{c}_- - \tilde{\rho}_{\mathrm{el}} = \frac{\bar{\lambda}_{\mathrm{D}}^2}{jB^2}\frac{2(j-1)\hat{E}^3 + j}{4\hat{E}^3 + 2}\frac{1}{\hat{E}} - \mathrm{e}^{\tilde{\phi}}. \tag{6.24}$$

Finally, the electrochemical potential in the system is found from Eqs. (6.23a) and (6.23c),

$$\tilde{\mu}_+ = \ln(\tilde{c}_+) + \tilde{\phi} = -\frac{2}{3}j\hat{E}^3 - \ln\left[\frac{jB^2}{\bar{\lambda}_{\mathrm{D}}^2}\frac{4\hat{E}^3 + 2}{2(1+j)\hat{E}^3 + j}\hat{E}\big(-\hat{E}\hat{x}_0\big)^j\right]. \tag{6.25}$$

Given values of the salt current $\tilde{J}_+$ and the water-ion current $\tilde{J}_{\mathrm{w}}$, the above analysis yields analytical expressions for all the relevant fields in both the LEN region and the ESC region.

6.4 The water-ion current

The preceding analysis is independent of the chosen reaction model, and only assumes that hydroxide is the dominant water ion in the compartment. To find a relation between $\tilde{J}_{\mathrm{w}}$ and $\tilde{J}_+$ it is however necessary to introduce a reaction expression into the model. Below, we consider two specific models of the water-splitting reaction. We find that, regardless of the specific reaction expression, the transport model derived above imposes some restrictions on the relation between $\tilde{J}_{\mathrm{w}}$ and $\tilde{J}_+$.

6.4.1 Transport-limited water splitting

Initially, we shall assume that the system is transport limited so that the water-ion concentrations are related via Eq. (6.10). Even with this constraint, it is not apparent how $\tilde{J}_{\mathrm{w}}$ and $\tilde{J}_{+}$ are related to each other. In the numerical simulations, the magnitude of the water-ion current is determined self-consistently by requiring continuity of the fields across the permselective membrane. But, since the analytical model does not apply inside the EDL's, this method of constraining $\tilde{J}_{\mathrm{w}}$ can not be employed here.

As a starting point, we note that there is only significant water-splitting in the overlimiting regime, so we can restrict our attention to that regime. Inside the ESC, diffusion is small compared to electromigration, meaning that the water-ion current Eq. (6.14b) takes the form

$$2\tilde{J}_{\mathrm{w}} \approx -\tilde{c}_{\mathrm{w}}\partial_{\tilde{x}}\tilde{\phi}. \tag{6.26}$$

There is a positive charge density in the ESC, so the electric field increases for increasing $\tilde{x}$. Because $\tilde{J}_{\mathrm{w}}$ is constant, this in turn means that $\tilde{c}_{\mathrm{w}}$ must decrease for increasing $\tilde{x}$. However, because of the relation Eq. (6.10), $\tilde{c}_{\mathrm{w}}$ has a minimum value,

$$\min(\tilde{c}_{\mathrm{w}}) = 2\sqrt{\delta_H}n, \tag{6.27}$$

so at $\tilde{x} = 1$ we must always have $\tilde{J}_{\mathrm{w}} \geq -\sqrt{\delta_H}n\partial_{\tilde{x}}\tilde{\phi}$. Since there is no reason for $\tilde{J}_{\mathrm{w}}$ to take on values larger than what is required, we use the lower bound on this inequality as the constraint on $\tilde{J}_{\mathrm{w}}$. That is, we determine the water-ion current from

$$\partial_{\tilde{x}}\tilde{\phi}|_{\tilde{x}=1} = -\frac{\tilde{J}_{\mathrm{w}}}{\sqrt{\delta_H}n}. \tag{6.28}$$

Inserting this condition in Eq. (6.20) and solving for $\tilde{J}_{+}$ we find

$$\tilde{J}_{+} = \tilde{J}_{\mathrm{w}}\frac{1 + \tilde{J}_{\mathrm{w}} + \frac{\bar{\lambda}_{\mathrm{D}}^2}{2\delta_H n^2}\tilde{J}_{\mathrm{w}}^2}{\sqrt{\delta_H}n + \tilde{J}_{\mathrm{w}}}. \tag{6.29}$$

Together with Eq. (6.20) this relation completely specifies the problem and allow for the computation of I-V curves as well as field distributions.

In Fig. 6.4 we plot numerical and analytical concentration distributions for a transport-limited system with $\tilde{J}_{+} = 1.5$, $\bar{\lambda}_{\mathrm{D}} = 0.001$, and $n = 0.0002$. The analytical water-ion current $\tilde{J}_{\mathrm{w}}$ is determined from Eq. (6.29). Outside the EDL there is seen to be very good agreement between the analytical and numerical concentration distributions. In Fig. 6.5 and Fig. 6.6 the analytical and numerical salt currents $\tilde{J}_{+}$ and water-ion currents $\tilde{J}_{\mathrm{w}}$ are plotted versus bias voltage $\tilde{V}_0$ for $\bar{\lambda}_{\mathrm{D}} = \{10^{-4}, 10^{-5}\}$ and $n = \{10^{-5}, 10^{-4}, 3 \times 10^{-4}\}$. Also here, the agreement between analytical and numerical results is quite good. Like in Chapter 4 part of the discrepancy between the results is due to the finite width of the EDL adjoining the membrane.

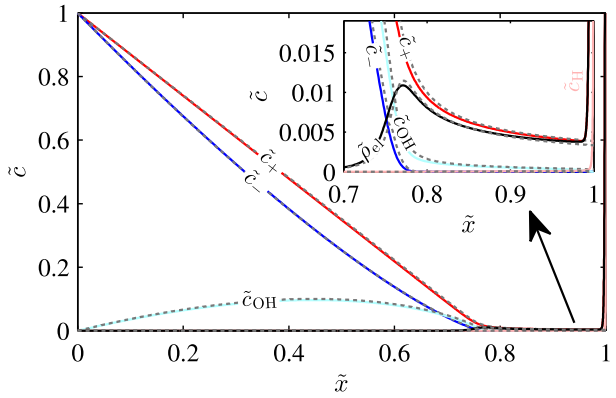

Figure 6.4: Numerical (full colored lines) and analytical (gray dashed) concentration distributions assuming transport-limited reactions. The parameter values are $\tilde{J}_+ = 1.5$, $\bar{\lambda}_{\rm D} = 0.001$, $n = 0.0002$, and the analytical water-ion current $\tilde{J}_{\rm w}$ is determined from Eq. (6.29).

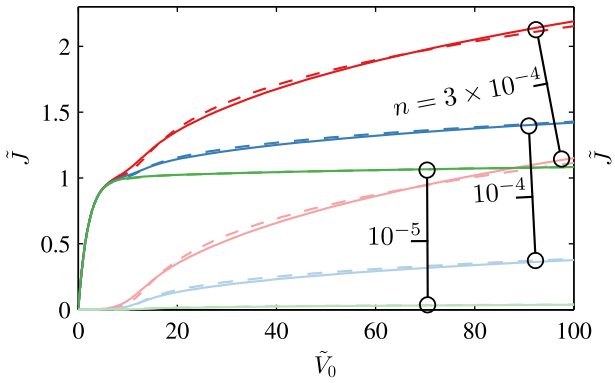

Figure 6.5: Numerical (full) and analytical (dashed) salt and water-ion currents plotted versus bias voltage $\tilde{V}_0$ for $\bar{\lambda}_{\rm D} = 10^{-4}$. The dark lines denote the salt current $\tilde{J}_+$ and the bright lines denote the corresponding water-ion current $\tilde{J}_{\rm w}$. The results assume transport-limited reactions.

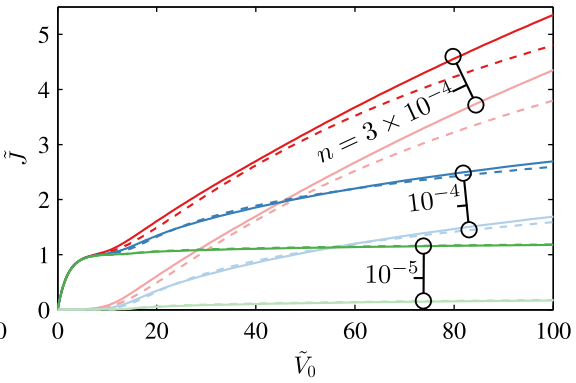

Figure 6.6: Numerical (full) and analytical (dashed) salt and water-ion currents plotted versus bias voltage $\tilde{V}_0$ for $\bar{\lambda}_{\rm D} = 10^{-5}$. The dark lines denote the salt current $\tilde{J}_+$ and the bright lines denote the corresponding water-ion current $\tilde{J}_{\rm w}$. The results assume transport-limited reactions.

6.4.2 Water splitting at finite reaction rate

At finite reaction rates the reasonably simple picture from above breaks down. Rather than being related via Eq. (6.6), $\tilde{c}_{\rm H}$ and $\tilde{c}_{\rm OH}$ are now determined from the transport equations Eq. (6.3) with the reaction rate Eq. (6.8). In general, we have to solve the transport-reaction problem numerically, but in the case of slow reactions $\tilde{k}_{\rm w} \ll 1$ it is possible to derive some simple analytical results.

When the reaction rate is the limiting factor, the water-ion concentrations just to the left of the membrane are very much out of equilibrium, $\tilde{c}_{\rm H}\tilde{c}_{\rm OH} \ll 1$. Thus, in a significant part of the ESC the reaction rate is given as

$$\tilde{R} \approx \tilde{k}_{\rm w}. \tag{6.30}$$

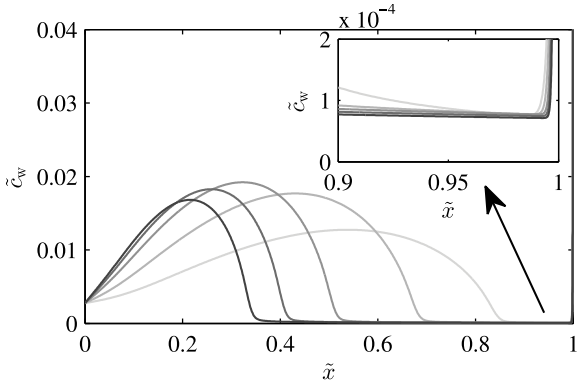

Figure 6.7: Numerically calculated water-ion concentration $\tilde{c}_w$ for $\tilde{k}_w = 0.1$, $\bar{\lambda}_D = 10^{-3}$, $n = 10^{-3}$, and $\tilde{J}_+ = \{1.2, 1.5, 2, 2.5, 3\}$. The shade of the lines indicate the magnitude of $\tilde{J}_+$, with $\tilde{J}_+ = 1.2$ having the lightest shade and $\tilde{J}_+ = 3$ the darkest.

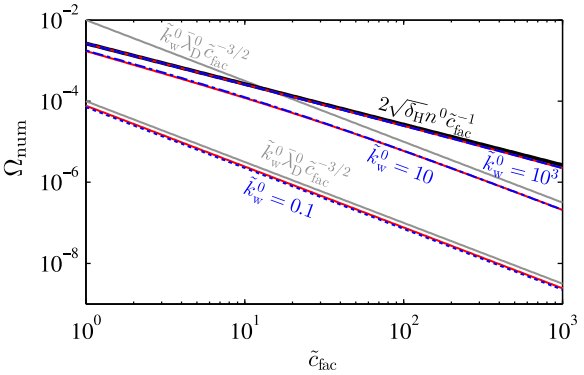

Figure 6.8: Numerically calculated values of Ω plotted versus $\tilde{c}_{fac}$ for $\bar{\lambda}_D^0 = 10^{-3}$ and $n^0 = 10^{-3}$. The reaction constant $\tilde{k}_w^0$ takes on the values 0.1 (short dashes), 10 (alternating short and long dashes), and 1000 (long dashes). For each value of $\tilde{k}_w^0$, Ω_{num} was calculated for both $\tilde{J}_+ = 1.5$ (red) and $\tilde{J}_+ = 3$ (blue). Also shown are the reaction limited scalings Eq. (6.34) (gray) and the transport-limited expression Eq. (6.27) (black).

At the left membrane interface the hydroxide is swept left by the electric field, but no new hydroxide is supplied from the membrane interior at the right. The hydronium is swept right by the electric field, and since there is a significant reaction in much of the ESC, some new hydronium is supplied from the left. It follows that $\tilde{c}_H \gg \tilde{c}_{OH}$ just to the left of the membrane.

Since diffusion is small in the ESC, we can write the divergence of $\tilde{J}_H$ as

$$R = \partial_{\tilde{x}} \tilde{J}_H \approx -\frac{\delta_H}{2} \partial_{\tilde{x}} \left\{ \tilde{c}_H \partial_{\tilde{x}} \tilde{\phi} \right\} \approx -\frac{\delta_H}{2} \tilde{c}_H \partial_{\tilde{x}}^2 \tilde{\phi} = \frac{\delta_H}{2} \tilde{c}_H \frac{\tilde{\rho}_{el}}{2\bar{\lambda}_D^2}, \tag{6.31}$$

which means that

$$\tilde{c}_w(1) \approx \delta_H \tilde{c}_H(1) \approx 4\tilde{k}_w \frac{\bar{\lambda}_D^2}{\tilde{\rho}_{el}(1)} \approx 4\tilde{k}_w \frac{B^2}{j} \sqrt{\hat{x}_1}. \tag{6.32}$$

In the overlimiting regime this expression varies quite slowly with the currents $\tilde{J}_+$ and $\tilde{J}_w$. It therefore provides an almost constant boundary condition for the water-ion transport, in much the same way as Eq. (6.27) did in the transport limited case. In Fig. 6.7 numerical results for $\tilde{c}_w$ are plotted for $\tilde{k}_w = 0.1$, $\bar{\lambda}_D = 10^{-3}$, $n = 10^{-3}$, and varying $\tilde{J}_+$. The water-ion concentration at the entrance to the EDL is seen to vary very little with $\tilde{J}_+$. Because the water-ion concentration at the entrance to the EDL is an important parameter, we introduce a separate symbol for this concentration,

$$\Omega = \tilde{c}_w, \quad \text{At the entrance to the EDL.} \tag{6.33}$$

In the numerical calculations Ω equals the minimum value of $\tilde{c}_w$ in the system, and in the analytical calculations it equals the water-ion concentration $\tilde{c}_w(1)$ evaluated at $\tilde{x} = 1$. We

introduce appropriate subscripts Ω_{num} and Ω_{anl} to distinguish between the numerical and analytical cases.

The water-ion concentration (6.32) scales with the system parameters as

$$\Omega_{\text{anl}} = \tilde{c}_{\text{w}}(1) \sim \tilde{k}_{\text{w}} B^{3/2} \sim \tilde{k}_{\text{w}} \bar{\lambda}_{\text{D}}. \tag{6.34}$$

Interestingly, the reaction-limited water-ion concentration (6.32) scales with system concentration as $\Omega_{\text{anl}} \sim c_0^{-3/2}$, whereas the transport-limited expression (6.27) scales as $\Omega_{\text{anl}} \sim c_0^{-1}$. To test these scalings we introduce a scale factor $\tilde{c}_{\text{fac}}$ for the reservoir concentration, so that

$$\bar{\lambda}_{\text{D}} = \frac{\bar{\lambda}_{\text{D}}^0}{\sqrt{\tilde{c}_{\text{fac}}}}, \tag{6.35a}$$

$$n = \frac{n^0}{\tilde{c}_{\text{fac}}}, \tag{6.35b}$$

$$\tilde{k}_{\text{w}} = \frac{\tilde{k}_{\text{w}}^0}{\tilde{c}_{\text{fac}}}. \tag{6.35c}$$

In Fig. 6.8, numerical results for Ω are plotted versus $\tilde{c}_{\text{fac}}$, for a reaction constant of $\tilde{k}_{\text{w}}^0 = \{0.1, 10, 10^3\}$ and a cation current of $\tilde{J}_+ = \{1.5, 3\}$. For large $\tilde{k}_{\text{w}}^0$, Ω_{num} follows the analytical expression (6.27), and at low $\tilde{k}_{\text{w}}^0$ it follows the scaling from Eq. (6.34). At the intermediate value $\tilde{k}_{\text{w}}^0 = 10$, there is a transition between the high and low $\tilde{k}_{\text{w}}^0$ behavior. It is also seen that in all three reaction regimes Ω_{num} varies very little between $\tilde{J}_+ = 1.5$ and $\tilde{J}_+ = 3$.

One of the main points we want to stress, is that at overlimiting current the water-ion concentration just outside the EDL varies slowly with $\tilde{J}_+$. This seems to be true regardless of how fast the reactions are, and is found even in simulations with a spatially varying reaction constant. The implication of this is that an expression similar to Eq. (6.29) may apply even for systems that are not transport limited. At overlimiting current this generalized form of Eq. (6.29) is

$$\tilde{J}_+ = 1 + \tilde{J}_{\text{w}} + \frac{2\bar{\lambda}_{\text{D}}^2}{\Omega^2} \tilde{J}_{\text{w}}^2, \tag{6.36}$$

or equivalently,

$$\log 10\big[\tilde{J}_+ - \tilde{J}_{\text{w}} - 1\big] = \log 10 \left(\frac{2\bar{\lambda}_{\text{D}}^2}{\Omega^2} \right) + 2 \log 10\big(\tilde{J}_{\text{w}}\big). \tag{6.37}$$

Thus, we expect that a double logarithmic plot of $\tilde{J}_+ - \tilde{J}_{\text{w}} - 1$ versus $\tilde{J}_{\text{w}}$ will yield a straight line with slope 2. Also, we expect that the extension of the line crosses the vertical axis at $\log 10 \left(\frac{2\bar{\lambda}_{\text{D}}^2}{\Omega} \right)$.

In Fig. 6.9 we show double logarithmic plots of $\tilde{J}_+ - \tilde{J}_{\text{w}} - 1$ versus $\tilde{J}_{\text{w}}$ for $n = 10^{-3}$, $\bar{\lambda}_{\text{D}} = 10^{-3}$, and $\tilde{k}_{\text{w}} = \{0.1, 1, 100\}$. It is seen, that the lines do deviate somewhat from the straight lines we were expecting. The reason for this is that Ω does in fact have a slight

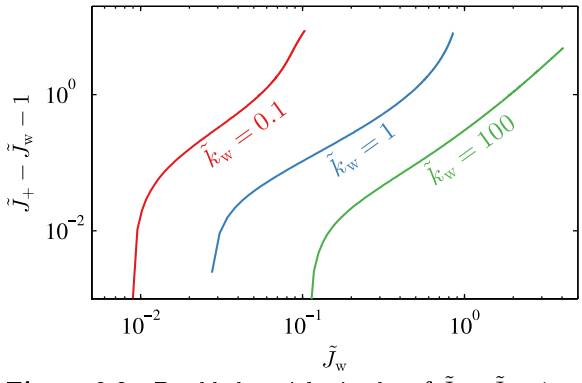

Figure 6.9: Double logarithmic plot of $\tilde{J}_+ - \tilde{J}_w - 1$ versus $\tilde{J}_w$ obtained from numerical simulations with $\bar{\lambda}_D = 10^{-3}$ and $n = 10^{-3}$ at finite reaction rate. Due to slow variations in Ω the lines deviate slightly from the expected straight lines.

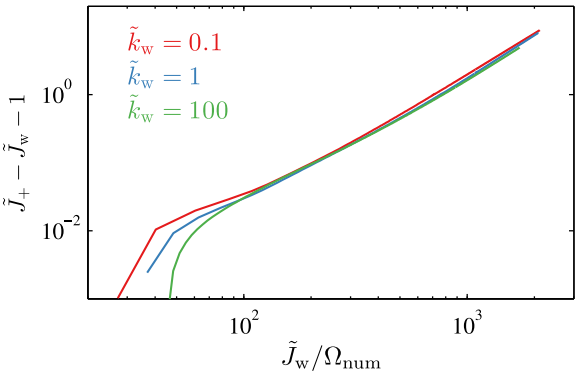

Figure 6.10: Same as Fig. 6.9, but now plotted versus $\tilde{J}_w/\Omega_{num}$ instead of versus $\tilde{J}_w$. In this plot, where the variations in Ω are factored out, the curves nearly collapse on the same straight line.

$\tilde{J}_+$ dependence. In Fig. 6.10 the same lines are plotted, but with the x-axis scaled with Ω_{num}. Now the three lines collapse on one approximately straight line. This confirms that Eq. (6.36) does apply to the numerical results.

Because we know that the currents behave as Eq. (6.36), we can estimate the average value of the prefactor $2\bar{\lambda}_D^2/\Omega^2$ from the values of $\tilde{J}_+$ and $\tilde{J}_w$,

$$\left\langle 2\bar{\lambda}_D^2/\Omega^2 \right\rangle = \left\langle \frac{\tilde{J}_+ - \tilde{J}_w - 1}{\tilde{J}_w^2} \right\rangle, \tag{6.38}$$

where we only average over values with $\tilde{J}_+ - \tilde{J}_w - 1 > 0.05$. In Fig. 6.11 we show plots of $\tilde{J}_+ - \tilde{J}_w - 1$ (full lines) and $\left\langle (\tilde{J}_+ - \tilde{J}_w - 1)/\tilde{J}_w^2 \right\rangle \tilde{J}_w^2$ (dashed lines) versus $\tilde{J}_w$. The expression $\left\langle (\tilde{J}_+ - \tilde{J}_w - 1)/\tilde{J}_w^2 \right\rangle \tilde{J}_w^2$ is seen to capture the average behavior of $\tilde{J}_+ - \tilde{J}_w - 1$ to a reasonable degree.

Since the currents in Fig. 6.9, Fig. 6.10, and Fig. 6.11 come from a numerical simulation, we have access to the true value of the prefactor $2\bar{\lambda}_D^2/\Omega^2$. In Fig. 6.12 the prefactor $2\bar{\lambda}_D^2/\Omega_{num}^2$ normalized by its approximate value Eq. (6.38) is plotted versus $\tilde{J}_w$ in the region where $\tilde{J}_+ - \tilde{J}_w - 1 > 0.05$. It is seen that Eq. (6.38) gives a decent estimate of the average value of the prefactor. Also, we see that the prefactor varies at most by a factor of three over a decade. In comparison $\tilde{J}_w$ varies by a factor of 100 over a decade.

To summarize, we have found that the currents in the system approximately follow Eq. (6.36), and given a dataset of $\tilde{J}_+$ and $\tilde{J}_w$ we can approximate the mean value of the prefactor $2\bar{\lambda}_D^2/\Omega^2$. In the following section we apply these results to a set of experimental data.

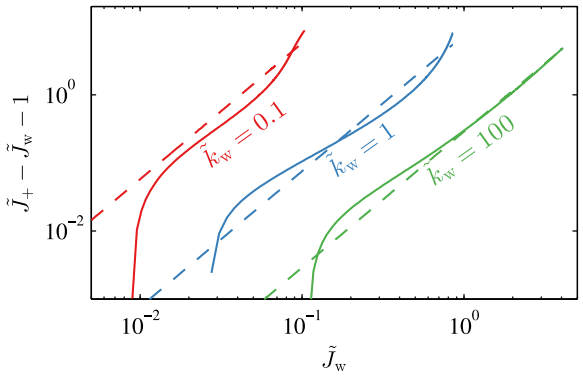

Figure 6.11: Same as Fig. 6.9, but now with the addition of dashed lines with the expression $\langle(\tilde{J}_+ - \tilde{J}_w - 1)/\tilde{J}_w^2\rangle\tilde{J}_w^2$.

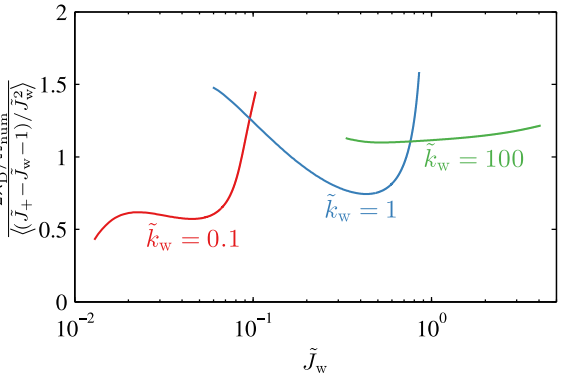

Figure 6.12: Plot of the prefactor $2\bar{\lambda}_D^2/\Omega_{num}^2$ normalized by $\langle(\tilde{J}_+ - \tilde{J}_w - 1)/\tilde{J}_w^2\rangle$. The parameter values are still $\bar{\lambda}_D = 10^{-3}$ and $n = 10^{-3}$.

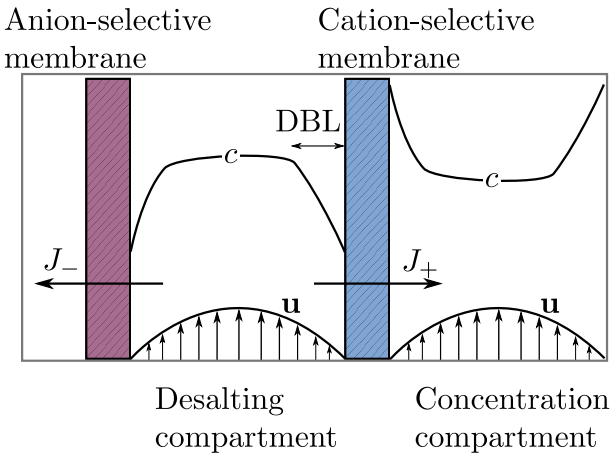

Figure 6.13: Sketch of a desalting compartment and a concentration compartment. The compartments are divided by cation and anion-selective membranes. The concentration distribution in the desalting compartment forms a diffusion boundary layer (DBL) near the cation-selective membrane.

6.5 Relation to experiments

The simple reservoir-compartment-membrane system used in the analysis is convenient for theoretical work, but the somewhat idealized nature of the system makes it unsuitable for experiments. A typical experimental setup consists of a periodic structure of desalting and concentration compartments, separated by anion and cation-selective membranes [87, 89]. To flush out the desalinated or concentrated liquid a velocity field is applied in the compartments parallel to the membrane interfaces. A sketch of a part of such a setup is seen in Fig. 6.13, where a typical concentration profile is also shown. It is seen that even though there is no reservoir in the desalting compartment, a diffusion boundary layer (DBL) has formed, in which the transport approximates the transport in the simple reservoir-compartment-membrane system. With appropriate definitions of equivalent

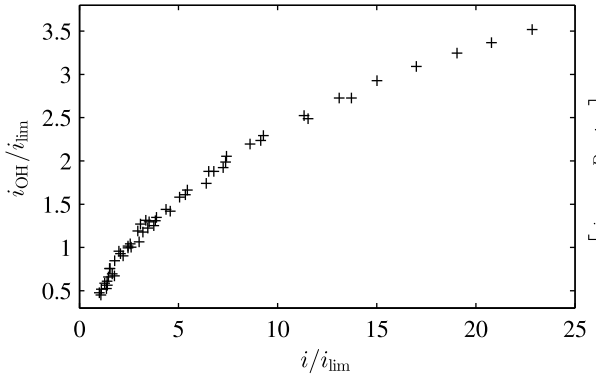

Figure 6.14: Experimental hydroxide current i_{OH} plotted versus the salt current i. The data points are extracted from Fig. 5 in Ref. [90].

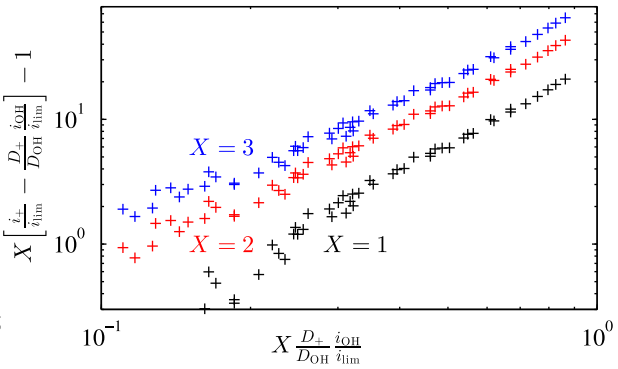

Figure 6.15: Plot of $\left[\frac{i}{i_{\mathrm{lim}}}-\frac{D_+}{D_{\mathrm{OH}}}\frac{i_{\mathrm{OH}}}{i_{\mathrm{lim}}}\right]X-1$ versus $\frac{D_+}{D_{\mathrm{OH}}}\frac{i_{\mathrm{OH}}}{i_{\mathrm{lim}}}$ for $X=\{1,2,3\}$. The degree to which the experimental data points collapse on a straight line varies with X.

reservoir concentration c_0 and the equivalent compartment length L, the simple analysis given above therefore still gives a good description of the transport in the diffusion boundary layer. As an example of how to apply this, we consider the experimental data in Fig. 6.14. The data is extracted from Fig. 5 in Ref. [90]. The currents seen in Fig. 6.14 are the dimensional hydroxide current density i_{OH}, the dimensional cation current density i, and the limiting current i_{lim} obtained from a model of diffusion with a cross flow. As seen in the original figure in Ref. [90] the data points are from 10 different measurement series with different parameter values. Equating the dimensional current densities in our model with the experimental current densities we find

$$\tilde{J}_{\mathrm{w}}=\frac{J_{\mathrm{w}}}{\frac{2D_{\mathrm{OH}}c_0}{L}}=\frac{i_{\mathrm{lim}}}{\frac{2D_{\mathrm{OH}}c_0}{L}}\frac{i_{\mathrm{OH}}}{i_{\mathrm{lim}}}=\frac{i_{\mathrm{lim}}}{\frac{2D_+c_0}{L}}\frac{D_+}{D_{\mathrm{OH}}}\frac{i_{\mathrm{OH}}}{i_{\mathrm{lim}}}, \tag{6.39}$$

$$\tilde{J}_+=\frac{J_+}{\frac{2D_+c_0}{L}}=\frac{i_{\mathrm{lim}}}{\frac{2D_+c_0}{L}}\frac{i}{i_{\mathrm{lim}}}. \tag{6.40}$$

The term $\tilde{J}_+-\tilde{J}_{\mathrm{w}}-1$ occurring in Eq. (6.36) can therefore be written

$$\tilde{J}_+-\tilde{J}_{\mathrm{w}}-1=\left[\frac{i}{i_{\mathrm{lim}}}-\frac{D_+}{D_{\mathrm{OH}}}\frac{i_{\mathrm{OH}}}{i_{\mathrm{lim}}}\right]X-1, \tag{6.41}$$

with

$$X=\frac{i_{\mathrm{lim}}}{\frac{2D_+c_0}{L}}. \tag{6.42}$$

Since the equivalent reservoir concentration c_0 and compartment length L are not entirely well defined in the experimental system, it is in general difficult to calculate the value of X. However, for properly defined c_0 and L we expect that $i_{\mathrm{lim}}\propto c_0/L$, so the value of X will be largely independent of c_0 and L. We can therefore use X as a fitting parameter.

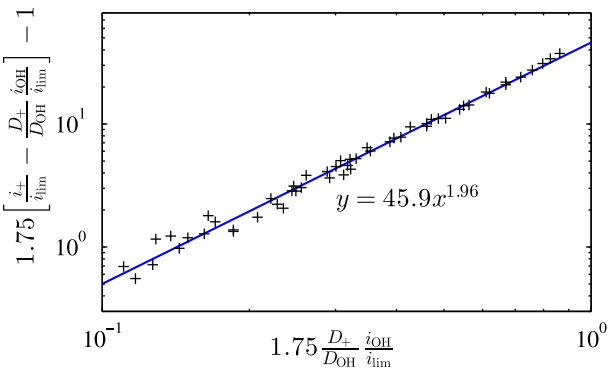

Figure 6.16: Plot of $\left[\frac{i}{i_{\rm lim}} - \frac{D_+}{D_{\rm OH}}\frac{i_{\rm OH}}{i_{\rm lim}}\right] X - 1$ versus $\frac{D_+}{D_{\rm OH}}\frac{i_{\rm OH}}{i_{\rm lim}}$ for the best value of $X = 1.75$. The slope of the fitted line 1.96 is quite close to the theoretical value of 2.

In Fig. 6.15 is shown a double logarithmic plot of $\left[\frac{i}{i_{\rm lim}} - \frac{D_+}{D_{\rm OH}}\frac{i_{\rm OH}}{i_{\rm lim}}\right] X - 1$ versus $\frac{D_+}{D_{\rm OH}}\frac{i_{\rm OH}}{i_{\rm lim}}$ for $X = \{1, 2, 3\}$. The degree to which the data points conform to a straight line is seen to vary with the value of X. To determine the optimal value of X we fit a straight line to the data points and quantify the goodness of fit by the R^2-value. R^2 has its maximum $R^2 = 0.988$ at $X = 1.75$. For $X = 1.75$ the slope of the straight line is 1.96, which is quite close to the slope of 2 predicted by the analytical model, see Fig. 6.16. It is important to note that in fitting the value of X we did not make any requirements on the slope of the fitted line. Thus, the slope of 1.96 truly is something that emerges from the analysis.

A result of the above analysis is the value of the prefactor,

$$\frac{2\bar{\lambda}_{\rm D}^2}{\Omega^2} \approx 45.9. \tag{6.43}$$

Oddly, all of the data points, some of them with salt concentrations differing from each other, seem to have roughly the same value of the prefactor. In contrast, the transport-limited prefactor scales with c_0 as c_0^1 and the reaction limited prefactor scales as c_0^2. We can therefore conclude that the reaction kinetics in the experiment differs from these two simple models. The true reaction model must give a prefactor which does not scale with the reservoir concentration c_0.

6.6 Addition of an acid or base

So far we have investigated systems where the ions derive from a dissolved salt. We will now proceed with a more general treatment, where we allow for some concentration of acid $\tilde{c}_{\rm a}$ or base $\tilde{c}_{\rm b}$ in the reservoirs in analogy with Ref. [55]. The acid or base is assumed to be strong so that it dissociates completely, and for simplicity we assume that the conjugate base to the acid is the same as the negative salt ion and that the conjugate acid to the base is the same as the positive salt ion. For instance the salt could be NaCl, the acid HCl and the base NaOH.

Firstly, we consider a system where some concentration $\tilde{c}_{\rm b}$ of base is added to the system. The ion concentrations are normalized with the total cation concentration at the

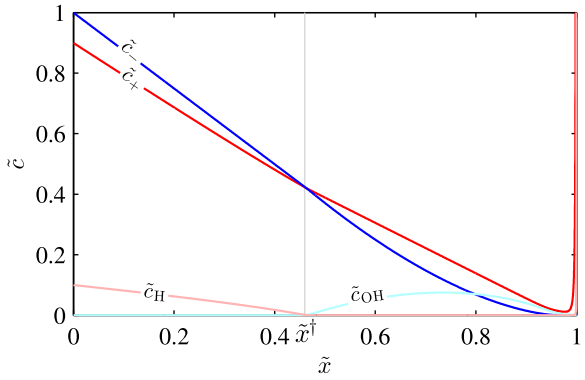

Figure 6.17: Numerical result for the concentration distribution in a transport-limited system with $\bar{\lambda}_{\mathrm{D}} = 0.001$, $n = 0.001$, $\tilde{c}_{\mathrm{a}} = 0.1$, and $\tilde{J}_+ = 1.1$. To the left of the transition point $\tilde{x}^\dagger$ hydronium is the dominant water ion, and to the right of $\tilde{x}^\dagger$ hydroxide is the dominant water ion.

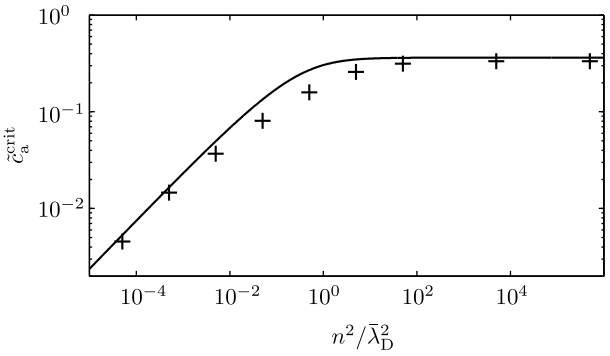

Figure 6.18: The critical acid concentration plotted versus $n^2/\bar{\lambda}_{\mathrm{D}}^2$ in a transport-limited system. At large $n^2/\bar{\lambda}_{\mathrm{D}}^2$ the critical acid concentration approaches its asymptotic value $1/(1+\delta_H)$.

inlet, i.e. the sum of the salt and the base concentrations. We thus have $\tilde{c}_+(0) = 1$, $\tilde{c}_-(0) = 1 - \tilde{c}_{\mathrm{b}}$ and $\tilde{c}_{\mathrm{OH}}(0) = \tilde{c}_{\mathrm{b}}$. Like in Section 6.3 hydroxide dominates over hydronium, so the relevant transport equation for the water ions is Eq. (6.14b),

$$2\tilde{J}_{\mathrm{w}} \approx \partial_{\tilde{x}}\tilde{c}_{\mathrm{w}} - \tilde{c}_{\mathrm{w}}\partial_{\tilde{x}}\tilde{\phi}, \tag{6.44}$$

but with the difference that $\tilde{c}_{\mathrm{w}}(0) = \tilde{c}_{\mathrm{b}}$ rather than $\tilde{c}_{\mathrm{w}}(0) = (1+\delta)n \approx 0$. We can rewrite the transport equation

$$\begin{aligned} 2\tilde{J}_{\mathrm{w}} &\approx \partial_{\tilde{x}}\tilde{c}_{\mathrm{w}} - \tilde{c}_{\mathrm{w}}\partial_{\tilde{x}}\tilde{\phi} \\ &= \partial_{\tilde{x}}(\tilde{c}_{\mathrm{w}} - \tilde{c}_{\mathrm{b}}e^{\tilde{\phi}}) - (\tilde{c}_{\mathrm{w}} - \tilde{c}_{\mathrm{b}}e^{\tilde{\phi}})\partial_{\tilde{x}}\tilde{\phi} \\ &= \partial_{\tilde{x}}\tilde{c}'_{\mathrm{w}} - \tilde{c}'_{\mathrm{w}}\partial_{\tilde{x}}\tilde{\phi}, \end{aligned} \tag{6.45}$$

where $\tilde{c}'_{\mathrm{w}} = \tilde{c}_{\mathrm{w}} - \tilde{c}_{\mathrm{b}}e^{\tilde{\phi}}$ and $\tilde{c}'_{\mathrm{w}}(0) = 0$. The $\tilde{c}_{\mathrm{b}}e^{\tilde{\phi}}$ term behaves exactly like the stationary salt anions, suggesting the introduction of $\tilde{c}'_- = \tilde{c}_- + \tilde{c}_{\mathrm{b}}e^{\tilde{\phi}}$ with $\tilde{c}'_-(0) = 1$. In conclusion the present problem can be mapped onto the problem in Section 6.3. Adding a base to a system is therefore equivalent to adding a salt of its conjugate acid.

The situation becomes more complex when an acid is added to the reservoir. In this case two quite different situations can result, depending on the amount of added acid. For high acid concentrations the amount of hydronium ions suppress water splitting at the membrane, and the hydronium ions essentially act as a conserved cation. For low acid concentrations hydroxide may begin to dominate the water ion transport at some point and water splitting can occur as in the treatment in Section 6.3. In Fig. 6.17 this situation is illustrated.

To quantify what is meant by 'high' and 'low' acid concentrations we analyze the system in more detail. From Fig. 6.17 it is seen that there are two distinct regions in the solution.

To the left hydronium dominates and there is local electroneutrality, while the right part of the channel is equivalent to the system analyzed in Section 6.3. In the left part of the channel the system is locally electroneutral, and it is easily found that the concentration fields are given as

$$\tilde{c}_- = e^{\tilde{\phi}} = 1 - (\tilde{J}_+ + \tilde{J}_\mathrm{w}/\delta_H)\tilde{x}, \tag{6.46a}$$

$$\tilde{c}_\mathrm{H} = \frac{\tilde{J}_\mathrm{w}/\delta_H}{\tilde{J}_+ + \tilde{J}_\mathrm{w}/\delta_H} e^{\tilde{\phi}} + \left[\tilde{c}_\mathrm{a} - \frac{\tilde{J}_\mathrm{w}/\delta_H}{\tilde{J}_+ + \tilde{J}_\mathrm{w}/\delta_H}\right] e^{-\tilde{\phi}}, \tag{6.46b}$$

$$\tilde{c}_+ = \frac{\tilde{J}_+}{\tilde{J}_+ + \tilde{J}_\mathrm{w}/\delta_H} e^{\tilde{\phi}} + \left[1 - \tilde{c}_\mathrm{a} - \frac{\tilde{J}_+}{\tilde{J}_+ + \tilde{J}_\mathrm{w}/\delta_H}\right] e^{-\tilde{\phi}}, \tag{6.46c}$$

where the concentration fields are normalized with the sum of the acid and salt concentrations at the inlet and $\tilde{c}_\mathrm{a}$ is the normalized acid concentration at the inlet.

In the limit where there is no water splitting at the membrane, the currents are just related via the reservoir concentrations of hydronium and salt cation,

$$\frac{\tilde{J}_\mathrm{w}/\delta_H}{\tilde{J}_+} = \frac{\tilde{c}_\mathrm{a}}{1 - \tilde{c}_\mathrm{a}} \quad , \quad \text{no water splitting.} \tag{6.47}$$

If there is water splitting there will be a transition point $\tilde{x}^\dagger$ where the hydronium concentration vanishes. Solving Eq. (6.46a) and Eq. (6.46b) for $\tilde{x}^\dagger$ we find

$$\tilde{x}^\dagger = \frac{1}{\tilde{J}_+ + \tilde{J}_\mathrm{w}/\delta_H}\left[1 - \sqrt{1 - \frac{\tilde{J}_+ + \tilde{J}_\mathrm{w}/\delta_H}{\tilde{J}_\mathrm{w}/\delta_H}\tilde{c}_\mathrm{a}}\right], \tag{6.48}$$

and at that point the salt concentration is

$$\tilde{c}^\dagger = \tilde{c}_+(\tilde{x}^\dagger) = \tilde{c}_-(\tilde{x}^\dagger) = \sqrt{1 - \frac{\tilde{J}_+ + \tilde{J}_\mathrm{w}/\delta_H}{\tilde{J}_\mathrm{w}/\delta_H}\tilde{c}_\mathrm{a}}. \tag{6.49}$$

At $\tilde{x} = 1$ the electric field is determined by Eq. (6.19) corrected with the new boundary conditions Eq. (6.48) and Eq. (6.49)

$$1 + \frac{\bar{\lambda}_\mathrm{D}^2(\partial_{\tilde{x}}\tilde{\phi})^3}{2(\tilde{J}_+ + \tilde{J}_\mathrm{w})} = \left[\frac{\tilde{J}_+ - \tilde{J}_\mathrm{w}}{\tilde{J}_+ + \tilde{J}_\mathrm{w}}(1 - \tilde{x}^\dagger) - \frac{\tilde{c}^\dagger}{\tilde{J}_+ + \tilde{J}_\mathrm{w}}\right]\partial_{\tilde{x}}\tilde{\phi}. \tag{6.50}$$

Just when water splitting is initiated $\tilde{J}_\mathrm{w}$ and $\tilde{J}_+$ are still related via Eq. (6.47), and we can approximate

$$\tilde{c}_+^\dagger \approx 0, \tag{6.51}$$

$$\tilde{x}^\dagger \approx \frac{1}{\tilde{J}_+ + \tilde{J}_\mathrm{w}/\delta_H}. \tag{6.52}$$

Furthermore, since water splitting is only significant in the overlimiting regime we can neglect the 1 term in Eq. (6.50) and obtain

$$\frac{\bar{\lambda}_{\mathrm{D}}^2(\partial_{\tilde{x}}\tilde{\phi})^2}{2} = \tilde{J}_+ - \tilde{J}_{\mathrm{w}} - \frac{\tilde{J}_+ - \tilde{J}_{\mathrm{w}}}{\tilde{J}_+ + \tilde{J}_{\mathrm{w}}/\delta_H}. \tag{6.53}$$

Inserting the boundary condition Eq. (6.26) with Eq. (6.33), and using $\frac{\tilde{J}_{\mathrm{w}}/\delta}{\tilde{J}_+} = \frac{\tilde{c}_{\mathrm{a}}}{1-\tilde{c}_{\mathrm{a}}}$ we find a quadratic equation for $\tilde{J}_{\mathrm{w}}$,

$$\frac{2\delta_H\bar{\lambda}_{\mathrm{D}}^2}{\Omega^2}\tilde{J}_{\mathrm{w}}^2 = \tilde{J}_{\mathrm{w}}\frac{1-(1+\delta_H)\tilde{c}_{\mathrm{a}}}{\tilde{c}_{\mathrm{a}}} - 1 + (1+\delta_H)\tilde{c}_{\mathrm{a}}. \tag{6.54}$$

This equation has a solution when the determinant is non-negative, i.e. when

$$\tilde{c}_{\mathrm{a}} \leq \tilde{c}_{\mathrm{a}}^{\mathrm{crit}} = \frac{-(1+\delta_H) + \sqrt{(1+\delta_H)^2 + 32\delta_H\frac{\bar{\lambda}_{\mathrm{D}}^2}{\Omega^2}}}{16\delta_H\frac{\bar{\lambda}_{\mathrm{D}}^2}{\Omega^2}} \tag{6.55}$$

For values of $\tilde{c}_{\mathrm{a}}$ higher than the critical value $\tilde{c}_{\mathrm{a}}^{\mathrm{crit}}$ there are no solutions which allow for water splitting. In Fig. 6.18 analytical and numerical results for the critical acid concentration $\tilde{c}_{\mathrm{a}}^{\mathrm{crit}}$ are plotted versus $\frac{\Omega^2}{4\delta_H\bar{\lambda}_{\mathrm{D}}^2} = \frac{n^2}{\bar{\lambda}_{\mathrm{D}}^2}$ in a transport-limited system. Numerically the critical concentration is determined as follows. When there is no water splitting the currents are related as in Eq. (6.47). The critical concentration is then defined to be the minimum value of $\tilde{c}_{\mathrm{a}}$ for which $\frac{\tilde{J}_{\mathrm{w}}/\delta_H}{\tilde{J}_+} \geq 1.01\frac{\tilde{c}_{\mathrm{a}}}{1-\tilde{c}_{\mathrm{a}}}$, within the voltage sweep interval $0 < \tilde{V}_0 < 100$.

While the specific results in Fig. 6.18 are only valid for a transport-limited system, the expression (6.55) does not rely on a particular reaction expression. We therefore expect the existence of a critical acid concentration to be a valid prediction regardless of the reaction mechanism. In fact, since Ω enters in the expression (6.55), measuring the critical acid concentration could be yet another way of probing the reaction kinetics of a system.

6.7 Conclusion

We have generalized the analytical model in Chapter 4 to account for the influence of water ions. Given values of the cation current $\tilde{J}_+$ and the water-ion current $\tilde{J}_{\mathrm{w}}$, the model yields analytical expressions for all the relevant fields and concentration distributions. In general, the link between $\tilde{J}_+$ and $\tilde{J}_{\mathrm{w}}$ depends on the kinetics of the water dissociation reaction. However, regardless of reaction kinetics the analytical transport model puts some quite specific restrictions on the relationship between $\tilde{J}_+$ and $\tilde{J}_{\mathrm{w}}$. Besides improving our understanding of water-splitting at permselective membranes, this relationship can be used to probe the water-ion concentration in the ESC, and maybe even say something about the reaction kinetics in an experimental system. The model is successfully fitted to experimental data from Ref. [90]. Finally, we investigated the effect of adding an acid or a base to the reservoir.

Chapter 7

Electrodeposition: Stability analysis

In the systems we have encountered so far the ion-selective interfaces play an important role, but they are not themselves a dynamic part of the system. That is, in those systems the behavior of the ion-selective interface is unaffected by the behavior of the remainder of the system. While this is a reasonable way of describing transport across a chemically stable permselective membrane, it does not necessarily apply when the ion-selective interface is a metal electrode. The reason for this difference is that the ions deposit onto an electrode surface, whereas they pass straight through a permselective membrane. At long time scales the morphology of the electrode may therefore change appreciably.

In some circumstances, the ions deposit uniformly onto the electrode, so that an initially flat electrode stays flat during the growth process. However, like many systems involving transport between matter in different phases, the electrode interface is prone to morphological instabilities which can break the symmetry and lead to ramified growth patterns [39, 91, 122, 51, 86]. Besides the basic interest we might have in studying these interesting patterns, a better understanding of the ramification process could be hugely important for the many technological applications where electrodeposition plays a role. These applications include battery technology, electroplating, and production of metal powders and microstructures [36, 96, 37, 70, 95, 105, 120, 129, 45, 107, 24].

Superficially, electrodeposition belongs to the large class of diffusion-limited aggregation (DLA) problems, in which the interface growth can be modeled in terms of a simple solute diffusion model and a probability of sticking to the interface [131, 130]. However, while a simple diffusion model may give an adequate description of the transport in the linear underlimiting regime, it is clearly inadequate in the nonlinear overlimiting regime. Furthermore, simple DLA models totally fail to take the complicated reaction kinetics occurring at the electrode into account.

In the related interfacial problem of metal solidification, phase-field models have been applied widely and with considerable success [52, 61]. In recent years those phase-field models have been adapted to model electrolyte transport and applied to the electrodeposition problem [106, 17, 67, 31]. This adaptation has, however, met with some major obstacles. In the simplest form of metal solidification one only has to deal with two fields; a phase-field parameter ξ and a temperature field T. On the other hand, a phase-field

model of electrodeposition must, as a minimum, include the cation concentration c_+, the anion concentration c_-, the electron concentration c_e, a phase-field parameter ξ, and the electric potential ϕ [41, 42]. In addition, the model has to take the nonlinear reaction kinetics into account. So far, no phase-field model of electrodeposition has succeeded in properly implementing all these fields. For instance, only the 1D models of Guyer *et al.* [41, 42] and Deng *et al.* [23] allow for deviations from electroneutrality, and that comes at a computational cost which is prohibitive for 2D simulations. In some other models, which assume local electroneutrality, nonlinear reaction models are tentatively included [17, 67]. However, it is unclear how these reaction models relate to their sharp-interface equivalents. Also, the behavior of these models is sensitive to the width of the interface region and to the interpolation function used in that region [68].

To circumvent the shortcomings of the established models we pursue a different solution strategy. Rather than defining the interface via a smoothly varying time-dependent parameter as in the phase-field models, we employ a sharp-interface model, in which the interface is moved for each discrete time step. In this model the nonlinear electrode reactions are easily implemented, and as seen in the preceding chapters it is straight-forward to account for non-zero space-charge densities.

In this chapter we study the stability of a flat electrode interface under perturbations of varying wavelength. Numerous studies of morphological stability during electrodeposition already exist, but so far none has taken the effects of an extended space-charge region into account [115, 43, 29]. Intuitively, we expect the electrode to become increasingly unstable as the magnitude of the field gradients at the interface increases. The overlimiting regime, which is omitted in the existing models, might therefore be the regime which is most relevant to the stability problem. In fact, this point has already been argued by Chazalviel in his 1990 paper [14].

We follow the approach of Sundstrom and Bark [115], and investigate steady electrodeposition in a system composed of an electrolyte sandwiched between two planar metal electrodes. We find both numerical and analytical solutions to the stability problem. In the numerical solution we assume that the reaction rates follow a standard Butler–Volmer expression with constant charge-transfer coefficients. However, our analytical solutions cover a more general class of reaction kinetics, including e.g. Marcus kinetics and Butler–Volmer–Frumkin kinetics [76, 7, 126, 10].

This chapter is based on material from our paper Ref. [84], which can be found in Appendix G.

7.1 Model system

Following Sundstrom and Bark [115], we consider a binary electrolyte trapped between two co-planar metal electrodes at $x = 0$ and $x = 2L$. The electrolyte has initial concentration c_0 and is assumed symmetric with valence Z. The coordinate system is moving in the negative x-direction with velocity U, which is related to the average deposition rate on the electrodes. We consider the dilute solution limit, in which the effect of the moving coordinate system is negligible everywhere except in the surface evolution equation. A

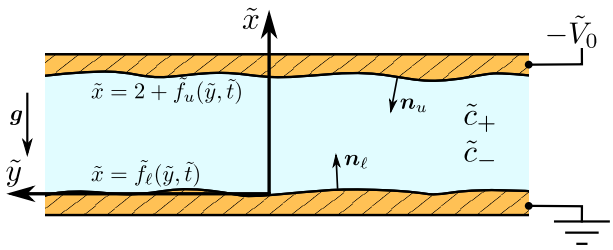

Figure 7.1: Sketch of the studied system with lower and upper electrode surfaces at $\tilde{x} = \tilde{f}_\ell(\tilde{y}, \tilde{t})$ and $\tilde{x} = 2 + \tilde{f}_u(\tilde{y}, \tilde{t})$, respectively. The coordinates are given relative to the moving frame of reference, following the mean rate of deposition on the electrode surfaces.

sketch of the system is shown in Fig. 7.1.

In the analysis, we investigate the stability of the electrodes under y-dependent perturbations along the x-direction. However, our analysis is general and applies to perturbations along any direction in the yz plane.

7.2 Governing equations

Using the standard normalizations, see Section 2.2, the equations governing the ion transport are

$$\frac{D_+}{D_\pm}\tilde{\boldsymbol{J}}_\pm = -\tilde{c}_\pm \tilde{\boldsymbol{\nabla}}\tilde{\mu}_\pm, \tag{7.1}$$

$$\partial_{\tilde{t}}\tilde{c}_\pm = -\tilde{\boldsymbol{\nabla}} \cdot \tilde{\boldsymbol{J}}_\pm, \tag{7.2}$$

where the time-derivative was included, since the growth of the electrode makes the problem unsteady. At the electrodes, the current of anions vanishes, while the current of cations is given by a reaction expression

$$\boldsymbol{n}_p \cdot \tilde{\boldsymbol{J}}_- = 0, \tag{7.3a}$$

$$\boldsymbol{n}_p \cdot \tilde{\boldsymbol{J}}_+ = -\tilde{R}_p, \tag{7.3b}$$

where $\tilde{R}_p$ is the normalized reaction rate at the lower and upper electrode, respectively, as indicated by the subscript $p = \ell, u$. As discussed in Section 2.6.2, we model the reaction rates $\tilde{R}_u$ and $\tilde{R}_\ell$ using a reaction expression with the general form

$$\tilde{R}_p = K_0 \left[\tilde{c}_+ \mathrm{e}^{-\bar{\gamma}\tilde{\kappa}+\alpha_\mathrm{c}(\tilde{\phi},\tilde{c}_+)Z(\tilde{\phi}+\tilde{V}_p)} - \mathrm{e}^{-\bar{\gamma}\tilde{\kappa}-\alpha_\mathrm{a}(\tilde{\phi},\tilde{c}_+)Z(\tilde{\phi}+\tilde{V}_p)}\right], \tag{7.4}$$

Here, K_0 is the dimensionless version of the dimensionfull rate constant k_0 for the electrode reaction,

$$K_0 = \frac{k_0}{2D_+c_0/L}, \tag{7.5}$$

$\tilde{V}_p$ is the normalized electrode potential, $\tilde{\kappa}$ is the normalized curvature of the surface, and $\bar{\gamma}$ is the non-dimensionalized version of the dimensionfull surface energy γ,

$$\bar{\gamma} = \frac{a^3\gamma}{k_{\mathrm{B}}TL}. \tag{7.6}$$

The factor a^3 which was introduced in this expression is the volume of a single cation. The $\bar{\gamma}\tilde{\kappa}$ term in Eq. (7.4) therefore measures the surface energy per ion, and constitutes an energy barrier for the reaction. At under-coordinated sites with a large positive curvature $\tilde{\kappa}$, the surface energy acts to reduce the reaction rate. Conversely, at over-coordinated sites with a large negative curvature $\tilde{\kappa}$, the surface energy acts to increase the reaction rate. The surface energy $\bar{\gamma}\tilde{\kappa}$ therefore has a stabilizing influence on perturbations to the electrode surface.

We allow the cathodic and anodic charge-transfer coefficients α_{c} and α_{a} to vary with the potential $\tilde{\phi}$ and the cation concentration $\tilde{c}_+$. As discussed in Section 2.6.2, this means that Eq. (7.4) can represent a wide range of reaction models from classical Butler–Volmer kinetics to Marcus kinetics and Butler–Volmer–Frumkin kinetics [115, 126, 7]. In agreement with most realistic reaction models, we do impose one restriction on the charge transfer coefficients, namely that they vary slowly as a function of $\tilde{\phi}$ and $\ln(\tilde{c}_+)$,

$$\partial_{\tilde{\phi}} \left\{ \alpha_{\mathrm{c}}(\tilde{\phi}, \tilde{c}_+)\phi \right\} \approx \alpha_{\mathrm{c}}(\tilde{\phi}, \tilde{c}_+), \tag{7.7}$$

$$\partial_{\ln(\tilde{c}_+)} \left\{ \alpha_{\mathrm{c}}(\tilde{\phi}, \tilde{c}_+) \ln(\tilde{c}_+) \right\} \approx \alpha_{\mathrm{c}}(\tilde{\phi}, \tilde{c}_+). \tag{7.8}$$

The electrostatic part of the problem is governed by the standard Poisson equation,

$$2\bar{\lambda}_{\mathrm{D}}^2 \tilde{\nabla}^2 \tilde{\phi} = -Z\tilde{c}_+ + Z\tilde{c}_-. \tag{7.9}$$

Rather than explicitly modeling the electric double layers adjoining the electrodes we employ the GCP framework from Section 2.7 and implement the boundary condition

$$\boldsymbol{n}_u \cdot \tilde{\boldsymbol{\nabla}} \tilde{c}_+ = 0, \tag{7.10}$$

at the upper electrode. Also, since the anions can not enter or leave the system, the total number of anions is conserved,

$$\int_\Omega (\tilde{c}_- - 1)\, \mathrm{d}V = 0. \tag{7.11}$$

We introduce functions $\tilde{x} = \tilde{f}_p(\tilde{y})$ describing the position of the upper and lower electrode u and ℓ. The time evolution of $\tilde{f}_p$ is determined by the single-ion volume a^3 and the current into the electrode,

$$\left(\partial_{\tilde{t}} \tilde{f}_\ell - \tilde{U}\right) \boldsymbol{e}_x \cdot \boldsymbol{n}_\ell = -a^3 c_0 \boldsymbol{n}_\ell \cdot \tilde{\boldsymbol{J}}_+, \qquad \text{Anode,} \tag{7.12a}$$

$$\left(\partial_{\tilde{t}} \tilde{f}_u - \tilde{U}\right) \boldsymbol{e}_x \cdot \boldsymbol{n}_u = -a^3 c_0 \boldsymbol{n}_u \cdot \tilde{\boldsymbol{J}}_+, \qquad \text{Cathode.} \tag{7.12b}$$

Here, the filling factor $a^3 c_0$ is much less than unity, since we are dealing with dilute solutions. The normalized velocity $\tilde{U}$ of the coordinate system accounts for the mean current into or out of the electrodes, and $\partial_{\tilde{t}} \tilde{f}_p$ accounts for local deviations from the mean current. The curvature $\tilde{\kappa}$ and the normal vectors are related to the surface function $\tilde{f}_p$ by

$$\boldsymbol{n}_\ell = \frac{\boldsymbol{e}_x - \boldsymbol{e}_y \partial_{\tilde{y}} \tilde{f}_\ell}{\sqrt{1 + (\partial_{\tilde{y}} \tilde{f}_\ell)^2}}, \quad \boldsymbol{n}_u = \frac{-\boldsymbol{e}_x + \boldsymbol{e}_y \partial_{\tilde{y}} \tilde{f}_u}{\sqrt{1 + (\partial_{\tilde{y}} \tilde{f}_u)^2}}, \tag{7.13a}$$

$$\tilde{\kappa}_\ell = \frac{\partial_{\tilde{y}}^2 \tilde{f}_\ell}{\sqrt{1 + (\partial_{\tilde{y}} \tilde{f}_\ell)^2}}, \quad \tilde{\kappa}_u = -\frac{\partial_{\tilde{y}}^2 \tilde{f}_u}{\sqrt{1 + (\partial_{\tilde{y}} \tilde{f}_u)^2}}. \tag{7.13b}$$

7.3 Perturbation

The stability of the electrode growth is investigated using linear perturbation theory. That is, we impose a small perturbation on a steady-state base state, and investigate how the perturbation evolves. The base state is identified by a superscript "0" and the first-order perturbation by superscript "1",

$$\tilde{f}_p(\tilde{y}, \tilde{t}) \approx \tilde{f}_p^1(\tilde{y}, \tilde{t}), \tag{7.14a}$$

$$\tilde{c}_\pm(\tilde{x}, \tilde{y}, \tilde{t}) \approx \tilde{c}_\pm^0(\tilde{x}) + \tilde{c}_\pm^1(\tilde{x}, \tilde{y}, \tilde{t}), \tag{7.14b}$$

$$\tilde{\phi}(\tilde{x}, \tilde{y}, \tilde{t}) \approx \tilde{\phi}^0(\tilde{x}) + \tilde{\phi}^1(\tilde{x}, \tilde{y}, \tilde{t}). \tag{7.14c}$$

In first-order perturbation theory, we substitute the second-order factor $\sqrt{1 + (\partial_{\tilde{y}} \tilde{f}_p)^2}$ in Eq. (7.13) by unity,

$$\boldsymbol{n}_\ell \approx \boldsymbol{e}_x - \boldsymbol{e}_y \partial_{\tilde{y}} \tilde{f}_\ell^1, \qquad \boldsymbol{n}_u \approx -\boldsymbol{e}_x + \boldsymbol{e}_y \partial_{\tilde{y}} \tilde{f}_u^1, \tag{7.15a}$$

$$\tilde{\kappa}_\ell \approx \partial_{\tilde{y}}^2 \tilde{f}_\ell^1, \qquad \tilde{\kappa}_u \approx -\partial_{\tilde{y}}^2 \tilde{f}_u^1. \tag{7.15b}$$

To find the field values at the perturbed surface, we Taylor expand to first order and obtain

$$\tilde{\phi}(\tilde{f}_\ell^1, \tilde{y}, \tilde{t}) \approx \tilde{\phi}^0(0) + \partial_{\tilde{x}} \tilde{\phi}|_0 \tilde{f}_\ell^1(\tilde{y}, \tilde{t}) + \tilde{\phi}^1(0, \tilde{y}, \tilde{t}), \tag{7.16a}$$

$$\tilde{\boldsymbol{\nabla}} \tilde{\phi}(\tilde{f}_\ell^1, \tilde{y}, \tilde{t}) \approx \partial_{\tilde{y}} \tilde{\phi}^1|_0 \boldsymbol{e}_{\tilde{y}} + \left(\partial_{\tilde{x}} \tilde{\phi}^0|_0 + \partial_{\tilde{x}}^2 \tilde{\phi}^0|_0 \tilde{f}_\ell^1 + \partial_{\tilde{x}} \tilde{\phi}^1|_0 \right) \boldsymbol{e}_x.$$

Similar expressions apply for $\tilde{c}_\pm$ and at the upper electrode. Evaluating the reaction rate at the lower electrode and expanding to first order, we find

$$\tilde{R}_\ell \approx \tilde{R}_\ell^0 + \tilde{R}_\ell^1, \tag{7.17a}$$

$$\frac{\tilde{R}_\ell^0}{K_0} = \tilde{c}_+^0 \mathrm{e}^{\alpha_\mathrm{c} Z(\tilde{\phi}^0 + \tilde{V}_\ell)} - \mathrm{e}^{-\alpha_\mathrm{a} Z(\tilde{\phi}^0 + \tilde{V}_\ell)}, \tag{7.17b}$$

$$\begin{aligned} \frac{\tilde{R}_\ell^1}{K_0} = {} & \mathrm{e}^{\alpha_\mathrm{c} Z(\tilde{\phi}^0 + \tilde{V}_\ell)} \left[\tilde{c}_+^1 + \partial_{\tilde{x}} \tilde{c}_+^0 \tilde{f}_\ell^1 + \tilde{c}_+^0 (\alpha_\mathrm{a} + \alpha_\mathrm{c}) Z \left[\tilde{\phi}^1 + \partial_{\tilde{x}} \tilde{\phi}^0 \tilde{f}_\ell^1 \right] \right] \\ & + \frac{\tilde{R}_\ell^0}{K_0} \left[-\bar{\gamma} \partial_{\tilde{y}}^2 \tilde{f}_\ell^1 - \alpha_\mathrm{a} Z \left[\tilde{\phi}^1 + \partial_{\tilde{x}} \tilde{\phi}^0 \tilde{f}_\ell^1 \right] \right], \end{aligned} \tag{7.17c}$$

where all fields are evaluated at $\tilde{x} = 0$, and the expression for $\tilde{R}_\ell^0$ was used to simplify the expression for $\tilde{R}_\ell^1$. Since the charge transfer coefficients vary slowly with $\tilde{\phi}$ and $\ln(\tilde{c}_+)$, we have neglected their first order contributions. Similar expressions apply at the upper electrode. Hence, the full zeroth-order problem becomes

$$0 = -\partial_{\tilde{x}} \tilde{J}_\pm^0, \tag{7.18a}$$

$$2\frac{D_+}{D_\pm}\tilde{J}_\pm^0 = -\partial_{\tilde{x}}\tilde{c}_\pm^0 \mp Z\tilde{c}_\pm^0 \partial_{\tilde{x}}\tilde{\phi}^0, \tag{7.18b}$$

$$2\bar{\lambda}_\mathrm{D}^2 \partial_{\tilde{x}}^2 \tilde{\phi}^0 = -Z(\tilde{c}_+^0 - \tilde{c}_-^0) = -\tilde{\rho}_\mathrm{el}^0, \tag{7.18c}$$

with the following boundary conditions and constraints

$$\tilde{J}_-^0(0) = 0, \qquad \tilde{J}_-^0(2) = 0, \tag{7.19a}$$

$$\tilde{J}_+^0(0) = -\tilde{R}_\ell^0, \qquad \tilde{J}_+^0(2) = \tilde{R}_u^0, \tag{7.19b}$$

$$\int_0^2 \left(\tilde{c}_-^0 - 1\right) \mathrm{d}\tilde{x} = 0, \qquad \partial_{\tilde{x}}\tilde{c}_+^0(2) = 0, \tag{7.19c}$$

and the mean growth velocity $\tilde{U}$ derived from Eq. (7.12),

$$\tilde{U} = a^3 c_0 \tilde{J}_+^0. \tag{7.20}$$

Similarly, the first-order problem is given by

$$\partial_{\tilde{t}}\tilde{c}_\pm^1 = -\tilde{\boldsymbol{\nabla}} \cdot \tilde{\boldsymbol{J}}_\pm^1, \tag{7.21a}$$

$$2\frac{D_+}{D_\pm}\tilde{\boldsymbol{J}}_\pm^1 = -\tilde{\boldsymbol{\nabla}}\tilde{c}_\pm^1 \mp Z\tilde{c}_\pm^0 \tilde{\boldsymbol{\nabla}}\tilde{\phi}^1 \mp Z\tilde{c}_\pm^1 \tilde{\boldsymbol{\nabla}}\tilde{\phi}^0, \tag{7.21b}$$

$$2\bar{\lambda}_\mathrm{D}^2 \tilde{\nabla}^2 \tilde{\phi}^1 = -Z(\tilde{c}_+^1 - Z\tilde{c}_-^1), \tag{7.21c}$$

and the boundary conditions,

$$\boldsymbol{e}_x \cdot \tilde{\boldsymbol{J}}_-^1(2) = 0, \qquad \boldsymbol{e}_x \cdot \tilde{\boldsymbol{J}}_-^1(0) = 0, \tag{7.22a}$$

$$\boldsymbol{e}_x \cdot \tilde{\boldsymbol{J}}_+^1(2) = \tilde{R}_u^1, \qquad \boldsymbol{e}_x \cdot \tilde{\boldsymbol{J}}_+^1(0) = -\tilde{R}_\ell^1, \tag{7.22b}$$

$$\partial_{\tilde{x}}^2 \tilde{c}_+^0(2)\tilde{f}_u^1 + \partial_{\tilde{x}}\tilde{c}_+^1(2) = 0, \tag{7.22c}$$

together with the first-order electrode growth rates $\partial_{\tilde{t}}\tilde{f}_\ell^1$ and $\partial_{\tilde{t}}\tilde{f}_u^1$ derived from Eq. (7.12),

$$\partial_{\tilde{t}}\tilde{f}_\ell^1 = a^3 c_0 \tilde{R}_\ell^1, \qquad \partial_{\tilde{t}}\tilde{f}_u^1 = -a^3 c_0 \tilde{R}_u^1. \tag{7.23}$$

To find the eigenmodes, we make the following harmonic ansatz for the first-order fields,

$$\tilde{c}_\pm^1(\tilde{x}, \tilde{y}, \tilde{t}) = \tilde{c}_\pm^*(\tilde{x})\mathrm{e}^{\tilde{\Gamma}\tilde{t} + i\tilde{k}\tilde{y}}, \tag{7.24a}$$

$$\tilde{\phi}^1(\tilde{x}, \tilde{y}, \tilde{t}) = \tilde{\phi}^*(\tilde{x})\mathrm{e}^{\tilde{\Gamma}\tilde{t} + i\tilde{k}\tilde{y}}, \tag{7.24b}$$

$$\tilde{f}_p^1(\tilde{y}, \tilde{t}) = F_p \mathrm{e}^{\tilde{\Gamma}\tilde{t} + i\tilde{k}\tilde{y}}, \tag{7.24c}$$

where $\tilde{\Gamma}$ is the nondimensional growth rate of the perturbation, and $\tilde{k}$ is the wavenumber of the transverse eigenmode. For convenience we also define

$$\tilde{R}_p^1 = \tilde{R}_p^* \mathrm{e}^{\tilde{\Gamma}\tilde{t}+i\tilde{k}\tilde{y}}. \tag{7.24d}$$

With this ansatz, the first-order bulk equations become

$$2\frac{D_+}{D_\pm}\tilde{\Gamma}\tilde{c}_\pm^* = -\tilde{k}^2(\tilde{c}_\pm^* \pm Z\tilde{c}_\pm^0\tilde{\phi}^*) + \partial_{\tilde{x}}\left\{\partial_{\tilde{x}}\tilde{c}_\pm^* \pm Z\tilde{c}_\pm^*\partial_{\tilde{x}}\tilde{\phi}^0 \pm Z\tilde{c}_\pm^0\partial_{\tilde{x}}\tilde{\phi}^*\right\} \tag{7.25a}$$

$$2\bar{\lambda}_\mathrm{D}^2(\partial_{\tilde{x}}^2\tilde{\phi}^* - \tilde{k}^2\tilde{\phi}^*) = -Z(\tilde{c}_+^* - \tilde{c}_-^*), \tag{7.25b}$$

and the first-order reaction rate at the lower electrode is

$$\begin{aligned}\frac{\tilde{R}_\ell^*}{K_0} = \mathrm{e}^{\alpha_\mathrm{c}Z(\tilde{\phi}^0+\tilde{V}_\ell)}&\left[\tilde{c}_+^* + \partial_{\tilde{x}}\tilde{c}_+^0F_\ell + \tilde{c}_+^0(\alpha_\mathrm{a}+\alpha_\mathrm{c})Z\left[\tilde{\phi}^* + \partial_{\tilde{x}}\tilde{\phi}^0F_\ell\right]\right] \\ &+ \frac{\tilde{R}_\ell^0}{K_0}\left[-\bar{\gamma}\tilde{k}^2F_\ell - \alpha_\mathrm{a}Z\left[\tilde{\phi}^* + \partial_{\tilde{x}}\tilde{\phi}^0F_\ell\right]\right].\end{aligned} \tag{7.26}$$

Inserting the ansatz in the growth equations (7.23) yields

$$\tilde{\Gamma}F_\ell = a^3c_0\tilde{R}_\ell^*, \qquad \tilde{\Gamma}F_u = -a^3c_0\tilde{R}_u^*. \tag{7.27}$$

Since the stability problem is linear we can set F_u to unity, meaning that the magnitude of the remaining first-order fields are given relative to the amplitude of the upper electrode perturbation.

7.4 Analysis

The lower electrode does not go unstable by itself, so as long as the perturbation wavelength is considerably smaller than the distance between the electrodes, i.e. when $\tilde{k} \gtrsim 1$, we can disregard the lower electrode from the stability problem. In that case analytical solutions can be derived in both the underlimiting regime and in the overlimiting regime.

7.4.1 Underlimiting regime

At currents below the limiting current $\tilde{J}_+^0 < 1$ the electrolyte is locally electroneutral,

$$\tilde{c} = \tilde{c}_+ = \tilde{c}_-. \tag{7.28}$$

Assuming that the time derivative in the first-order problem (the left hand side in Eq. (7.25a)) is negligible, we can express the salt concentration $\tilde{c}$ via a Boltzmann factor,

$$\tilde{c} = \mathrm{e}^{Z\tilde{\phi}} = \mathrm{e}^{Z(\tilde{\phi}^0+\tilde{\phi}^1)} \approx \mathrm{e}^{Z\tilde{\phi}^0} + \mathrm{e}^{Z\tilde{\phi}^0}Z\tilde{\phi}^1 = \tilde{c}^0 + \tilde{c}^1. \tag{7.29}$$

The zero-order solutions are well known,

$$\tilde{c}^0 = 1 - \tilde{J}^0(\tilde{x}-1), \quad Z\tilde{\phi}^0 = \ln\left[1 - \tilde{J}^0(\tilde{x}-1)\right], \tag{7.30}$$

and using the electroneutrality assumption in Eq. (7.25a) we find that $\tilde{c}^*$ is determined by

$$0 = \partial_{\tilde{x}}^2 \tilde{c}^* - \tilde{k}^2 \tilde{c}^*. \tag{7.31}$$

This equation has two solutions, but as long as the perturbation wavelength is considerably smaller than the electrode spacing, the solution which increases with $\tilde{x}$ is dominant,

$$\tilde{c}^* \approx C \mathrm{e}^{\tilde{k}(\tilde{x}-2)}, \tag{7.32}$$

where C is a constant to be determined. Eq. (7.29) then yields

$$\tilde{\phi}^* = \frac{1}{Z}\frac{\tilde{c}^*}{\tilde{c}^0} = \frac{1}{Z}\frac{C\mathrm{e}^{\tilde{k}(\tilde{x}-2)}}{1-\tilde{J}^0(\tilde{x}-1)}. \tag{7.33}$$

At the upper electrode the first-order reaction rate is

$$\begin{aligned}\frac{\tilde{R}_u^*}{K_0} = \mathrm{e}^{\alpha_c Z(\tilde{\phi}^0+\tilde{V}_u)}&\left[\tilde{c}_+^* + \partial_{\tilde{x}}\tilde{c}_+^0 + \tilde{c}_+^0(\alpha_a+\alpha_c)Z\left[\tilde{\phi}^* + \partial_{\tilde{x}}\tilde{\phi}^0\right]\right] \\ &+ \frac{\tilde{R}_u^0}{K_0}\left[\bar{\gamma}\tilde{k}^2 - \alpha_a Z\left[\tilde{\phi}^* + \partial_{\tilde{x}}\tilde{\phi}^0\right]\right],\end{aligned} \tag{7.34}$$

and evaluating the fields at $\tilde{x} = 2$, this expression becomes

$$\frac{\tilde{R}_u^*}{K_0} = (1+\alpha_a+\alpha_c)(C-\tilde{J}^0)\mathrm{e}^{\alpha_c Z(\tilde{\phi}^0+\tilde{V}_u)} + \frac{\tilde{J}^0}{K_0}\left[\bar{\gamma}\tilde{k}^2 - \alpha_a\frac{C-\tilde{J}^0}{1-\tilde{J}^0}\right]. \tag{7.35}$$

Inserting the first-order current into the upper electrode $\tilde{R}_u^* = \tilde{J}^* = -\partial_{\tilde{x}}\tilde{c}^* = -\tilde{k}C$ and solving for C, we obtain

$$C = \tilde{J}^0\frac{(1+\alpha_a+\alpha_c)K_0\mathrm{e}^{\alpha_c Z(\tilde{\phi}^0+\tilde{V}_u)} - \alpha_a\frac{\tilde{J}^0}{1-\tilde{J}^0} - \bar{\gamma}\tilde{k}^2}{(1+\alpha_a+\alpha_c)K_0\mathrm{e}^{\alpha_c Z(\tilde{\phi}^0+\tilde{V}_u)} - \alpha_a\frac{\tilde{J}^0}{1-\tilde{J}^0} + \tilde{k}}. \tag{7.36}$$

From Eq. (7.27) the growth rate $\tilde{\Gamma}$ can be expressed as

$$\tilde{\Gamma} = -a^3 c_0 \tilde{J}^* = a^3 c_0 \tilde{k} C, \tag{7.37}$$

so we have

$$\tilde{\Gamma} = a^3 c_0 \tilde{k}\tilde{J}^0\frac{\beta - \bar{\gamma}\tilde{k}^2}{\beta + \tilde{k}}, \tag{7.38}$$

with the parameter β given as

$$\beta = (1+\alpha_a+\alpha_c)K_0\mathrm{e}^{\alpha_c Z(\tilde{\phi}^0+\tilde{V}_u)} - \alpha_a\frac{\tilde{J}^0}{1-\tilde{J}^0}. \tag{7.39}$$

To test whether the time derivatives in the first-order problem really are negligible, we compare the time derivative term $2\tilde{\Gamma}\tilde{c}^*$ with the transverse diffusion term $\tilde{k}^2\tilde{c}^*$. Since Eq. (7.38) implies that $\tilde{\Gamma} \leq a^3 c_0 \tilde{k}\tilde{J}^0$, our assumption is justified if

$$2a^3 c_0 \tilde{J}^0 \ll \tilde{k}. \tag{7.40}$$

Consequently, because $a^3 c_0 \ll 1$ for dilute systems and $\tilde{J}^0$ is of order unity, it is justified to neglect the time derivative, unless the perturbation wavelength is comparable to the electrode spacing.

7.4.2 Overlimiting regime

For currents exceeding the limiting current the field gradients are large close to the upper electrode, and this makes the electrode interface much more unstable. It follows that a larger $\tilde{k}$ value will be needed for the surface tension to stabilize the system, so the most unstable $\tilde{k}$ value will be larger than for less driven systems. We might therefore expect that Eq. (7.25b) primarily is a balance between $\partial_{\tilde{x}}\tilde{\phi}^*$ and $\tilde{k}^2\tilde{\phi}^*$ in the region of interest. This leads us to making the ansatz

$$\tilde{\phi}^* = \Phi \mathrm{e}^{\tilde{k}(\tilde{x}-2)}, \tag{7.41}$$

where Φ is a constant. We now consider Eq. (7.25a) for the cation concentration, neglecting the left hand side,

$$0 = -\partial_{\tilde{x}}\left\{-\partial_{\tilde{x}}\tilde{c}_+^* - Z\tilde{c}_+^*\partial_{\tilde{x}}\tilde{\phi}^0 - Z\tilde{c}_+^0\partial_{\tilde{x}}\tilde{\phi}^*\right\} - \tilde{k}^2\big(\tilde{c}_+^* + Z\tilde{c}_+^0\tilde{\phi}^*\big). \tag{7.42}$$

We assume that the terms $\partial_{\tilde{x}}\tilde{c}_+^*$ and $Z\tilde{c}_+^*\partial_{\tilde{x}}\tilde{\phi}^0$ are negligible and insert the ansatz Eq. (7.41),

$$\begin{aligned} 0 &\approx Z\partial_{\tilde{x}}\tilde{c}_+^0\tilde{k}\tilde{\phi}^* + Z\tilde{c}_+^0\tilde{k}^2\tilde{\phi}^* - \tilde{k}^2\big(\tilde{c}_+^* + Z\tilde{c}_+^0\tilde{\phi}^*\big) \\ &= Z\partial_{\tilde{x}}\tilde{c}_+^0\tilde{k}\tilde{\phi}^* - \tilde{k}^2\tilde{c}_+^*, \end{aligned} \tag{7.43}$$

implying that

$$\tilde{c}_+^* \approx \frac{Z}{\tilde{k}}\partial_{\tilde{x}}\tilde{c}_+^0\tilde{\phi}^*. \tag{7.44}$$

In the overlimitign regime the first-order current is approximately

$$2\tilde{J}_+^* \approx -Z\tilde{c}_+^0\partial_{\tilde{x}}\tilde{\phi}^* = -Z\tilde{k}\tilde{c}_+^0\Phi, \tag{7.45}$$

at the upper electrode. The zeroth-order diffusive contribution is also very small at the upper electrode, meaning that the reaction rate Eq. (7.34) simplifies as

$$\begin{aligned} \tilde{R}_u^* &\approx K_0\mathrm{e}^{\alpha_\mathrm{c}Z(\tilde{\phi}^0+\tilde{V}_u)}\tilde{c}_+^0(\alpha_\mathrm{a}+\alpha_\mathrm{c})Z\big[\tilde{\phi}^* + \partial_{\tilde{x}}\tilde{\phi}^0\big] + \tilde{R}_u^0\left[\bar{\gamma}\tilde{k}^2 - \alpha_\mathrm{a}Z\big(\tilde{\phi}^* + \partial_{\tilde{x}}\tilde{\phi}^0\big)\right] \\ &\approx K_0\mathrm{e}^{\alpha_\mathrm{c}Z(\tilde{\phi}^0+\tilde{V}_u)}(\alpha_\mathrm{a}+\alpha_\mathrm{c})\big[\tilde{c}_+^0Z\Phi - 2\tilde{J}^0\big] + \tilde{R}_u^0\left[\bar{\gamma}\tilde{k}^2 - \alpha_\mathrm{a}\left(Z\Phi - \frac{2\tilde{J}^0}{\tilde{c}_+^0}\right)\right]. \end{aligned} \tag{7.46}$$

Inserting $\tilde{R}_u^* = \tilde{J}_+^* \approx -\frac{1}{2}Z\tilde{k}\tilde{c}_+^0\Phi$ and using $\tilde{\Gamma} = -a^3c_0\tilde{J}_+^*$, we find

$$\tilde{\Gamma} = a^3c_0\tilde{k}\tilde{J}^0\frac{\beta - \bar{\gamma}\tilde{k}^2}{\beta + \tilde{k}}, \tag{7.47a}$$

with

$$\beta = 2(\alpha_\mathrm{a}+\alpha_\mathrm{c})K_0\mathrm{e}^{\alpha_\mathrm{c}Z(\tilde{\phi}^0+\tilde{V}_u)} - \alpha_\mathrm{a}\frac{2\tilde{J}^0}{\tilde{c}_+^0}, \tag{7.47b}$$

$$\tilde{c}_+^0 \approx \frac{\bar{\lambda}_\mathrm{D}}{Z}\sqrt{\frac{2\tilde{J}^0}{1-\frac{1}{\tilde{J}^0}}}. \tag{7.47c}$$

Here, the cation concentration at the electrode was obtained from the analysis in Chapter 4. The solution from Chapter 4 can also be used to validate the assumptions leading to Eq. (7.47a), see Ref. [84].

7.4.3 Unified analysis

The instability growth rate in both regimes is given by the same expression,

$$\tilde{\Gamma} = a^3 c_0 \tilde{k} \tilde{J}^0 \frac{\beta - \bar{\gamma}\tilde{k}^2}{\beta + \tilde{k}}, \tag{7.48}$$

where only the expression for β differs slightly between the two regimes. We can therefore derive some general expressions, which apply in both regimes.

The critical wavenumber $\tilde{k}_\mathrm{c}$, where the electrode interface is marginally stable, is found by setting the nominator in Eq. (7.48) equal to zero,

$$\tilde{k}_\mathrm{c} = \sqrt{\frac{\beta}{\bar{\gamma}}}. \tag{7.49}$$

To find the wavenumber $\tilde{k}_\mathrm{max}$, at which $\tilde{\Gamma}$ attains its maximum $\tilde{\Gamma}_\mathrm{max}$, we set the derivative of $\tilde{\Gamma}$ equal to zero and solve for $\tilde{k}$,

$$\begin{aligned}\tilde{k}_\mathrm{max} = \frac{\beta}{2}\Bigg[&\left(\frac{2 - \beta\bar{\gamma} + 2\sqrt{1-\beta\bar{\gamma}}}{\beta\bar{\gamma}}\right)^{1/3} \\ &+ \left(\frac{2 - \beta\bar{\gamma} + 2\sqrt{1-\beta\bar{\gamma}}}{\beta\bar{\gamma}}\right)^{-1/3} - 1\Bigg],\end{aligned} \tag{7.50}$$

with the asymptotic solutions,

$$\tilde{k}_\mathrm{max} \approx \begin{cases} \left(\frac{\beta}{3\bar{\gamma}}\right)^{1/2}, & \text{for} \quad \bar{\gamma}\beta \gg 1, \\ \left(\frac{\beta^2}{2\bar{\gamma}}\right)^{1/3} - \frac{\beta}{2}, & \text{for} \quad \bar{\gamma}\beta \ll 1. \end{cases} \tag{7.51}$$

The factors $K_0 \mathrm{e}^{\alpha_\mathrm{c} Z(\tilde{\phi}^0 + \tilde{V}_u)}$ appearing in both expressions for β are found by solving the zero order reaction expression

$$\tilde{J}^0 = \tilde{R}_u^0 = K_0 \left[\tilde{c}_+^0 \mathrm{e}^{\alpha_\mathrm{c} Z(\tilde{\phi}^0 + \tilde{V}_u)} - \mathrm{e}^{-\alpha_\mathrm{a} Z(\tilde{\phi}^0 + \tilde{V}_u)}\right]. \tag{7.52}$$

Since the charge-transfer coefficients α_a and α_c may depend on $\tilde{\phi}^0$ and $\tilde{c}_+^0$ there is no general solution to Eq. (7.52). In the limit $K_0 \ll 1$ the deposition term in Eq. (7.52) dominates, and we simply have

$$K_0 \mathrm{e}^{\alpha_\mathrm{c} Z(\tilde{\phi}^0 + \tilde{V}_u)} \approx \frac{\tilde{J}^0}{\tilde{c}_+^0}. \tag{7.53}$$

In that limit β becomes

$$\beta \approx (1+\alpha_\mathrm{c})\frac{\tilde{J}^0}{1-\tilde{J}^0}, \quad \text{Underlimiting regime,} \tag{7.54a}$$

$$\beta \approx 2\alpha_\mathrm{c}\frac{\tilde{J}^0}{\tilde{c}^0_+} \quad \text{Overlimiting regime.} \tag{7.54b}$$

In the case of simple Butler–Volmer kinetics with constant charge transfer coefficients $\alpha_\mathrm{c} = \alpha_\mathrm{a} = \frac{1}{2}$, it is also possible to obtain simple solutions to Eq. (7.52). In that case we find

$$\beta = \frac{\tilde{J}^0}{1-\tilde{J}^0}\left[\frac{1}{2} + \sqrt{1+4\left(\frac{K_0}{\tilde{J}^0}\right)^2(1-\tilde{J}^0)}\right], \quad \text{Underlimiting regime,} \tag{7.55a}$$

$$\beta = \frac{\tilde{J}^0}{\tilde{c}^0_+}\sqrt{1+4\left(\frac{K_0}{\tilde{J}^0}\right)^2\tilde{c}^0_+}, \quad \text{Overlimiting regime.} \tag{7.55b}$$

7.5 Numerical solution

In the numerical simulations we choose to model the reaction using simple Butler–Volmer kinetics with $\alpha_\mathrm{a} = \alpha_\mathrm{c} = \frac{1}{2}$. To limit the parameter space, we choose fixed, physically reasonable values for the parameters listed in Table 7.1. The values are chosen to correspond to copper electrodes in a copper sulfate solution. We note that the surface tension is quite difficult to determine experimentally, and most measurements are carried out at temperatures around 1000 °C [124, 62]. *Ab initio* calculations can give some impression of the behaviour at lower temperatures [112], but these can hardly stand alone. Extrapolating the linear fit of Ref. [124] down to 0 K yields surface tension values close to those obtained from *ab initio* calculations in Ref. [112]. This makes it somewhat plausible to apply the

Table 7.1: Fixed parameter values used in the numerics. a: Calculated using the exchange current $I_0 = 30\ \mathrm{A\,m^{-2}}$ from Ref. [123] and $k_0 = I_0/(Ze)$. b: The cube root of the volume per atom in solid copper [69].

Parameter	Symbol	Value
Cation diffusivity[69]	D_+	$0.714 \times 10^{-9}\mathrm{m^2\,s^{-1}}$
Anion diffusivity[69]	D_-	$1.065 \times 10^{-9}\mathrm{m^2\,s^{-1}}$
Ion valence	Z	2
Surface energy	γ	$1.85\ \mathrm{J\,m^{-2}}$
Temperature	T	300 K
Permittivity of water	ϵ_w	$6.90 \times 10^{-10}\mathrm{F\,m^{-1}}$
Charge-transfer coefficients	$\alpha_\mathrm{c}, \alpha_\mathrm{a}$	$\frac{1}{2}$
Reaction constant[a]	k_0	$9.4 \times 10^{19}\mathrm{m^{-2}\,s^{-1}}$
Diameter of a copper atom[b]	a	0.228 nm

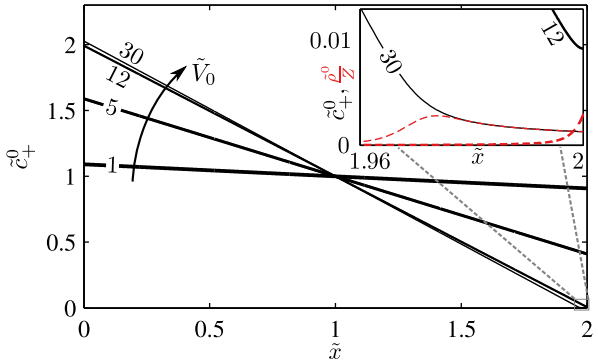

Figure 7.2: Zeroth-order cation concentrations $\tilde{c}_+^0$ shown in full black lines and zeroth-order charge densities $\tilde{\rho}_{\mathrm{el}}^0/Z$ shown in dashed red lines. The inset shows the fields close to the electrode. In the simulation the parameter values $c_0 = 10$ mM, $L = 10$ µm, and $\tilde{V}_0 = \{1, 5, 12, 30\}$ were used.

model from Ref. [124] in the region of interest around 300 K. This yields a copper-gas surface energy of 1.92 J/m^2. The contact angle at the copper-water interface is very small [121], so finding the copper-water surface energy is just a matter of subtracting the surface energy of water from that of copper. The resulting surface energy is $\tilde{\Gamma} \approx 1.85$ J/m^2, as listed in Table 7.1. These choices leave us with three free parameters, which are the bias voltage $\tilde{V}_0$, the electrolyte concentration c_0, and the system length L.

The solution procedure is as follows: First, the zeroth-order problem is solved for a given set of parameters. Then the first-order problem is solved for a range of wavenumbers $\tilde{k}$. For each $\tilde{k}$ value, the corresponding growth rate $\tilde{\Gamma}$ and perturbation amplitude of the lower electrode, F_ℓ, are obtained. In Fig. 7.2, the zeroth-order cation concentration $\tilde{c}_+^0$ and space-charge density $\tilde{\rho}_{\mathrm{el}}^0$ are shown for $c_0 = 10$ mM, $L = 10$ µm and varying bias voltage $\tilde{V}_0$. It is seen, that when the bias voltage exceeds $\tilde{V}_0 \simeq 12$, local electroneutrality is violated near the cathode. For $\tilde{V}_0 = 30$ the nonequilibrium space-charge region extends far (0.04) into the electrolyte.

7.6 Results

For plotting purposes we introduce the dimensionfull perturbation wavelength $\lambda = 2\pi L/\tilde{k}$. In Fig. 7.3, the growth rate $\tilde{\Gamma}$ is plotted versus λ for $\tilde{V}_0 = 30$, $c_0 = 10$ mM, and $L = 10$ µm. Visible in the figure is a stable region for wavelengths smaller than the critical wavelength $\lambda_{\mathrm{c}} = 51$ nm, and an unstable region for larger wavelengths. The most unstable wavelength we denote $\lambda_{\max}$, and the corresponding growth rate we denote $\tilde{\Gamma}_{\max}$.

To enable a more compact representation of the data, we introduce a gray-scale contour plot of the magnitude of $\tilde{\Gamma}$, as illustrated in Fig. 7.4. Here, $\tilde{\Gamma}$ is plotted versus the wavelength λ for $\tilde{V}_0 = \{5,\ 10,\ 15,\ 20,\ 25,\ 30\}$. The gray scale in the λ-$\tilde{V}_0$ plane is created by projecting the $\tilde{\Gamma}$ values from the above curves onto the plane. The solid blue line in the (λ, $\tilde{V}_0$)-plane marks the crest of the hill, thus representing the most unstable wavelength for each value of $\tilde{V}_0$.

In Fig. 7.5, we make use of the contour plots to show results for twelve sets of (c_0, L)-

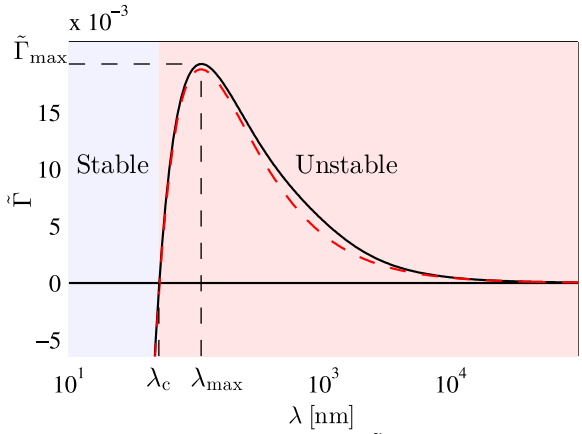

Figure 7.3: The growth rate $\tilde{\Gamma}$ plotted versus the perturbation wavelength λ for $\tilde{V}_0 = 30$, $c_0 = 10$ mM, and $L = 10$ µm. The full black line shows the growth rate obtained from numerical simulations, and the dashed red line shows the growth rate according to the analytical model Eq. (7.48) with Eq. (7.55b). For perturbation wavelengths smaller than the critical wavelength $\lambda_c = 51$ nm the system is stable and for larger wavelengths it is unstable. At the most unstable wavelength $\lambda_{max} = 110$ nm the growth rate is $\tilde{\Gamma}_{max} = 0.0193$.

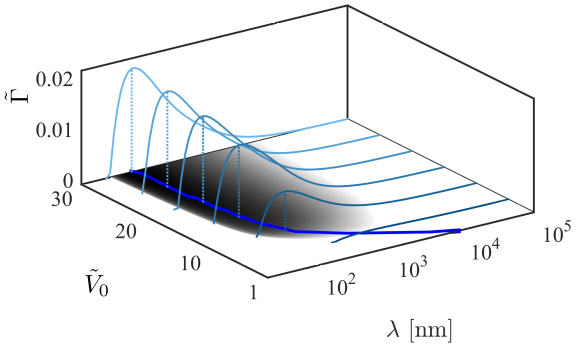

Figure 7.4: The growth rate $\tilde{\Gamma}$ plotted versus the perturbation wavelength λ and voltage $\tilde{V}_0$ for $c_0 = 10$ mM, and $L = 10$ µm. The cyan space curves are plots of $\tilde{\Gamma}$ versus λ for $\tilde{V}_0 = \{5, 10, 15, 20, 25, 30\}$. The shade of the in plane contour plot is based on the logarithm of $\tilde{\Gamma}$, which is why there are no contours in the low λ limit where $\tilde{\Gamma}$ is negative. The thick blue in plane line marks the crest of the hill, i.e. it marks the most unstable wavelength for each value of $\tilde{V}_0$.

values. In each contour plot, $\tilde{\Gamma}$ is normalized by its maximum value, which is given above each plot. Shown in thick lines are λ_{max} in yellow and λ_c in black. The corresponding analytical results are shown in dashed blue and dotted green lines, respectively. The thin black lines show contours, where $\tilde{\Gamma}$ equals $\{0.01, 0.2, 0.7\}$ times the maximum value. There is a clear tendency in all of the panels that the growth rate $\tilde{\Gamma}$ increases rapidly with $\tilde{V}_0$, and the most unstable wavelength decreases as $\tilde{V}_0$ increases. Across the panels, the maximum growth rate is seen to increase for increasing c_0 and increasing L. Also, the most unstable wavelength λ_{max} and the critical wavelength λ_c become smaller as c_0 increases and as L decreases.

A common feature seen in all of the panels, is the kink in the $\tilde{V}_0$-versus-λ_{max} and $\tilde{V}_0$-versus-λ_c lines. At this kink, the slope of the lines changes markedly. The kink is located at the voltage, where the current reaches the limiting current, and it thus signifies that there is a qualitatively different behavior for over- and underlimiting current. This qualitative difference between the two regimes is in accordance with the analytical models. We also see that the kink voltage changes with c_0 and L. Specifically, it increases with c_0 and decreases with L. The main reason for this behavior is easily understood with reference to the zeroth-order Butler-Volmer reaction expression (7.17b). Setting the current in the system to the limiting current $\tilde{J}^0 = 1$, the reaction rates at the electrodes become

$$\boldsymbol{e}_x \cdot \boldsymbol{n}_p = -K_0 \left[\tilde{c}_+^0 e^{\alpha_c Z(\tilde{\phi}^0 + \tilde{V}_p)} - e^{-\alpha_a Z(\tilde{\phi}^0 + \tilde{V}_p)} \right]. \tag{7.56}$$

At the cathode, the first term in the bracket dominates, and at the anode the other.

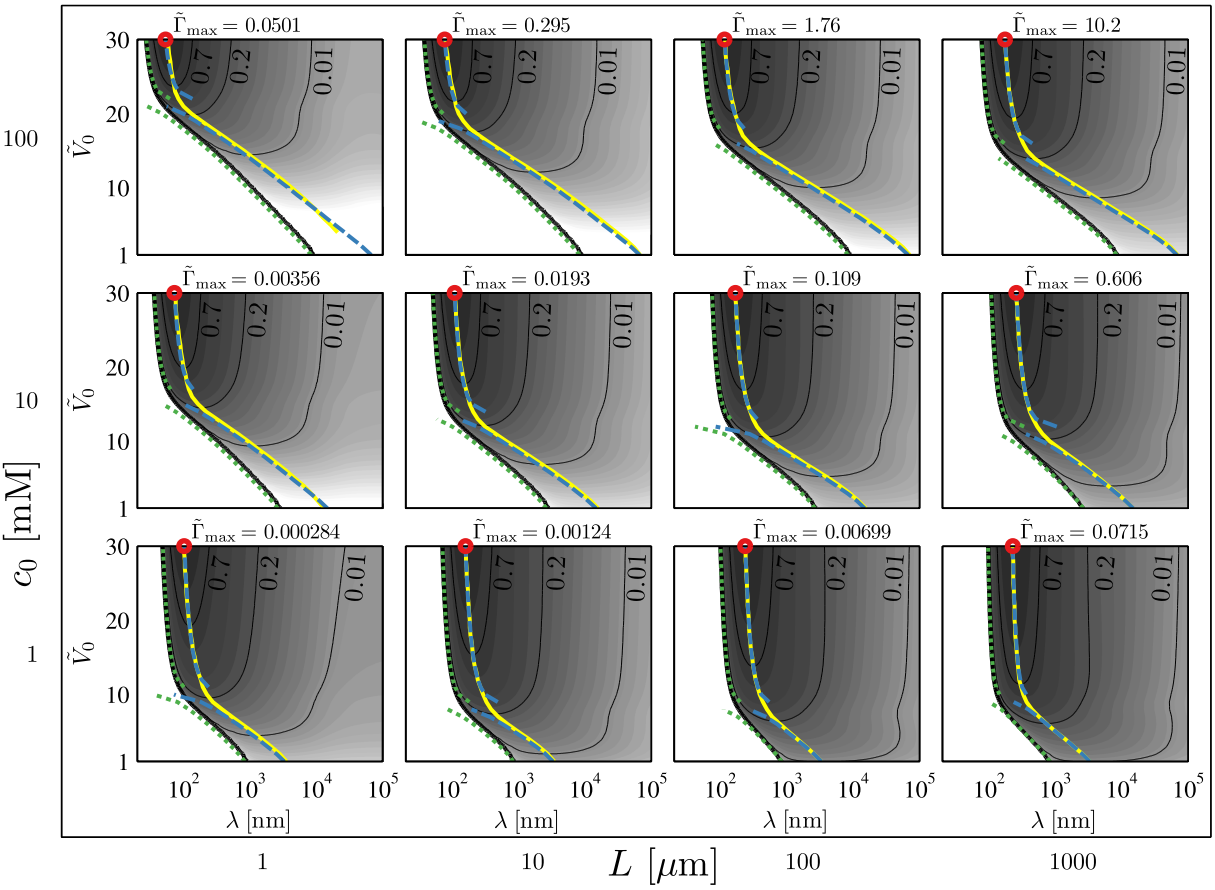

Figure 7.5: Contour plots of $\tilde{\Gamma}$ plotted versus wavelength λ and voltage $\tilde{V}_0$ for $c_0 = \{1\text{ mM}, 10\text{ mM}, 100\text{ mM}\}$ and $L = \{1\text{ µm}, 10\text{ µm}, 100\text{ µm}, 1\text{ mm}\}$. In each plot, $\tilde{\Gamma}$ is normalized by its maximum value, and the contours are logarithmically spaced. The maximum value $\tilde{\Gamma}_{max}$ of $\tilde{\Gamma}$ is given on top of each plot, and the point where the maximum value is attained is indicated with a red circle. The three thin black lines in each plot indicate contours where $\tilde{\Gamma}$ equals 0.01, 0.2, and 0.7 times $\tilde{\Gamma}_{max}$. The thick yellow line marks λ_{max} for each value of $\tilde{V}_0$, and the dashed blue lines mark the two corresponding analytical limits. The thick black line marks λ_c for each value of $\tilde{V}_0$, and the dotted green lines mark the two corresponding analytical limits.

Therefore, both potential drops over the electrode interfaces scale as

$$\Delta\tilde{V} \sim -\ln(K_0) = \ln\left(\frac{2D_+c_0}{k_0 L}\right), \tag{7.57}$$

which increases monotonically with increasing c_0/L. As a consequence, the total potential drop at the limiting current also increases with increasing c_0/L, just as observed in Fig. 7.5.

In addition to the instability growth rate $\tilde{\Gamma}$, which gives a time scale for the development of instabilities, it is useful to have a measure for the characteristic instability length scale. For instance, we would like to estimate the thickness of the deposited layer, when instabilities start to develop. We define this instability length scale as the product of the zeroth-order growth rate Eq. (7.20) and the instability time scale at the most unstable

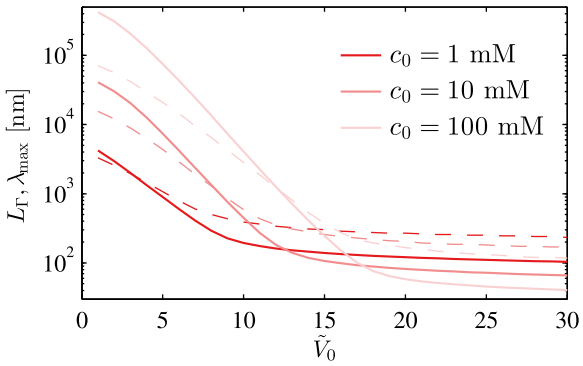

Figure 7.6: The instability length scale L_Γ (full line) and most unstable wavelength $\lambda_{\max}$ (dashed line) plotted versus bias voltage $\tilde{V}_0$. The concentration varies between the values $c_0 = \{1\text{ mM}, 10\text{ mM}, 100\text{ mM}\}$ and the length $L = 100$ µm was used.

wavelength

$$L_\Gamma = L\frac{a^3 c_0 \tilde{J}_+^0}{\tilde{\Gamma}_{\max}}, \tag{7.58}$$

where the pre-factor L ensures a dimensionfull expression. In Fig. 7.6, we plot the instability length L_Γ versus applied voltage $\tilde{V}_0$ for $L = 100$ µm and varying c_0. The most unstable wavelength $\lambda_{\max}$ is also plotted in the same figure (dashed lines). It is seen that L_Γ decreases as $\tilde{V}_0$ increases, but for small voltages L_Γ is largest for high concentrations, while the opposite is true for high voltages. The reason for this reversal is that the interfacial voltage drops are largest for large c_0. At small voltages the bulk driving force in the systems with large c_0 is therefore small, and this causes the system to be less unstable than the low c_0 systems. We also see that $\lambda_{\max}$ scales in the same way as L_Γ. While the reason for this is not immediately obvious, it is seen to follow from the analytical expressions. Inserting Eq. (7.48) in Eq. (7.58) yields

$$L_\Gamma = \frac{\lambda_{\max}}{2\pi}\frac{\beta + \frac{2\pi L}{\lambda_{\max}}}{\beta - \bar{\gamma}\left(\frac{2\pi L}{\lambda_{\max}}\right)^2}, \tag{7.59}$$

which confirms the approximate scaling between L_Γ and $\lambda_{\max}$. The connection between L_Γ and $\lambda_{\max}$ implies that $\lambda_{\max}$ sets the scale, not only for the variations in the horizontal direction, but also for variations in the vertical direction. We might therefore expect that the ramified electrodeposits, emerging at much longer times than $\tilde{\Gamma}_{\max}^{-1}$, have a universal length scale roughly set by $\lambda_{\max}$.

7.7 Conclusion

The main feature which distinguishes our stability analysis form previous stability analyses is the inclusion of the overlimiting regime [115, 43, 29]. As shown in Refs. [39, 45] the overlimiting regime is highly relevant for ramified growth, so the inclusion of this regime

is a significant extension of the previous studies. Indeed, as seen in Fig. 7.5, the instability growth rate is markedly increased in the overlimiting regime, as compared to the underlimiting regime.

An important motivation for the present study is that it provides a means of validating the behavior of more elaborate numerical models in the initial stages of the growth. In Chapter 8 we make such a validation of the sharp-interface model employed in that chapter.

In the numerical model we employ the widely used Butler–Volmer model with equal cathodic and anodic charge-transfer coefficients. The analytical model is, however, not restricted to this particular reaction model. In deriving the analytical results we only required that the charge-transfer coefficients vary slowly with the interfacial potential drop and the cation concentration. Thus, we expect the analytical model to apply equally well to Marcus kinetics and Butler–Volmer kinetics with asymmetric charge-transfer coefficients. Also, the effects of an electric double layer can be included implicitly by applying the Frumkin correction.

Chapter 8

Sharp-interface model of electrodeposition

In this chapter we present a sharp-interface model of two-dimensional ramified growth during quasi-steady electrodeposition. The development of this new model of electrodeposition is motivated by the shortcomings of the established phase-field models, namely their failure to take charge densities into account and to properly implement nonlinear electrode reactions [41, 42, 106, 68, 67, 17, 31]. Originally, our interest in the electrodeposition problem was motivated by the work of Han and Bazant on electrodeposition in charged porous media [45, 44]. In these systems, the space-charge density is an indispensable part of the relevant physics, even at underlimiting currents. This very much served to highlight the inadequacies of the conventional electroneutral models, and prompted us to search for alternate modeling approaches.

The presented sharp-interface model relies on two basic assumptions. Firstly, like most previous models, we only model the electrode growth in two dimensions. This is consistent with some experiments in which ramified growth is confined to a single plane and is effectually two dimensional [122, 33, 66, 65]. However, for most systems the growth occurs in all three dimensions. There will obviously be some discrepancy between our 2D results and the 3D reality, but we are hopeful that our 2D model does in fact capture much of the essential behavior. Secondly, the sharp-interface model is only applicable once the initial transients in the concentration distribution have died out. In its current form the model is therefore mainly suitable for small systems, in which the diffusive time scale is reasonably small.

This chapter is based on material from our paper Ref. [85], which can be found in Appendix H.

8.1 Model system

The model system consists of two initially flat parallel metal electrodes of width W placed a distance of $2L$ apart. In the space between the electrodes is a binary symmetric electrolyte of concentration c_0, in which the cation is identical to the electrode material. The electrodes

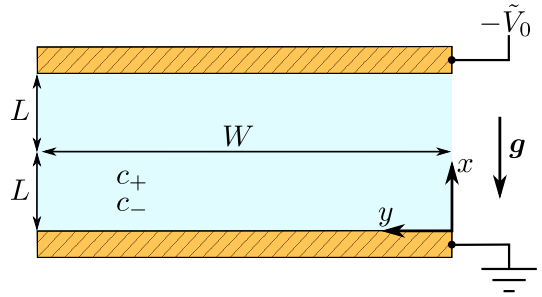

Figure 8.1: Sketch of the initial geometry of the system. Two co-planar metal electrodes of width W are placed a distance of $2L$ apart. The gap between them is filled by an electrolyte with cation concentration c_+ and anion concentration c_-. A voltage difference of $\tilde{V}_0$ is applied between the electrodes.

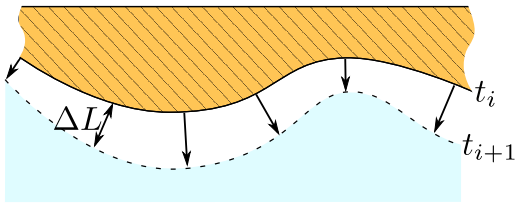

Figure 8.2: Sketch of the electrode growth. The electrode surface at time t_i is indicated with a full line. In the time step $t_{i+1}-t_i$ an amount of material ΔL, which may vary with position, is deposited on the electrode. On basis of the deposited material the geometry at time t_{i+1} is created (indicated with a dashed line).

can thus act as both sources and sinks for the cation, whereas the anion can neither enter nor leave the system. A voltage difference $\tilde{V}_0$ is applied between the two electrodes, driving cations towards the top electrode and anions toward the bottom electrode. A sketch of the system is shown in Fig. 8.1.

By depositing onto the top electrode we ensure that the ion concentration increases from top to bottom, so we do not have to take the possibility of gravitational convection into account. To limit the complexity of the treatment, we also disregard any electro-osmotic motion, which may arise in the system. We note, however, that the sharp-interface model would be well suited to investigate the effects of electro-osmosis, since the space charge density is an integral part of the model.

8.2 Solution method

The basic idea in our solution method is to solve the transport-reaction problem for each time step, and then use the calculated currents to find the amount of material deposited at each point on the electrode. Based on this deposition rate the geometry is updated, and the transport-reaction problem is solved for a new time step, as illustrated in Fig. 8.2.

The major difficulty in employing this method is that when the geometry is updated the computational domain is also remeshed, so there is no straight-forward way of continuing from the old solution of the transport-reaction problem. One way of getting around this issue is to separate the time scales in the problem. More to the point, we assume that the growth of the electrode happens so slowly, compared to the transport time scales, that the transport problem always is in quasi steady-state. By treating the transport-reaction problem as being in steady state in each time step, a solution can be computed without reference to solutions at previous time steps.

Obviously, the quasi steady-state assumption is flawed in the initial time after a voltage is applied to the system, as the application of a voltage gives rise to some transients in the transport problem. However, after the initial transients have died out the assumption is quite reasonable, except for the case of very concentrated electrolytes. To see that, we consider the thickness ΔL of the electrode growth in a time interval Δt,

$$\Delta L = a^3 \Delta t J_+, \tag{8.1}$$

where a^3 is the volume of a metal atom in the solid phase and J_+ is the current density of metal ions entering the electrode. The current density is on the order of the limiting current $2c_0 D_+/L$, so the time scale associated with an electrode growth of ΔL is

$$\Delta t = \frac{\Delta L}{a^3 J_+} \sim \frac{L \Delta L}{2 D_+ c_0 a^3}. \tag{8.2}$$

On the other hand, the transport time scale $t_{\text{diff}}^{\Delta L}$ associated with the distance ΔL is

$$t_{\text{diff}}^{\Delta L} \sim \frac{\Delta L^2}{2 D_+}. \tag{8.3}$$

The ratio of the transport time scale to the growth time scale is thus

$$\frac{t_{\text{diff}}^{\Delta L}}{\Delta t} \sim \frac{\Delta L}{L} c_0 a^3, \tag{8.4}$$

which is indeed very much smaller than unity.

As mentioned above, our model does not apply to the initial time after the voltage is applied. To estimate how this impacts our results, we make a comparison of the important time scales. The time it takes for the transients to die out is given by the diffusion time,

$$t_{\text{diff}}^{L} = \frac{L^2}{2 D_+}. \tag{8.5}$$

We define an instability time scale t_{inst}, in terms of the growth rate $\Gamma_{\max}$ of the most unstable harmonic perturbation to the electrode surface,

$$t_{\text{inst}} \sim \frac{1}{\Gamma_{\max}}. \tag{8.6}$$

It is apparent that if

$$t_{\text{diff}}^{L} \lesssim t_{\text{inst}}, \tag{8.7}$$

then nothing interesting happens to the electrode surface in the time it takes the transients to disappear. In this case our quasi-steady approach is therefore justified.

Even if $t_{\text{diff}}^{L} \gg t_{\text{inst}}$ our approach may be justified. If the total deposition time is much larger than t_{diff}^{L}, then what happens in the time before the transients die out is largely unimportant for the growth patterns observed in the end. Thus, though the quasi-steady assumption seems restrictive, it actually allows us to treat a fairly broad range of systems.

8.3 Governing equations

Unlike in the previous chapters we retain the dimensional form of the governing equations, and only nondimensionalize a few select fields. The ion-transport is determined by the usual Nernst–Planck equations,

$$\boldsymbol{J}_\pm = -D_\pm c_0 \tilde{c}_\pm \boldsymbol{\nabla} \tilde{\mu}_\pm, \tag{8.8a}$$

$$\mu_\pm = \ln(\tilde{c}_\pm) \pm Z\tilde{\phi}, \tag{8.8b}$$

$$0 = -\boldsymbol{\nabla} \cdot \boldsymbol{J}_\pm. \tag{8.8c}$$

The electrostatic part of the problem is governed by the Poisson equation,

$$2\lambda_\mathrm{D}^2 \nabla^2 \tilde{\phi} = -\tilde{\rho}_\mathrm{el} = -Z\tilde{c}_+ + Z\tilde{c}_-, \tag{8.9}$$

At the electrodes the anion flux vanishes,

$$\boldsymbol{n} \cdot \boldsymbol{J}_- = 0, \tag{8.10}$$

and the cation flux is given by a reaction expression

$$\boldsymbol{n} \cdot \boldsymbol{J}_+ = -R. \tag{8.11}$$

Rather than explicitly modeling the quasi-equilibrium electric double layers at the electrodes, we employ the GCP framework from Section 2.7, and implement a condition of vanishing cation gradient at the cathode,

$$\boldsymbol{n} \cdot \boldsymbol{\nabla} \tilde{c}_+ = 0. \tag{8.12}$$

The last degree of freedom is removed by requiring global conservation of anions,

$$\int_\Omega \left(\tilde{c}_- - 1\right) \mathrm{d}V = 0. \tag{8.13}$$

In dimensional form the reaction rate from the previous chapter is

$$R = k_0 \left[\tilde{c}_+ e^{-\bar{\gamma}^* \kappa + \alpha_\mathrm{c} Z(\tilde{\phi} + \tilde{V})} - e^{-\bar{\gamma}^* \kappa - \alpha_\mathrm{a} Z(\tilde{\phi} + \tilde{V})}\right], \tag{8.14}$$

where we assume constant charge-transfer coefficients. The definition of $\bar{\gamma}^*$ used in Eq. (8.14) differs slightly from the definition of $\bar{\gamma}$ encountered in the previous chapter,

$$\bar{\gamma}^* = \frac{a^3 \gamma}{k_\mathrm{B} T}. \tag{8.15}$$

The sharp-interface reaction expression (8.14) is one of the features which sets our model apart from previous modeling approaches. In Appendix B we give a brief overview of the relation between sharp-interface reaction expressions like Eq. (8.14), and the nonlinear reaction expressions employed in phase-field models like Refs. [68, 67, 17, 31].

8.4 Numerical stability

Due to the surface energy term in the reaction expression, the surface is prone to numerical instability. In an attempt to reach the energetically favorable surface shape, the solver will sequentially overshoot and undershoot the correct solution. The fundamental issue we are facing is that the problem at hand is numerically stiff. As long as we are using an explicit time-integration method we are therefore likely to encounter numerical instabilities.

8.4.1 Updating the interface position

The straight-forward way of updating the position $\boldsymbol{r}$ of the interface is to use the explicit Euler method,

$$\boldsymbol{r}(t + \Delta t) = \boldsymbol{r}(t) + \boldsymbol{n}a^3 \Delta t R(t), \tag{8.16}$$

where $R(t)$ is the (position dependent) reaction rate at time t. To avoid numerical instabilities, we should instead use the implicit Euler method,

$$\boldsymbol{r}(t + \Delta t) = \boldsymbol{r}(t) + \boldsymbol{n}a^3 \Delta t R(t + \Delta t), \tag{8.17}$$

where the reaction rate is evaluated at the endpoint instead of at the initial point. This is however easier said than done. $R(t + \Delta t)$ depends on $\boldsymbol{r}(t + \Delta t)$ as well as on the concentration and potential distribution at $t + \Delta t$. Even worse, through the curvature $R(t + \Delta t)$ also depends on the spatial derivatives of $\boldsymbol{r}(t + \Delta t)$.

The way forward is to exploit that only part of the physics give rise to numerical instabilities. It is therefore sufficient to evaluate the problematic surface energy at $t + \Delta t$ and evaluate the remaining terms at t. For our purposes we can therefore make the approximation

$$R(t + \Delta t) \approx R\big(t, \kappa(t + \Delta t)\big), \tag{8.18}$$

where κ is the curvature. This does still make for a quite complicated nonlinear PDE, but we are getting closer to something tractable. The difference in curvature between t and $t + \Delta t$ is small (otherwise we are taking too big time steps), so we can approximate

$$R\big(t, \kappa(t + \Delta t)\big) \approx R\big(t, \kappa(t)\big) + R'\big(t, \kappa(t)\big)\Delta\kappa, \tag{8.19}$$

where R' denotes R differentiated with respect to κ and $\Delta\kappa = \kappa(t + \Delta t) - \kappa(t)$. The curvature can be written as

$$\kappa = \frac{\partial \theta}{\partial s}, \tag{8.20}$$

where θ is the tangential angle of the interface and s is the arc length along the interface. We therefore have

$$\Delta\kappa = \kappa(t + \Delta t) - \kappa(t) = \frac{\partial \theta_2}{\partial s_2} - \frac{\partial \theta_1}{\partial s_1}, \tag{8.21}$$

where we have adopted the shorthand notation 1 and 2 for time t and $t+\Delta t$, respectively. The arc lengths s_1 and s_2 will obviously differ for any nonzero displacement, but this is a small effect compared to the angle difference. As an approximation we therefore use $s_2 \approx s_1$ and obtain

$$\Delta\kappa \approx \frac{\partial(\theta_2 - \theta_1)}{\partial s_1}. \tag{8.22}$$

The tangential angle is a function of the surface parametrization,

$$\tan(\theta_1) = \frac{\partial y_1}{\partial x_1}. \tag{8.23}$$

For small displacements we can approximate

$$\tan(\theta_2) = \frac{\partial y_2}{\partial x_2} = \frac{\partial(y_1 + \Delta y)}{\partial(x_1 + \Delta x)} \approx \tan(\theta_1) + \frac{\partial \Delta y}{\partial x_1} - \tan(\theta_1)\frac{\partial \Delta x}{\partial x_1}. \tag{8.24}$$

The difference in tangential angles can then be written

$$\begin{aligned} \theta_2 - \theta_1 &= \arctan\left[\tan(\theta_1) + \frac{\partial \Delta y}{\partial x_1} - \tan(\theta_1)\frac{\partial \Delta x}{\partial x_1}\right] - \theta_1 \\ &\approx \frac{1}{1+\tan^2(\theta_1)}\left[\frac{\partial \Delta y}{\partial x_1} - \tan(\theta_1)\frac{\partial \Delta x}{\partial x_1}\right]. \end{aligned} \tag{8.25}$$

Returning to the implicit Euler method Eq. (8.17), we project it onto the normal vector to obtain

$$\Delta L = a^3 \Delta t R(t+\Delta t) \approx a^3 \Delta t \left[R\big(t,\kappa(t)\big) + R'\big(t,\kappa(t)\big)\Delta\kappa\right], \tag{8.26}$$

where $\Delta L = \boldsymbol{n} \cdot \big[\boldsymbol{r}(t+\Delta t) - \boldsymbol{r}(t)\big]$. The increments in the x and y directions are related to ΔL via

$$\Delta x = n_x \Delta L, \quad \Delta y = n_y \Delta L. \tag{8.27}$$

Inserting these in Eq. (8.25) and writing out the curvature difference $\Delta\kappa$, we obtain a linear PDE for the displacement ΔL

$$\frac{\Delta L - a^3 \Delta t R\big(t,\kappa(t)\big)}{a^3 \Delta t R'\big(t,\kappa(t)\big)} = \Delta\kappa = \frac{\partial}{\partial s_1}\left\{\frac{n_y - n_x \tan(\theta_1)}{1+\tan^2(\theta_1)}\frac{\partial \Delta L}{\partial x_1}\right\}. \tag{8.28}$$

In the limit $\Delta\kappa = 0$ this equation reduces to the original forward Euler method (8.16).

8.4.2 Correction for the curvature

In the previous derivation, we did not take into account that the local curvature slightly changes the relation between amount of deposited material and surface displacement ΔL. The deposited area in an angle segment $d\theta$ can be calculated as

$$dA = \frac{d\theta}{2\pi}\left[\pi\left(\frac{1}{\kappa} + \Delta L\right)^2 - \pi\frac{1}{\kappa^2}\right] = \frac{d\theta}{2}\left[\Delta L^2 + 2\frac{\Delta L}{\kappa}\right]. \tag{8.29}$$

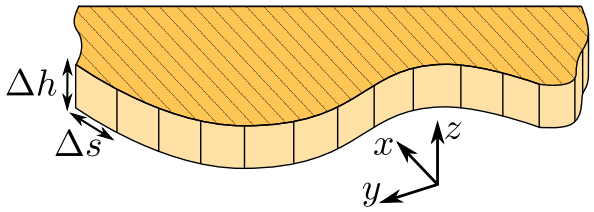

Figure 8.3: Three-dimensional extension of our two-dimensional model. The electrode interface can vary in the xy-plane according to the calculated ion-currents, but it has a fixed depth Δh in the z-direction. The interface is also divided into a number of bins of width Δs in the xy-plane. Each bin thus has the area $\Delta h \Delta s$.

The line segment ds is related to the angle segment as $ds = d\theta/\kappa$. This means that

$$a^3 \Delta t R(t + \Delta t) = \frac{dA}{ds} = \frac{\kappa}{2}\left[\Delta L^2 + 2\frac{\Delta L}{\kappa}\right] = \Delta L + \frac{\kappa}{2}\Delta L^2. \tag{8.30}$$

Using this expression in Eq. (8.26) yields the slightly nonlinear PDE, with the term $\frac{1}{2}\kappa\Delta L^2$,

$$\frac{\Delta L + \frac{\kappa}{2}\Delta L^2 - a^3 \Delta t R\big(t, \kappa(t)\big)}{a^3 \Delta t R'\big(t, \kappa(t)\big)} = \frac{\partial}{\partial s_1}\left\{\frac{n_y - n_x \tan(\theta_1)}{1 + \tan^2(\theta_1)}\frac{\partial \Delta L}{\partial x_1}\right\}, \tag{8.31}$$

in place of Eq. (8.28).

8.5 Noise

An important part of the problem is the noise in the system, since the noise is what triggers the morphological instability and leads to formation of dendrites. Exactly how the noise should be defined is however a matter of some uncertainty. Most previous work uses a thermal white noise term with a small, but seemingly arbitrary amplitude. In this work we use a slightly different approach, in which we assume that the noise is entirely attributed to shot noise.

As it turns out, this approach requires us to be more specific about how our 2D model is related to the three-dimensional reality. In Fig. 8.3 a sketch of the tree-dimensional electrode is shown. The electrode interface is free to vary in the xy-plane, but has a fixed depth Δh in the z-direction. Obviously, most real electrodeposits will have a more complicated behavior in the z-direction, but for electrodeposits grown in a planar confined geometry this is actually a reasonable description.

Solving the transport-reaction problem yields the current density at each point along the electrode surface, that is the average number of ions arriving per surface area per time. The mean number Q of ions arriving in an electrode section of size $\Delta h \Delta s$ in a time interval Δt is thus

$$Q = J_+ \Delta h \Delta s \Delta t. \tag{8.32}$$

Since the ions are discrete entities, the actual number of arriving ions will, however, fluctuate randomly around the mean Q with some spread σ. We assume that within the time

interval Δt, the arrival of each ion is statistically uncorrelated with the arrival of each other ion. It can then be shown that, as long as $Q \gtrsim 10$, the number of arriving ions follow a normal distribution with mean Q and standard deviation

$$\sigma = \sqrt{Q}. \tag{8.33}$$

This corresponds to an extra random current density

$$J_{\text{rand}} = \frac{\sqrt{Q}}{\Delta h \Delta s \Delta t} q_{\text{rand}} = \sqrt{\frac{J_+}{\Delta h \Delta s \Delta t}} q_{\text{rand}}, \tag{8.34}$$

where q_{rand} is a random number taken from a normal distribution with mean 0 and standard deviation 1. This in turn corresponds to a random electrode growth of

$$\Delta L_{\text{rand}} = a^3 \sqrt{\frac{J_+ \Delta t}{\Delta h \Delta s}} q_{\text{rand}}. \tag{8.35}$$

Now, there is something slightly weird about this expression for the random growth: it seems that the random growth becomes larger the smaller the bin size Δs is. However, as the bin size becomes smaller the weight of that bin in the overall behavior is also reduced. The net effect is that the bin size Δs does not matter for the random growth, see Appendix C for a more thorough treatment.

The bin depth Δh, on the other hand, does matter for the random growth. Since our model is not concerned with what happens in the z-direction, we simply have to choose a physically reasonable value of Δh, and accept that our choice will have some impact on the simulations. This is a price we pay for applying a 2D model to a 3D phenomenon.

8.6 Numerical solution

Following Chapter 3, the governing equations and boundary conditions Eqs. (8.8a), (8.8b), (8.8c), (8.9), (8.10), (8.11), (8.12), (8.13), (8.14), and (8.31) are rewritten in weak form and implemented in the mathematics module of COMSOL. For each time step the following steps are carried out: First, a list of points defining the current electrode surface is loaded into COMSOL, and the surface is created using a cubic spline interpolation between the given points. The computational domain is meshed using a mesh size of Δs at the electrode surface, a mesh size of l in a small region next to the electrode, and a much coarser mesh in the remainder of the domain. Next, the curvature of the surface is calculated at each point. The solution from the previous time step is then interpolated onto the new grid, to provide a good initial guess for the transport-reaction problem. Then the transport-reaction problem is solved. Based on the solution to the transport-reaction problem the electrode growth ΔL is calculated by solving Eq. (8.31) on the electrode boundary. At each mesh point a small random contribution $\Delta L_{\text{rand}} = a^3 \Delta t J_{\text{rand}}$ is then added to ΔL. Finally, the new x and y positions are calculated by adding $n_x(\Delta L + \Delta L_{\text{rand}})$ and $n_y(\Delta L + \Delta L_{\text{rand}})$ to the old x and y positions.

The new x and y positions are exported to MATLAB. In MATLAB any inconsistencies arising from the electrode growth are resolved. If, for instance, the electrode surface

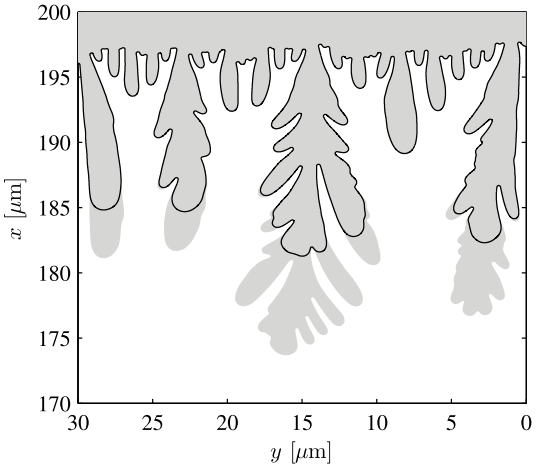

Figure 8.4: Electrode interface at two different time steps for $c_0 = 1$ mM and $V_0 = 10$. In this simulation no part of the domain was rendered passive at any time. The gray area indicates the electrode after 30 hours and 22 minutes, and the black lines indicates the electrode interface after 24 hours and 2 minutes. In the upper part of the domain the electrode interface is virtually unchanged between the two times.

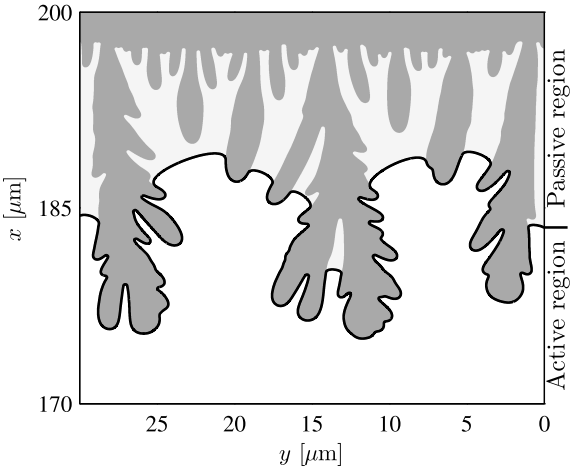

Figure 8.5: Division of the computational domain into a passive and an active region. The reduced interface (thick black line) divides the domain into an active region (white) and a passive region (light gray). The dark gray area shows the real cathode. The example is taken from a simulation with $c_0 = 1$ mM and $\tilde{V}_0 = 10$ after deposition for 31 hours and 28 minutes.

intersects on itself, the points closest to each other at the intersection position are merged and any intermediate points are discarded. This corresponds to creating a hollow region in the electrode which is no longer in contact with the remaining electrolyte. The points are then interpolated so that they are evenly spaced, and exported to COMSOL so that the entire procedure can be repeated for a new time step.

8.6.1 Reduction of the computational domain

At the cathode the mesh is much finer than in the remainder of the domain. The number of mesh points, and hence the computation time, therefore roughly scales with the length of the electrolyte-cathode interface. This has the unfortunate consequence that the computation time for each time step increases drastically, when branching structures emerge at the cathode. To lower the computation time we exploit the fact that the vast majority of the current enters near the tips of the dendritic structures. The parts of the cathode which are not near the tips can therefore be left fixed in time and thus removed from the simulation, without changing the results appreciably. This part of the domain is denoted the passive region. In regions where the current density is less than 0.001 times the maximum value, we thus substitute the real, ramified electrode with a smooth line connecting the parts of the electrode with larger currents. The procedure is carried out in such a way that the real electrode surface can always be recovered from the reduced surface. For a few select examples we have verified that the results are unchanged by this simplifying procedure. An example of this is shown in Fig. 8.4. Here, the electrode interface is plotted at two dif-

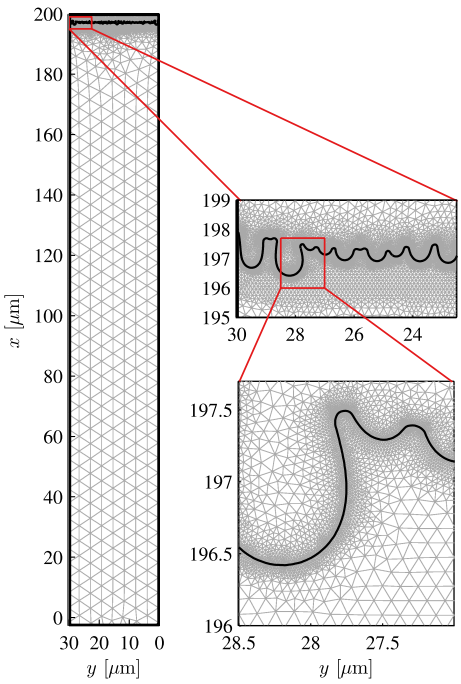

Figure 8.6: Example of domain meshing at varying magnification. The example is taken from a simulation with $c_0 = 1$ mM and $\tilde{V}_0 = 10$ after deposition for 7 hours and 50 minutes. The wiggly black line is the cathode surface. The light gray lines are the mesh boundaries and the red lines show the sections that are magnified. The mesh elements above the cathode surface are only used for storing the solution between time steps.

ferent time steps for $c_0 = 1$ mM and $\tilde{V}_0 = 10$. In the simulation no part of the domain was rendered passive. It is seen that a big part of the domain is virtually unchanged between the two times. It would therefore not have changed the results appreciably if part of the domain had been kept passive.

In Fig. 8.5 is shown an example electrode surface together with the reduced surface. It is seen that the length of the electrolyte-cathode interface is heavily reduced by excluding parts of the electrode from the computation.

8.6.2 Parameter values

Like in Chapter 7 we limit the parameter space by choosing fixed, physically reasonable values for the parameters listed in Table 7.1.

From the analysis in Chapter 7 we expect the critical wavelength to be the smallest feature in the problem, so we choose the mesh size accordingly. We set the mesh size at the electrode to $\Delta s = 0.1\lambda_c$, since our investigations, see Section 8.6.3, show that this is a suitable resolution. We also require that the mesh size does not exceed 0.1 times the local radius of curvature. In the bulk part of the system we use a relatively coarse triangular mesh with mesh size $W/6$. Close to the cathode, in a region $l = 0.5$ µm from the electrode surface, we use a triangular mesh with mesh size $l/4$. See Fig. 8.6 for a meshing example.

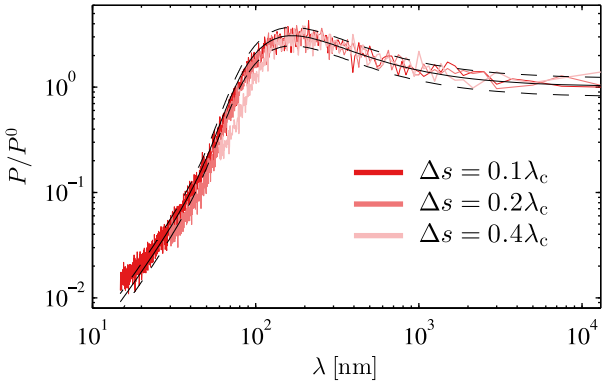

Figure 8.7: Power spectra averaged over 50 runs for three different mesh sizes, $\Delta s = \{0.1\lambda_c, 0.2\lambda_c, 0.4\lambda_c\}$. In each run we used $M = 100$ time steps of $\Delta t = 0.64$ s and the parameter values $c_0 = 10$ mM, $L = 100$ µm, and $\tilde{V}_0 = 30$. The full black line shows the analytical result and the dashed black lines show the analytical standard error on the mean. The result for $\Delta s = 0.1\lambda_c$ is shown in dark red, the result for $\Delta s = 0.2\lambda_c$ is shown in medium red, and the result for $\Delta s = 0.4\lambda_c$ is shown in bright red.

We choose a fixed value for the bin depth $\Delta h = 0.2\lambda_c$. In accordance with the analysis in Appendix C the time step Δt is chosen so that it is always smaller than $0.5/\Gamma_{max}$. In addition, the time step is chosen so that at each point on the cathode, the growth during the time step is smaller than the local radius of curvature.

We fix the length L to 100 µm. According to the time-scale analysis in Section 8.2 and the instability growth rates found in Chapter 7, the quasi-steady state approximation is valid for $L = 100$ µm. The width W of the system is set to $W = 200\lambda_c$, rounded to the nearest micrometer. This makes for a system that is broad enough to exhibit interesting growth patterns, while having a reasonable computation time. The growth is somewhat affected by the symmetry boundaries at $y = 0$ and $y = W$, especially at later times.

These choices leave us with two free parameters, which are the bias voltage $\tilde{V}_0$ and the electrolyte concentration c_0. We solve the system for $c_0 = \{1 \text{ mM}, 10 \text{ mM}, 100 \text{ mM}\}$ and $\tilde{V}_0 = \{10, 20, 30\}$.

8.6.3 Validation

The random nature of the phenomena we are investigating poses obvious challenges when it comes to validating the numerical simulations. The individual steps in the computation can be, and have been, thoroughly tested and validated, but testing whether the aggregate behavior after many time steps is correct is a much taller order. At some level, we simply have to trust that, if the individual steps are working correctly, then the aggregate behavior is also correct. To support this view, there is one test we can make of the aggregate behavior in the very earliest part of the simulation.

In the early stages of the simulation the electrode surface is deformed so little, that the linear stability analysis from Chapter 7 should still be valid. We thus have an analytical expression for the wavelength dependent growth rate Γ, which we can compare with the growth rates found in the numerical simulations. In Appendix C we calculate an expression

for the average power spectrum of the cathode interface after deposition for a time t_{tot}, given the type of noise described in Section 8.5,

$$\langle P_n \rangle = a^6 \frac{J_+}{2\Delta h W \Gamma_n} \left[e^{2\Gamma_n t_{\text{tot}}} - 1 \right], \tag{8.36}$$

where Γ_n is the growth rate of the n'th wavelength $\lambda_n = W/n$ component in the noise spectrum. We also find the standard deviation $\text{SD}(P_n)$ of the power spectrum

$$\text{SD}(P_n) \approx \sqrt{2} \langle P_n \rangle. \tag{8.37}$$

Because the standard deviation of P_n is so large compared to the mean value, it is necessary to average over many runs before a meaningful comparison with Eq. (8.36) can be made. Averaging the power spectrum over 50 simulations brings the standard error on the mean down to 20 percent times the mean value, at which point a reasonable comparison can be made. In Fig. 8.7 the power spectrum averaged over 50 runs is shown for three different mesh sizes, $\Delta s = \{0.1\lambda_c, 0.2\lambda_c, 0.4\lambda_c\}$. In each run we used $M = 100$ time steps of $\Delta t = 0.64$ s and the parameter values $c_0 = 10$ mM, $L = 100$ µm, and $\tilde{V}_0 = 30$. The chosen step size corresponds to $0.01/\Gamma_{\text{max}}$. The analytical result (8.36) is also shown together with the standard error on the mean. The power spectra are normalized with the power P^0 obtained for $\Gamma = 0$,

$$P^0 = a^6 \frac{J_+ t_{\text{tot}}}{\Delta h W}. \tag{8.38}$$

It is seen that for $\Delta s = 0.4\lambda_c$ some of the power in the small wavelength components is filtered out. As the mesh size is decreased to $\Delta s = 0.2\lambda_c$ and $\Delta s = 0.1\lambda_c$ the low wavelength components are represented increasingly well.

In the above treatment, the time step was chosen very small compared to the instability time scale, $\Delta t = 0.01/\Gamma_{\text{max}}$. This was done to approach the limit of continuous time, and thus enable the best possible comparison with the analytical theory. Such a short time step is, however, impractical for the much longer simulations in the remainder of the paper. In those simulations we use time steps as large as $\Delta t = 0.5/\Gamma_{\text{max}}$. Due to the coarser time resolution employed in the remaining simulations, we expect their power spectrum to deviate somewhat from the almost ideal behavior seen in Fig. 8.7.

8.7 Results

We let the simulations run until the cathode has grown 25 µm. The time t_0 it takes to reach this point varies greatly with the parameters, mainly because the limiting current scales with c_0. In Fig. 8.8 the cathode surfaces are shown along with heat plots showing the relative magnitude of the current density at the last time step. The white line shows the position of the reduced interface at the last time step, and the gray area shows the actual position and shape of the cathode. The gray electrodeposits have different shades corresponding to $0.25t_0$, $0.5t_0$, $0.75t_0$, and t_0. The heat plot shows the value of J_+^{norm},

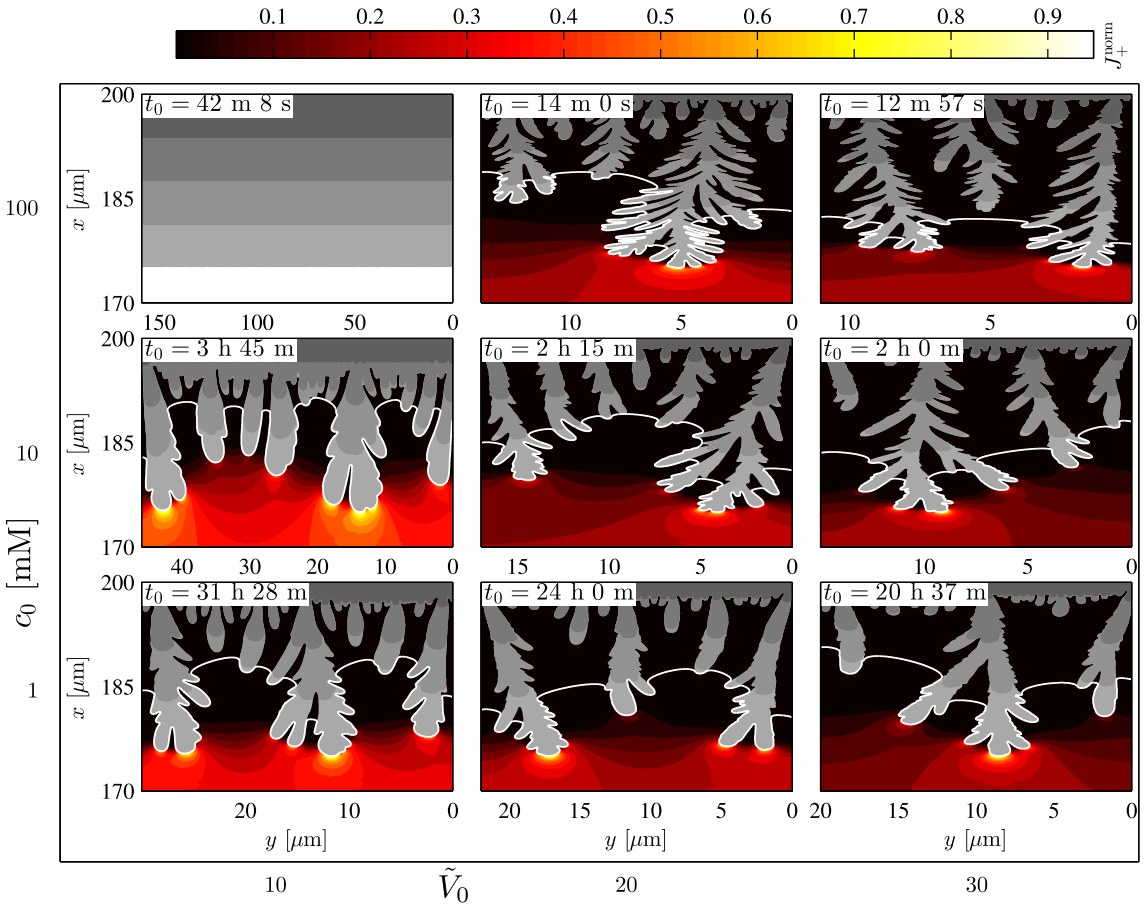

Figure 8.8: Electrodeposits in the $\tilde{V}_0$-c_0 plane obtained for $L = 100$ µm, $c_0 = \{1\text{ mM}, 10\text{ mM}, 100\text{ mM}\}$ and $\tilde{V}_0 = \{10, 20, 30\}$. The aspect ratio varies between the panels, since the width W of the simulated region is always set to $200\lambda_c$. The gray area has different shades corresponding to times t_0 (light), $0.75t_0$ (darker), $0.5t_0$ (darker yet), $0.25t_0$ (darkest). The white line indicates the reduced surface at time t_0. The contours in the liquid represent the relative magnitude of the cation current.

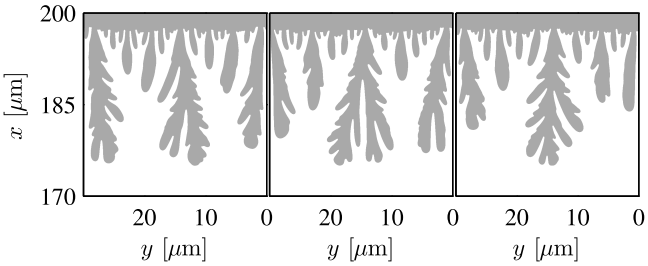

Figure 8.9: Three simulations of electrodeposits using the same parameter values $L = 100$ µm, $c_0 = 1$ mM, and $\tilde{V}_0 = 10$. The electrodeposits are clearly different from one another, but they do share some general features.

which is the magnitude of the cation current density normalized with its maximum value.

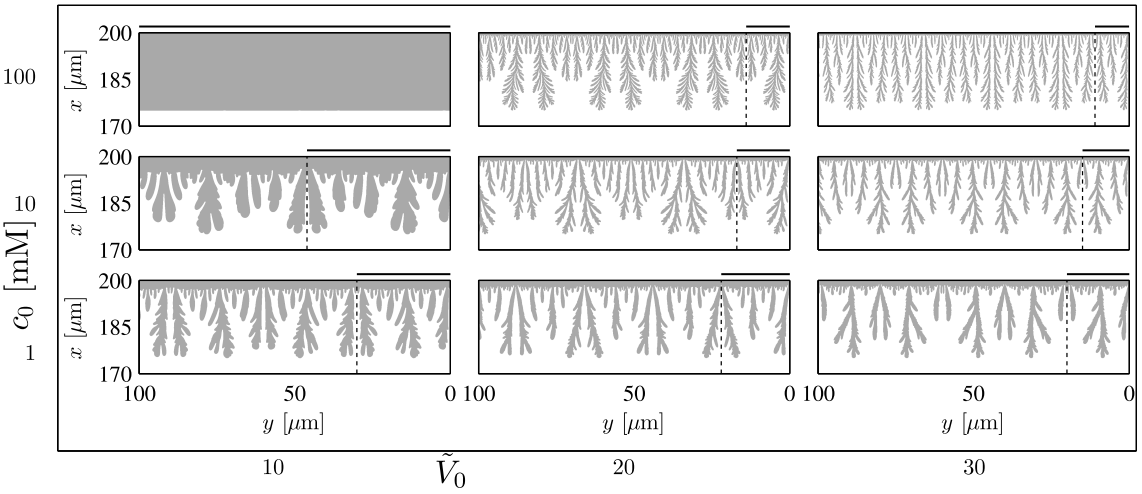

Figure 8.10: Extended electrodeposits in the $\tilde{V}_0$-c_0 plane obtained by mirroring those from Fig. 8.8 in their symmetry axes until the width equals 100 µm. The dashed line indicates the first mirror plane, i.e. the part between the dashed line and $y = 100$ µm are obtained by repeating the part marked by a black line. Here, in contrast to Fig. 8.8, the aspect ratio is constant across the panels.

In each panel J_+^{norm} thus varies from 0 to 1.

To investigate the reproducibility of the results we have repeated the simulation of the $c_0 = 1$ mM, $\tilde{V}_0 = 10$ system two times. All three electrodeposits are seen in Fig. 8.9. The electrodeposits are clearly different from one another, as expected for a random process, but they are also seen to share some general features. These shared features are most easily appreciated by comparing the electrodeposits in Fig. 8.9 to the electrodeposits in Fig. 8.8. It is seen that the electrodeposits in Fig. 8.9 are much more similar to each other, than to any of the remaining electrodeposits in Fig. 8.8. Thus, the results are reproducible in the sense, that the random electrodeposits have some general features that are determined by the parameter values.

When interpreting the plots in Fig. 8.8, we should be mindful that the aspect ratio is not the same in each panel. The reason for this is that the vertical axis has the same length, 30 µm, in each panel, while the length of the horizontal axis, W, varies between panels. In Fig. 8.10 we show adapted versions of the panels from Fig. 8.8. The subfigures in Fig. 8.10 are created by repeatedly mirroring the subfigures from Fig. 8.8 until their horizontal length is 100 µm. Obviously, the resulting extended cathodes are somewhat artificial, since we have imposed some symmetries, which would not be present in a simulation of a system with $W = 100$ µm. Nevertheless, we find the subfigures in Fig. 8.10 useful, since they give a rough impression of the appearance of wider systems and allow for easier comparison of length scales between panels.

8.7.1 Rationalizing the cathode morphologies

The cathode morphologies observed in Fig. 8.8 and Fig. 8.10 are a function of several factors, some of which we attempt to outline below. First, we consider the time t_0 it takes

before part of the cathode reaches $x = 175$ µm. As seen from Eq. (8.1), this time is mainly a function of the limiting current. This explains the approximately inverse scaling with c_0, which the times in Fig. 8.8 have. The current density also increases with $\tilde{V}_0$, which is why the time t_0 decreases slightly as $\tilde{V}_0$ increases. Finally, the time t_0 scales with the filling factor. This is the reason why t_0 is much larger in the upper left panel of Fig. 8.8, than in either of the two other top row panels.

It is apparent from the lack of ramified growth, that the cathode in the upper left panel in Fig. 8.8 is considerably more stable than the other systems in the leftmost column. To explain this variation in stability, we refer to Fig. 7.6. There it is shown that the instability length scale is on the order of 50 µm for $c_0 = 100$ mM at $\tilde{V}_0 = 10$, while it is considerably lower for $c_0 = 10$ mM and $c_0 = 1$ mM. Fig. 7.6 also shows that for $\tilde{V}_0 > 18$ the instability length scale decreases in size as the concentration increases. The same tendency is observed in Fig. 8.10.

From the subfigures in Fig. 8.10 it appears that there is a connection between the thickness of the layer deposited before the instabilities develop, and the characteristic length scale of the ramified electrodeposits. The analysis in Chapter 7 suggests that there is indeed such a connection and, moreover, that both lengths should scale with the most unstable wavelength for the given parameters, see Eq. (7.59). To test this assertion, we plot the thickness δ_{inst} of the layer deposited before the instabilities develop, versus the most unstable wavelength λ_{max}. We exclude the $c_0 = 100$ mM, $\tilde{V}_0 = 10$ system, since instabilities have not yet developed in this system. The resulting plot is seen in Fig. 8.11 together with a linear fit. Although there is a good amount of scatter around the linear fit, it is seen to capture the general trend reasonably well.

We would like to make a similar plot with the characteristic length scale δ_{char} of the ramified electrodeposits on the y-axis. To extract δ_{char}, we follow the approach in Ref. [38] and calculate the so-called Minkowski dimension of each electrodeposit. In doing this we only consider the part of the electrodeposit lying between 170 µm and 190 µm, and as before we exclude the $c_0 = 100$ mM, $\tilde{V}_0 = 10$ system. In this work we are actually not interested in the Minkowski dimension itself, but rather in a partial result that follows from the analysis. In a range of length scales the electrodeposits appear roughly fractal, but below a certain length scale the electrodeposits are locally smooth. The length scale at which this transition occurs can be extracted from the analysis, and we use this length as the characteristic length scale δ_{char} of the electrodeposit, see Appendix D. In Fig. 8.12 we plot δ_{char} versus λ_{max}, together with a linear fit of the data. While it is clear from the plot that δ_{char} and λ_{max} are correlated to some degree, this is a more tenuous correlation than the one between δ_{inst} and λ_{max}.

Evidently, λ_{max} plays an important role for the morphology of the electrodeposits. However, δ_{inst} and δ_{char} alone are not sufficient to characterize the electrodeposits. As seen in the top row of Fig. 8.10, the characteristic length scale δ_{char} varies very little between $\tilde{V}_0 = 20$ and $\tilde{V}_0 = 30$. Yet, the morphology still changes appreciably.

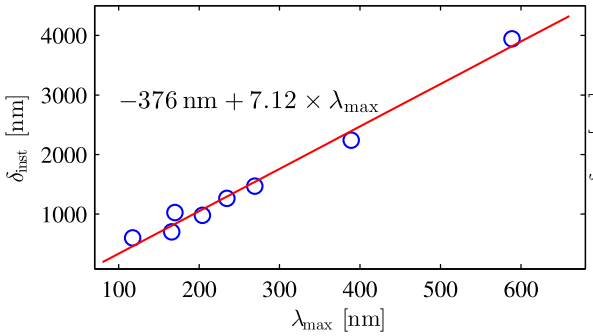

Figure 8.11: The instability length scale δ_{inst} obtained from the simulations, plotted versus the most unstable wavelength λ_{max}. Also, a linear fit highlighting the roughly linear dependence is shown.

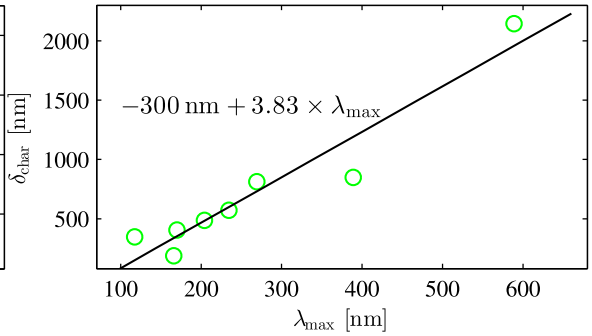

Figure 8.12: The characteristic length scale δ_{char} obtained from the simulations, plotted versus the most unstable wavelength λ_{max}. Also, a linear fit highlighting the roughly linear dependence is shown.

8.7.2 Decoupling of the factors affecting the electrode morphology

The observations in the previous section suggest, that the electrodeposit morphology may be rationalized in terms of a few simple quantities. The wavelength λ_{max} of the most unstable perturbation is an obvious candidate for such a quantity, due to its connection with the characteristic length scale of the electrodeposits. The other quantity is less apparent, but since λ_{max} is a length scale, we search among the remaining length scales in the problem. It turns out, that besides the system dimension there is only one other length scale, namely the width l_{ESC} of the extended space-charge region. Like λ_{max}, we estimate this length from the unperturbed problem $l_{\text{ESC}} = (1 - 1/\tilde{J}_+^0)L$. It is in fact reasonable to expect that l_{ESC} influences the morphology of the electrodeposits. Outside the ESC, the ion-transport is governed by a simple linear ambipolar diffusion equation. The ambipolar diffusion equation has no built-in length scale, and the transport only depends on the ion concentration at the domain boundaries. However, the ESC modifies the location of these domain boundaries by laying as an envelope around the electrodeposits. See Fig. 8.13 for an illustration. Thus, seen from the electroneutral bulk system the structure of the cathode becomes smeared out by the ESC. The amount of smearing is determined by the width l_{ESC} of the ESC.

Our hypothesis is that the scale of the electrodeposits is set by λ_{max} and that l_{ESC} modifies the appearance in a more qualitative sense. To test this hypothesis we vary λ_{max} and l_{ESC} independently and calculate electrodeposits for nine sets of parameter values. In Fig. 8.14 we show contours of λ_{max} and l_{ESC} in the $\tilde{V}_0$-c_0 plane. These contours define a new coordinate system, in which λ_{max} and l_{ESC} are orthogonal to one another. The nine intersection points of the gray lines indicate the nine sets of parameter values we investigate.

In each of the nine simulations we set the width of the domain to $W = 200\lambda_{\text{max}}$, and we let the electrodeposits grow until they reach a distance of $W = 200\lambda_{\text{max}}$ from their starting point. In Fig. 8.15 the resulting electrodeposits are shown in the λ_{max}-l_{ESC} coordinate system. In each plot the axis is scaled to $W = 200\lambda_{\text{max}}$, so the real physical

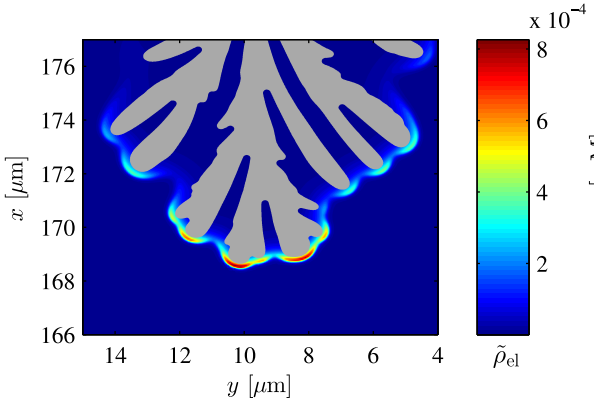

Figure 8.13: Plot of the space-charge density near a dendrite tip. The outer edge of the ESC forms an envelope around the electrodeposit.

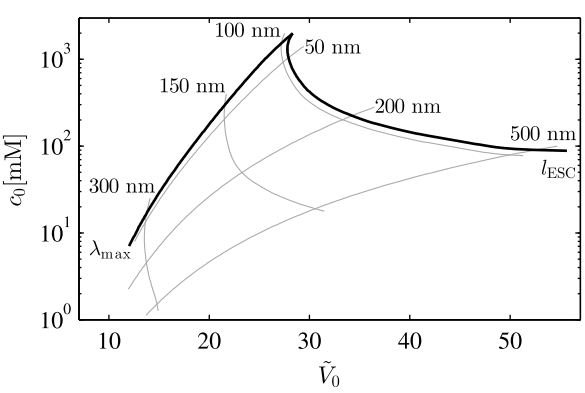

Figure 8.14: Contours of constant λ_{max} and l_{ESC} in the $\tilde{V}_0$-c_0 plane. The contours define a new λ_{max}-l_{ESC} coordinate system.

dimensions vary by a factor of three from $\lambda_{\text{max}} = 100$ nm to $\lambda_{\text{max}} = 300$ nm. This result is part of work in progress, and this is the reason why the $\lambda_{\text{max}} = 150$ nm, $l_{\text{ESC}} = 50$ nm system is still missing. Also, the $\lambda_{\text{max}} = 300$ nm, $l_{\text{ESC}} = 50$ nm system is not fully grown.

First and foremost, we notice that the smallest characteristic dimensions have more or less the same size in all the panels of Fig. 8.15. Since the axes are scaled by $W = 200\lambda_{\text{max}}$ this is in agreement with the considerations in Section 8.7.1. Secondly, we see that the qualitative appearance is not only a function of l_{ESC}. For instance, the morphology varies quite a lot along the top row in Fig. 8.15. On the other hand, the systems along the diagonal seem to share some qualitative features. In hindsight, the reason for this is painfully obvious: We have hypothesized that the scale of the electrodeposits is set by λ_{max}, yet we have expressed l_{ESC} in SI units. In order to obtain a proper orthogonalization of the effects, we should of course have expressed l_{ESC} in units of λ_{max}. Along the diagonal in Fig. 8.15 $l_{\text{ESC}}/\lambda_{\text{max}}$ has comparatively small variations, and this presumably explains why the deposits are relatively similar there. Thus, although we have not succeeded in decoupling the factors which determine the electrode morphology, this preliminary investigation points out some promising directions for future work.

8.8 Conclusion

Our model improves on existing models in three important ways: it can treat systems at overlimiting current including the extended space-charge region, it allows for a proper reaction boundary condition, and it can be tested against results from sharp-interface stability analyses. Our model is, however, not without issues of its own. Perhaps the most apparent of these is the quasi-steady-state assumption. This assumption limits the applicability of the model to short systems, in which the diffusion time is small compared to the deposition time, as discussed in Section 8.2. In principle the phase-field models are superior to our model in this aspect, since they do not have this limitation. However, it is not of practical relevance, as all of the published phase-field simulations are for systems so

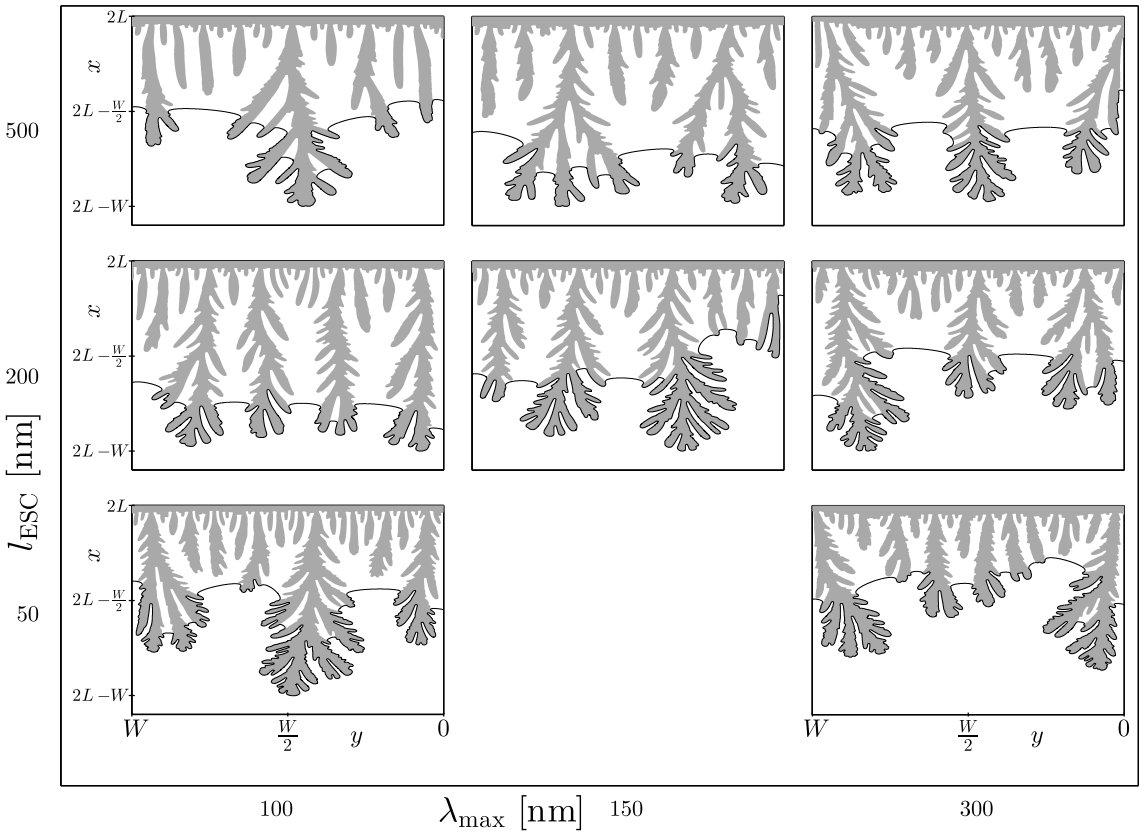

Figure 8.15: Electrodeposits in the λ_{max}-l_{ESC} plane. The axes are scaled with $W = 200\lambda_{\mathrm{max}}$, so the real physical dimensions vary along the λ_{max} axis. In the scaled units shown here, the smallest features of the electrodeposits are seen to have roughly the same size in all the panels.

short that the quasi-steady-state assumption is valid anyway [106, 67, 17].

It is well known, that the strong electric fields at the dendrite tips give rise to electro-osmotic velocity fields in the system [34, 35, 47]. To simplify the treatment and bring out the essential physics of electrodeposition, we have chosen not to include fluid dynamics and advection in our model. However, as seen in Chapter 5 it is straightforward to include these effects.

The standard Butler–Volmer model used in this work is a first step towards realistic boundary conditions. As discussed in Section 2.6.2 a more elaborate model might include Marcus kinetics and an explicit or implicit inclusion of the electric double layer. However, any of these reaction models can be easily implemented in the framework of the sharp-interface model, and as such the specific Butler–Volmer model employed in this work does not constitute a fundamental limitation. Furthermore, the preliminary investigations in Section 8.7.1 and Section 8.7.2 indicate, that the electrode morphology might be explainable in terms of the simple parameters λ_{max} and $l_{\mathrm{ESC}}/\lambda_{\mathrm{max}}$. If that is the case, the influence of the specific reaction expression will mainly enter through its effect on λ_{max} and $l_{\mathrm{ESC}}/\lambda_{\mathrm{max}}$.

Since our sharp-interface model includes, or allows for the easy inclusion of, most effects which are important for electrodeposition in 2D, a natural next step is to see how our results compare to experimental eleectrodeposits. Unfortunately, most such experimental data are viewed at the millimeter or centimeter scale, whereas our simulation results are at the micrometer scale. In one paper, Ref. [70], the electrodeposits are probed at the micrometer scale, but the results do not make for the best comparison, since the morphology of their electrodeposits was a result of adding a surface active molecule. We hope that as more experimental results become available, it will be possible to perform rigorous tests of our model. In the meantime, further investigations into the factors determining the electrode morphology seem a fruitful endeavor.

Chapter 9

Conclusion and outlook

9.1 Conclusion

In this thesis we have investigated a range of nonlinear transport and growth phenomena occurring during concentration polarization at overlimiting current. In the studies we have employed a complementary combination of numerical and analytical methods. The detailed numerical simulations have provided insight into the important physical mechanisms, while the analytical models have generalized the specific numerical results, as well as aided in the interpretation of the numerical results.

First, we investigated the fundamental concentration polarization problem of an overlimiting current running through the extended space-charge region. Building on an assumption of a quasi-uniform charge density distribution (QCD), we derived an analytical model for the transport in a system with an extended space-charge region. The model is distinguished by being highly accurate as well as easy to use. We demonstrated the versatility of the model by deriving a selection of results characterizing the extended space-charge region. We believe that this model is an important theoretical tool, as it gives a simple and quite accurate description of a frequently encountered feature of concentration polarization.

Second, we investigated concentration polarization in a microchannel with charged channel walls. Our work on this problem was inspired by a previous paper [27], which treated some of the important mechanisms while leaving a few open questions. Principal among these questions was the role of advection in the microchannel. To answer this question we employed a hierarchy of models including a full numerical model, a boundary layer model, and a selection of analytical models. We found that the advective transport can be divided into a bulk contribution and a surface contribution. The first of these vanishes for sufficiently long and thin channels, while the latter is present regardless of channel aspect ratio. In the limit of long, thin channels we derived an accurate analytical models, which extends the model published in Ref. [27] by including surface advection as well as surface diffusion.

Third, we investigated water splitting at a permselective membrane during concentration polarization. We first employed a very simple reaction model, where we assumed that the reactions were so fast, that the autodissociation reaction was in equilibrium at

all times. For this simple system we were able to derive a reasonably accurate analytical model for the combined transport-reaction problem. Surprisingly, the analytical model had a more general applicability than initially thought. Thus, in a slightly modified form, the model gave a good description of the transport in systems with more complicated reaction models. We believe that this analytical model could prove a valuable tool in the study and interpretation of water splitting at permselective membranes. As an example of this, we fitted experimental data from the literature to the analytical model.

Fourth, we studied the morphological stability of an electrode during electrodeposition. We developed both numerical and analytical models for the instability growth rate as a function of the perturbation wavelength. These models extended previous studies of the stability problem by applying in the important overlimiting regime, as well as the commonly studied underlimiting regime. From the analytical results we derived an expression for the instability length scale, which indicated that the most unstable wavelength obtained from the stability problem, might also set the length scale of the electrodeposits after the ramified deposits have developed.

Finally, we investigated the development of ramified electrodeposits using a novel sharp-interface model. The development of this new model was motivated by the shortcomings of the established phase-field models, which only apply in the underlimiting regime and implement the nonlinear electrode reactions in a contentious way. Our model was validated in the initial stages of the growth by comparison with the results of the stability analysis. The sharp-interface model includes, or allows for the easy inclusion of, most effects which are important for electrodeposition in two dimensions. We are therefore hopeful that this model could aid in developing a more quantitative understanding of electrodeposition and ramified growth.

9.2 Outlook

The work presented in this thesis answers some important questions in the field of concentration polarization, but it also points out some promising directions for future work.

With our work in Chapter 5 the important transport phenomena in a microchannel during concentration polarization are well understood. However, since the channel wall charge can be modified by chemical reactions, these transport phenomena may change depending on the dynamics of water splitting and the character of the chemical groups at the channel walls [49, 5, 3, 2, 9, 48]. This constitutes a very rich problem with couplings between chemical reactions, ion-transport, fluid flow, and electrostatics. The problem is quite difficult to treat, and in particular to rationalize in terms of few parameters, but nevertheless it is interesting direction for future work. Perhaps of greater interest is the generalization from one microchannel to a network of interconnected channels, representing a microporous material. Currently, this generalization is being pursued in the group of Ali Mani at Stanford [1].

Pertaining to the water splitting problem, our analytical model seems a promising tool for rationalizing the ion transport and reaction kinetics. The simple analytical connection between the salt current and the water-ion current provides a convenient probe of the

water-ion concentration at the entrance to the EDL. Since the behavior of this water-ion concentration depends on the reaction model, this also happens to be an indirect probe of the reaction kinetics. For instance, we found that the choice of reaction kinetics impacts the way the water-ion concentration at the EDL entrance scales with the salt concentration. Further numerical work with varying reaction models, could provide more such connections between water-ion concentration and reaction kinetics. In an experimental setting, these relations would enable us to draw conclusions about the reaction kinetics, based on the measured salt and water-ion currents.

The sharp-interface model employed in the work on electrodeposition lends itself to several extensions and generalizations. These include an extension to a more elaborate reaction model, inclusion of crystal anisotropy in the surface energy, and inclusion of fluid flow and advection. An obvious direction to take, is to generalize the current quasi-steady model to a fully time-dependent model. We have in fact already made this generalization, but since the time-dependent model is associated with greater computational costs, we have only carried out a few simulations with this model. The most promising direction to pursue at this time, is probably a more thorough study of the factors affecting the electrode morphology. The investigations we have already carried out, suggest that the most unstable wavelength $\lambda_{\max}$ and the width l_{ESC} of the ESC measured in units of $\lambda_{\max}$, may be the main factors determining the electrode morphology. Further numerical simulations could reveal whether that is indeed the case.

Appendix A

Additional results for Chapter 5

To supplement the results in Chapter 5, we include here the I-V characteristics for $\alpha = 0.01$ and $\alpha = 0.1$. For the first case, the FULL model is left out, and only the boundary layer (BNDF) model and the analytical (ASCA, ASC and ABLK) models are included.

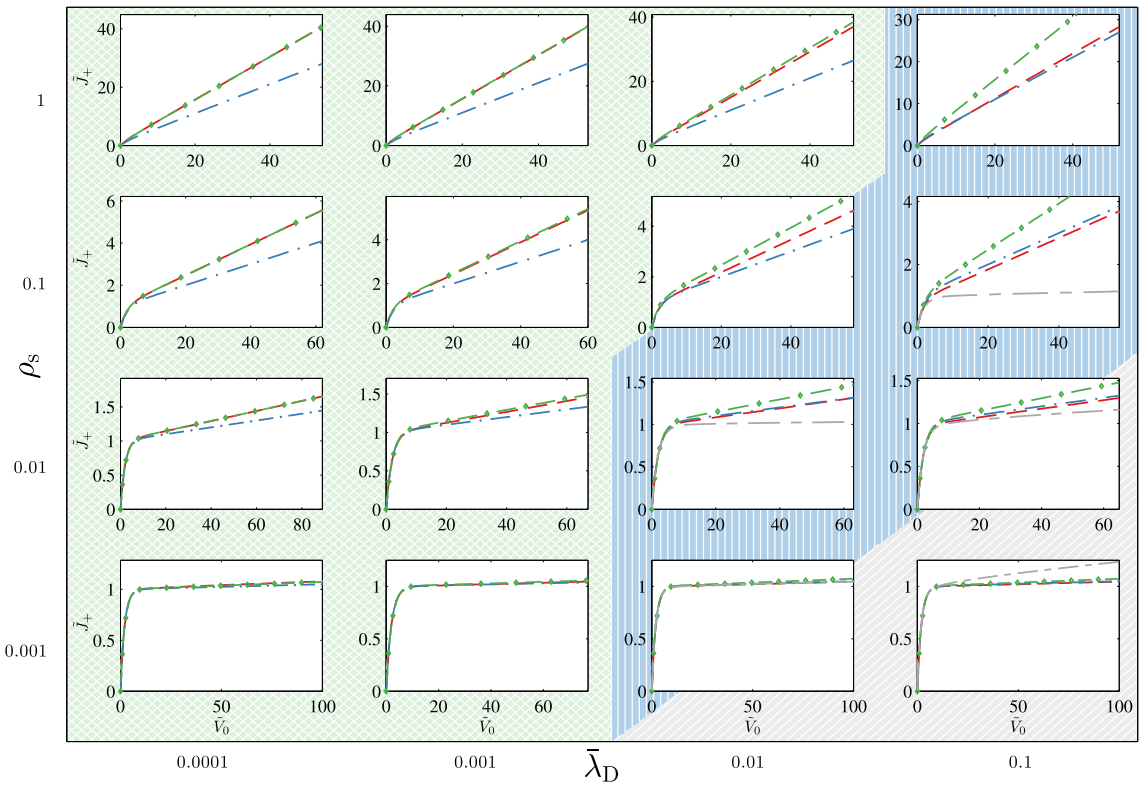

Figure A.1: *I-V* characteristics for $\alpha = 0.01$, $\bar{\lambda}_D = \{0.0001, 0.001, 0.01, 0.1\}$, and $\rho_s = \{0.001, 0.01, 0.1, 1\}$. The dashed (red) curves are obtained from the BNDF model. The (blue) dash-dot curves are from the ASC model, and the (green) dash-diamond curves are from the ASCA model. The (gray) long-dash-short-dash curves are obtained from the ABLK model. The background patterns indicate the dominant overlimiting conduction mechanism. The (green) cross-hatched pattern indicate that surface advection and surface conduction are the dominant mechanisms. The (blue) vertically hatched pattern indicate that surface conduction without surface advection is the dominant mechanism. The (gray) skew-hatched pattern indicate that bulk conduction through the ESC is the dominant mechanism. Intermediate cases are indicated with mixed background patterns.

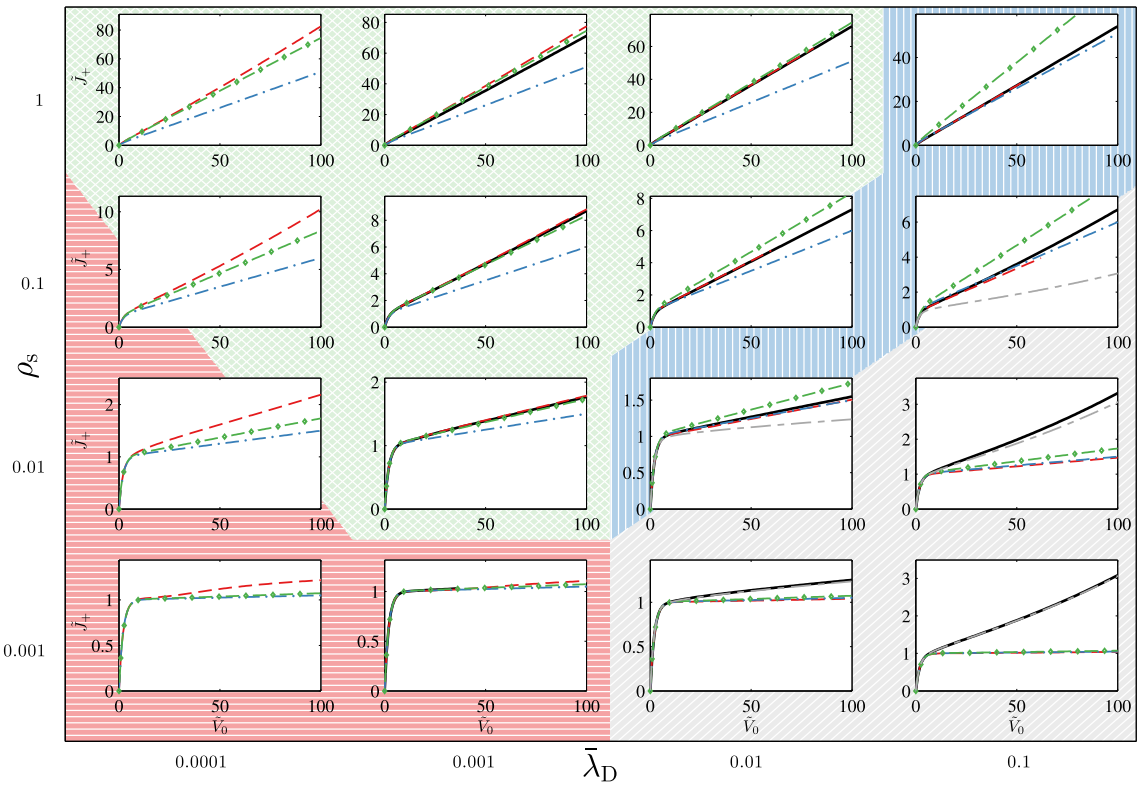

Figure A.2: I-V characteristics for $\alpha = 0.1$, $\bar{\lambda}_D = \{0.0001, 0.001, 0.01, 0.1\}$, and $\rho_s = \{0.001, 0.01, 0.1, 1\}$. The full (black) line show the characteristics obtained from the FULL model. The dashed (red) curves are obtained from the BNDF model. The (blue) dash-dot curves are from the ASC model, and the (green) dash-diamond curves are from the ASCA model. The (gray) long-dash-short-dash curves are obtained from the ABLK model. The background patterns indicate the dominant overlimiting conduction mechanism. The (green) cross-hatched pattern indicate that surface advection and surface conduction are the dominant mechanisms. The (blue) vertically hatched pattern indicate that surface conduction without surface advection is the dominant mechanism. The (red) horizontally hatched pattern indicate that bulk advection is the dominant mechanism. The (gray) skew-hatched pattern indicate that bulk conduction through the ESC is the dominant mechanism. Intermediate cases are indicated with mixed background patterns.

Appendix B

Phase-field models of reaction kinetics

An important feature of the eletrodeposition model presented in Chapter 8 is that it allows for a proper nonlinear reaction model at the electrode interface. The reaction model Eq. (8.14) is equivalent to the expression (2.72)

$$R = i_0 \left[e^{-\alpha_c Z\tilde{\eta}} - e^{\alpha_a Z\tilde{\eta}} \right], \tag{B.1}$$

$$i_0 = k_0 c_+^{1-\alpha} e^{-\bar{\gamma}^* \kappa}, \tag{B.2}$$

where i_0 is the exchange current density.

In phase-field models a phase-field parameter $\xi \in [0;1]$ is used to distinguish between the solid phase ($\xi = 1$) and the aqueous phase ($\xi = 0$). In the interface region the phase-field parameter ξ varies smoothly between 0 and 1. To determine the dynamics of the system a free energy $F[\xi, c_i, \phi]$ (or grand free energy $\Omega[\xi, \mu_i, \phi]$) is introduced, which, as a function of ξ, interpolates between the free energy of a pure electrolyte and the free energy of a pure electrode. Using a variational approach the ion-currents can be found from the free energies,

$$\boldsymbol{J}_i = -D_i c_i \boldsymbol{\nabla} \frac{\delta F}{\delta c_i}, \tag{B.3}$$

and together with the relevant conservation equations this defines the ion-transport problem.

The fundamental assumption in phase-field models of reaction kinetics is, that a similar variational approach can be used to define the overpotential as a local field quantity,

$$\tilde{\eta}_l[\xi, c_i, \phi] \propto \frac{\delta F}{\delta \xi}, \quad \text{or} \quad \tilde{\eta}_l[\xi, \mu_i, \phi] \propto \frac{\delta \Omega}{\delta \xi}, \tag{B.4}$$

where we have omitted the proportionality constants, and the subscript in $\tilde{\eta}_l$ denotes that it is a local overpotential. The total overpotential $\tilde{\eta}$ is defined as the integral of the local overpotential $\tilde{\eta}_l$ over the interface region,

$$\tilde{\eta} = \frac{1}{\delta} \int \tilde{\eta}_l[\xi, c_i, \phi] \, \mathrm{d}x, \tag{B.5}$$

where δ is the width of the interface region and we have assumed the system to be one-dimensional. The phase-field parameter ξ is then assumed to evolve according to the Butler–Volmer like expression

$$\partial_t \xi \propto \left[e^{-\alpha_c Z \tilde{\eta}_l[\xi, c_i, \phi]} - e^{\alpha_a Z \tilde{\eta}_l[\xi, c_i, \phi]} \right], \tag{B.6}$$

where, again, we omitted the proportionality constant. The current into the electrode corresponds to the phase-field growth rate $\partial_t \xi$ integrated over the interface region,

$$\begin{aligned} I &\propto \int \partial_t \xi \, \mathrm{d}x \\ &\propto \int \left[e^{-\alpha_c Z \tilde{\eta}_l[\xi, c_i, \phi]} - e^{\alpha_a Z \tilde{\eta}_l[\xi, c_i, \phi]} \right] \mathrm{d}x. \end{aligned} \tag{B.7}$$

Superficially, this expression looks fairly similar to the Butler–Volmer model Eq. (B.1). However, in general the two expressions are not identical. The reason for this is that the total overpotential $\tilde{\eta}$ occurring in Eq. (B.1) is the integral over the local overpotential $\tilde{\eta}_l$ occurring in Eq. (B.7). Thus, Eq. (B.1) and Eq. (B.7) yield identical results if, and only if, the local overpotential $\tilde{\eta}_l$ has a form which makes it indifferent to the order in which integration and exponentiation are performed. Although this condition is satisfied for small or constant overpotentials, there is no way of guaranteeing it in general. Consequently, we expect Eq. (B.7) to differ from Eq. (B.1) in most cases.

Another issue with the phase-field models of reaction kinetics is, that the connection between the electric potential $\tilde{\phi}$ and the total overpotential $\tilde{\eta}$ is not apparent. From Eq. (2.67) we expect that

$$\tilde{\eta} = \Delta\tilde{\phi} - \Delta\tilde{\phi}_{\mathrm{eq}}, \tag{B.8}$$

where $\Delta\tilde{\phi}$ is the potential difference across the electrode interface, and $\Delta\tilde{\phi}_{\mathrm{eq}}$ is the potential difference in equilibrium. However, there does not seem to be any guarantee that this is true for phase-field reaction kinetics. In general, since most phase-field models of electrodeposition lack a simple sharp-interface limit [68], it is difficult to relate the parameters in a phase-field reaction model to those in the corresponding sharp-interface model.

The above objections to the phase-field reaction models do not necessarily mean that those models are wrong. After all, the Butler–Volmer model or similar nonlinear reaction models are by no means exact, so it is entirely possible that phase-field reaction models approximate the true reaction kinetics equally well. However, in lack of convincing reasons to believe that this is the case, the various sharp-interface reaction models remain the preferable way of modeling electrode reactions.

Appendix C

Initial growth of the electrode

In the initial part of the simulation the electrode is so flat that the linear stability analysis from Chapter 7 gives a good description of the growth. We parameterize the cathode position as

$$x = X(t) + f(y,t), \tag{C.1}$$

where $f(y,t)$ is the y-dependent deviation from the mean electrode position $X(t)$. According to the linear stability analysis each mode grows exponentially in time with the growth factor Γ. After a time t an initial perturbation,

$$f(y,0) = \sum_{n=1}^{N} a_n e^{ik_n y}, \tag{C.2}$$

has therefore evolved to

$$f(y,t) = \sum_{n=1}^{N} a_n e^{\Gamma_n t} e^{ik_n y}. \tag{C.3}$$

We note that some of the growth rates Γ_n can be negative. In our simulation we add new perturbations with small time intervals, which we, for the purpose of this analysis, assume to be evenly spaced. After M time intervals Δt the surface is therefore described by

$$f(y, M\Delta t) = \sum_{m=0}^{M} \sum_{n=1}^{N} a_{nm} e^{\Gamma_n (M-m)\Delta t} e^{ik_n y}. \tag{C.4}$$

We are interested in the average power of each mode

$$\langle P_n \rangle = \left\langle \left| \sum_{m=0}^{M} a_{nm} e^{\Gamma_n (M-m)\Delta t} \right|^2 \right\rangle. \tag{C.5}$$

The coefficients are random and uncorrelated with zero mean. On average the cross-terms in the sum therefore cancel and we can simplify,

$$\begin{aligned}\langle P_n\rangle &= \left\langle \sum_{m=0}^{M} |a_{nm}|^2 e^{2\Gamma_n(M-m)\Delta t} \right\rangle \\ &= \langle |a_n|^2\rangle \sum_{m=0}^{M} e^{2\Gamma_n(M-m)\Delta t} \\ &= \langle |a_n|^2\rangle \frac{e^{2\Gamma_n(M+1)\Delta t}-1}{e^{2\Gamma_n\Delta t}-1}. \end{aligned} \tag{C.6}$$

The variance of the power is given as

$$\mathrm{Var}(P_n) = \langle P_n^2\rangle - \langle P_n\rangle^2. \tag{C.7}$$

The first of these terms is

$$\begin{aligned}\langle P_n^2\rangle &= \left\langle \left(\left| \sum_{m=0}^{M} a_{nm} e^{\Gamma_n(M-m)\Delta t} \right|^2 \right)^2 \right\rangle \\ &= e^{4\Gamma_n M\Delta t} \left\langle \left(\left| \sum_{m=0}^{M} a_{nm} q^m \right|^2 \right)^2 \right\rangle, \end{aligned} \tag{C.8}$$

where $q = e^{-\Gamma_n\Delta t}$. Writing out the absolute value

$$\langle P_n^2\rangle = e^{4\Gamma_n M\Delta t} \left\langle \left(\sum_{m'=0}^{M}\sum_{m=0}^{M} a_{nm} a_{nm'}^* q^{m+m'} \right)^2 \right\rangle, \tag{C.9}$$

where superscript $*$ denotes complex conjugation. Because the coefficients are uncorrelated with mean 0, only the terms including $|a_{nm}|^2|a_{nm'}|^2$ survive in the average of the square,

$$\begin{aligned}\langle P_n^2\rangle &= e^{4\Gamma_n M\Delta t} \left\langle \frac{1}{2} \sum_{m'=0}^{M}\sum_{m=0}^{M} 6|a_{nm}|^2|a_{nm'}|^2 q^{2(m+m')} \right\rangle \\ &= 3e^{4\Gamma_n M\Delta t} \sum_{m'=0}^{M}\sum_{m=0}^{M} \left\langle |a_{nm}|^2|a_{nm'}|^2\right\rangle q^{2(m+m')}. \end{aligned} \tag{C.10}$$

Here, the factor of six comes from the binomial coefficient and the factor of a half takes into account that the double sum counts each combination twice. Now, there are two possibilities; either $m \neq m'$ or $m = m'$. In the first case $|a_{nm}|^2$ and $|a_{nm'}|^2$ are uncorrelated, meaning that

$$\left\langle |a_{nm}|^2|a_{nm'}|^2\right\rangle = \left\langle |a_n|^2\right\rangle^2. \tag{C.11}$$

Whereas if $m = m'$, then

$$\left\langle |a_{nm}|^2 |a_{nm'}|^2 \right\rangle = \left\langle |a_n|^4 \right\rangle . \tag{C.12}$$

This means that

$$\begin{aligned}
\langle P_n^2 \rangle &= 3e^{4\Gamma_n M\Delta t} \left\langle |a_n|^2 \right\rangle^2 \sum_{m'\neq m}^{M} \sum_{m=0}^{M} q^{2(m+m')} \\
&\quad + 3e^{4\Gamma_n M\Delta t} \left\langle |a_n|^4 \right\rangle \sum_{m=0}^{M} q^{4m} \\
&= 3e^{4\Gamma_n M\Delta t} \left\langle |a_n|^2 \right\rangle^2 \sum_{m'=0}^{M} \sum_{m=0}^{M} q^{2(m+m')} \\
&\quad + 3e^{4\Gamma_n M\Delta t} \left(\left\langle |a_n|^4 \right\rangle - \left\langle |a_n|^2 \right\rangle^2 \right) \sum_{m=0}^{M} q^{4m} \\
&= 3\langle P_n \rangle^2 \\
&\quad + 3e^{4\Gamma_n M\Delta t} \left(\left\langle |a_n|^4 \right\rangle - \left\langle |a_n|^2 \right\rangle^2 \right) \frac{q^{4(M+1)} - 1}{q^4 - 1}.
\end{aligned} \tag{C.13}$$

The variance of the power is thus given as

$$\mathrm{Var}(P_n) = 2\langle P_n \rangle^2 + \left(\left\langle |a_n|^4 \right\rangle - \left\langle |a_n|^2 \right\rangle^2 \right) \frac{e^{4\Gamma_n (M+1)\Delta t} - 1}{e^{4\Gamma_n \Delta t} - 1}. \tag{C.14}$$

If $\Gamma_n \Delta t \ll 1$ we can expand the denominators of $\langle P_n \rangle^2$ and the last term. We find that they scale as $4(\Gamma_n \Delta t)^2$ and $4\Gamma_n \Delta t$, respectively. In the limit $\Gamma_n \Delta t \ll 1$ the first term thus dominates over the second, so to a good approximation we have

$$\mathrm{Var}(P_n) \approx 2\langle P_n \rangle^2, \tag{C.15}$$

$$\mathrm{SD}(P_n) \approx \sqrt{2}\langle P_n \rangle. \tag{C.16}$$

In the simulations the surface perturbations have the form

$$f(y, 0) = \sum_{n=1}^{N} b_n h(y - n\Delta y), \tag{C.17}$$

where,

$$h(y) = \begin{cases} 1, & 0 \leq y \leq \Delta s, \\ 0, & \text{else.} \end{cases} \tag{C.18}$$

We take the absolute square of $f(y,0)$ given as both Eq. (C.2) and Eq. (C.17), and integrate over the domain to obtain

$$\begin{aligned}\int_0^W |f(y,0)|^2 \,\mathrm{d}y &= \sum_{n=1}^{N} |b_n|^2 \int_0^W |h(y-n\Delta y)|^2 \,\mathrm{d}y \\ &= \Delta s \sum_{n=1}^{N} |b_n|^2, \end{aligned} \tag{C.19}$$

$$\begin{aligned}\int_0^W |f(y,0)|^2 \,\mathrm{d}y &= \sum_{n=1}^{N} |a_n|^2 \int_0^W |e^{ik_n y}|^2 \,\mathrm{d}y \\ &= W \sum_{n=1}^{N} |a_n|^2. \end{aligned} \tag{C.20}$$

The mean square of b_n is thus related to the mean square of a_n as

$$\langle |a_n|^2 \rangle = \frac{\Delta s}{W} \langle |b_n|^2 \rangle = \frac{1}{N} \langle |b_n|^2 \rangle. \tag{C.21}$$

From Eq. (8.35) we have that

$$\langle |b_n|^2 \rangle = a^6 \frac{J_+ \Delta t}{\Delta h \Delta s}. \tag{C.22}$$

Inserting in Eq. (C.6) we find

$$\langle P_n \rangle = \frac{1}{N} a^6 \frac{J_+ \Delta t}{\Delta h \Delta s} \frac{e^{2\Gamma_n (M+1)\Delta t} - 1}{e^{2\Gamma_n \Delta t} - 1} \tag{C.23}$$

$$= a^6 \frac{J_+ \Delta t}{\Delta h W} \frac{e^{2\Gamma_n (t_{\mathrm{tot}} + \Delta t)} - 1}{e^{2\Gamma_n \Delta t} - 1}, \tag{C.24}$$

which is seen to be independent of the bin size Δs. We also introduced the total time $t_{\mathrm{tot}} = M\Delta t$. In a consistent scheme the power spectrum should of course only depend on the total time, and not on the size Δt of the time steps. For small values of $\Gamma_n \Delta t$ we can expand the denominator and neglect the Δt in the nominator,

$$\langle P_n \rangle \approx a^6 \frac{J_+}{2\Delta h W \Gamma_n} \left[e^{2\Gamma_n t_{\mathrm{tot}}} - 1 \right]. \tag{C.25}$$

So, as long as $2\Gamma_n \Delta t \ll 1$ the power spectrum does not depend on the size of the time step.

For larger values of $2\Gamma_n \Delta t$ the power spectrum does depend on the size of the time step. However, as long as $2\Gamma_n \Delta t \lesssim 1$, we do not expect the overall morphology of the electrode to have a significant dependence on the time step.

Appendix D

Characteristic length scale of electrodeposits

To find the characteristic length scale δ_{char} of the ramified electrodeposits we follow Ref. [38] and use the box-counting method to calculate the Minkowski dimension of the deposit perimeter. As a first step in calculating the Minkowski dimension, we place a square grid with side length ϵ over each deposit, and count the number $N(\epsilon)$ of boxes it takes to completely cover the perimeter of the part of the deposit lying between $x = 170$ µm and $x = 190$ µm. An example is shown in Fig. D.1.

For a proper fractal geometry, the Minkowski dimension is defined as

$$\delta_{\text{M}} = -\lim_{\epsilon \to 0} \frac{\ln\left[N(\epsilon)\right]}{\ln(\epsilon)}. \tag{D.1}$$

The electrodeposits we are investigating are not fractal at all length scales, but in a range of length scales, we can calculate an approximate Minkowski dimension as the negative slope in a $\ln\left[N(\epsilon)\right]$ vs $\ln(\epsilon)$ plot. In Fig. D.2 such a plot is seen, together with linear fits in each of the two approximately linear regions. The Minkowski dimension at small ϵ is nearly unity, indicating that the deposit perimeter is locally smooth at this length scale. For larger values of ϵ the Minkowski dimension deviates from unity, because the deposit is approximately fractal in this size range. At the transition point between these two regions is the smallest length scale, which is related to the morphology of the electrodeposit. This length scale we denote the characteristic length δ_{char}. Technically, we define δ_{char} as the point where the linear fits from each region cross each other, as indicated in Fig. D.2.

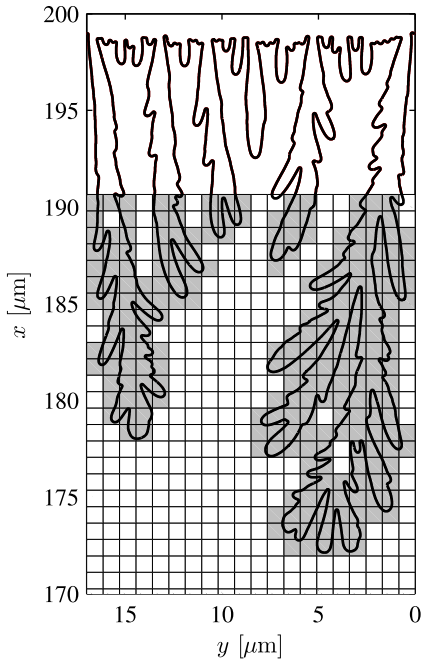

Figure D.1: The box-counting method illustrated on the electrodeposit obtained for $c_0 = 10$ mM and $V_0 = 20$. The boxes that cover part of the deposit perimeter are shown in gray and the remaining boxes are shown in white. In this example the grid size is $\epsilon = 0.85$ µm and the number of boxes it takes to cover the perimeter is $N(\epsilon) = 234$.

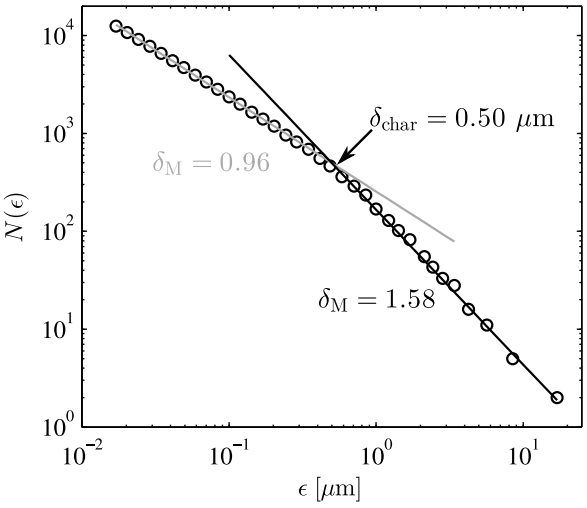

Figure D.2: The number $N(\epsilon)$ of boxes it takes to cover the electrodeposit plotted vs the box side length ϵ. A linear fit is shown in each of the two approximately linear regions, and the Minkowski dimension in each region is indicated. The crossing point between the linear fits is marked by an arrow, and the characteristic dimensions $\delta_{\mathrm{char}} = 0.50$ µm is calculated based on this crossing point.

Appendix E

Paper published in Phys Rev E

Title: Transport-limited water splitting at ion-selective interfaces during concentration

Authors: Christoffer P. Nielsen and Henrik Bruus.

Reference: Published in Physical Review E **89**, 042405 (2014) (14 pages)

Transport-limited water splitting at ion-selective interfaces during concentration polarization

Christoffer P. Nielsen and Henrik Bruus
Department of Physics, Technical University of Denmark, DTU Physics Building 309, DK-2800 Kongens Lyngby, Denmark
(Received 11 December 2013; revised manuscript received 27 March 2014; published 15 April 2014)

We present an analytical model of salt- and water-ion transport across an ion-selective interface based on an assumption of local equilibrium of the water-dissociation reaction. The model yields current-voltage characteristics and curves of water-ion current versus salt-ion current, which are in qualitative agreement with experimental results published in the literature. The analytical results are furthermore in agreement with direct numerical simulations. As part of the analysis, we find approximate solutions to the classical problem of pure salt transport across an ion-selective interface. These solutions provide closed-form expressions for the current-voltage characteristics, which include the overlimiting current due to the development of an extended space-charge region. Finally, we discuss how the addition of an acid or a base affects the transport properties of the system and thus provide predictions accessible to further experimental tests of the model.

DOI: 10.1103/PhysRevE.89.042405 PACS number(s): 68.05.−n, 47.57.jd, 82.39.Wj, 82.45.Mp

I. INTRODUCTION

Ion transport across an ion-selective interface, such as a nanochannel, an electrode, or an ion-selective membrane, has found numerous applications in, e.g., dialysis, desalination, battery and fuel cell technology, electrochemistry, and microfluidic systems [1–7]. A common feature of ion transport across ion-selective interfaces is the phenomenon known as concentration polarization, in which the ion concentration undergoes depletion next to the interface leading to a decrease in conductivity [1]. In the classical one-dimensional local electroneutrality (LEN) modeling of the problem, the conductivity goes to zero as the voltage drop over the system is increased, and the current approaches the so-called limiting current. Experimentally it has, however, been found that many concentration-polarized systems can sustain a significant overlimiting current [1,8,9]. A number of mechanisms have been suggested as explanation for this overlimiting current: these include the development of an extended space-charge region (ESC) [10–12], electro-osmotic instabilities (EOI) [13,14], water splitting [15,16], current-induced membrane discharge (CIMD) [17], and surface conduction in microchannels [18]. Increasing amounts of evidence points to EOI as the primary mechanism in systems where advection is not suppressed by the geometry [9,14]. However, because of the experimental and theoretical difficulties associated with investigating concentration polarization, no unified picture describing the relative importance of mechanisms in different regimes has yet emerged. Concentration polarization is therefore still very much an open problem, warranting additional investigations into the underlying mechanisms.

In this paper, we investigate the effect of water splitting and an extended space-charge region on systems exhibiting concentration polarization. Apart from being relevant for classical concentration polarization in macroscopic systems, our investigation of water splitting is motivated by the recent studies which highlight the importance of reactions between hydronium and surface groups in microsystems [19–22].

Water splitting has long been investigated as a possible cause of overlimiting current in systems exhibiting concentration polarization [15,23,24]. In 1979, Kharkats predicted that besides adding to the total current in the system, a water-ion current is also able to increase, or exalt, the current of salt ions above the limiting current [16]. Since then, the effect and origin of the water-ion current has drawn considerable attention, and experiments have largely confirmed the fundamentals of Kharkats prediction [25–29]. It is reasonably well understood that the origin of the water-ion current is water dissociation taking place in a region close to the ion-selective interface. In many experiments, the magnitude of the water-ion current does, however, indicate a reaction rate much larger than what should be possible, considering only the bulk dissociation rates [1,30]. A number of models have been suggested to explain this remarkable feature. Some of these ascribe the increased reaction rate to catalytic interactions with membrane surface groups [25,31,32], while others use that the dissociation rate is increased in strong electric fields and employ a phenomenological function with one or more fitting parameters to describe this dependence [26,30,33,34]. In lack of conclusive evidence in support of either theory, the only thing that can be said with some confidence is that the actual reaction kinetics is probably exceedingly complicated.

In this work, we avoid the subject of the detailed reaction kinetics altogether by simply assuming that the dissociation rate is so large that the water-ion current is transport limited rather than reaction limited. Put in another way, we assume local equilibrium of the water ions everywhere in the system as done in Refs. [17,35]. Since the analysis given in this paper is based on this assumption, experiments supporting our conclusions would serve to corroborate the underlying assumption of local equilibrium of the water-dissociation reaction. In particular, the techniques allowing for individual measurements of salt current and water-ion current, such as titration-based methods [26,27], are highly relevant, as many of our results and predictions depend explicitly on both these currents.

Even for systems where the water-equilibrium assumption is not justified, the presented analysis is valuable since it provides an upper bound to the currents which can be obtained (assuming that the equilibrium constant K_w remains fixed). Also, since the developed model employs a minimum of assumptions about the system, it is an excellent model to benchmark more detailed reaction models against. It has

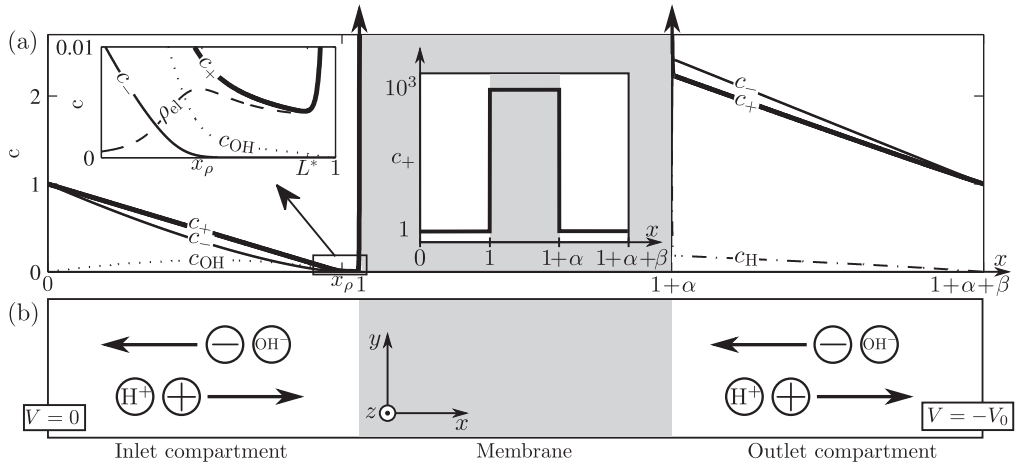

FIG. 1. (a) Normalized concentrations of salt ions (c_+ and c_-) and water ions (c_{OH} and c_H) plotted versus normalized position x. The curves are obtained from a numerical simulation (see Sec. V). The top left inset is a zoom of the space-charge region (SCR) in front of the membrane. The SCR is composed of an extended space-charge region (ESC) from around x_ρ to L^*, and a quasiequilibrium electric double layer (EDL) from L^* to 1. The center inset is a plot of the normalized cation concentration c_+ showing the very high concentration inside the membrane $1 < x < 1 + \alpha$ (gray). (b) Sketch of the studied system with salt ions (+ and −) and water ions (H^+ and OH^-). An inlet compartment ($0 < x < 1$) and an outlet compartment ($1 + \alpha < x < 1 + \alpha + \beta$) separated by an ion-selective nanoporous membrane. To the left ($x = 0$) and right ($x = 1 + \alpha + \beta$), the system is connected to reservoirs of well-defined salt concentration and pH. The system is translationally invariant in the yz plane parallel to the membrane.

for instance been a success criterion for reaction models that they are able to replicate the characteristic S shape (increase-plateau-increase, see Sec. V B) of the experimental current-voltage curves [34]. However, such S-shaped current-voltage curves are found even in our simple model, which suggests that they are a result of the transport properties of the system rather than the detailed reaction kinetics.

To simplify the treatment and bring forth the fundamental physics of water splitting, we study a system which is translationally invariant parallel to the ion-selective interface, and we use a one-dimensional (1D) model to describe this essentially one-dimensional system. By employing a 1D model, we disregard the possibility of spontaneous symmetry breaking, occurring at higher voltages in the form of electro-osmotic instabilities (EOI) [13,14], as this effect can only be described in a full three-dimensional (3D) model. For a number of systems where advection is suppressed by gels, microchannels, or porous structures, disregarding EOI is actually justified, and even when that is not the case our model provides a way to study the behavior before EOI sets in as well as the transition to EOI.

As a concrete realization of a system exhibiting concentration polarization, we investigate transport between two reservoirs across an ion-selective membrane. We have chosen this particular system for our study because the boundary conditions provided by the reservoirs are both simple and well defined. These features render the analysis conceptually simple, and for the water-splitting part of the problem, a reservoir is the simplest way of providing well-defined boundary conditions on the hydronium and hydroxide ions. Although the ideal reservoir boundary condition is a theoretical construct, it is possible to realize systems resembling the model system. An example of this is an electrodialysis cell as illustrated in Ref. [1]. Moreover, the simple solutions obtained from the studied system can be transformed into solutions for systems with more complicated boundary conditions. In Sec. VII we give examples of such transformations.

II. MODEL SYSTEM

The one-dimensional model system stretching along the x axis is shown in Fig. 1. It consists of a central ion-selective membrane of length αL connected to two well-mixed reservoirs, to the left and right, through two compartments of lengths L and βL, respectively. The membrane is assumed to be much thicker than the local Debye length, so that the interior of the membrane can be treated as locally electroneutral. The reservoirs have well-defined pH, and there is a potential difference V_0 between them. The left reservoir has salt concentration c_0 and the right reservoir has salt concentration $c_R c_0$. The system is translationally invariant in the yz plane parallel to the membrane. In Fig. 1(a) are shown typical normalized concentration distributions versus normalized position. These are obtained from the numerical simulations described in Sec. V. The top left inset shows the ion and charge concentrations in the space-charge region (SCR) near the membrane and two points x_ρ and L^* are defined for later use: x_ρ denotes the position of the peak in space-charge density and L^* denotes the beginning of the quasiequilibrium electric double layer (EDL). The part of the SCR lying outside the EDL, i.e., from around x_ρ to L^*, we denote the extended space-charge region (ESC). Inside the membrane, the concentration of anions vanishes while the concentration of cations becomes very large ($\sim 10^3$ times the reservoir concentration, depending on system parameters). In Fig. 1(b) is shown a sketch of the model system. The ions in the model are positive and negative salt ions with concentration c_+ and c_-, respectively, as well as hydronium and hydroxide ions (water ions) with concentration c_H and c_{OH}, respectively.

III. GOVERNING EQUATIONS

We consider monovalent ions and normalize the ion concentrations by the reservoir salt concentration $c_0 = c_+(0) = c_-(0)$. The electrical potential ϕ is normalized by the thermal voltage $V_T = k_B T/e$ and the position by the length L. The cation current is normalized by the classical limiting current $J_{lim} = 2D_+c_0/L$, the anion current is normalized by $2D_-c_0/L$, while J_H and J_{OH} are both normalized by $2D_{OH}c_0/L$. The nondimensionalized ion currents are

$$2J_+ = -\partial_x c_+ - c_+\partial_x\phi, \tag{1a}$$

$$2J_- = -\partial_x c_- + c_-\partial_x\phi, \tag{1b}$$

$$2J_H = -\delta\partial_x c_H - \delta c_H\partial_x\phi, \tag{1c}$$

$$2J_{OH} = -\partial_x c_{OH} + c_{OH}\partial_x\phi, \tag{1d}$$

where we have introduced the diffusivity ratio $\delta \equiv D_H/D_{OH} = 1.75$. In the remainder of the paper, we are primarily concerned with nondimensional quantities. For the rare exceptions of dimensionful quantities, these will be indicated by a tilde.

In steady state the relevant Nernst-Planck equations for the salt ions are

$$\partial_x J_\pm = 0. \tag{2}$$

Similar equations govern the motion of hydronium and hydroxide, with the addition of a reaction term R, which derives from the autoprotolytic reaction of water

$$0 = -\partial_x J_H + R, \tag{3a}$$

$$0 = -\partial_x J_{OH} + R. \tag{3b}$$

Here, the reaction rates are identical since the reaction

$$H_3O^+ + OH^- \rightleftharpoons 2H_2O \tag{4}$$

produces or consumes one unit of each species. Introducing the water-ion current $J_w \equiv J_H - J_{OH}$ we obtain a single transport equation for the water ions

$$\partial_x J_w = 0. \tag{5}$$

The fundamental assumption in this work is that the time scale of the autoprotolysis is much shorter than the transport time of hydronium and hydroxide. That is, we work in the limit of high Damköhler number, for which the hydronium and hydroxide concentrations are simply related via the equilibrium constant $K_w = \tilde{c}_{OH}\tilde{c}_H$, which for dimensionless concentrations can be written as

$$c_{OH}\, c_H = n^2, \quad \text{with} \quad n = \frac{\sqrt{K_w}}{c_0}. \tag{6}$$

The final governing equation is the Poisson equation

$$2\bar{\lambda}_D^2\partial_x^2\phi = -c_+ + c_- - c_H + c_{OH}, \tag{7a}$$

$$\bar{\lambda}_D \equiv \frac{\lambda_D}{L} = \frac{1}{L}\sqrt{\frac{\epsilon_w V_T}{2ec_0}}, \tag{7b}$$

where the nondimensionalized Debye length $\bar{\lambda}_D$ has been introduced, with e being the unit charge and ϵ_w the permittivity of water. Since $\bar{\lambda}_D^2$ is a small parameter, any small deviation from charge neutrality will greatly affect the potential in a manner which tends to restore charge neutrality. This observation is the basis of the often used local electroneutrality (LEN) assumption, where the bulk liquid is assumed electroneutral and the only deviation from electroneutrality is in the Debye layer.

The membrane is modeled as having a high density N_m of frozen negative charges (normalized by c_0), a porosity ϵ_P, a permittivity ϵ_m, and a tortuosity τ. Inside the membrane, the currents and the Poisson equation are therefore modified as

$$2J_i = \frac{\epsilon_P}{\tau}(-\partial_x c_i \pm c_i\partial_x\phi), \tag{8a}$$

$$\frac{\epsilon_m}{\epsilon_w}2\bar{\lambda}_D^2\partial_x^2\phi = \epsilon_P(-c_+ + c_- - c_H + c_{OH}) + N_m. \tag{8b}$$

Most ion-selective membranes have a complex structure [36–38] making it difficult to properly determine the values of N_m, ϵ_P, ϵ_m, and τ. In this work we will, however, only consider cases with $N_m \gg 1$, for which the potential drop over the membrane is negligible regardless of the membrane width αL and the value of the membrane parameters N_m, ϵ_P, ϵ_m, and τ.

The problem is closed by appropriate boundary conditions at either reservoir. At the left reservoir, the potential is set to zero and the normalized concentrations take the values $c_\pm = 1$, $c_H = c_{OH} = n$. At the right reservoir, the potential is set to $-V_0$ and the normalized concentrations take the values $c_\pm = c_R$, $c_H = c_{OH} = n$.

IV. ANALYTICAL TREATMENT

In this section, we derive analytical expressions for the potential ϕ and concentration fields c_i given as functions of the salt- and water-ion currents J_+ and J_w. As a result of the analysis, we find simple scaling laws for some of the characteristic features in the problem.

A. Basic analysis

For the simple system without water ions we know from Refs. [1,10,39] and numerical simulations that the left compartment is composed of three regions: a locally electroneutral diffusion layer, and a space-charge region (SCR), which can be subdivided into an extended space-charge region (ESC) and a quasiequilibrium electric double layer (EDL). This situation is sketched in Fig. 1(a).

Initially, we only consider the left compartment outside the EDL, i.e., the region extending from 0 to L^* in the inset of Fig. 1(a). In the analysis we will assume that $L^* = 1$, which as analyzed in the Supplemental Material, Sec. I A [40], is a good assumption for a wide range of parameter values. We introduce the effective water-ion density c_w and write

$$c_w \equiv \delta c_H + c_{OH}, \tag{9a}$$

$$2J_w = \partial_x c_w - c_w\partial_x\phi - 2\delta\partial_x c_H \approx \partial_x c_w - c_w\partial_x\phi. \tag{9b}$$

We can discard the $2\delta\partial_x c_H$ term because the hydroxide concentration is very much larger than the hydronium concentration in the entire LEN region, and in the ESC region, where this may not be the case, diffusion plays a negligible role compared to electromigration.

We assume that the membrane is completely impenetrable to anions, so that $J_- = 0$. The results can readily be

generalized to the case of $J_- \neq 0$. Subtracting Eq. (1b) from Eq. (9b) we obtain

$$2J_\mathrm{w} = \partial_x(c_\mathrm{w} + c_-) - (c_\mathrm{w} + c_-)\partial_x\phi \tag{10a}$$

$$\approx \partial_x c_+ - c_+\partial_x\phi + 2\bar{\lambda}_\mathrm{D}^2\partial_x^3\phi - 2\bar{\lambda}_\mathrm{D}^2\partial_x\phi\partial_x^2\phi, \tag{10b}$$

where Eq. (7a) with $(1+\delta)c_\mathrm{H} \approx 0$ has been used. This might introduce an error as we have just argued that $c_\mathrm{w} \gg c_\mathrm{H}$ does not necessarily hold in the ESC. The majority of the charge density in the ESC does, however, derive from the salt ions, so reasonable results may still be obtained with this approximation, as verified by our numerical simulations in Sec. V.

Adding (subtracting) Eq. (10b) to (from) Eq. (1a) we obtain

$$J_+ + J_\mathrm{w} = -c_+\partial_x\phi + \bar{\lambda}_\mathrm{D}^2\partial_x^3\phi - \bar{\lambda}_\mathrm{D}^2\partial_x\phi\partial_x^2\phi, \tag{11a}$$

$$J_+ - J_\mathrm{w} = -\partial_x c_+ - \bar{\lambda}_\mathrm{D}^2\partial_x^3\phi + \bar{\lambda}_\mathrm{D}^2\partial_x\phi\partial_x^2\phi. \tag{11b}$$

The second of these equations is easily integrated

$$(J_+ - J_\mathrm{w})x - \kappa = -c_+ - \bar{\lambda}_\mathrm{D}^2\partial_x^2\phi + \frac{\bar{\lambda}_\mathrm{D}^2}{2}(\partial_x\phi)^2, \tag{12}$$

where we have introduced the integration constant $\kappa = c_+(0) + \bar{\lambda}_\mathrm{D}^2\partial_x^2\phi|_{x=0} - \frac{\bar{\lambda}_\mathrm{D}^2}{2}(\partial_x\phi)^2|_{x=0}$. For the studied system κ is very close to unity since $c_+(0) = 1$ and $-\bar{\lambda}_\mathrm{D}^2\partial_x^2\phi|_{x=0} + \frac{\bar{\lambda}_\mathrm{D}^2}{2}(\partial_x\phi)^2|_{x=0} \ll 1$ for most relevant parameter values. In the following analysis, we keep κ as an arbitrary constant. However, when plotting analytical results we have used the approximation $\kappa = 1$. The validity of this approximation is studied in the Supplemental Material, Sec. I B [40].

Multiplying Eq. (12) by $\partial_x\phi$ and subtracting it from Eq. (11a), we obtain a single ordinary differential equation for the potential ϕ:

$$J_+ + J_\mathrm{w} - [(J_+ - J_\mathrm{w})x - \kappa]\partial_x\phi = \bar{\lambda}_\mathrm{D}^2\partial_x^3\phi - \frac{\bar{\lambda}_\mathrm{D}^2}{2}(\partial_x\phi)^3. \tag{13}$$

This equation has previously been derived in various forms, for instance, in Refs. [10,39,41]. A common way of deriving solutions to this equation is to use the method of matched asymptotic expansions [12,39,42,43]. We will use a slightly simpler approach which omits the EDL, while still capturing the essential physics of the problem.

Let us consider the magnitude of the terms in Eq. (13) in each of the distinct regions. In the electroneutral diffusion layer, only the terms on the left of Eq. (13) matter since the entire right-hand side stem from the Poisson equation. In the ESC, the charge density can obviously not be neglected, and the terms on the right-hand side come into play. The right-hand side terms scale as $\bar{\lambda}_\mathrm{D}^2\partial_x^3\phi \sim \bar{\lambda}_\mathrm{D}^2\frac{\Delta\phi}{\Delta x^3}$ and $\bar{\lambda}_\mathrm{D}^2(\partial_x\phi)^3 \sim \bar{\lambda}_\mathrm{D}^2\frac{\Delta\phi^3}{\Delta x^3}$, where Δx and $\Delta\phi$ is the width of the ESC and the potential drop over the ESC, respectively. Because the conductivity in the ESC is small (few charge carriers), the potential drop over the ESC will be large. It follows that $\bar{\lambda}_\mathrm{D}^2(\partial_x\phi)^3 \gg \bar{\lambda}_\mathrm{D}^2\partial_x^3\phi$, and as discussed in the Supplemental Material, Sec. I C [40], it is therefore reasonable to neglect the $\bar{\lambda}_\mathrm{D}^2\partial_x^3\phi$ term in Eq. (13). We then end up with a simple algebraic equation for the electric field, valid in the left compartment outside the EDL:

$$1 + \frac{\bar{\lambda}_\mathrm{D}^2}{2(J_+ + J_\mathrm{w})}(\partial_x\phi)^3 = \left[\frac{J_+ - J_\mathrm{w}}{J_+ + J_\mathrm{w}}x - \frac{\kappa}{J_+ + J_\mathrm{w}}\right]\partial_x\phi. \tag{14}$$

Since $2\bar{\lambda}_\mathrm{D}^2\partial_x^3\phi = -\partial_x\rho_\mathrm{el}$ the above assumption corresponds to assuming a quasiuniform distribution of the charge density. This method of simplifying the problem has previously been used by Urtenov *et al.* [41] and dubbed the assumption of quasiuniform charge density distribution. However, so far this assumption has only been used to simplify numerical calculations, and not to obtain analytical solutions.

To simplify the analysis, we introduce a scaled electric field $\hat{E}$ and a scaled position $\hat{x}$, defined by

$$\hat{E} \equiv -B\partial_x\phi, \quad \text{with} \quad B \equiv \left[\frac{\bar{\lambda}_\mathrm{D}^2}{2(J_+ + J_\mathrm{w})}\right]^{1/3} \tag{15}$$

and

$$\hat{x} \equiv \frac{1}{B}\left[\frac{J_+ - J_\mathrm{w}}{J_+ + J_\mathrm{w}}x - \frac{\kappa}{J_+ + J_\mathrm{w}}\right]. \tag{16}$$

This enables us to recast Eq. (14) as

$$-1 + \hat{E}^3 = \hat{x}\hat{E}. \tag{17}$$

Before actually solving this equation, we can use it to derive some results characterizing the ESC. The scaled charge density $\hat{\rho}_\mathrm{el} = \partial_{\hat{x}}\hat{E}$ is found by implicit differentiation $3\hat{E}^2\partial_{\hat{x}}\hat{E} = \hat{E} + \hat{x}\partial_{\hat{x}}\hat{E}$, which results in

$$\partial_{\hat{x}}\hat{E} = \frac{\hat{E}}{3\hat{E}^2 - \hat{x}}. \tag{18}$$

Differentiating $\partial_{\hat{x}}\hat{E}$ again, it is found that the point of maximum charge density is at $\hat{x} = 0$ and that

$$\max(\hat{\rho}_\mathrm{el}) = \hat{\rho}_\mathrm{el}(0) = \tfrac{1}{3}. \tag{19}$$

The simple form of this result is due to Eq. (17) being trivial for $\hat{x} = 0$. The scaled charge density can be related to the unscaled charge density using

$$\rho_\mathrm{el} = -2\bar{\lambda}_\mathrm{D}^2\partial_x^2\phi = \frac{2\bar{\lambda}_\mathrm{D}^2}{B}\partial_x\hat{x}\partial_{\hat{x}}\hat{E}$$

$$= \left[32\bar{\lambda}_\mathrm{D}^2\frac{(J_+ - J_\mathrm{w})^3}{J_+ + J_\mathrm{w}}\right]^{1/3}\hat{\rho}_\mathrm{el}. \tag{20}$$

From Fig. 1 it is seen that the point of maximum charge density marks the left edge of the ESC. Inserting $\hat{x} = 0$ in Eq. (16) we find that the beginning of the ESC is at $x_\rho = \kappa/(J_+ - J_\mathrm{w})$, and therefore it has the width $1 - x_\rho$. For the studied system $\kappa \approx 1$, so for $J_+ - J_\mathrm{w}$ exceeding unity the extended space-charge region can make up a significant part of the channel. Inside the ESC, Eq. (17) yields $\hat{E} \sim \sqrt{\hat{x}}$ and the electric field scales as

$$-\partial_x\phi = \frac{\hat{E}}{B} \sim \frac{\sqrt{\hat{x}}}{B} = \frac{\sqrt{2}}{\bar{\lambda}_\mathrm{D}}\sqrt{(J_+ - J_\mathrm{w})x - \kappa}. \tag{21}$$

To leading order, these scalings are equivalent to others reported in the literature [12,39,44].

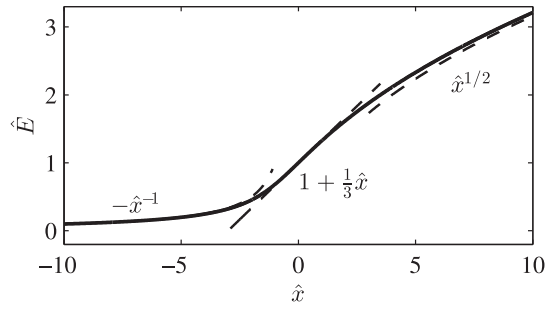

FIG. 2. Plot of scaled electric field $\hat{E}$ versus scaled position $\hat{x}$ (full line) from Eq. (23). The dashed lines show the limiting behavior for $\hat{x} \to -\infty$, $\hat{x} \to 0$, and $\hat{x} \to \infty$.

To proceed beyond this point, we write the general solution to Eq. (17):

$$\hat{E} = -\frac{1}{2^{1/3}}\left(-1+\sqrt{1-\frac{4}{27}\hat{x}^3}\right)^{1/3} e^{i\omega} - \frac{2^{1/3}}{3}\hat{x}\left(-1+\sqrt{1-\frac{4}{27}\hat{x}^3}\right)^{-1/3} e^{-i\omega}, \tag{22}$$

where $\omega = 0$, $\frac{2\pi}{3}$, or $\frac{4\pi}{3}$. We require that the solution is real and find

$$\hat{E} = \begin{cases} \hat{E}_- & \text{for} \quad \hat{x} \leqslant 0, \\ \hat{E}_+ & \text{for} \quad \hat{x} \geqslant 0, \end{cases} \tag{23}$$

which is continuous and differentiable at $\hat{x} = 0$ and where

$$\hat{E}_\pm = \pm\frac{1}{2^{1/3}}\left(\pm 1 \mp \sqrt{1-\frac{4}{27}\hat{x}^3}\right)^{1/3} \pm \frac{2^{1/3}}{3}\hat{x}\left(\pm 1 \mp \sqrt{1-\frac{4}{27}\hat{x}^3}\right)^{-1/3}. \tag{24}$$

In Fig. 2, the scaled electric field $\hat{E}$ is plotted for $-10 < \hat{x} < 10$ along with the asymptotic expressions.

It is noted that although this approach, like the method of matched asymptotic expansions [39,44,45], deals with different expressions inside and outside the ESC, the expressions used here are different branches of the same solution and as such they are matched by construction. This is a distinct advantage of the present approach, and it allows for an integration of the electric field to find the potential drop over the system.

We would like to relate the currents to the potential drop rather than the electric field. The task of integrating $\hat{E}$ is simplified considerably by using Eq. (18) to make a change of variable:

$$\hat{\phi} = -\int \hat{E}\, d\hat{x} = -\int \hat{E}\frac{1}{\partial_{\hat{x}}\hat{E}}\, d\hat{E} = -\int 2\hat{E}^2 + \frac{1}{\hat{E}}\, d\hat{E} = -\frac{2}{3}[\hat{E}^3 - \hat{E}^3(\hat{x}_0)] - \ln\left(\frac{\hat{E}}{\hat{E}(\hat{x}_0)}\right), \tag{25a}$$

where $\hat{x}_0 \equiv -\kappa/[B(J_+ + J_w)]$ [Eq. (16) with $x = 0$]. Equivalently, we define $\hat{x}_1 \equiv (J_+ - J_w - \kappa)/[B(J_+ + J_w)]$ [Eq. (16) with $x = 1$].

The unscaled potential ϕ is related to the scaled potential $\hat{\phi}$ as

$$\phi = \int \partial_x \phi\, dx = -\frac{1}{B}\frac{1}{\partial_x \hat{x}}\int \hat{E}\, d\hat{x} = j\hat{\phi}, \tag{25b}$$

where $j \equiv (J_+ + J_w)/(J_+ - J_w)$ has been introduced for convenience. At the inlet $\hat{E}$ is small so we can make the approximations $\hat{E}^3(\hat{x}_0) \approx 0$ and $\hat{E}(\hat{x}_0) \approx -\frac{1}{\hat{x}_0}$ and find the simpler expression

$$\phi \approx -\tfrac{2}{3} j\hat{E}^3 - j\ln(-\hat{E}\hat{x}_0). \tag{25c}$$

The cation concentration is obtained from Eq. (12),

$$c_+ = \frac{\bar{\lambda}_D^2}{B^2}\left[\frac{1}{2\hat{E}} + \frac{1}{j}\partial_{\hat{x}}\hat{E}\right], \tag{26a}$$

and since the anions are Boltzmann distributed,

$$c_- = e^{\phi} = e^{j\hat{\phi}}. \tag{26b}$$

To make the further calculation internally consistent, we again use $(1+\delta)c_H \approx 0$, and find from the Poisson equation that

$$c_w = c_+ - c_- - \rho_{el} = \frac{\bar{\lambda}_D^2}{B^2}\left[\frac{1}{2\hat{E}} - \frac{1}{j}\partial_{\hat{x}}\hat{E}\right] - e^{j\hat{\phi}}. \tag{26c}$$

In conclusion, our model gives analytical expressions for all the relevant fields ϕ, $c_\pm$, and c_w as a function of the position x and the salt- and water-ion currents J_+ and J_w. This part of the analysis is completely general and does not rely on the specific type of ion-selective interface; the nature of the ion-selective interface is only important for the behavior inside the EDL.

In the Supplemental Material [40], we provide an analysis of the limitations of the approximations employed in this section. We find that the derived expressions are valid when $\bar{\lambda}_D^2 J_+^2 \ll 1$ and $\bar{\lambda}_D \ll 1$. In the overlimiting regime, it also has to be the case that $\bar{\lambda}_D^{2/3} J_+^{-1/3} \ll 1$. We also find corrections to the theory which can extend its validity beyond these limits. However, for typical system parameters these corrections are minute, and for that reason we have chosen just to state them in the Supplemental Material [40].

B. Case without water-ion current

Initially, we consider the simple case of zero water-ion current $J_w = 0$. In this limit, the problem only depends on the parameter $\bar{\lambda}_D$ and the potential is given by Eq. (25). Since this result gives a closed-form expression for the potential, valid at both underlimiting and overlimiting currents, we consider it to be an extension of earlier asymptotic expressions, valid only in the overlimiting regime, given in Refs. [11,12].

To find the approximate dependence on $\bar{\lambda}_D$ we consider the limit $\hat{E}^3(\hat{x}_1) \gg 1$, for which $\hat{E}(\hat{x}_1)$ is given by $\hat{E}(\hat{x}_1) \approx \sqrt{\hat{x}_1}$ and the potential at $x = 1$ becomes

$$\phi(1) \approx -\frac{2}{3}\hat{x}_1^{3/2} - \ln(-\sqrt{\hat{x}_1}\hat{x}_0) = -\frac{2}{3}\left[\frac{2(J_+ - \kappa)^3}{\bar{\lambda}_D^2 J_+^2}\right]^{1/2} - \frac{1}{2}\ln\left[\frac{2(J_+ - \kappa)}{\bar{\lambda}_D^2 J_+^2}\right] \approx -\frac{2\sqrt{2}}{3}\frac{(J_+ - \kappa)^{3/2}}{\bar{\lambda}_D J_+} + \ln(\bar{\lambda}_D). \tag{27}$$

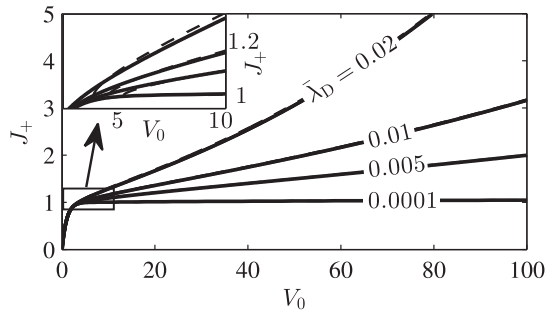

FIG. 3. Salt current J_+ plotted versus voltage V_0 in the case of vanishing water-ion current J_w and for $\kappa = 1$. Full line is the analytical expression (25), and the dashed line is the asymptotic expression (27). Only near the limiting current $J_+ \gtrsim 1$ do the two cases deviate appreciably (see the inset).

The first term on the right-hand side dominates, so for a given overlimiting current, the potential drop will roughly scale with $\bar{\lambda}_D^{-1}$. This agrees well with the intuitive picture, that the more strictly electroneutrality is enforced, the greater is the potential drop required to create the ESC and drive a current. In Fig. 3, the current is plotted versus the voltage difference for varying $\bar{\lambda}_D$ and $\kappa = 1$. The full analytical solution is shown with a full line and the asymptotic solution is shown with a dashed line (only for $J_+ > 1$).

C. Influence of water ions

To find a relation between J_+ and J_w, when water ions are taken into account, we need another constraint on one of the fields. It is, however, not apparent which constraint we should use or, for that matter, that a simple and physically justified constraint even exists. In the numerical simulations, as we shall later see, the value of J_w is determined self-consistently by simply requiring continuity of the fields through the membrane. The analytical model does, however, break down in the EDL, so this method of constraining J_w can not be employed here.

Instead, we use a boundary condition which is not entirely rigorous, but does have the appeal of being very simple. Let us consider Eq. (9b) in the ESC where diffusion is small compared to electromigration:

$$2J_w \approx -c_w \partial_x \phi. \tag{28}$$

There is a positive charge density in the ESC so the electric field increases for increasing x. Because J_w is divergence free, this in turn means that c_w must decrease for increasing x. However, c_w has a minimum value $\min(c_w) = 2\sqrt{\delta}n$ because of the relation Eq. (6), so at $x = 1$ we must always have $J_w \geqslant -\sqrt{\delta}n\partial_x\phi$. For all but the lowest currents (whose contributions are negligible), it seems that this is indeed the constraint which creates the water-ion current, i.e., we determine the water-ion current from

$$\partial_x \phi|_{x=1} = -\frac{J_w}{\sqrt{\delta}n}. \tag{29}$$

By inserting this in Eq. (14) and solving for J_+, we find a relation between J_+ and J_w:

$$J_+ = J_w \frac{\kappa + J_w + \frac{\bar{\lambda}_D^2}{2\delta n^2} J_w^2}{\sqrt{\delta}n + J_w}. \tag{30}$$

Using this relation together with Eq. (25), the current-voltage characteristic for the system can be evaluated for any set of parameters. We note that this boundary condition is the only place where the equilibrium constant enters in the analysis, so a more general treatment allowing the equilibrium constant to vary can be implemented by an appropriate modification of n in Eq. (30).

It is instructive to consider some limiting cases. For overlimiting currents, where $J_w \gg \sqrt{\delta}n$, Eq. (30) yields a simple expression for J_w in terms of J_+:

$$J_w \approx \frac{\delta n^2}{\bar{\lambda}_D^2}\left(-1 + \sqrt{1 + \frac{2\bar{\lambda}_D^2}{\delta n^2}(J_+ - \kappa)}\right). \tag{31}$$

Expanding this in the two limits $\frac{2\bar{\lambda}_D^2}{\delta n^2}(J_+ - \kappa) \sim \frac{\bar{\lambda}_D^2}{n^2} \ll 1$ and $\frac{2\bar{\lambda}_D^2}{\delta n^2}(J_+ - \kappa) \sim \frac{\bar{\lambda}_D^2}{n^2} \gg 1$, we find

$$J_w \approx \begin{cases} J_+ - \kappa & \text{for } \frac{\bar{\lambda}_D^2}{n^2} \ll 1, \\ \frac{\sqrt{2\delta}n}{\bar{\lambda}_D}\sqrt{J_+ - \kappa} & \text{for } \frac{\bar{\lambda}_D^2}{n^2} \gg 1. \end{cases} \tag{32}$$

The first of these limits we denote the Kharkats limit since he studied exactly the situation $J_+ = 1 + J_w$ where the overlimiting current is only due to screening by water ions [16]. The potential drop over the system is given by Eq. (25c), and using that $\hat{E}(\hat{x}_1) = -B\partial_x\phi|_{x=1} = B\frac{J_w}{\sqrt{\delta}n}$ we find

$$\begin{aligned}\phi(1) &\approx -\frac{2}{3}j\left(B\frac{J_w}{\sqrt{\delta}n}\right)^3 - j\ln\left(-B\frac{J_w}{\sqrt{\delta}n}\hat{x}_0\right) \\ &= -\frac{\bar{\lambda}_D^2}{3(J_+ - J_w)}\left(\frac{J_w}{\sqrt{\delta}n}\right)^3 - j\ln\left(\frac{J_w}{\sqrt{\delta}n}\frac{\kappa}{J_+ + J_w}\right).\end{aligned} \tag{33}$$

An interesting feature of this result is that even in the Kharkats limit $\bar{\lambda}_D^2/n^2 \ll 1$, where the entire overlimiting current is due to water-ion screening, the potential depends on $\bar{\lambda}_D$.

In the case of overlimiting current, the potential drop is determined by inserting Eq. (31) in Eq. (33). In the Kharkats limit $\bar{\lambda}_D^2/n^2 \ll 1$ given in Eq. (32), we obtain

$$\begin{aligned}\phi(1) \approx &-\frac{\bar{\lambda}_D^2}{3}\left(\frac{J_+ - \kappa}{\sqrt{\delta}n}\right)^3 \\ &-\left(\frac{2}{\kappa}J_+ - 1\right)\ln\left(\frac{J_+ - \kappa}{\sqrt{\delta}n}\frac{1}{2J_+ - \kappa}\right),\end{aligned} \tag{34a}$$

while in the opposite limit $\bar{\lambda}_D^2/n^2 \gg 1$ we find

$$\phi(1) \approx -\frac{2\sqrt{2}}{3}\frac{(J_+ - \kappa)^{3/2}}{\bar{\lambda}_D J_+} + \ln(\bar{\lambda}_D). \tag{34b}$$

A remarkable conclusion can immediately be drawn from these expressions. In the limit $\bar{\lambda}_D^2/n^2 \ll 1$, the potential drop for a given normalized current J_+ is seen to increase with $\bar{\lambda}_D$. This is opposite to the conclusion in the $J_w = 0$ analysis, and it can be viewed as a result of the coupling between J_w and

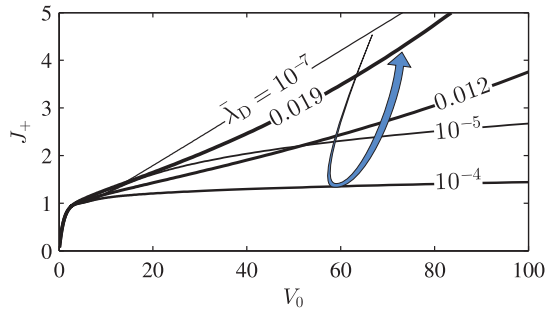

FIG. 4. (Color online) Salt current J_+ from Eqs. (25) and (30) plotted versus voltage V_0 for $n = 10^{-4}$, $\kappa = 1$, and $\bar{\lambda}_D$ varying from 10^{-7} (thin) to 0.019 (thick). The curved arrow indicates the nonmonotonous dependence on $\bar{\lambda}_D$.

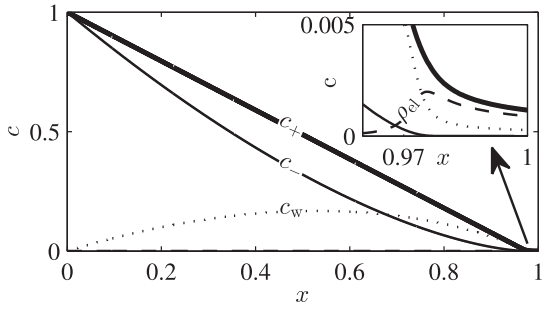

FIG. 5. The analytical expression [Eq. (26)] for the concentration fields c_+, c_-, c_w, and ρ_{el} plotted versus position x for $n = 10^{-4}$, $\bar{\lambda}_D = 10^{-4}$, $\kappa = 1$, and $J_w = 0.3$. The corresponding salt current is found from Eq. (30) to be $J_+ = 1.325$. The inset shows the behavior in the ESC close to the membrane.

$\partial_x\phi$, which is brought about by the boundary condition (29). We also see that the potential drop scales inversely with n as expected.

In the other limit $\bar{\lambda}_D^2/n^2 \gg 1$, we recover the $\bar{\lambda}_D^{-1}$ scaling from the $J_w = 0$ analysis as well as the ϕ expression (27). The potential drop over the system will thus have a nonmonotonous dependence on $\bar{\lambda}_D$. This behavior is seen in Fig. 4, where the salt current J_+ is plotted versus voltage for fixed n and varying $\bar{\lambda}_D$. It is seen that for some parameter values, e.g., $\bar{\lambda}_D = 10^{-5}$ we obtain the characteristic S-shaped current-voltage curve found in experiments [8,26,46,47]. This indicates, at least on a qualitative level, that the developed model captures the relevant physics of the problem.

D. Concentration fields

The concentration fields found in our analysis exhibit a very rich structure, and it is generally difficult to describe their behavior in simple terms.

In Fig. 5, the concentration fields are shown for a given set of parameters. Outside the ESC, the fields behave as in the simple LEN theory, with c_+ decreasing linearly with x, c_- scaling as $(c_+)^j$, and c_w given by the difference $c_+ - c_-$:

$$c_+ \approx \kappa - (J_+ - J_w)x, \tag{35a}$$

$$c_- \approx [\kappa - (J_+ - J_w)x]^j, \tag{35b}$$

$$c_w \approx \kappa - (J_+ - J_w)x - [\kappa - (J_+ - J_w)x]^j. \tag{35c}$$

Since J_w is determined via Eq. (30), these seemingly simple relations do in fact have a quite complicated dependence on all of the parameters J_+, $\bar{\lambda}_D$, and n. It is seen that the expressions break down inside the extended space-charge region $x > x_\rho = \kappa/(J_+ - J_w)$.

In the ESC, the existence of a nonzero charge density complicates matters further. The charge density has a peak at the beginning of the ESC,

$$\rho_{el}(x_\rho) = \tfrac{2}{3}2^{2/3}\bar{\lambda}_D^{2/3}(J_+ - J_w)(J_+ + J_w)^{-1/3}, \tag{36a}$$

and in the ESC it decays as

$$\rho_{el} \approx 2^{1/2}\bar{\lambda}_D(J_+ - J_w)[(J_+ - J_w)x - \kappa]^{-1/2}. \tag{36b}$$

In the limit $\bar{\lambda}_D^2/n^2 \gg 1$, where the influence of water ions is negligible, the expressions simplify as

$$\rho_{el}(x_\rho) \approx \tfrac{2}{3}2^{2/3}\bar{\lambda}_D^{2/3}J_+^{2/3}, \tag{37a}$$

$$\rho_{el} \approx 2^{1/2}\bar{\lambda}_D J_+ (J_+ x - \kappa)^{-1/2}. \tag{37b}$$

In this case, both the peak charge density and the charge density inside the ESC increase with J_+.

In the Kharkats limit $\bar{\lambda}_D^2/n^2 \ll 1$, where $J_+ \approx \kappa + J_w$, the charge density at x_ρ simplifies as

$$\rho_{el}(x_\rho) \approx \tfrac{2}{3}2^{2/3}\bar{\lambda}_D^{2/3}\kappa\,(2J_+ - \kappa)^{-1/3}. \tag{38a}$$

Here, the peak charge density surprisingly decreases with increasing J_+. Also, in this limit the ESC will be very small since $x_\rho = \kappa/(J_+ - J_w) \approx 1$. The reduction in width and magnitude of the ESC will act to suppress EOI in the $\bar{\lambda}_D^2/n^2 \ll 1$ limit. This is similar to the effect of current-induced membrane discharge as described in Ref. [17]. In the literature it has been reported that EOI sets in around $V_0 = 20$ [48]. As seen from Fig. 4 and the results in Sec. V B, water splitting sets in at a lower voltage, which leads us to believe that a suppression of EOI will in fact occur in this limit.

E. Total potential drop

The developed analytical model gives a general description, valid for any ion-selective interface, of the inlet compartment outside the EDL. To enable comparison with the numerical simulations of a membrane system, a simple model for the potential drop over the remainder of the system is developed.

Inside the membrane there is a very large density N_m of immobile negative charges. To screen these charges, an equally large density of positive ions accumulates. It follows that the conductivity in the membrane is very large, so that the potential drop over the membrane is negligible compared to the other potential drops in the system. While the potential drop inside the membrane can safely be neglected, the potential drops $\Delta\phi_{m1}$ and $\Delta\phi_{m2}$ over the two membrane interfaces are in general non-negligible. To determine them, we use the assumption of quasiequilibrium to relate the concentrations just outside the membrane to the concentrations inside the membrane via a Boltzmann factor. Charge neutrality in the

membrane then gives

$$0 = -N_m + \epsilon_P(c_+ - c_- + c_H - c_{OH}) \approx -N_m + \epsilon_P[c_+(1) + c_H(1)]\, e^{-\Delta\phi_{m1}}, \quad (39)$$

where we used that the concentration of anions in the membrane is negligible. The same argument applies to both membrane interfaces, so the total potential change across the membrane is

$$\Delta\phi_m = \ln\left(\frac{c_+(1) + c_H(1)}{c_+(1+\alpha) + c_H(1+\alpha)}\right). \quad (40)$$

In the outlet channel, local charge neutrality is an excellent approximation and the water-ion current is totally dominated by hydronium. From the transport equations [Eqs. (1) and (2)], we therefore find

$$c_+ + c_H = c_- = c_R e^{\phi+V_0}, \quad (41a)$$

$$c_R + \left(J_+ + \frac{J_w}{\delta}\right)(1 + \alpha + \beta - x) = c_R e^{\phi+V_0}. \quad (41b)$$

Here, we used that $1+\alpha < x < 1+\alpha+\beta$ in the outlet channel and $\phi(1+\alpha+\beta) = -V_0$. In conclusion, the total potential drop across the entire system is

$$V_0 = -[\phi(1) - \phi(0)] - \Delta\phi_m - [\phi(1+\alpha+\beta) - \phi(1+\alpha)] = -\phi(1) - \ln[c_+(1) + c_H(1)] + 2\ln\left[c_R + \beta\left(J_+ + \frac{J_w}{\delta}\right)\right], \quad (42)$$

where $\phi(1)$ is given in Eq. (25), c_+ and c_H are given in Eq. (26), and the relation between the currents is given in Eq. (30). It is seen that in the limit $\beta = 0$ and $c_R = 1$, the potential drop is just the change in electrochemical potential of the positive ions from inlet reservoir to membrane.

V. NUMERICAL SIMULATIONS

A. Numerical implementation

The numerical simulations are carried out in the commercially available finite element software COMSOL MULTIPHYSICS (ver. 4.3a). Following Gregersen *et al.* [49], the equations (1), (2), (5), (6), (7a), and (8) are rewritten in weak form and implemented in the mathematics module of COMSOL. In the numerical simulations and in the comparisons with theory we have used $\alpha = \beta = 1$ and $c_R = 1$. This choice only gives a small loss of generality since the results are weakly sensitive to these values, as seen from Eq. (42). We use the following boundary conditions: $c_\pm(0) = 1$, $c_H(0) = c_{OH}(0) = n$, $\phi(0) = 0$ and $c_\pm(3) = 1$, $c_H(3) = c_{OH}(3) = n$, and $\phi(3) = -V_0$. To improve the numerical stability of the problem, we have made a change of variable, so that the logarithm of the concentration fields have been used as dependent variables instead of the concentration fields themselves.

The code has been successfully validated both against known analytical results in various special cases, and by performing careful mesh-convergence analyses as in Ref. [49]. Subsequently, the model system has been solved for c_0 increasing from 0.1 to 100 mM in six steps and for L increasing from 1 μm to 10 mm in eight steps. Thus, a total of 63 configurations have been investigated. For each set of parameters, the bias voltage V_0 was varied from 0 to 100 in 160 steps (smaller steps at small V_0). In total, this resulted in 10 080 data points of which 8056 have an overlimiting current $J_+ > 1$.

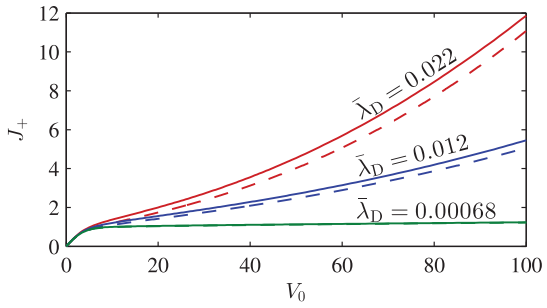

FIG. 6. (Color online) Salt current J_+ plotted versus voltage V_0 for varying $\bar{\lambda}_D$ neglecting the water-ion current J_w. The full lines are numerical simulations and the dashed lines are the corresponding analytical results from Eq. (42) for $\kappa = 1$ and with Eqs. (25) and (26) inserted.

B. Numerical results

First, we present the results for the case without water ions. In this case, the problem only depends on one parameter, namely, $\bar{\lambda}_D$. In Fig. 6, the salt current J_+ is plotted versus the bias voltage V_0 for three values of $\bar{\lambda}_D$ (full lines). It should be noted that the normalization current is different for the three cases. The analytical expression from Eq. (42) with Eqs. (25) and (26) inserted is also shown (dashed lines). For small $\bar{\lambda}_D$, the current saturates at the limiting current as found in the LEN analysis, while significant deviation from the LEN expression is found for larger $\bar{\lambda}_D$ values. The seen deviations from the LEN expression agree well with our expectation that in the limit of very large $\bar{\lambda}_D$, a linear I-V curve should result.

The analytical I-V curves are seen to agree well with the numerical results. The main reason for the small discrepancy is that the width of the EDL becomes non-negligible for large $\bar{\lambda}_D$, and therefore the length L^* begins to deviate significantly from the assumed value $L^* = 1$. The wide range of values of $\bar{\lambda}_D$, where the approximation $L^* = 1$ is valid, is determined in the Supplemental Material, Sec. I A [40].

When water ions are taken into account, the problem depends on the normalized equilibrium constant $n = \sqrt{K_w}/c_0$ and the normalized Debye length $\bar{\lambda}_D$. In Fig. 7, the current-voltage curves are plotted for varying n and for two different values of $\bar{\lambda}_D$. The analytical expression Eq. (42) with Eqs. (25), (26), and (30) inserted is also shown with dashed lines. The light curves shown in the figures are the water-ion currents J_w, and it is seen that the salt currents J_+ nearly equal the classical limiting current plus the water-ion current. This is as expected from Eq. (32) since all the considered cases are in the Kharkats limit $\bar{\lambda}_D^2/n^2 \ll 1$. It is seen that several of the curves exhibit the characteristic S shape found in experiments [8,26,46,47]. An interesting observation is that there is a family of curves, an example being the $n = 3.2 \times 10^{-4}$ curve in Fig. 7(a), for which the overlimiting current closely resembles the overlimiting

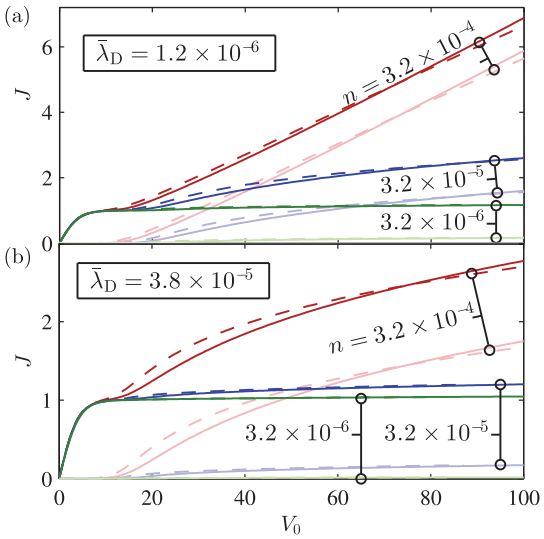

FIG. 7. (Color online) (a) Salt current J_+ (dark) and water-ion current J_w (light) plotted versus voltage V_0 for $\bar{\lambda}_D = 1.2 \times 10^{-6}$ and $n = 3.2 \times 10^{-6}$, 3.2×10^{-5}, and 3.2×10^{-4}. The full lines are numerical simulations and the dashed lines are the corresponding analytical results from Eq. (42) for $\kappa = 1$ and with Eqs. (25), (26), and (30) inserted. (b) Same as above, but with $\bar{\lambda}_D = 3.8 \times 10^{-5}$.

current caused by EOI [9,14]. These curves are, however, found in the $\bar{\lambda}_D^2/n^2 \ll 1$ limit where EOI is suppressed. During a measurement series, where the concentration is varied, one might therefore go from a EOI dominated regime to a water-ion current dominated regime, without observing significant qualitative differences in the I-V curves.

From the analysis in Sec. IV C, it is clear that the overlimiting current may be due to either screening by water ions or the development of an extended space-charge region. Which effect is dominant depends on the parameters of the problem. To illustrate this dependence, the overlimiting current

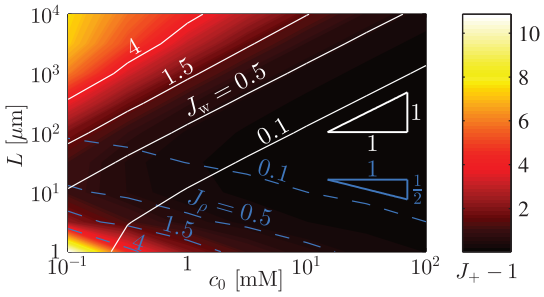

FIG. 8. (Color online) Numerically calculated color plot from 0 (black) to 10.8 (white) of the overlimiting salt current $J_+ - 1 = J_\rho + J_w$ at $V_0 = 100$ as a function of the reservoir concentration c_0 and the compartment length L. The full lines indicate contours $J_w = 0.1$, 0.5, 1.5, and 4.0. The dashed lines are contours for the current due to the extended space-charge region $J_\rho = 0.1$, 0.5, 1.5, and 4.0. The slope indications (triangles) show the approximate scalings $L \sim c_0^{-1/2}$ for the J_ρ contours and $L \sim c_0$ for the J_w contours from Eqs. (34b) and (34a), respectively. The following parameter values were used in converting from n and $\bar{\lambda}_D$ to c_0 and L: $\epsilon_w = 6.90 \times 10^{-10}$ F/m, $V_T = 25.8$ mV, $e = 1.602 \times 10^{-19}$ C, and $K_w = 10^{-14}$ M^2.

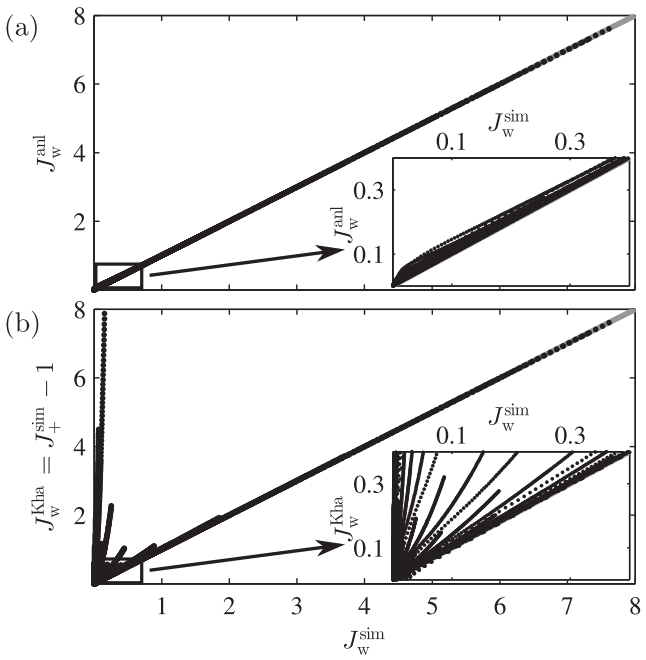

FIG. 9. (a) The analytical water-ion current J_w^{anl} from Eq. (30) with $\kappa = 1$ plotted versus the simulated water-ion current J_w^{sim} for the 8056 sets of values for $\bar{\lambda}_D$, n, and J_+, as defined in the last paragraph of Sec. V A, all having an overlimiting current $J_+ > 1$. The inset zooms in on the zero-current limit. (b) Same as above, except that J_w^{anl} is substituted by the Kharkats expression $J_w^{Kha} = J_+^{sim} - 1$.

at $V_0 = 100$ is plotted in Fig. 8 along with contour lines showing the current due to water-ion screening J_w (white), and charge neutrality violation $J_\rho = J_+ - 1 - J_w$ (dark).

In the following, we make a more systematic comparison between the analytical model and the results of the numerical simulation. We begin by evaluating the model for water splitting. For each set of parameters $\bar{\lambda}_D$, n, and J_+ used in the simulations the water-ion current J_w was calculated using Eq. (30), and in Fig. 9(a) it is plotted versus the water-ion current which was actually observed in the simulations. Only the cases $J_+ > 1$ are shown since J_w nearly vanishes in the underlimiting regime. It is seen that the developed model captures the majority of the dependence. To better appreciate the level of agreement, the simple Kharkats result $J_w^{Kha} = J_+ - 1$ is shown in Fig. 9(b).

The total model giving the current-voltage relation for the system has also been evaluated. In Fig. 10, the salt current has been calculated according to Eqs. (25), (26), (30), and (42) and plotted versus the salt current obtained from simulations using the same parameter values. There is seen to be some scatter around perfect agreement between the two models, but the overall behavior is definitely captured by the analytical model.

VI. ADDITION OF ACID OR BASE

So far, we have investigated systems where the ions derive from a dissolved salt. We will now proceed with a more general treatment, where we allow for some concentration of acid c_a or base c_b in the reservoirs in analogy with Ref. [50]. The acid or

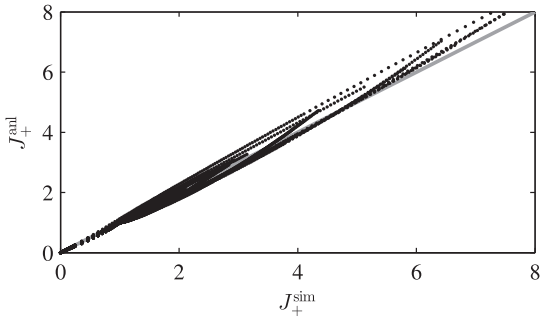

FIG. 10. The analytical salt current J_+^{anl} from Eqs. (25), (26), (30), and (42) with $\kappa = 1$ plotted versus the simulated salt current J_+^{sim} for all 1080 sets of values for $\bar{\lambda}_{\mathrm{D}}$, n, and V_0, as defined in the last paragraph of Sec. V A.

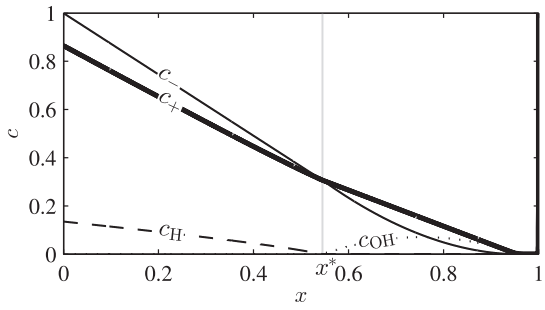

FIG. 11. Numerical simulation of the concentrations of salt ions (c_+ and c_-) and water ions (c_{OH} and c_{H}) plotted versus position x in a system with acid concentration $c_{\mathrm{a}} = 0.135$ and voltage drop $V_0 = 100$. For $x < x^*$ (left of the vertical gray line), hydronium behaves as a conserved cation, and the system is well described by a LEN model. For $x > x^*$ hydroxide is the dominant water ion, and the system behaves as the aqueous salt solution analyzed in Sec. IV.

base is assumed to be strong so that it dissociates completely, and for simplicity we assume that the conjugate base to the acid is the same as the negative salt ion and that the conjugate acid to the base is the same as the positive salt ion. For instance, the salt could be NaCl, the acid HCl, and the base NaOH. We use $\kappa = 1$ throughout this section.

First, we consider a system where some concentration c_{b} of base is added to the system. The ion concentrations are normalized with the total cation concentration at the inlet, i.e., the sum of the salt and the base concentrations. We thus have $c_+(0) = 1$, $c_-(0) = 1 - c_{\mathrm{b}}$, and $c_{\mathrm{OH}}(0) = c_{\mathrm{b}}$. Like in Sec. IV, hydroxide dominates over hydronium, so the relevant transport equation for the water ions is [Eq. (9b)]

$$2J_{\mathrm{w}} \approx \partial_x c_{\mathrm{w}} - c_{\mathrm{w}} \partial_x \phi, \tag{43}$$

but with the difference that $c_{\mathrm{w}}(0) = c_{\mathrm{b}}$ rather than $c_{\mathrm{w}}(0) = (1+\delta)n \approx 0$. We can rewrite the transport equation

$$\begin{aligned} 2J_{\mathrm{w}} &\approx \partial_x c_{\mathrm{w}} - c_{\mathrm{w}} \partial_x \phi \\ &= \partial_x (c_{\mathrm{w}} - c_{\mathrm{b}} e^{\phi}) - (c_{\mathrm{w}} - c_{\mathrm{b}} e^{\phi}) \partial_x \phi \\ &= \partial_x c'_{\mathrm{w}} - c'_{\mathrm{w}} \partial_x \phi, \end{aligned} \tag{44}$$

where $c'_{\mathrm{w}} \equiv c_{\mathrm{w}} - c_{\mathrm{b}} e^{\phi}$ and $c'_{\mathrm{w}}(0) = 0$. The $c_{\mathrm{b}} e^{\phi}$ term behaves exactly like the stationary salt anions, suggesting the introduction of $c'_- \equiv c_- + c_{\mathrm{b}} e^{\phi}$ with $c'_-(0) = 1$.

In conclusion, the present problem can be mapped onto the problem in Sec. IV. Adding a base to a system is therefore equivalent to adding a salt of its conjugate acid. It is noted that to the right of the membrane hydronium dominates the water-ion transport, so in this region it will make a slight difference to add a base to the reservoir.

The situation becomes more complex when an acid is added to the reservoir. In this case, two quite different situations can result, depending on the amount of added acid. For high acid concentrations, the amount of hydronium ions suppress water splitting at the membrane, and the hydronium ions essentially act as a conserved cation. For low acid concentrations, hydroxide may begin to dominate the water-ion transport at some point and water splitting can occur as in the treatment in Sec. IV. In Fig. 11, this situation is illustrated.

To quantify what is meant by "high" and "low" acid concentrations, we analyze the system in more detail. From Fig. 11 it is seen that there are two distinct regions in the solution. To the left hydronium dominates and there is local electroneutrality, while the right part of the channel is equivalent to the system analyzed in Sec. IV. In the left part of the channel, it is easily found that the concentration fields are given as

$$c_- = e^{\phi} = 1 - (J_+ + J_{\mathrm{w}}/\delta)x, \tag{45a}$$

$$c_{\mathrm{H}} = \frac{J_{\mathrm{w}}/\delta}{J_+ + J_{\mathrm{w}}/\delta} e^{\phi} + \left[c_{\mathrm{a}} - \frac{J_{\mathrm{w}}/\delta}{J_+ + J_{\mathrm{w}}/\delta} \right] e^{-\phi}, \tag{45b}$$

$$c_+ = \frac{J_+}{J_+ + J_{\mathrm{w}}/\delta} e^{\phi} + \left[1 - c_{\mathrm{a}} - \frac{J_+}{J_+ + J_{\mathrm{w}}/\delta} \right] e^{-\phi}, \tag{45c}$$

where the concentration fields are normalized with the sum of the acid and salt concentrations at the inlet and c_{a} is the normalized acid concentration at the inlet. In the limit where there is no water splitting at the membrane, the currents are just related via the reservoir concentrations of hydronium and salt cation

$$\frac{J_{\mathrm{w}}/\delta}{J_+} = \frac{c_{\mathrm{a}}}{1 - c_{\mathrm{a}}}, \quad \text{no water splitting.} \tag{46}$$

If there is water splitting, there will be a transition point x^* where the hydronium concentration vanishes. Solving Eqs. (45a) and (45b) for x^* we find

$$x^* = \frac{1}{J_+ + J_{\mathrm{w}}/\delta} \left[1 - \sqrt{1 - \frac{J_+ + J_{\mathrm{w}}/\delta}{J_{\mathrm{w}}/\delta} c_{\mathrm{a}}} \right]. \tag{47}$$

At that point, the salt concentration is

$$c^* \equiv c_+(x^*) = c_-(x^*) = \sqrt{1 - \frac{J_+ + J_{\mathrm{w}}/\delta}{J_{\mathrm{w}}/\delta} c_{\mathrm{a}}}. \tag{48}$$

In the right part of the channel, the electric field is determined by Eq. (14) corrected with the new boundary conditions (47) and (48):

$$1 + \frac{\bar{\lambda}_{\mathrm{D}}^2 (\partial_x \phi)^3}{2(J_+ + J_{\mathrm{w}})} = \left[\frac{J_+ - J_{\mathrm{w}}}{J_+ + J_{\mathrm{w}}} (x - x^*) - \frac{c^*}{J_+ + J_{\mathrm{w}}} \right] \partial_x \phi. \tag{49}$$

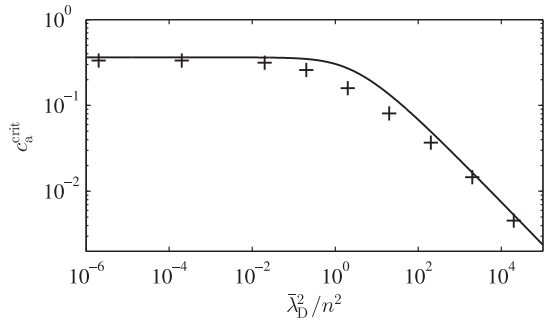

FIG. 12. The critical value c_a^{crit} of the acid concentration, corresponding to the onset of water-splitting suppression, plotted versus $\bar{\lambda}_D^2/n^2$. The full line is the analytical expression given in Eq. (52), and the points "+" denote results from numerical simulations.

Inserting the boundary condition (29) and introducing $G \equiv \frac{J_w/\delta}{J_+}$ this equation can be recast as a quadratic equation for J_+:

$$\frac{\bar{\lambda}_D^2}{2}\left(\frac{\sqrt{\delta}G}{n}\right)^3 J_+^2 - (1-\delta G)\left(\frac{\sqrt{\delta}G}{n}\right)J_+ = -\left[\frac{1-\delta G}{1+G}(1-c^*)+c^*\right]\left(\frac{\sqrt{\delta}G}{n}\right)+(1+\delta G). \quad (50)$$

Just at the point where water splitting begins, G will still equal $\frac{c_a}{1-c_a}$ as in Eq. (46) and c^* will be very close to 0. Furthermore, the terms with $(\frac{\sqrt{\delta}G}{n})$ dominate over the term $1+\delta G$, so near that point we can simplify the equation as

$$\frac{\bar{\lambda}_D^2}{2}\left(\frac{\sqrt{\delta}G}{n}\right)^2 J_+^2 - (1-\delta G)J_+ \approx -\frac{1-\delta G}{1+G}. \quad (51)$$

This equation has a solution when the determinant is nonnegative, i.e., when

$$\frac{c_a}{1-c_a} = G \leqslant \frac{1-\delta+\sqrt{(1-\delta)^2+4\delta\left(1+2\bar{\lambda}_D^2/n^2\right)}}{2\delta\left(1+2\bar{\lambda}_D^2/n^2\right)}. \quad (52)$$

For higher values of c_a, there are no solutions which allow for water splitting. The value of c_a for which there is an equal sign in Eq. (52), corresponding to the onset of water-splitting suppression, is denoted the critical acid concentration c_a^{crit}. In Fig. 12, analytical and numerical results for the critical acid concentration are plotted versus $\bar{\lambda}_D^2/n^2$. Numerically, the critical concentration is determined as follows. When there is no water splitting, the currents are related as in Eq. (46). The critical concentration is then defined to be the minimum value of c_a for which $\frac{J_w/\delta}{J_+} \geqslant 1.01\frac{c_a}{1-c_a}$, within the voltage sweep interval $0 < V_0 < 100$.

The existence of a critical acid concentration, and its approximate value, is expected to be a robust prediction, which is valid even under circumstances where the assumption of an equilibrated water-dissociation reaction breaks down.

VII. GENERALIZATION TO OTHER SYSTEMS

The analysis in this paper has so far been concerned with the reservoir-compartment-membrane-compartment-reservoir system sketched in Fig. 1. The difficult part of the analysis, carried out in Sec. IV A, is however largely system independent, and in this section we show examples of generalizations to other systems.

In Sec. IV A, we find the potential drop over the inlet compartment as a function of the currents. The only other parameters we use in the analysis are the reservoir salt concentration $c_+(0) = c_-(0) = 1$ and water-ion concentration $c_H(0) = c_{OH}(0) = n \approx 0$. By modifying these boundary conditions appropriately, the results for the already studied system can be related to other systems exhibiting concentration polarization. We give two such examples in the following.

A. Membrane-compartment-membrane system

We consider a system composed of a compartment of normalized length unity with cation-selective membranes on either side. In the compartment is an electrolyte of normalized concentration unity.

Whereas the membranes in an electrodialysis cell alternate between cation and anion selectivity [1], both membranes in this system have the same selectivity. We can thus regard this system as the symmetrical counterpart to the asymmetric electrodialysis cell. With respect to the symmetry, the system has similarities to those studied in Refs. [39,45,51], except for the fact that they have electrodes as ion-selective elements rather than membranes.

Due to the ion-selective membranes, the anions can not leave the compartment, and we have the constraint

$$\int_0^1 c_-\,dx = 1, \quad (53)$$

instead of the boundary condition $c_-(0) = 1$ from before. As in the original analysis, we only consider the part of the system lying outside the quasiequilibrium EDL's adjoining the membranes. Since hydronium dominates inside the membranes and hydroxide dominates in the compartment, there is a crossover approximately at $x = 0$ where the concentrations are equal $c_H(0) = c_{OH}(0) = n \approx 0$ as in the earlier analysis. Our task is now to find a value of κ which is consistent with the constraint in Eq. (53). We use that the anion concentration is negligible outside the LEN region, and to a good approximation we therefore have

$$\int_0^1 c_-dx = \int_0^1 c_-^{LEN}dx. \quad (54)$$

Inserting from Eq. (35b) we obtain

$$\int_0^1 c_-^{LEN}dx = \int_0^{\min\{1,\kappa/(J_+-J_w)\}} [\kappa-(J_+-J_w)x]^j dx = \begin{cases} \frac{\kappa^{j+1}}{2J_+} & \text{for} \quad \kappa \leqslant (J_+-J_w), \\ \frac{\kappa^{j+1}}{2J_+} - \frac{[\kappa-(J_+-J_w)]^{j+1}}{2J_+} & \text{for} \quad \kappa \geqslant (J_+-J_w). \end{cases} \quad (55)$$

The lower case corresponds to the underlimiting case where water splitting is negligible. In that case, we can simplify as

$$\int_0^1 c_-^{\mathrm{LEN}} dx \approx \kappa - \frac{J_+}{2} \quad \text{for} \quad \kappa \gg (J_+ - J_{\mathrm{w}}). \tag{56}$$

From the constraint we then find

$$\kappa = \begin{cases} (2J_+)^{\frac{J_+ - J_{\mathrm{w}}}{2J_+}} & \text{for} \quad 2 \lesssim J_+, \\ 1 + \frac{J_+}{2} & \text{for} \quad 2 \gtrsim J_+. \end{cases} \tag{57}$$

With this expression for κ the boundary condition (29) yields a transcendental equation for the relation between J_+ and J_{w}. Using this relation together with Eq. (25), the I-V curve for the system can be found. In the case of negligible water-ion current, the I-V curve can be obtained directly by inserting Eq. (57) in Eq. (25).

B. Electrode-compartment-electrode system

We consider a system composed of a compartment of normalized length unity with electrodes on either side. In the compartment is an electrolyte of normalized concentration unity. The electrolyte is formed by dissolving a salt of the electrode metal, which in the case of copper electrodes could be $CuSO_4$. Since only the metal ions can enter or leave the electrodes, the electrodes act as ion-selective elements similarly to the previously studied membranes. This system is similar to those studied in Refs. [39,45,51]. However, we do not consider the potential drops in the EDL's adjoining the electrodes. As before, the anions (here SO_4^-) can not leave the system so we have the constraint

$$\int_0^1 c_- dx = 1. \tag{58}$$

So far, the system is equivalent to the membrane-compartment-membrane system. However, whereas the membranes are only sensitive to the charge of the ions, the electrodes also select based on the ion species. This implies that the hydronium ions can not leave the system either, and they will accumulate in the left part of the compartment while hydroxide accumulates to the right. We can put this in terms of a constraint by noting that hydronium and hydroxide are created in equal amounts

$$\int_0^1 c_{\mathrm{H}} dx = \int_0^1 c_{\mathrm{OH}} dx. \tag{59}$$

In Sec. VI, we treated a system where hydronium dominates to the left due to the addition of an amount of acid c_{a} to the reservoir. By letting c_{a} vary to satisfy Eq. (59) and letting κ vary to satisfy Eq. (58), we can therefore map the present problem onto the original reservoir-compartment-membrane-compartment-reservoir problem. Because of the need to split the system into a hydronium dominated part and a hydroxide dominated part, this mapping is however significantly more involved than the one in Sec. VII A. For this reason, we will not bring the full analysis here, but we note that it is in principle a simple matter which mainly requires some bookkeeping with the different regions.

VIII. DISCUSSION

The results presented in this paper are based on the assumption of a locally equilibrated water-dissociation reaction. Whether this assumption is correct is at present not known, but since our theoretical predictions rely on this assumption, an experimental test of our predictions would constitute a (partial) test of the underlying assumptions.

From the analytical model, several useful results are obtained. Our main theoretical result Eq. (25) provides the potential $\phi(1)$ at the beginning of the EDL, for a general ion-selective interface with both a water-ion current and the extended space-charge region taken into account. In certain limits, this result can be simplified to Eq. (34). The effects of water splitting are accounted for by Eq. (30), which provides a relation between the salt current J_+ and the water-ion current J_{w}.

The potential drop across the EDL and the rest of the system depends on the specific ion-selective interface and gives a small correction to the potential. For the specific ion-selective membrane system studied in this work, these corrections are included in Eq. (42), and in Sec. VII we show examples of generalizations to other systems. The model also provides the detailed structure of the extended space-charge region and yields the simple expression Eq. (20) for the maximum value of the charge density ρ_{el}. The analytical model has been successfully tested against direct numerical simulations (see, e.g., Fig. 10 containing a plot of J_+^{anl} versus J_+^{sim}).

Even if the fundamental assumption of a locally equilibrated water-dissociation reaction is not entirely correct, the analytical model is still useful since it provides an upper bound to the water-ion current, as long as the equilibrium constant K_{w} does not change appreciably. For instance, Fig. 8 shows that in a large portion of the parameter space the influence of water ions is negligible. Since this is an upper bound, we can conclude that water splitting is unimportant for these parameter values regardless of the reaction speed. As described in Sec. IV C, it would be a relatively simple matter to extend the analysis to allow for a varying K_{w}.

A strength of the analysis given in this paper is that several of the derived expressions are comparatively easy to test experimentally since they only depend on a few parameters which can either be estimated or fitted. Consider, for instance, Eq. (31) for the water-ion current J_{w}, which in dimensionful terms can be rewritten as $\tilde{J}_{\mathrm{w}}$:

$$\tilde{J}_{\mathrm{w}} \approx \frac{2D_{\mathrm{OH}}}{\gamma D_+}\left[-1 + \sqrt{1 + \gamma\left(\frac{\tilde{J}_+}{J_{\mathrm{lim}}} - 1\right)}\right] J_{\mathrm{lim}}, \tag{60}$$

where $J_{\mathrm{lim}} = 2D_+ c_0/L$ is the limiting current, and where $\gamma = (D_{\mathrm{OH}}/D_{\mathrm{H}})\, c_0 \epsilon_{\mathrm{w}} k_{\mathrm{B}} T/(L^2 K_{\mathrm{w}} e^2)$ is a dimensionless parameter. Given knowledge of the reservoir concentration c_0 and the length L of the diffusive boundary layer, it is possible to calculate γ and J_{lim} from the definitions. Since Eq. (60) is derived under the assumption of an equilibrated water-dissociation reaction, a set of experimental data which fits it would corroborate that assumption and our model.

Another prediction which can be experimentally tested is the existence of a critical acid concentration $c_{\mathrm{a}}^{\mathrm{crit}}$ for the onset of water-splitting suppression, which may be tested

experimentally using the titration method [26,27]. For acid concentrations c_a above c_a^{crit}, we predict that the water-ion current and the salt current will be proportional. When c_a is reduced below c_a^{crit}, given by Eq. (52), the water-ion current will begin to exceed the value given by Eq. (46). If, instead, a base is added to the system, we predict that there will be no such critical concentration, and adding an amount of base will in fact be equivalent to adding the same amount of salt. It should be noted that these predictions assume that an added acid or base does not significantly alter the properties of the membrane through chemical reactions. For a chemically stable membrane such as nafion, this should be a good assumption.

In the analytical treatment, it was found that water splitting will act to suppress EOI in the limit of $\bar{\lambda}_D^2/n^2 \ll 1$. We have not verified this prediction by full 3D numerical simulations of EOI, but since water splitting begins at a lower voltage than EOI, it is likely that a suppression of EOI will in fact occur.

Lastly, we emphasize the simplicity and versatility of the employed mathematical method. The reduction of the problem to the simple algebraic equation (17) for the electric field hugely simplifies the analysis and gives a good description of the ESC not involving singularities: unlike in the method of matched asymptotic expansions, the fields in this approach do not diverge at the entrance to the ESC, and for this reason closed-form expressions for every relevant quantity can be obtained with ease.

IX. CONCLUSION

In this paper, we have developed analytical and numerical models for the current through and the voltage drop across an ion-selective interface, taking into account both the effect of the extended space-charge region adjoining the interface as well as the effect of water splitting and screening by water ions. Specifically, we have investigated the transport through an ion-selective membrane, but the fundamental results apply to any ion-selective interface.

The fundamental assumption in the analysis is that the autodissociation of water happens on a much shorter time scale than the transport of water ions, i.e., we study transport-limited processes. The validity of this assumption is dependent on the particular system under study, but in general the model gives an upper bound to the currents which can be obtained, given a fixed equilibrium constant K_w, for the water-splitting reaction.

In the analytical model, the assumption of quasiuniform charge density distribution has been used to simplify the treatment. The analytical and the numerical models compare favorably and both models exhibit some of the characteristic behavior observed in experiments. The developed analytical model is readily testable in experiments, as it gives both detailed expressions for the current-voltage characteristics, simple scaling laws with few parameters, and predictions about the system behavior upon addition of an acid or a base.

[1] V. V. Nikonenko, N. D. Pismenskaya, E. I. Belova, P. Sistat, P. Huguet, G. Pourcelly, and C. Larchet, Adv. Colloid Interface Sci. **160**, 101 (2010).

[2] S. J. Kim, S. H. Ko, K. H. Kang, and J. Han, Nat. Nanotechnol. **5**, 297 (2010).

[3] M. Park, X. Zhang, M. Chung, G. B. Less, and A. M. Sastry, J. Power Sources **195**, 7904 (2010).

[4] M. Winter and R. J. Brodd, Chem. Rev. **104**, 4245 (2004).

[5] P. Malek, J. M. Ortiz, B. S. Richards, and A. I. Schaefer, J. Membr. Sci. **435**, 99 (2013).

[6] Y. Tanaka, H. Uchino, and M. Murakami, Membr. Water Treat. **3**, 63 (2012).

[7] V. Etacheri, R. Marom, R. Elazari, G. Salitra, and D. Aurbach, Energy Environ. Sci. **4**, 3243 (2011).

[8] M. Taky, G. Pourcelly, F. Lebon, and C. Gavach, J. Electroanal. Chem. **336**, 171 (1992).

[9] F. Maletzki, H. W. Rösler, and E. Staude, J. Membr. Sci. **71**, 105 (1992).

[10] W. H. Smyrl and J. Newman, Trans. Faraday Soc. **63**, 207 (1967).

[11] I. Rubinstein and L. Shtilman, J. Chem. Soc., Faraday Trans. 2 **75**, 231 (1979).

[12] E. Yariv, Phys. Rev. E **80**, 051201 (2009).

[13] I. Rubinstein and B. Zaltzman, Phys. Rev. E **62**, 2238 (2000).

[14] I. Rubinshtein, B. Zaltzman, J. Pretz, and C. Linder, Russ. J. Electrochem. **38**, 853 (2002).

[15] I. Rubinstein, J. Phys. Chem. **81**, 1431 (1977).

[16] Y. I. Kharkats, J. Electroanal Chem. **105**, 97 (1979).

[17] M. B. Andersen, M. van Soestbergen, A. Mani, H. Bruus, P. M. Biesheuvel, and M. Z. Bazant, Phys. Rev. Lett. **109**, 108301 (2012).

[18] E. V. Dydek, B. Zaltzman, I. Rubinstein, D. S. Deng, A. Mani, and M. Z. Bazant, Phys. Rev. Lett. **107**, 118301 (2011).

[19] S. H. Behrens and D. G. Grier, J. Chem. Phys. **115**, 6716 (2001).

[20] W. B. S. de Lint, P. M. Biesheuvel, and H. Verweij, J. Colloid Interface Sci. **251**, 131 (2002).

[21] K. L. Jensen, J. T. Kristensen, A. M. Crumrine, M. B. Andersen, H. Bruus, and S. Pennathur, Phys. Rev. E **83**, 056307 (2011).

[22] M. B. Andersen, J. Frey, S. Pennathur, and H. Bruus, J. Colloid Interface Sci. **353**, 301 (2011).

[23] M. Block and J. A. Kitchener, J. Electrochem. Soc. **113**, 947 (1966).

[24] A. A. Sonin and G. Grossman, J. Phys. Chem. **76**, 3996 (1972).

[25] R. Simons, Electrochim. Acta **30**, 275 (1985).

[26] V. V. Nikonenko, N. D. Pismenskaya, and E. I. Volodina, Russ. J. Electrochem. **41**, 1205 (2005).

[27] V. I. Zabolotsky, V. V. Nikonenko, N. D. Pismenskaya, E. V. Laktionov, M. K. Urtenov, H. Strathmann, M. Wessling, and G. H. Koops, Sep. Purif. Technol. **14**, 255 (1998).

[28] Y. Tanaka and M. Seno, J. Chem. Soc., Faraday Trans. 1 **82**, 2065 (1986).

[29] V. Mavrov, W. Pusch, O. Kominek, and S. Wheelwright, Desalination **91**, 225 (1993).

[30] Y. Tanaka, J. Membr. Sci. **350**, 347 (2010).

[31] R. Simons, Desalination **28**, 41 (1979).

[32] L. Jialin, W. Yazhen, Y. Changying, L. Guangdou, and S. Hong, J. Membr. Sci. **147**, 247 (1998).

[33] R. Simons, Electrochim. Acta **29**, 151 (1984).

[34] C.-O. Danielsson, A. Dahlkild, A. Velin, and M. Behm, Electrochim. Acta **54**, 2983 (2009).

[35] V. I. Zabolotskii, V. V. Nikonenko, N. M. Korzhenko, R. R. Seidov, and M. K. Urtenov, Russ. J. Electrochem. **38**, 810 (2002).
[36] C. Heitner-Wirguin, J. Membr. Sci. **120**, 1 (1996).
[37] T. Xu, J. Membr. Sci. **263**, 1 (2005).
[38] R. Nagarale, G. Gohil, and V. K. Shahi, Adv. Colloid Interface Sci. **119**, 97 (2006).
[39] K. T. Chu and M. Z. Bazant, SIAM J. Appl. Math. **65**, 1485 (2005).
[40] See Supplemental Material at http://link.aps.org/supplemental/10.1103/PhysRevE.89.042405 for an assessment of the impact of each approximation and the limits of its applicability.
[41] M. Urtenov, E. V. Kirillova, N. M. Seidova, and V. V. Nikonenko, J. Phys. Chem. B **111**, 14208 (2007).
[42] J. Newman, Trans. Faraday Soc. **61**, 2229 (1965).
[43] L. Højgaard Olesen, M. Z. Bazant, and H. Bruus, Phys. Rev. E **82**, 011501 (2010).
[44] A. S. Khair, Phys. Fluids **23**, 072003 (2011).
[45] M. Z. Bazant, K. T. Chu, and B. J. Bayly, SIAM J. Appl. Math. **65**, 1463 (2005).
[46] J. J. Krol, M. Wessling, and H. Strathmann, J. Membr. Sci. **162**, 145 (1999).
[47] M. Taky, G. Pourcelly, and C. Gavach, J. Electroanal. Chem. **336**, 195 (1992).
[48] C. L. Druzgalski, M. B. Andersen, and A. Mani, Phys. Fluids **25**, 110804 (2013).
[49] M. M. Gregersen, M. B. Andersen, G. Soni, C. Meinhart, and H. Bruus, Phys. Rev. E **79**, 066316 (2009).
[50] Y. I. Kharkats and A. V. Sokirko, J. Electroanal. Chem. **303**, 27 (1991).
[51] E. Yariv, SIAM J. Appl. Math. **71**, 2131 (2011).

Appendix F

Paper published in Phys Rev E

Title: Concentration polarization, surface currents, and bulk advection in a microchannel

Authors: Christoffer P. Nielsen and Henrik Bruus.

Reference: Published in Physical Review E **90**, 043020 (2014) (14 pages)

Concentration polarization, surface currents, and bulk advection in a microchannel

Christoffer P. Nielsen* and Henrik Bruus†
Department of Physics, Technical University of Denmark, DTU Physics Building 309, DK-2800 Kongens Lyngby, Denmark
(Received 20 August 2014; published 29 October 2014)

We present a comprehensive analysis of salt transport and overlimiting currents in a microchannel during concentration polarization. We have carried out full numerical simulations of the coupled Poisson-Nernst-Planck-Stokes problem governing the transport and rationalized the behavior of the system. A remarkable outcome of the investigations is the discovery of strong couplings between bulk advection and the surface current; without a surface current, bulk advection is strongly suppressed. The numerical simulations are supplemented by analytical models valid in the long channel limit as well as in the limit of negligible surface charge. By including the effects of diffusion and advection in the diffuse part of the electric double layers, we extend a recently published analytical model of overlimiting current due to surface conduction.

DOI: 10.1103/PhysRevE.90.043020 PACS number(s): 47.57.jd, 82.39.Wj, 66.10.−x, 47.61.−k

I. INTRODUCTION

Concentration polarization at electrodes or electrodialysis membranes has been an active field of study for many decades [1–3]. In particular, the nature and origin of the so-called overlimiting current, exceeding the diffusion-limited current, has attracted attention. A number of different mechanisms have been suggested as an explanation for this overlimiting current, most of which are probably important for some system configuration or another. The suggested mechanisms include bulk conduction through the extended space-charge region [4,5], current induced membrane discharge [6], water-splitting effects [7,8], electro-osmotic instability [9,10], and, most recently, electrohydrodynamic chaos [11,12].

In recent years, concentration polarization in the context of microsystems has gathered increasing interest [13–17]. This interest has been spurred both by the implications for battery [18] and fuel cell technology [19–21] and by the potential applications in water desalinization [22] and solute preconcentration [23–25]. In microsystems, surface effects are comparatively important, and for this reason their behavior fundamentally differs from bulk systems. For instance, an entirely new mode of overlimiting current enabled by surface conduction has been predicted by Dydek *et al.* [26,27], for which the current exceeding the diffusion-limited current runs through the depletion region inside the diffuse double layers screening the surface charges. This gives rise to an overlimiting current depending linearly on the surface charge, the surface-to-bulk ratio, and the applied potential. In addition to carrying a current, the moving ions in the diffuse double layers exert a force on the liquid medium, and thereby they create an electro-diffusio-osmotic flow in the channel. This fluid flow in turn affects the transport of ions, and the resulting Poisson-Nernst-Planck-Stokes problem has strong nonlinear couplings among diffusion, electromigration, electrostatics, and advection. While different aspects of the problem can be, and have been, treated analytically [28–30], the fully coupled system is in general too complex to allow for a simple analytical description.

In this paper we carry out full numerical simulations of the coupled Poisson-Nernst-Planck-Stokes problem, and in this way we are able to give a comprehensive description of the transport properties and the role of electro-diffusio-osmosis in microchannels during concentration polarization. To supplement the full numerical model, and to allow for fast computation of large systems, we also derive and solve an accurate boundary layer model. We rationalize the results in terms of three key quantities: the Debye length $\bar{\lambda}_D$ normalized by the channel radius, the surface charge ρ_s averaged over the channel cross section, and the channel aspect ratio α. In the limit of low aspect ratio we derive and verify a simple analytical expression for the current-voltage characteristic, which includes electromigration, diffusion, and advection in the diffuse double layers. The overlimiting conductance found in this model is approximately 3 times larger than the conductance found in Ref. [26], where diffusion and advection in the diffuse double layers is neglected. In the limit of negligible surface charge the numerical results agree with our previous analytical model [8] for the overlimiting current due to an extended space-charge region.

It has been shown in several papers that reactions between hydronium ions and surface groups can play an important role for the surface charge density and for the transport in microsystems [31–34]. This is especially true in systems exhibiting concentration polarization, as strong pH gradients often occur in such systems. However, in this work we limit ourselves to the case of constant surface charge density and defer the treatment of surface charge dynamics to future work.

II. THE MODEL SYSTEM

Our model system consists of a straight cylindrical microchannel of radius R and length L filled with an aqueous salt solution, which for simplicity is assumed binary and symmetric with valences Z and concentration fields c_+ and c_-. A reservoir having salt concentration c_0 is attached to one end of the channel and a cation-selective membrane to the other end. On the other side of the cation-selective membrane is another reservoir, but due to its relatively simple properties, this part of the system needs not be explicitly modeled and is only represented by an appropriate membrane boundary condition. The channel walls have a uniform surface charge

*chnie@fysik.dtu.dk
†bruus@fysik.dtu.dk

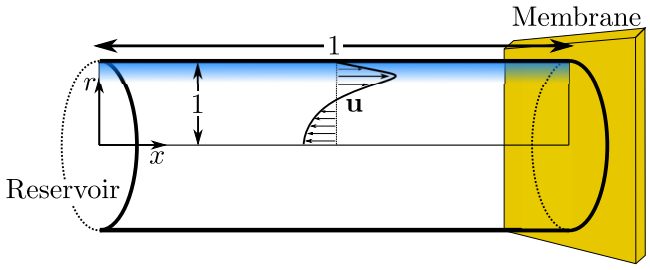

FIG. 1. (Color online) A sketch of the axisymmetric 2D system studied in this work. A microchannel of normalized length and radius unity connects a reservoir to the left to a cation-selective membrane to the right. To the right of the membrane is another reservoir, but this part of the system is only modeled through boundary conditions. The diffuse double layer adjoining the wall is shown as a shaded (blue) area and the arrows indicate a velocity field deriving from electro-diffusio-osmosis with back-pressure.

density σ, which is screened by the salt ions in the liquid over the characteristic length λ_D. In Fig. 1 a sketch of the system is shown. The diffuse double layer adjoining the wall is shown as a shaded (blue) area, and the arrows indicate a velocity field deriving from electro-diffusio-osmosis with back-pressure. We assume cylindrical symmetry and we can therefore reduce the full three-dimensional (3D) problem to a two-dimensional (2D) problem.

III. GOVERNING EQUATIONS

A. Nondimensionalization

In this work we use nondimensional variables, which are listed in Table I together with their normalizations. We further introduce the channel aspect ratio α and the nondimensional gradient operator $\boldsymbol{\nabla}$,

$$\alpha = \frac{R}{L}, \tag{1a}$$

$$\boldsymbol{\nabla} = \alpha \boldsymbol{e}_x \partial_x + \boldsymbol{e}_r \partial_r. \tag{1b}$$

TABLE I. Normalizations used in this work. c_0 is the reservoir concentration, Z is the valence of the ions, V_T is the thermal voltage, k_B is the Boltzmann constant, U_0 is a characteristic electro-osmotic velocity, ϵ_w is the permittivity of water, η is the viscosity of water, and D_+ and D_- are the diffusivities of the negative and positive ions, respectively.

Variable	Symbol	Normalization
Ion concentration	$c_\pm$	c_0
Electric potential	ϕ	$V_T = k_B T/(Ze)$
Electrochemical potential	$\mu_\pm$	$k_B T$
Current density	$\boldsymbol{J}_\pm$	$2D_+c_0/L$
Velocity	$\boldsymbol{u}$	$U_0 = \epsilon_w V_T^2/(\eta L)$
Pressure	p	$\eta U_0/R$
Body force density	$\boldsymbol{f}$	$c_0 k_B T/R$
Radial coordinate	r	R
Axial coordinate	x	L
Time	t	$R^2/(2D_+)$

B. Bulk equations

The nondimensional current density $\boldsymbol{J}_\pm$ of each ionic species of concentration $c_\pm$ is given by the electrochemical potentials $\mu_\pm$ and normalization Péclet numbers $\mathrm{Pe}^0_\pm$,

$$2\alpha \frac{D_+}{D_\pm} \boldsymbol{J}_\pm = -c_\pm \boldsymbol{\nabla}\mu_\pm + \alpha \mathrm{Pe}^0_\pm c_\pm \boldsymbol{u}, \tag{2a}$$

$$\mathrm{Pe}^0_\pm = \frac{LU_0}{D_\pm} = \frac{\epsilon_w V_T^2}{\eta D_\pm}. \tag{2b}$$

For dilute solutions, $\mu_\pm$ can be written as the sum of an ideal gas contribution and the electrostatic potential ϕ,

$$\mu_\pm = \ln(c_\pm) \pm \phi. \tag{2c}$$

In the absence of reactions, the ions are conserved, and the nondimensional Nernst-Planck equations read

$$\partial_t c_\pm = -\alpha \boldsymbol{\nabla} \cdot \boldsymbol{J}_\pm. \tag{3}$$

The Poisson equation governs ϕ,

$$\nabla^2 \phi = -\frac{1}{2}\frac{R^2}{\lambda_D^2}(c_+ - c_-) = -\frac{1}{2\bar{\lambda}_D^2}(c_+ - c_-), \tag{4}$$

where $\bar{\lambda}_D = \lambda_D/R$ is the normalized Debye length, for which $\lambda_D = \sqrt{k_B T \epsilon_w/(2Z^2 e^2 c_0)}$ is evaluated for the reservoir concentration c_0. Finally, we have the Stokes and continuity equations governing the velocity field $\boldsymbol{u}$, with x and r components u and v and the pressure p,

$$\frac{1}{\mathrm{Sc}}\partial_t \boldsymbol{u} = -\boldsymbol{\nabla} p + \nabla^2 \boldsymbol{u} + \frac{1}{2\alpha\bar{\lambda}_D^2}\boldsymbol{f}, \tag{5a}$$

$$0 = \boldsymbol{\nabla} \cdot \boldsymbol{u}. \tag{5b}$$

Here $\mathrm{Sc} = \eta/(\rho D_+)$ is the Schmidt number and $\boldsymbol{f}$ is the body force density acting on the fluid.

C. Thermodynamic forces

In an electrokinetic problem, there are essentially two ways of treating the thermodynamic forces driving the ion transport: The transport is viewed either as a result of diffusive and electric forces or as a result of gradients in the electrochemical potential. While the outcome of both approaches is the same, there are some advantages in choosing a certain viewpoint for a specific problem. As the form of Eq. (2a) suggests, we favor the electrochemical viewpoint in many parts of this paper.

In Fig. 2, a sketch of the model system is shown. The system consists of a reservoir on the left, which is connected to another reservoir to the right through a microchannel and an ion-selective membrane. An electric potential difference V_0 is applied between the two reservoirs. Typically, the electrical potential drop in the membrane interior is negligible due to the large number of charge carriers in this region, while it varies significantly across the quasiequilibrium double layers at the membrane interfaces, an effect known as Donnan potential drops [35]. In contrast, the cation electrochemical potential is nearly constant across the quasiequilibrium double layers and thus also across the entire membrane. Unless we want to explicitly model the membrane and the adjoining double layers, it is therefore much more convenient to use

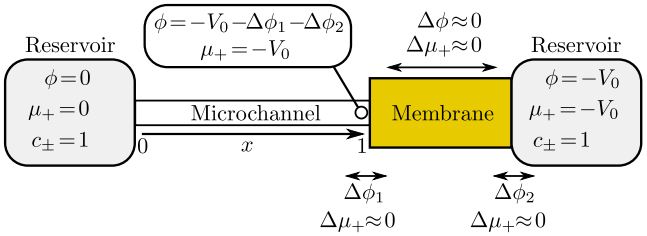

FIG. 2. (Color online) Sketch of the full physical system including both reservoirs of equal salt concentration. An electric potential difference V_0 is applied between the reservoirs, and the changes in electrochemical and electrical potential across the membrane and adjoining Donnan layers are indicated.

the electrochemical potential as control parameter than the electric potential.

Inside the microchannel there are also some advantages of emphasizing the electrochemical potentials. The diffuse double layers screening the surface charges are very close to local equilibrium, meaning that the electrochemical potentials are nearly constant across them. The gradients $\nabla\mu_\pm$ in electrochemical potentials therefore only have components tangential to the wall, and these components do not vary significantly with the distance from the wall. In contrast, diffusion and electromigration have components in both directions which vary greatly in magnitude through the diffuse double layers.

The electrochemical potentials also offer a convenient way of expressing the body force density $\boldsymbol{f}$ from Eq. (5a). Conventionally, the body force density is set to be the electrostatic force density $-\rho_{\rm el}\nabla\phi = -(c_+ - c_-)\nabla\phi$. By considering the forces on each constituent we can, however, formulate the problem in a way that is more convenient and better reveals the physics of the problem. The force acting on each particle is minus the gradient of its electrochemical potential. The force density can therefore be written as

$$\boldsymbol{f} = -c_+\nabla\mu_+ - c_-\nabla\mu_- - c_{\rm w}\nabla\mu_{\rm w}, \tag{6}$$

where $c_{\rm w} \gg c_\pm$ and $\mu_{\rm w}$ is the concentration and chemical potential of water, respectively. As opposed to $\mu_\pm$ given by the ideal gas Eq. (2c), $\mu_{\rm w}$ depends linearly on $c_\pm$ [36],

$$\mu_{\rm w} = -\frac{c_+ + c_-}{c_{\rm w}}, \tag{7a}$$

$$\boldsymbol{f} = -c_+\nabla\mu_+ - c_-\nabla\mu_- + \nabla(c_+ + c_-). \tag{7b}$$

If we insert the expressions for $\mu_\pm$, the force density reduces, as it should, to the usual electrostatic force density. It is, however, advantageous to keep the force density on this form, because it reveals the origin of each part of the force. For instance, if we insert a membrane which is impenetrable to ions, only the last term $\nabla(c_+ + c_-)$ in the force can drive a flow across the membrane, because the other forces are transmitted to the liquid via the motion of the ions. It is thus easy to identify $-(c_+ + c_-)$ as the osmotic pressure in the solution. Inserting Eq. (7b) for the force $\boldsymbol{f}$ in Eq. (5a) and absorbing the osmotic pressure into the new pressure $p' = p - (c_+ + c_-)$, we obtain

$$\frac{1}{\rm Sc}\partial_t\boldsymbol{u} = -\nabla p' + \nabla^2\boldsymbol{u} - \frac{1}{2\alpha\bar{\lambda}_{\rm D}^2}\left[c_+\nabla\mu_+ + c_-\nabla\mu_-\right]. \tag{8}$$

We could of course have absorbed any number of gradient terms into the pressure, but we have chosen this particular form of the Stokes equation due to its convenience when studying electrokinetics. In electrokinetics, electric double layers are ubiquitous, and since the electrochemical potentials are constant through the diffuse part of the electric double layers, the driving force in Eq. (8) is comparatively simple. Also, in this formulation there is no pressure buildup in the diffuse double layers. Both of these features simplify the numerical and analytical treatment of the problem.

D. Boundary conditions

To supplement the bulk equations (3), (4), (5b), and (8), we specify boundary conditions on the channel walls, at the reservoir, and at the membrane.

At the reservoir $x = 0$ we require that the flow $\boldsymbol{u}$ is unidirectional along the x axis, and at the channel wall $r = 1$ as well as at the membrane surface $x = 1$ we impose a no-slip boundary condition,

$$\boldsymbol{u} = u\,\boldsymbol{e}_x, \quad \text{at } x = 0, \tag{9a}$$

$$\boldsymbol{u} = \boldsymbol{0}, \quad \text{at } r = 1 \text{ or } x = 1. \tag{9b}$$

To find the distribution of the potential ϕ at the reservoir $x = 0$, we use the assumption of transverse equilibrium in the Poisson equation (4),

$$\frac{1}{r}\partial_r\left(r\partial_r\phi\right) = \frac{1}{\bar{\lambda}_{\rm D}^2}\sinh\phi, \quad \text{at } x = 0. \tag{10a}$$

Here $\alpha^2\partial_x^2\phi$ in $\nabla^2\phi$ is neglected in comparison with the large curvature $\frac{1}{r}\partial_r\left(r\partial_r\phi\right)$ in the r direction. The boundary conditions for ϕ are a symmetry condition on the cylinder axis $r = 0$, and a surface charge boundary condition at the wall $r = 1$,

$$\partial_r\phi = 0, \quad \text{at } r = 0, \tag{10b}$$

$$\boldsymbol{e}_r\cdot\nabla\phi = -\frac{R\sigma}{V_{\rm T}\epsilon_{\rm w}} = \frac{\rho_{\rm s}}{4}\frac{1}{\bar{\lambda}_{\rm D}^2}, \quad \text{at } r = 1. \tag{10c}$$

The parameter $\rho_{\rm s}$ is defined as

$$\rho_{\rm s} = -\frac{2\sigma}{zec_0R}, \tag{10d}$$

and physically it is the average charge density in a channel cross section, which is required to compensate the surface charge density. As explained in Ref. [26], $\rho_{\rm s}$ is closely related to the overlimiting conductance in the limit of negligible advection.

The boundary conditions for the ions are impenetrable channel walls at $r = 1$, and the membrane at $x = 1$ is impenetrable to anions while it allows cations to pass,

$$\boldsymbol{e}_r\cdot\boldsymbol{J}_\pm = 0, \quad \text{at } r = 1, \tag{11a}$$

$$\boldsymbol{e}_x\cdot\boldsymbol{J}_- = 0, \quad \text{at } x = 1. \tag{11b}$$

Next to the membrane there is a quasiequilibrium diffuse double layer, in which the cation concentration increases from the channel concentration to the concentration inside the membrane. Right where this double layer begins, there is a minimum in cation concentration, and we chose this as the

TABLE II. The models employed in this paper.

Abbreviation	Name	Described in
FULL	Full model (numerical)	Sec. III
BNDF	Boundary layer model, full (numerical)	Sec. IV
BNDS	Boundary layer model, slip (numerical)	Sec. IV
ASCA	Analytical model, surface conduction-advection	Sec. VC
ASC	Analytical model, surface conduction	Sec. VD
ABLK	Analytical model, bulk conduction	Sec. VE

boundary condition on the cations, i.e.,

$$\boldsymbol{e}_x \cdot \nabla c_+ = 0, \quad \text{at } x = 1. \tag{11c}$$

The last boundary conditions relate to $\mu_\pm$ and p'. At the reservoir $x = 0$, we require transverse equilibrium of the ions, which also leads to the pressure being constant,

$$\mu_\pm = 0, \quad \text{at } x = 0, \tag{12a}$$

$$p' = 0, \quad \text{at } x = 0. \tag{12b}$$

Finally, as discussed in Sec. III C, μ_+ at the membrane $x = 1$ is set by V_0,

$$\mu_+ = -V_0, \quad \text{at } x = 1. \tag{12c}$$

The above governing equations and boundary conditions completely specify the problem and enable a numerical solution of the full Poisson-Nernst-Planck-Stokes problem with couplings between advection, electrostatics, and ion transport. In the remainder of the paper we refer to the model specified in this section as the full model (FULL). See Table II for a list of all numerical and analytical models employed in this paper. An issue with the FULL model is that for many systems the computational costs of resolving the diffuse double layers and solving the nonlinear system of equations are prohibitively high. We are therefore motivated to investigate simpler ways of modeling the system, and this is the topic of the following section.

IV. BOUNDARY LAYER MODELS

To simplify the problem, we divide the system into a locally electroneutral bulk system and a thin region near the walls comprising the charged diffuse part of the double layer. The influence of the double layers on the bulk system is included via a surface current inside the boundary layer and an electro-diffusio-osmotic slip velocity.

To properly divide the variables into surface and bulk variables, we again consider the electrochemical potentials. In the limit of long and narrow channels the electrolyte is in transverse equilibrium, and the electrochemical potentials vary only along the x direction,

$$\mu_\pm(x) = \ln[c_\pm(x,r)] \pm \phi(x,r). \tag{13a}$$

Since the left-hand side is independent of r, it must be possible to pull out the x-dependent parts of $\ln[c_\pm(x,r)]$ and $\phi(x,r)$. We denote these parts $\bar{c}_\pm(x)$ and $\phi_{\text{bulk}}(x)$, respectively, and find

$$\mu_\pm(x) = \ln[\bar{c}_\pm(x)] + \ln\left[\frac{c_\pm(x,r)}{\bar{c}_\pm(x)}\right] \pm \phi_{\text{bulk}}(x) \pm \phi_{\text{eq}}(x,r), \tag{13b}$$

where the equilibrium potential $\phi_{\text{eq}}(x,r)$ is the remainder of the electric potential, $\phi_{\text{eq}} = \phi - \phi_{\text{bulk}}$. The r dependent parts must compensate each other, which implies a Boltzmann distribution of the ions in the r direction,

$$c_\pm(x,r) = \bar{c}_\pm(x) e^{\mp\phi_{\text{eq}}(x,r)}. \tag{13c}$$

The remainder of the electrochemical potentials is then

$$\mu_\pm(x) = \ln[\bar{c}_\pm(x)] \pm \phi_{\text{bulk}}(x). \tag{13d}$$

For further simplification, we assume that electroneutrality is only violated to compensate the surface charges, i.e., $\bar{c}_+ = \bar{c}_- = \bar{c}$. As long as surface conduction or electro-diffusio-osmosis causes some overlimiting current this is a quite good assumption, because in that case the bulk system is not driven hard enough to cause any significant deviation from charge neutrality. For thin diffuse double layers, $\bar{c}$ corresponds to the ion concentration at $r = 0$. However, if the Debye length is larger than the radius, $\bar{c}$ does not actually correspond to a concentration which can be found anywhere in the cross section, and for this reason $\bar{c}$ is often called the virtual salt concentration [28].

To describe the general case, where transverse equilibrium is not satisfied in each cross section, we must allow the bulk potential ϕ_{bulk} to vary in both the x and r directions. Then, however, the simple picture outlined above fails partially, and, consequently, we make the ansatz

$$c_\pm(x,r) = \bar{c}(x) e^{\mp\phi_{\text{eq}}(x,r)} + c'(x,r), \tag{14a}$$

where $c'(x,r)$ accounts for the deviations from transverse equilibrium. Close to the walls, i.e., in or near the diffuse double layer, we therefore have $c'(x,r) \approx 0$. Inserting this ansatz in Eqs. (2a) and (2c), the currents become

$$\begin{aligned} 2\alpha \frac{D_+}{D_\pm} \boldsymbol{J}_\pm &= -\nabla c_\pm \mp c_\pm \nabla\phi + \alpha \mathrm{Pe}^0_\pm c_\pm \boldsymbol{u} \\ &= -\nabla c' - e^{\mp\phi_{\text{eq}}} \nabla\bar{c} \mp \bar{c} e^{\mp\phi_{\text{eq}}} \nabla\phi_{\text{bulk}} \\ &\quad \mp c' \nabla(\phi_{\text{bulk}} + \phi_{\text{eq}}) + (\bar{c} e^{\mp\phi_{\text{eq}}} + c')\alpha \mathrm{Pe}^0_\pm \boldsymbol{u} \\ &= -\nabla(\bar{c} + c') \mp (\bar{c} + c')\nabla\phi_{\text{bulk}} \\ &\quad + (\bar{c} + c')\alpha \mathrm{Pe}^0_\pm \boldsymbol{u} \\ &\quad - (e^{\mp\phi_{\text{eq}}} - 1)\nabla\bar{c} \mp \bar{c}(e^{\mp\phi_{\text{eq}}} - 1)\nabla\phi_{\text{bulk}} \\ &\quad \mp c' \nabla\phi_{\text{eq}} + \bar{c}(e^{\mp\phi_{\text{eq}}} - 1)\alpha \mathrm{Pe}^0_\pm \boldsymbol{u}. \end{aligned} \tag{14b}$$

From $\boldsymbol{J}_\pm$, we construct two useful linear combinations, $\boldsymbol{J}_{\text{sum}}$ and $\boldsymbol{J}_{\text{dif}}$, as follows:

$$\begin{aligned} \alpha \boldsymbol{J}_{\text{sum}} &= \alpha\left(\boldsymbol{J}_+ + \frac{D_+}{D_-}\boldsymbol{J}_-\right) \\ &= -\nabla(\bar{c} + c') + \alpha \frac{\mathrm{Pe}^0_+ + \mathrm{Pe}^0_-}{2}(\bar{c} + c')\boldsymbol{u} \end{aligned}$$

$$- (\cosh\phi_{eq} - 1)\nabla\bar{c} + \bar{c}\sinh\phi_{eq}\nabla\phi_{bulk}$$
$$+ \alpha\left[\frac{Pe_+^0}{2}(e^{-\phi_{eq}} - 1) + \frac{Pe_-^0}{2}(e^{\phi_{eq}} - 1)\right]\bar{c}\boldsymbol{u}, \quad (15a)$$

$$\alpha \boldsymbol{J}_{dif} = \alpha\left(\boldsymbol{J}_+ - \frac{D_+}{D_-}\boldsymbol{J}_-\right)$$
$$= -(\bar{c} + c')\nabla\phi_{bulk} + \alpha\frac{Pe_+^0 - Pe_-^0}{2}(\bar{c} + c')\boldsymbol{u}$$
$$+ \sinh\phi_{eq}\nabla\bar{c} - (\cosh\phi_{eq} - 1)\,\bar{c}\nabla\phi_{bulk} - c'\nabla\phi_{eq}$$
$$+ \alpha\left[\frac{Pe_+^0}{2}(e^{-\phi_{eq}} - 1) - \frac{Pe_-^0}{2}(e^{\phi_{eq}} - 1)\right]\bar{c}\boldsymbol{u}. \quad (15b)$$

The gradient of ϕ_{eq} is only significant in the diffuse double layer, where, by construction, $c' \approx 0$. We therefore neglect the $-c'\nabla\phi_{eq}$ term in the expression for $\boldsymbol{J}_{dif}$. It is seen that for thin diffuse double layers the terms involving exponentials of ϕ_{eq} are much larger near the wall than in the bulk. For this reason we divide the currents into bulk and surface currents,

$$\boldsymbol{J}_{sum} = \boldsymbol{J}_{sum}^{bulk} + \boldsymbol{J}_{sum}^{surf}, \quad (16a)$$
$$\boldsymbol{J}_{dif} = \boldsymbol{J}_{dif}^{bulk} + \boldsymbol{J}_{dif}^{surf}. \quad (16b)$$

Here the bulk currents are just the electroneutral parts,

$$\alpha\boldsymbol{J}_{sum}^{bulk} = -\nabla c + \alpha Pe^0 c\boldsymbol{u}, \quad (17a)$$
$$\alpha\boldsymbol{J}_{dif}^{bulk} = -c\nabla\phi_{bulk} + \alpha\frac{1 - \delta_D}{1 + \delta_D}Pe^0 c\boldsymbol{u}, \quad (17b)$$

with $Pe^0 = (Pe_+^0 + Pe_-^0)/2$ and $\delta_D = D_+/D_-$. In addition, we have introduced the bulk salt concentration,

$$c(x,r) = \bar{c}(x) + c'(x,r), \quad (18)$$

which reduces to $\bar{c}(x)$ on the channel walls. We identify the term $-\nabla c$ in Eq. (17a) as the bulk diffusion and the term $\alpha Pe^0 c\boldsymbol{u}$ as the bulk advection. The Nernst-Planck equations corresponding to Eq. (17) are

$$(1 + \delta_D)\partial_t c = \nabla^2 c - \alpha Pe^0\nabla\cdot(c\boldsymbol{u}), \quad (19a)$$
$$(1 - \delta_D)\partial_t c = \nabla\cdot(c\nabla\phi_{bulk}) - \alpha\frac{1 - \delta_D}{1 + \delta_D}Pe^0\nabla\cdot(c\boldsymbol{u}). \quad (19b)$$

The surface currents are given by the remainder of the terms. Because the current of anions in the diffuse double layer is so much smaller than the current of cations, the two surface currents $\boldsymbol{J}_{sum}^{surf}$ and $\boldsymbol{J}_{dif}^{surf}$ are practically identical and equal to the cation current,

$$2\alpha\boldsymbol{J}_+^{surf} = -\bar{c}(e^{-\phi_{eq}} - 1)[\nabla\ln(\bar{c}) + \nabla\phi_{bulk}]$$
$$+ \bar{c}(e^{-\phi_{eq}} - 1)\,\alpha Pe_+^0\boldsymbol{u}. \quad (20)$$

In Fig. 3, the division of the system into a surface region and a bulk region is illustrated. The sketch also highlights the distinction between bulk and surface advection. The first term on the right-hand side of Eq. (20) we denote the surface conduction and the second term the surface advection. Since the surface currents are mainly along the wall we can describe

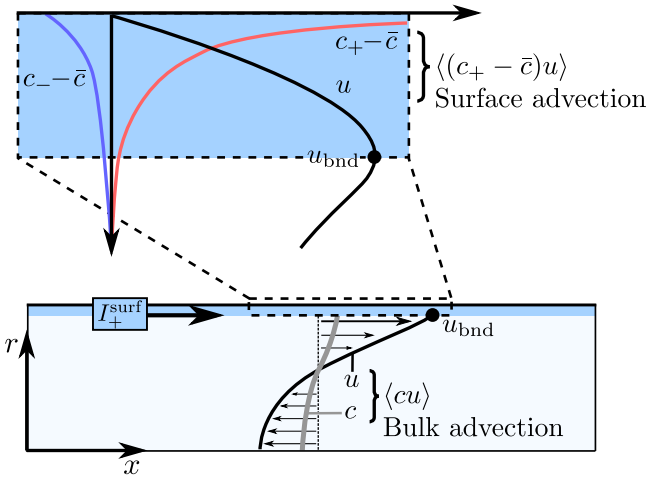

FIG. 3. (Color online) Sketch indicating the two regions in the boundary layer model. In the bulk region (lightly shaded) the boundary-driven velocity field u (black line), the salt concentration profile c (gray line), and the bulk advection $\langle cu\rangle$ are shown. In the boundary region (shaded and top zoom-in) the excess ion concentrations $c_\pm - \bar{c}$, the velocity field u, and the surface advection $\langle(c_\pm - \bar{c})u\rangle$ are shown.

them as scalar currents,

$$2\alpha I_+^{surf} = 2\alpha\langle\boldsymbol{e}_x\cdot\boldsymbol{J}_+^{surf}\rangle$$
$$= -\alpha\bar{c}\langle e^{-\phi_{eq}} - 1\rangle[\partial_x\ln(\bar{c}) + \partial_x\phi_{bulk}]$$
$$+ \alpha Pe_+^0\bar{c}\langle(e^{-\phi_{eq}} - 1)\,u\rangle, \quad (21)$$

where the cross-sectional average of any function $f(r)$ is given by the integral $\langle f(r)\rangle = \int_0^1 f(r)\,2r\,dr$. The first average is simplified by introducing the mean charge density $\rho_s = \langle c_+ - c_-\rangle$ in the channel needed to screen the wall charge. We then find

$$\bar{c}\langle e^{-\phi_{eq}} - 1\rangle = \rho_s + I_1, \quad (22a)$$
$$I_1 = \bar{c}\langle e^{\phi_{eq}} - 1\rangle, \quad (22b)$$

where I_1 is introduced for later use.

Before we proceed with a treatment of the remaining terms in the surface current, there is an issue we need to address: Because of the low concentration in the depletion region, the diffuse double layers are in general not thin in that region. However, the method is saved by the structure of the diffuse double layer in the depletion region. Since the Debye length $\bar{\lambda}_D$ is large in the depletion region the negative ζ potential is also large, $-\zeta \gg 1$. The majority of the screening charge is therefore located within the smaller Gouy length, $\bar{\lambda}_G \ll \bar{\lambda}_D$ [37,38]. In Fig. 4, the charge density and the potential are plotted near the channel wall for a system with $\bar{\lambda}_D = 0.01$ and $\rho_s = 1$. The charge density is seen to decay on the much smaller length scale $\bar{\lambda}_G$ than that of the potential, $\bar{\lambda}_D$. The normalized Gouy length is given as

$$\bar{\lambda}_G = \frac{\bar{\lambda}_D}{\sqrt{c}}\,\mathrm{asinh}\left(8\frac{\bar{\lambda}_D\sqrt{c}}{\rho_s}\right) \leqslant 8\frac{\bar{\lambda}_D^2}{\rho_s}, \quad (23)$$

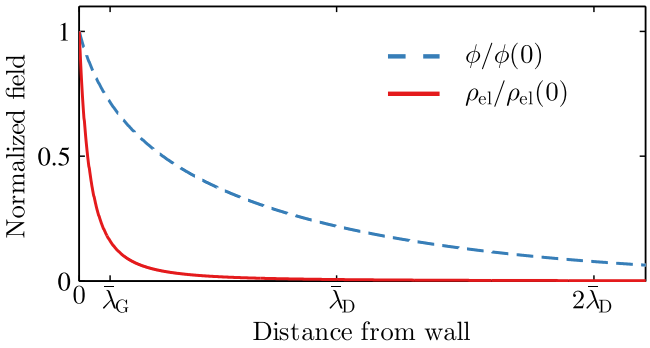

FIG. 4. (Color online) Normalized charge density $\rho_{el}/\rho_{el}(0)$ (full) and potential $\phi/\phi(0)$ (dashed) as a function of distance from a charged wall for $\bar{\lambda}_D = 0.01$ and $\rho_s = 1$. The Gouy length $\bar{\lambda}_G$ and the Debye length $\bar{\lambda}_D$ are indicated.

where the upper limit is a good approximation when $\sqrt{\bar{c}} \ll \rho_s/\bar{\lambda}_D$. The boundary layer method is therefore justified provided that

$$\bar{\lambda}_D \ll 1 \quad \text{or} \quad 8\frac{\bar{\lambda}_D^2}{\rho_s} \ll 1. \tag{24}$$

To determine the velocity field u, we consider the Stokes equation inside the diffuse double layer. In this region the flow is mainly along the wall, and velocity gradients along this direction can be neglected for most cases. The Stokes equation is therefore largely the balance,

$$\frac{1}{\mathrm{Sc}}\partial_t u = -\alpha\partial_x p' + \frac{1}{r}\partial_r(r\partial_r u) - \frac{1}{2}\frac{1}{\bar{\lambda}_D^2}(c_+\partial_x\mu_+ + c_-\partial_x\mu_-). \tag{25a}$$

Dimensional analysis shows that the characteristic time scale for the flow inside the diffuse double layer is given by $\bar{\lambda}_D^2/\mathrm{Sc}$. For typical systems, where $\mathrm{Sc} \gg 1$ and $\bar{\lambda}_D^2 \ll 1$, this time is very much shorter than the bulk diffusion time $\sim$1, the boundary diffusion time $\sim\bar{\lambda}_D^2$, and the time scale for the bulk flow $\sim 1/\mathrm{Sc}$. It is therefore reasonable to neglect the time-derivative term in Eq. (25a). Assuming Boltzmann distributed ions, $c_\pm = \bar{c}e^{\mp\phi_{eq}}$, and writing out the electrochemical potentials, we obtain

$$0 = -\alpha\partial_x p' + \frac{1}{r}\partial_r(r\partial_r u) + \frac{\bar{c}}{\bar{\lambda}_D^2}[\sinh\phi_{eq}\partial_x\phi_{bulk} - \cosh\phi_{eq}\partial_x\ln(\bar{c})]. \tag{25b}$$

Absorbing the bulk diffusive contribution into the new pressure p'' we find

$$0 = -\alpha\partial_x p'' + \frac{1}{r}\partial_r\{r\partial_r u\} + \frac{\bar{c}}{\bar{\lambda}_D^2}\sinh\phi_{eq}\partial_x\phi_{bulk} - \frac{\bar{c}}{\bar{\lambda}_D^2}[\cosh\phi_{eq} - \cosh(\phi_{eq}(0))]\,\partial_x\ln(\bar{c}). \tag{25c}$$

This equation is linear in u, so we can calculate the electro-osmotic velocity u_{eo}, the diffusio-osmotic velocity u_{do}, and the pressure-driven velocity u_p individually,

$$u = u_{eo} + u_{do} + u_p = u_{eo}^u\partial_x\phi_{bulk} + u_{do}^u\partial_x\ln(\bar{c}) + u_p, \tag{25d}$$

$$\frac{1}{r}\partial_r\left(r\partial_r u_{eo}^u\right) = -\frac{\bar{c}}{\bar{\lambda}_D^2}\sinh\phi_{eq}, \tag{25e}$$

$$\frac{1}{r}\partial_r\left(r\partial_r u_{do}^u\right) = \frac{\bar{c}}{\bar{\lambda}_D^2}[\cosh\phi_{eq} - \cosh(\phi_{eq}(0))], \tag{25f}$$

$$\frac{1}{r}\partial_r(r\partial_r u_p) = \alpha\partial_x p''. \tag{25g}$$

Here, we also introduced the unit velocity fields u_{eo}^u and u_{do}^u, which both have driving forces of unity. The electro-osmotic unit velocity u_{eo}^u is found by inserting $\sinh\phi_{eq}$ from the Poisson equation and integrating twice,

$$u_{eo}^u = (\zeta - \phi_{eq}). \tag{26}$$

In the limit $-\zeta \gg 1$, $\cosh\phi_{eq} - \cosh(\phi_{eq}(0)) \approx -\sinh\phi_{eq}$ and the diffusio-osmotic unit velocity u_{do}^u equals u_{eo}^u

$$u_{do} = (\zeta - \phi_{eq}), \quad \text{for } -\zeta \gg 1. \tag{27}$$

In general, the diffusio-osmotic velocity is not as easy to compute, and in practice it is most convenient just to solve Eq. (25f) numerically along with the ϕ_{eq} problem. The role of the pressure-driven velocity fields u_p is to ensure incompressibility of the liquid. Rather than dealing with this extra velocity field, we incorporate a pressure-driven flow into u_{eo}^u and u_{do}^u just large enough to ensure no net flux of water through a cross section,

$$u_{eo}^{up} = u_{eo}^u - 2\langle u_{eo}^u\rangle(1 - r^2), \tag{28}$$

$$u_{do}^{up} = u_{do}^u - 2\langle u_{do}^u\rangle(1 - r^2). \tag{29}$$

The velocity field thus can be written

$$u = u_{do}^{up}\,\partial_x\ln(\bar{c}) + u_{eo}^{up}\,\partial_x\phi_{bulk}, \tag{30}$$

with $\langle u\rangle = 0$. Using this, we can express the averaged advection term in the surface current Eq. (21) as

$$\bar{c}\langle(e^{-\phi_{eq}} - 1)\,u\rangle = I_2\,\partial_x\phi_{bulk} + I_3\,\partial_x\ln(\bar{c}), \tag{31a}$$

$$I_2 = \bar{c}\langle(e^{-\phi_{eq}} - 1)\,u_{eo}^{up}\rangle, \tag{31b}$$

$$I_3 = \bar{c}\langle(e^{-\phi_{eq}} - 1)\,u_{do}^{up}\rangle. \tag{31c}$$

The surface current can then be written as

$$2\alpha I_+^{surf} = -\alpha(\rho_s + I_1)[\partial_x\phi_{bulk} + \partial_x\ln(\bar{c})] + \alpha\mathrm{Pe}_+^0[I_2\partial_x\phi_{bulk} + I_3\partial_x\ln(\bar{c})]. \tag{32}$$

The current into the diffuse double layer from the bulk system is

$$\boldsymbol{n}\cdot\boldsymbol{J}_+ = \tfrac{1}{2}\alpha\partial_x I_+^{surf}, \tag{33}$$

where the factor of a half comes from the channel cross section divided by the circumference. Rather than resolve the diffuse double layers, we can therefore include their approximate influence through the boundary condition Eq. (33).

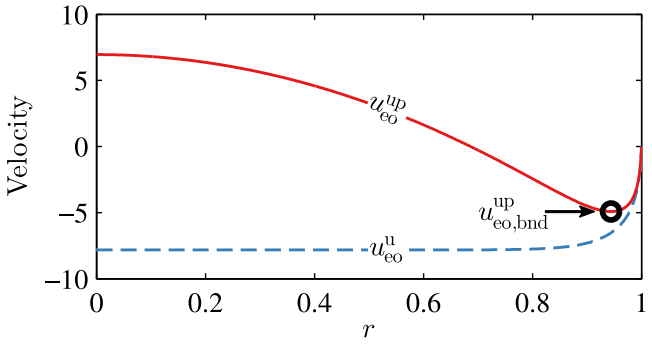

FIG. 5. (Color online) The electro-osmotic flow u_{eo}^{u} and the electro-osmotic flow u_{eo}^{up} with backpressure for $\rho_s = 10$ and $\bar{\lambda}_D = 0.05$. The effective boundary velocity $u_{eo,bnd}^{up}$ is also indicated.

In the locally electroneutral bulk system the Stokes and continuity equations become

$$\frac{1}{Sc}\partial_t \boldsymbol{u} = -\nabla p' + \nabla^2 \boldsymbol{u}, \tag{34a}$$

$$0 = \nabla \cdot \boldsymbol{u}. \tag{34b}$$

The effects of electro-osmosis and diffusio-osmosis are included via a boundary condition at the walls

$$\boldsymbol{u} = u_{bnd}\boldsymbol{e}_x = \left[u_{eo,bnd}^{up}\partial_x\phi_{bulk} + u_{do,bnd}^{up}\,\partial_x \ln(\bar{c})\right]\boldsymbol{e}_x, \quad \text{at } r = 1, \tag{35}$$

where $u_{eo,bnd}^{up}$ and $u_{do,bnd}^{up}$ are the minimum values of u_{eo}^{up} and u_{do}^{up}, i.e., the velocity at the point where the back-pressure-driven flow becomes significant. In Fig. 5 some of the discussed velocity fields are illustrated for $\rho_s = 10$ and $\bar{\lambda}_D = 0.05$. Note that $\partial_x\phi_{bulk}$ and $\partial_x \ln(\bar{c})$ will most often be negative, so the actual velocities in the channel differ from the plotted velocities with a sign and a numeric factor.

In the remainder of the paper we refer to the model developed in this section as the full boundary layer (BNDF) model. We also introduce the slip boundary layer (BNDS) model, in which the bulk couples to the boundary layers only through a slip velocity, while the boundary condition (33) for the normal current is substituted by $\boldsymbol{n}\cdot\boldsymbol{J}_+ = 0$. In other words, the BNDS and BNDF models are identical, except the BNDS model does not include the surface current. These models are listed in Table II along with the other models of the paper.

V. ANALYSIS

A. Scaling of bulk advection

To estimate the influence of bulk advection we consider the bulk current for a system in steady state,

$$\alpha \boldsymbol{J}_{sum}^{bulk} = -\nabla c + \alpha \mathrm{Pe}^0 c\boldsymbol{u}. \tag{36}$$

The average of this current in the x direction is

$$J_{sum}^{bulk} = \langle \boldsymbol{e}_x \cdot \boldsymbol{J}_{sum}^{bulk}\rangle = -\partial_x\langle c\rangle + \mathrm{Pe}^0\langle cu\rangle. \tag{37}$$

Since the membrane blocks the flow in one end, the net flow $\langle u\rangle$ in a channel cross section is zero and thus $\langle \bar{c}(x)u\rangle = \bar{c}(x)\langle u\rangle = 0$, which leads to

$$\langle cu\rangle = \langle[\bar{c}(x) + c'(x,r)]u\rangle = \langle c'(x,r)u\rangle. \tag{38}$$

Now the source of the deviation c' between $\bar{c}$ and c is the flow itself. In steady state, the dominant balance in Eq. (19a) is

$$\frac{1}{r}\partial_r(r\partial_r c) \approx \alpha^2 \mathrm{Pe}^0 \partial_x(cu), \tag{39a}$$

so c' must scale as

$$c' \sim \alpha^2 \mathrm{Pe}^0 \partial_x(\bar{c}u), \tag{39b}$$

which, on insertion in Eq. (37), yields

$$J_{sum}^{bulk} \sim -\partial_x\langle c\rangle + (\alpha \mathrm{Pe}^0)^2\langle\partial_x(\bar{c}u)u\rangle. \tag{39c}$$

This approximative expression reveals an essential aspect of the transport problem: With the chosen normalization the velocity, the diffusive current, the electromigration current, and the surface current do not depend on the aspect ratio α. The only term that depends on α is the bulk advection, and we see that for long slender channels ($\alpha \ll 1$) bulk advection vanishes, whereas it can be significant for short broad channels ($\alpha \gg 1$).

B. Local equilibrium models for small α

In the limit $\alpha \ll 1$, where bulk advection has a negligible effect, we can derive some simple analytical results. There the bulk concentration $c(x,r)$ equals the virtual concentration $\bar{c}(x)$, and the area-averaged bulk currents are

$$J_{sum}^{bulk} = -\partial_x\bar{c}(x), \tag{40a}$$

$$J_{dif}^{bulk} = -\bar{c}(x)\partial_x\phi_{bulk}(x). \tag{40b}$$

In steady state, these currents are equal and can change only if there is a current into or out of the boundary layer. The conserved current J_+ is therefore

$$J_+ = -\partial_x\bar{c}(x) + I_{surf} = -\bar{c}(x)\partial_x\phi_{bulk}(x) + I_{surf}. \tag{41}$$

It is readily seen that $\bar{c} = e^{\phi_{bulk}}$ is a solution to the equation. To proceed we need expressions for the integrals I_1, I_2, and I_3.

Initially, we neglect advection in the boundary layer as well and this leaves us with the equation

$$J_+ = -e^{\phi_{bulk}}\partial_x\phi_{bulk} - \tfrac{1}{2}(\rho_s + I_1)2\partial_x\phi_{bulk}. \tag{42}$$

If the Debye-Hückel limit is valid in the diffuse double layer, we can make the approximations

$$\rho_s = c\langle e^{-\phi_{eq}} - e^{\phi_{eq}}\rangle \approx -2c\langle\phi_{eq}\rangle, \tag{43a}$$

$$I_1 = c\langle e^{\phi_{eq}} - 1\rangle \approx c\langle\phi_{eq}\rangle \approx -\tfrac{1}{2}\rho_s, \tag{43b}$$

in which case J_+ reduces to the expression in Ref. [26],

$$J_+ = -\left(e^{\phi_{bulk}} + \frac{\rho_s}{2}\right)\partial_x\phi_{bulk}. \tag{44}$$

If, on the other hand, the diffuse double layer is in the strongly nonlinear regime, then the surface charge is compensated almost entirely by cations and to a good approximation,

$$I_1 \approx 0. \tag{45}$$

In that limit the current is

$$J_+ = -(e^{\phi_{bulk}} + \rho_s)\partial_x\phi_{bulk}, \tag{46}$$

i.e., the overlimiting conductance is twice the conductance found in Ref. [26]. Since the Debye length is large in the depletion region, we have $-\zeta \gg 1$, and the diffuse double layer is in the strongly nonlinear regime. Surface conduction is mainly important in the depletion region, so for most parameter values Eq. (46) is a fairly accurate expression for the current.

We now make a more general treatment, which is valid when the characteristic dimension of the diffuse double layer is much smaller than the channel curvature. In that limit we can approximate the equilibrium potential with the Gouy-Chapman solution,

$$\phi_{\mathrm{GC}} = 4\mathrm{artanh}\left\{\tanh\left[\frac{\zeta}{4}\right]\exp\left[-\sqrt{\bar{c}}\,\frac{y}{\bar{\lambda}_{\mathrm{D}}}\right]\right\}, \tag{47a}$$

$$\zeta = -2\mathrm{arsinh}\left[\frac{\rho_{\mathrm{s}}}{4d\bar{\lambda}_{\mathrm{D}}\sqrt{\bar{c}}}\right] \approx -2\ln\left[\frac{\rho_{\mathrm{s}}}{2d\bar{\lambda}_{\mathrm{D}}\sqrt{\bar{c}}}\right], \tag{47b}$$

where the last approximation is valid for $-\zeta \gtrsim 2$. In the following we assume that we are in this limit. The parameter d is the ratio of circumference to area of the channel ($d = 2$ for a cylindrical channel). Using the Gouy-Chapman solution we find an expression for I_1,

$$\begin{aligned} I_1 &= \bar{c}\langle e^{\phi_{\mathrm{eq}}} - 1\rangle \approx d\bar{c}\int_0^\infty (e^{\phi_{\mathrm{eq}}} - 1)\,dy \\ &= -2d\bar{\lambda}_{\mathrm{D}}\sqrt{\bar{c}}\,(1 - e^{\frac{1}{2}\zeta}) \\ &\approx 4d^2\frac{\bar{\lambda}_{\mathrm{D}}^2}{\rho_{\mathrm{s}}}\,\bar{c} - 2d\bar{\lambda}_{\mathrm{D}}\sqrt{\bar{c}}. \end{aligned} \tag{48}$$

In the limit of large potentials, $-\phi_{\mathrm{GC}} \gg 1$, we can approximate $\cosh\phi_{\mathrm{GC}} \approx -\sinh\phi_{\mathrm{GC}}$ and obtain

$$u_{\mathrm{eo}} = (\zeta - \phi_{\mathrm{GC}})\,\partial_x\phi_{\mathrm{bulk}}, \tag{49a}$$

$$u_{\mathrm{do}} \approx (\zeta - \phi_{\mathrm{GC}})\,\partial_x \ln(c). \tag{49b}$$

From this we find

$$\begin{aligned} &\langle\bar{c}(\zeta - \phi_{\mathrm{GC}})(e^{-\phi_{\mathrm{GC}}} - 1)\rangle \\ &\approx d\bar{c}\int_0^\infty (\zeta - \phi_{\mathrm{GC}})(e^{-\phi_{\mathrm{GC}}} - 1)\,dy \\ &= 4d\bar{\lambda}_{\mathrm{D}}\sqrt{\bar{c}}\left(1 - \frac{1}{2}\zeta - e^{-\frac{1}{2}\zeta}\right) \\ &\approx 4d\bar{\lambda}_{\mathrm{D}}\sqrt{\bar{c}} + 4d\bar{\lambda}_{\mathrm{D}}\sqrt{\bar{c}}\ln\left(\frac{\rho_{\mathrm{s}}}{2d\sqrt{\bar{c}}\bar{\lambda}_{\mathrm{D}}}\right) - 2\rho_{\mathrm{s}}. \end{aligned} \tag{50}$$

Inserting Eq. (50) in Eqs. (32) and (41) we obtain

$$\begin{aligned} J_+ = &-e^{\phi_{\mathrm{bulk}}}\partial_x\phi_{\mathrm{bulk}} \\ &- \left(\rho_{\mathrm{s}} + 4d^2\frac{\bar{\lambda}_{\mathrm{D}}^2}{\rho_{\mathrm{s}}}e^{\phi_{\mathrm{bulk}}} - 2d\bar{\lambda}_{\mathrm{D}}e^{\frac{1}{2}\phi_{\mathrm{bulk}}}\right)\partial_x\phi_{\mathrm{bulk}} \\ &- \mathrm{Pe}_+^0\Bigg[2\rho_{\mathrm{s}} - 4d\bar{\lambda}_{\mathrm{D}}e^{\frac{1}{2}\phi_{\mathrm{bulk}}} \\ &- 4d\bar{\lambda}_{\mathrm{D}}e^{\frac{1}{2}\phi_{\mathrm{bulk}}}\ln\left(\frac{\rho_{\mathrm{s}}}{2d}\frac{e^{-\frac{1}{2}\phi_{\mathrm{bulk}}}}{\bar{\lambda}_{\mathrm{D}}}\right)\Bigg]\partial_x\phi_{\mathrm{bulk}}. \end{aligned} \tag{51a}$$

Integration of this expression with respect to x leads to

$$\begin{aligned} J_+x = &\left(1 + 4d^2\frac{\bar{\lambda}_{\mathrm{D}}^2}{\rho_{\mathrm{s}}}\right)(1 - e^{\phi_{\mathrm{bulk}}}) - \rho_{\mathrm{s}}\big(1 + 2\mathrm{Pe}_+^0\big)\phi_{\mathrm{bulk}} \\ &- 4d\bar{\lambda}_{\mathrm{D}}(1 + 2\mathrm{Pe}_+^0)\big(1 - e^{\frac{1}{2}\phi_{\mathrm{bulk}}}\big) \\ &- 8d\mathrm{Pe}_+^0\bar{\lambda}_{\mathrm{D}}\left\{\left(1 + \ln\left[\frac{\rho_{\mathrm{s}}}{2d\bar{\lambda}_{\mathrm{D}}}\right]\right)(1 - e^{\frac{1}{2}\phi_{\mathrm{bulk}}}) \right. \\ &\left. + \frac{1}{2}\phi_{\mathrm{bulk}}\,e^{\frac{1}{2}\phi_{\mathrm{bulk}}}\right\}. \end{aligned} \tag{51b}$$

C. Analytical surface conduction and surface advection (ASCA) model

For $\bar{\lambda}_{\mathrm{D}} \ll 1$, the leading-order behavior of Eqs. (51a) and (51b) is

$$J_+ = -e^{\phi_{\mathrm{bulk}}}\partial_x\phi_{\mathrm{bulk}} - \rho_{\mathrm{s}}(1 + 2\mathrm{Pe}_+^0)\partial_x\phi_{\mathrm{bulk}}, \tag{52a}$$

$$J_+x = 1 - e^{\phi_{\mathrm{bulk}}} - \rho_{\mathrm{s}}(1 + 2\mathrm{Pe}_+^0)\phi_{\mathrm{bulk}}. \tag{52b}$$

In Eq. (52a) it is seen that the bulk conductivity $e^{\phi_{\mathrm{bulk}}}$ varies with the electric potential, whereas the surface conductivity $\rho_{\mathrm{s}}(1 + 2\mathrm{Pe}_+^0)$ is constant. At $x = 1$, the boundary condition for the potential is $\mu_+ = \ln(\bar{c}) + \phi_{\mathrm{bulk}} = 2\phi_{\mathrm{bulk}} = -V_0$, and from Eq. (52b) we obtain the current-voltage relation

$$J_+ = 1 - e^{-\frac{1}{2}V_0} + \rho_{\mathrm{s}}\big(\tfrac{1}{2} + \mathrm{Pe}_+^0\big)V_0. \tag{52c}$$

While this expression was derived with a cylindrical geometry in mind, it applies to most channel geometries. The only requirement is that the local radius of curvature of the channel wall is much larger than the Gouy length $\bar{\lambda}_{\mathrm{G}}$, so the potential is well approximated by the Gouy-Chapman solution.

This analytical model is called the surface conduction-advection (ASCA) model. As shown in Sec. VI B, it is very accurate in the limit of long slender channels, $\alpha \ll 1$.

D. Analytical surface conduction (ASC) model

For a system with a Gouy length on the order of unity, the screening charges are distributed across the channel in the depletion region. Advection therefore transports approximately as many cations towards the membrane as away from the membrane, and there is no net effect of surface advection. In this limit, Eq. (52c) reduces to the pure surface conduction expression

$$J_+ = 1 - e^{-\frac{1}{2}V_0} + \frac{\rho_{\mathrm{s}}}{2}V_0, \tag{53}$$

which we refer to as the analytical surface conduction (ASC) model.

E. Analytical bulk conduction (ABLK) model

In the limit of low surface charge and high $\bar{\lambda}_{\mathrm{D}}$, neither surface conduction nor advection matter much. In that limit the dominant mechanism of overlimiting current is bulk conduction through the extended space-charge region (ESC). This effect is not captured by the derived boundary layer model, since it assumes local electroneutrality. The development of an extended space-charge region can, however, be captured in

an analytical 1D model, and from Ref. [8] we have the limiting expression

$$-V_0 = \mu_+(1) \approx -\frac{2\sqrt{2}}{3}\frac{(J_+ - 1)^{3/2}}{\alpha\bar{\lambda}_D J_+} + 2\ln(\alpha\bar{\lambda}_D), \quad (54)$$

giving the overlimiting current-voltage characteristic due to conduction through the extended space-charge region. Expressions which are uniformly valid both at under- and overlimiting current are also derived in our previous work Ref. [8], but since these are rather lengthy we will not show them here. We refer to the full model from Ref. [8] as the analytical bulk conduction (ABLK) model, see Table II.

VI. NUMERICAL ANALYSIS

A. Numerical implementation

The numerical simulations are carried out in the commercially available finite element software COMSOL MULTIPHYSICS, version 4.3a. Following Gregersen *et al.* [39], the governing equations of the FULL, BNDF, and BNDS models are rewritten in weak form and implemented in the mathematics module of COMSOL. To improve the numerical stability of the problem we have made a change of variable, so the logarithm of the concentration fields have been used as dependent variables instead of the concentration fields themselves. The cross-sectional averages I_1, I_2, and I_3 [Eqs. (22b) and (31b)] as well as the slip velocity [Eq. (35)] are calculated and tabulated in a separate model.

In the theoretical treatment we found seven dimensionless numbers, which govern the behavior of the system. These are the Schmidt number Sc, the normalization Péclet number Pe^0, the diffusivity ratio δ_D, the aspect ratio α, the normalized Debye length $\bar{\lambda}_D$, the cross-sectionally averaged charge density ρ_s, and the applied bias voltage V_0. In the numerical simulations, we only consider steady-state problems, so Sc does not matter for the results. To further limit the parameter space, we have chosen fixed and physically reasonable values for a few of the parameters. The ionic diffusivities are assumed to be equal, i.e., $\delta_D = 1$. For a solution of potassium chloride with $D_{K^+} = 1.96\ \mathrm{m}^2/\mathrm{s}$ and $D_{Cl^-} = 2.03\ \mathrm{m}^2/\mathrm{s}$, this is actually nearly the case. The normalization Péclet number is set to $\mathrm{Pe}^0 = 0.235$, which is a realistic number for potassium ions in water at room temperature. This leaves us with four parameters, α, $\bar{\lambda}_D$, ρ_s, and V_0, which govern the system behavior. We mainly present our results in the form of I-V characteristics, i.e., sweeps in V_0, since the important features of the transport mechanisms can most often be inferred from these. We vary the other parameters as follows: the aspect ratio α takes on the values {0.01,0.05,0.1,0.2}, the normalized Debye length $\bar{\lambda}_D$ takes the values {0.0001,0.001,0.01,0.1}, and the averaged charge density ρ_s takes the values {0.001,0.01,0.1,1}. The parameters and their values or range of values are listed in Table III. The $\bar{\lambda}_D = 0.0001$ systems are only solved in the BNDF model, since a full numerical solution with resolved diffuse double layers is computationally costly in this limit $\bar{\lambda}_D \ll 1$. The boundary layer model is very accurate in the small $\bar{\lambda}_D$ limit, so the lack of a full numerical solution for $\bar{\lambda}_D = 0.0001$ is not a concern.

TABLE III. Parameters and their values or range of values. The Schmidt number is irrelevant since we are considering steady-state problems. To simplify the analysis, Pe^0 and δ_D are fixed.

Parameter	Symbol	Value/range
Schmidt number	Sc	N/A
Normalization Péclet number	Pe^0	0.235
Diffusivity ratio	δ_D	1
Aspect ratio	α	0.01–0.2
Normalized Debye length	$\bar{\lambda}_D$	0.0001–0.1
Average surface charge density	ρ_s	0.001–1
Bias voltage	V_0	0–100

To verify the numerical scheme we have made comparisons with known analytical results in various limits and carried out careful mesh convergence analyses for selected sets of parameter values.

B. Parameter dependence of I-V characteristics

The results of the simulations are presented in the following way: For each α value a $(\bar{\lambda}_D, \rho_s)$ grid is made, and in each grid point is shown the corresponding I-V characteristic. The I-V characteristics obtained from the simulations are supplemented with relevant analytical results. To aid in the interpretation of the results, Fig. 6 shows the trends we expect on the basis of the governing equations and our analysis. Surface conduction and surface advection is expected to increase with ρ_s and bulk advection is expected to increase with ρ_s and α and decrease with $\bar{\lambda}_D$. Bulk conduction through the extended space-charge region is expected to increase with $\alpha\bar{\lambda}_D$.

In Figs. 7 and 8 the numerically calculated I-V characteristics are plotted for a long slender channel ($\alpha = 0.05$) and a short broad channel ($\alpha = 0.2$), respectively. In the Supplemental Material [40] additional results for $\alpha = 0.01$ and $\alpha = 0.1$ are given. The results for the FULL model with resolved diffuse double layers (defined in Sec. III) are shown in

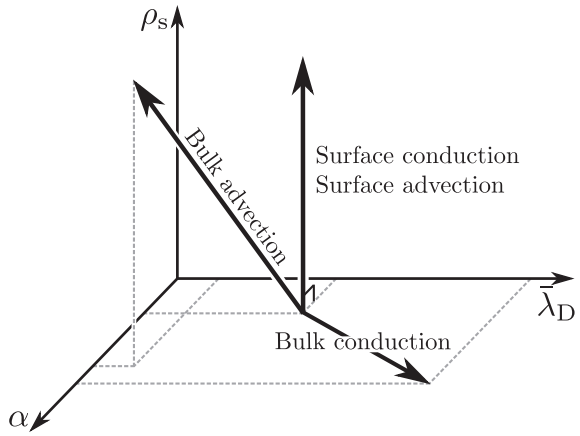

FIG. 6. Directions of increase of the various mechanisms of overlimiting current. Bulk advection increases with α and ρ_s and decreases with $\bar{\lambda}_D$. Surface conduction and surface advection increases with ρ_s, and bulk conduction through the ESC increases with $\alpha\bar{\lambda}_D$.

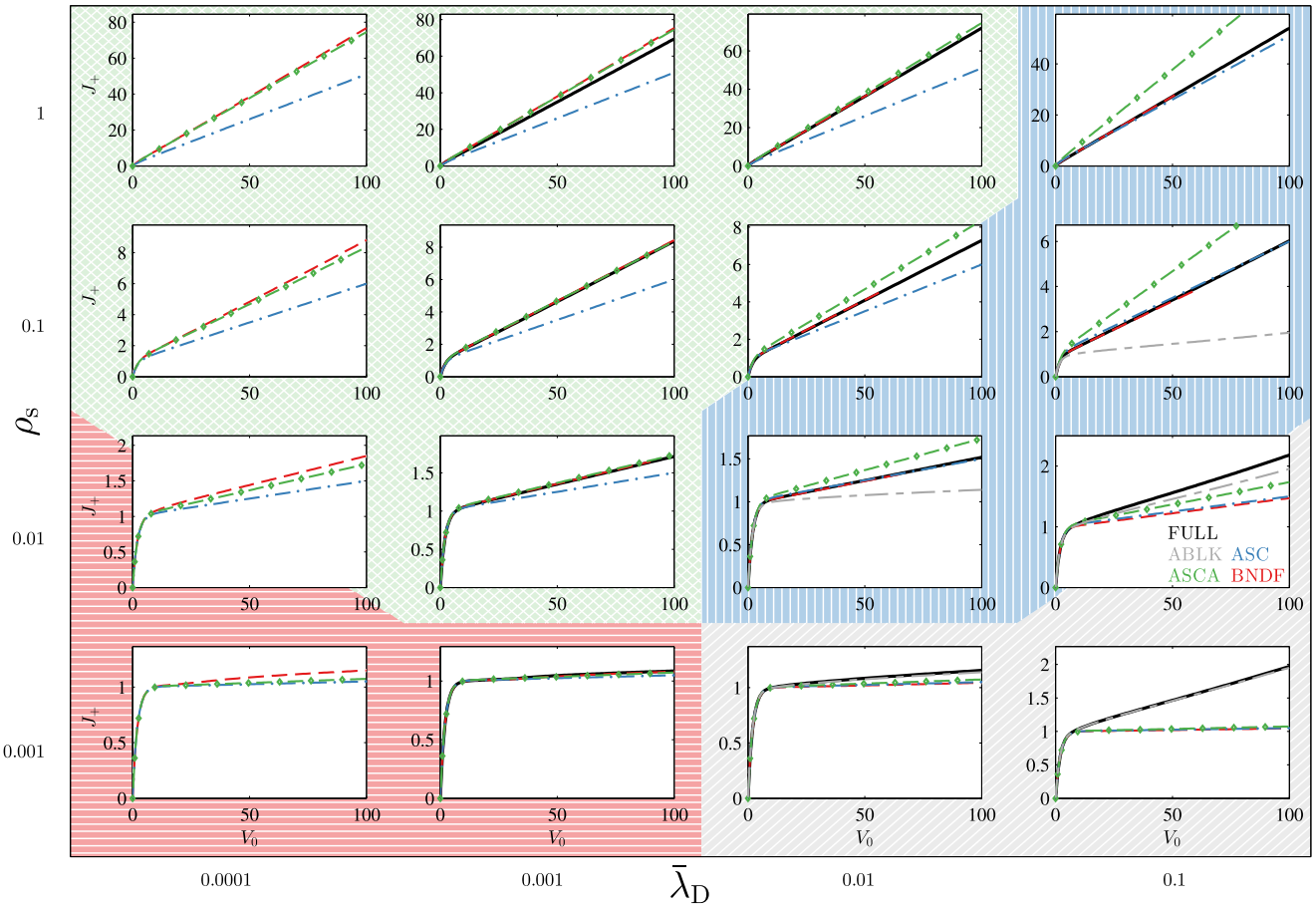

FIG. 7. (Color online) I-V characteristics for $\alpha = 0.05$, $\bar{\lambda}_D = \{0.0001, 0.001, 0.01, 0.1\}$, and $\rho_s = \{0.001, 0.01, 0.1, 1\}$. The full (black) line show the characteristics obtained from the FULL model. The dashed (red) curves are obtained from the BNDF model. The (blue) dash-dot curves are from the ASC model, and the (green) dash-diamond curves are from the ASCA model. The (gray) long-dash-short-dash curves are obtained from the ABLK model. The background patterns indicate the dominant overlimiting conduction mechanism. The (green) cross-hatched pattern indicate that surface advection and surface conduction are the dominant mechanisms. The (blue) vertically hatched pattern indicate that surface conduction without surface advection is the dominant mechanism. The (red) horizontally hatched pattern indicate that bulk advection is the dominant mechanism. The (gray) skew-hatched pattern indicate that bulk conduction through the ESC is the dominant mechanism. Intermediate cases are indicated with mixed background patterns.

a full (black) line. The results for the BNDF model (defined in Sec. IV) are shown in a dashed (red) line. The long-dash-short-dash (gray) line is obtained from the ABLK model [note that Eq. (54) gives the asymptotic version of this curve]. The dash-dot (blue) line is the analytical curve from the ASC model, and the dash-diamond (green) line is the analytical curve from the ASCA model. To help structure the results the I-V characteristics have been given a background pattern (colored), which indicate the dominant conduction mechanisms. A light cross-hatched (green) background indicates that the dominant mechanisms are surface conduction and surface advection. A dark horizontally hatched (red) background indicates that bulk advection is the dominant mechanism. Dark with vertical hatches (blue) indicate that surface conduction without surface advection is the dominant mechanism and light with skewed hatches (gray) indicates that the dominant mechanism is bulk conduction through the extended space-charge region. A split background indicates that the overlimiting current is the result of two different mechanisms. In the case of a split cross-hatched/vertically hatched background, the split indicates that surface conduction is important and that surface advection plays a role, but that this role is somewhat reduced due to backflow along the channel axis.

We first consider the case $\alpha = 0.05$ shown in Fig. 7. Here the aspect ratio α is so low that the effects of bulk advection are nearly negligible. As a consequence, the numerical [dashed (red) and full (black) lines] and analytical [dash-diamond (green) line] curves nearly match each other in a large portion of the parameter space [light cross-hatched (green) region]. Although there is a small region in which bulk advection does play a role [dark horizontally hatched (red) region], the overlimiting current due to bulk advection is small for all of the investigated $\bar{\lambda}_D$ and ρ_s values. In the right part (high $\bar{\lambda}_D$) of Fig. 7 the effects of bulk and surface advection are negligible. For high ρ_s values surface conduction dominates [dark vertically hatched (blue) region] and for low ρ_s bulk conduction through the ESC dominates [light skew-hatched (gray) region].

The case of $\alpha = 0.2$, shown in Fig. 8, follows the same basic pattern as the $\alpha = 0.05$ case. As expected from Fig. 6, the

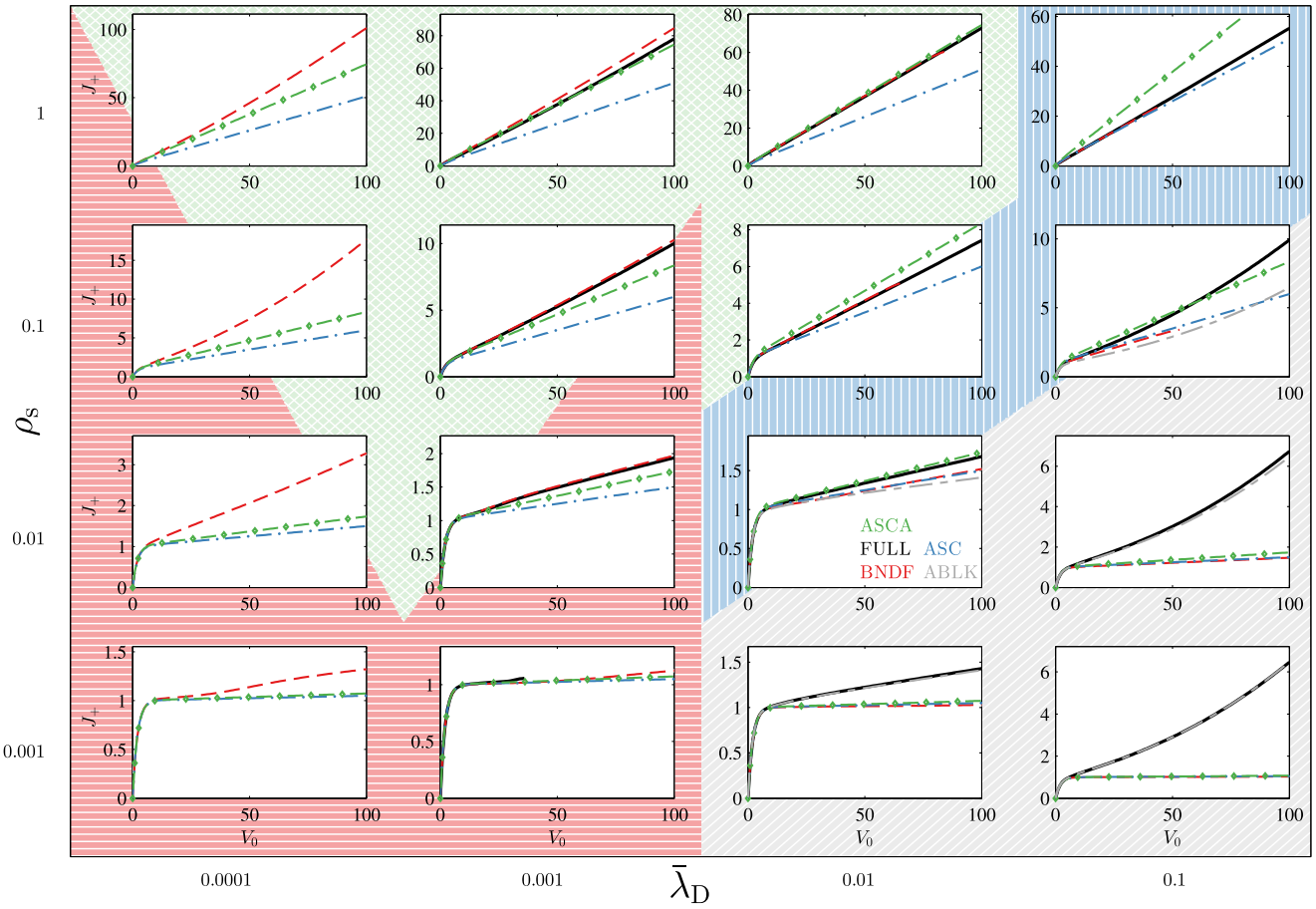

FIG. 8. (Color online) Same I-V characteristics as Fig. 7, except that here $\alpha = 0.2$ instead of 0.05.

regions where bulk advection [dark (red) horizontal hatches] or bulk conduction [light (gray) skewed hatches] dominates grow as α is increased. Inside the regions an increase in magnitude of both effects is also seen. The picture that emerges is that in the long channel limit $\alpha \lesssim 0.05$ the effects of bulk advection are negligible, and for small $\bar{\lambda}_D$ the overlimiting current is entirely due to surface conduction and surface advection. For bulk advection to cause a significant overlimiting current the channel has to be relatively short, $\alpha \gtrsim 0.1$, and the normalized Debye length has to be small, $\bar{\lambda}_D \lesssim 0.001$.

C. Field distributions

In Fig. 9 some of the important fields are plotted for two different sets of parameter values. The fields are obtained from the BNDF model. To the left, in Figs. 9(a), 9(b), and 9(c), the fields are given for a system with $\bar{\lambda}_D = 0.0001$, $\rho_s = 0.01$, $\alpha = 0.2$, and $V_0 = 60$, and, to the right, in Figs. 9(d), 9(e), and 9(f), the fields are given for a system with $\bar{\lambda}_D = 0.001$, $\rho_s = 0.1$, $\alpha = 0.05$, and $V_0 = 60$. The colors indicate the relative magnitude (black, low value; white, high value) of the fields within each panel. Comparing Figs. 9(c) and 9(f) we see that the depletion region is bigger in Fig. 9(f) than Fig. 9(c), which is as expected since the current in Fig. 9(f) is larger than in Fig. 9(c) (cf. Figs. 7 and 8). It is also noted that the transverse distribution of the concentration is much less uniform in Fig. 9(c) than in Fig. 9(f). Due to this nonuniformity (see Sec. V A), system (a)-(b)-(c) has a net current contribution from bulk advection, whereas bulk advection contributes negligibly to the current in the transversally uniform system (d)-(e)-(f). In Fig. 9(a), we see that the majority of the current is carried in the bulk until $x \sim 0.9$, at which point it enters the boundary layer. In Fig. 9(d), on the other hand, the current enters the boundary layer already at $x \sim 0.3$, because the amount of bulk advection is insufficient to carry a bulk current into the depletion region.

D. Coupling between bulk advection and the surface current

As seen in Figs. 7 and 8, the limits of surface advection and surface conduction, of surface conduction, and of bulk conduction through the ESC are well described by our analytical models. The analytical models do not describe the transitions between the limiting behaviors, but the essentials of the involved mechanisms are well understood. It is thus mainly the bulk advection which requires a more thorough investigation. As pointed out in Refs. [29,41–43], the effects of bulk advection can to some extent be understood in terms of a Taylor-Aris-like model of hydrodynamic dispersion. However, in those papers surface conduction and surface advection is neglected on account of their small contribution to the total current in the investigated limits. It turns out that in the context

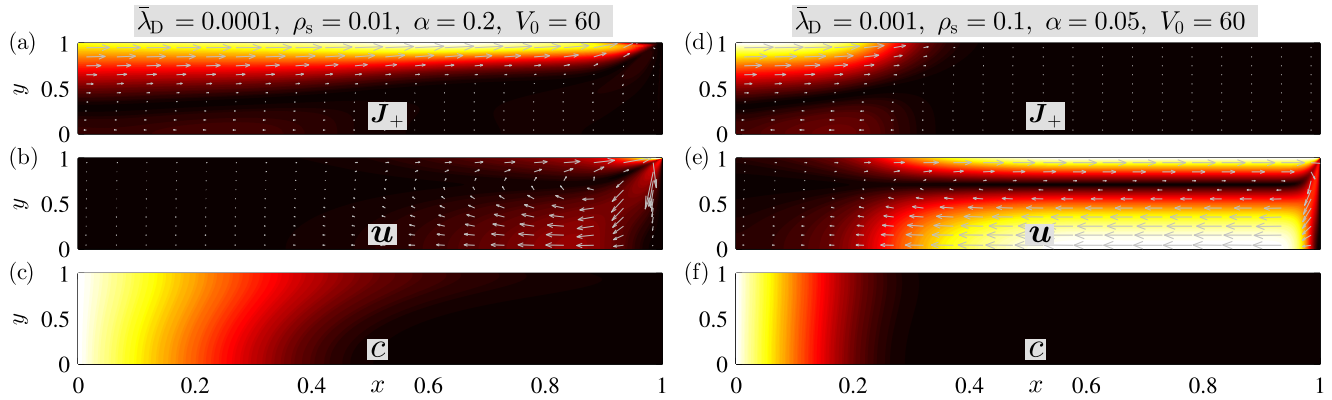

FIG. 9. (Color online) For a system with $\bar{\lambda}_D = 0.0001$, $\rho_s = 0.01$, $\alpha = 0.2$, and $V_0 = 60$ is plotted (a) cation current $\boldsymbol{J}_+$, (b) velocity $\boldsymbol{u}$, and (c) salt concentration c. For a system with $\bar{\lambda}_D = 0.001$, $\rho_s = 0.1$, $\alpha = 0.05$, and $V_0 = 60$ is plotted the (d) cation current $\boldsymbol{J}_+$, (e) velocity $\boldsymbol{u}$, and (f) salt concentration c. The fields are obtained from the BNDF model, and the colors indicate the relative magnitude (black, low; white, high) of the fields within each panel, while arrows represent vector fields.

of concentration polarization the surface currents do in fact play a crucial role for the bulk advection, even when the surface currents themselves only give a minute contribution to the total current. Our boundary layer model is ideally suited to demonstrate just that point, since it allows us to artificially turn off the surface currents while keeping the electro-diffusio-osmotic flow. In Fig. 10(a) I-V characteristics obtained from the BNDF [dashed (red) line] and BNDS [dotted (purple) line] models are plotted for $\alpha = 0.2$, $\bar{\lambda}_D = 0.0001$, and $\rho_s = 0.001$. For comparison the I-V characteristic from the ASCA model, which includes surface conduction and surface advection but excludes bulk advection, is also plotted. In Fig. 10(b) the same curves are plotted with $\rho_s = 0.1$ instead of 0.001. Comparing the BNDF model [dashed (red)] with the ASCA model [dash-diamond (green)], it is seen that bulk advection plays a significant role in these regimes. In light of this it is indeed remarkable that the BNDS model, which includes bulk advection but excludes surface currents [dotted (purple) line], exhibits no overlimiting current at all. We conclude that the surface current is, in some way, a prerequisite for significant bulk advection.

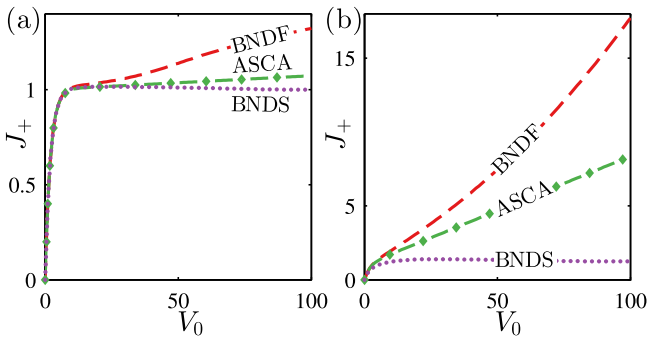

FIG. 10. (Color online) (a) I-V characteristics highlighting the role of the surface current for bulk advection. $\alpha = 0.2$, $\bar{\lambda}_D = 0.0001$, and $\rho_s = 0.001$. The dashed (red) curve is obtained from the BNDF model and the dash-diamond (green) curve is from the ASCA model. The dotted (purple) curve is obtained from the BNDS model, in which the surface current has been artificially removed while the electro-diffusio-osmotic slip velocity is kept. (b) Same as in (a) but with $\rho_s = 0.1$.

Our investigations suggest that the reason for this highly nonlinear coupling between bulk advection and the surface current is that the surface current sets the length of the depletion region before bulk advection sets in. The large gradients in electrochemical potentials, and thereby the large electro-diffusio-osmotic velocities, exist in the depletion region, so a wide depletion region implies a wide region with significant advection. In the limit of zero surface current, the depletion region only extends over a tiny region next to the membrane. In this region there is a huge electro-diffusio-osmotic flow towards the membrane, but the effects of that flow are not felt very far away, because it is compensated by the back-pressure-driven flow over a quite small distance. When there is a surface current the depletion region will eventually, as the driving potential is increased, extend so far away from the membrane that back-pressure does not immediately compensate the electro-diffusio-osmotic flow. In that situation, bulk advection may begin to play a role. The need for a sufficiently large depletion region is seen by the plateau in the BNDF I-V characteristic in Fig. 10(a). What happens is that, as a function of voltage, the current increases to the limiting current, remains there for a while, and then, once the depletion region is sufficiently developed, increases further due to bulk advection. To quantify these notions we derive a simple estimate of the extent of the depletion region.

Before bulk advection sets in, the overlimiting current is entirely due to the surface current, and in this regime the behavior is well described by the ASCA model Eqs. (52b) and (52c). There is some ambiguity in defining exactly which parts of the system constitute the depletion region. By definition, the depletion region comprises the parts of the system, which are depleted of charge carriers. However, since there are always some charge carriers present, we have to decide on a concentration which counts as sufficiently depleted. There are a number of legitimate choices for this concentration, but for the purposes of this analysis, we define the depletion region as the part of the system where the surface conductivity exceeds

the bulk conductivity. Consequently, at the beginning of the depletion region, we have from Eq. (52a)

$$e^{\phi_{\text{bulk}}} = \rho_s(1 + 2\text{Pe}_+^0). \tag{55}$$

From Eq. (52c), we find the current in the overlimiting case as

$$J_+ \approx 1 + \rho_s\left(\tfrac{1}{2} + \text{Pe}_+^0\right)V_0, \tag{56}$$

and from Eq. (52b) the relation between position x and bulk potential ϕ_{bulk} is

$$J_+ x \approx 1 - e^{\phi_{\text{bulk}}} - \rho_s(1 + 2\text{Pe}_+^0)\phi_{\text{bulk}}. \tag{57}$$

Inserting Eqs. (55) and (56) into Eq. (57) we find the position x_0 where the depletion region begins,

$$x_0 = \frac{1 - \rho_s(1 + 2\text{Pe}_+^0)\{1 + \ln[\rho_s(1 + 2\text{Pe}_+^0)]\}}{1 + \rho_s\left(\frac{1}{2} + \text{Pe}_+^0\right)V_0}. \tag{58}$$

For a small overlimiting current, the denominator is close to unity, and this implies that before bulk advection becomes important, the width $1 - x_0$ of the depletion region is approximately given by

$$1 - x_0 \approx \rho_s(1 + 2\text{Pe}_+^0)\left\{\frac{V_0}{2} + 1 + \ln\left[\rho_s(1 + 2\text{Pe}_+^0)\right]\right\}. \tag{59}$$

We can use this expression for the width of the depletion region to test our hypothesis that the extent of the depletion region determines the onset of bulk advection. If the hypothesis is true, we should find that the overlimiting current $J_+^{\text{overlim}} = J_+ - (1 - e^{-\frac{1}{2}V_0})$ only depends on ρ_s and V_0 through the expression for $1 - x_0$,

$$J_+^{\text{overlim}}(\rho_s, V_0) \to J_+^{\text{overlim}}(1 - x_0[\rho_s, V_0]). \tag{60}$$

In Fig. 11(a) and 11(b) the overlimiting current J_+^{overlim} obtained from the BNDF model is plotted for $\rho_s = \{0.0001, 0.0002, 0.0003, 0.0004, 0.0005\}$, $\bar{\lambda}_D = 0.0001$, and $\alpha = 0.05$ versus V_0 and $1 - x_0$, respectively. The characteristic features in the curves are seen to coincide when the curves are plotted versus $1 - x_0$. In contrast, no unifying behavior is seen when the curves are plotted versus V_0. The numerical results thus corroborate our hypothesis that the initiation of significant bulk advection is determined by the extent of the depletion region.

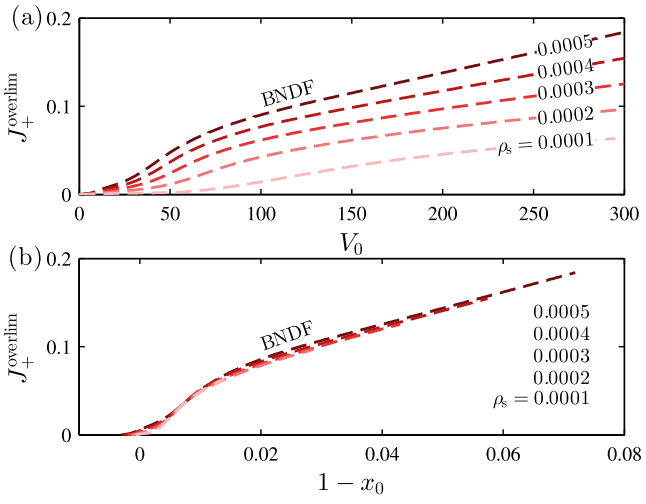

FIG. 11. (Color online) (a) The overlimiting current J_+^{overlim} obtained from the BNDF model for $\bar{\lambda}_D = 0.0001$, $\alpha = 0.05$, and $\rho_s = \{0.0001, 0.0002, 0.0003, 0.0004, 0.0005\}$ plotted versus V_0. (b) Same as in (a) but plotted versus $1 - x_0$.

E. Issues with the numerical models

Before concluding, we are obligated to comment on the shortcomings of the numerical models, i.e., the FULL model and the BNDF model. In the $\rho_s = 0.001$, $\bar{\lambda}_D = 0.001$ panel of Fig. 8 the FULL model [full (black) line] is seen to break down right around $V_0 \sim 40$. The reason for this breakdown is that electro-diffusio-osmosis is relatively weak and that the ESC is prone to electro-osmotic instability at this $\bar{\lambda}_D$ value. The employed steady-state model is not well suited for modeling instabilities and therefore the model breaks down at this relatively low voltage. Because the magnitude of the ESC charge density scales as $(\alpha\bar{\lambda}_D)^{2/3}$ we do not expect this to be an issue for the $\bar{\lambda}_D = 0.0001$ or $\alpha = 0.05$ cases [8]. Another issue seen in Figs. 7 and 8 is that in the upper right quadrant ($\rho_s \geqslant 0.1$ and $\bar{\lambda}_D \geqslant 0.01$) the BNDF model [dashed (red) curve] breaks down somewhere between $V_0 \sim 40$ and $V_0 \sim 70$. The reason for this breakdown is that the Gouy length is not small in this region, as is required by the boundary layer model. The BNDF model breaks down, even though the systems in question are close to the simple transverse equilibrium configuration. The reason for this is that when the Gouy length is large, the boundary layer model underestimates the transverse transport in the system, and this eventually leads to a breakdown, when the transverse bulk transport cannot keep up with the longitudinal surface transport.

VII. CONCLUSION

In this paper, we have made a thorough combined numerical and analytical study of the transport mechanisms in a microchannel undergoing concentration polarization. We have rationalized the behavior of the system and identified four mechanisms of overlimiting current: surface conduction, surface advection, bulk advection, and bulk conduction through the extended space-charge region (ESC). In the limits where surface conduction, surface advection, or bulk conduction through the ESC dominates we have derived accurate analytical models for the ion transport and verified them numerically. In the limit of long, narrow channels these models are in excellent agreement with the numerical results. We have found that bulk advection is mainly important for short, broad channels, and using numerical simulations we have quantified this notion and outlined the parameter regions with significant bulk advection. A noteworthy discovery is that the development of bulk advection is strongly dependent on the surface current, even in the cases where the surface current contributes much less to the total current than bulk advection. The numerical simulations have been carried out using both a full numerical model with resolved diffuse double layers and an accurate boundary layer model suitable in the limit of small Gouy lengths.

[1] M. Eisenberg, C. Tobias, and C. Wilke, J. Electrochem. Soc. **101**, 306 (1954).
[2] M. Porter, Ind. Eng. Chem. Prod. Res. Dev. **11**, 234 (1972).
[3] V. V. Nikonenko, N. D. Pismenskaya, E. I. Belova, P. Sistat, P. Huguet, G. Pourcelly, and C. Larchet, Adv. Colloid Interface Sci. **160**, 101 (2010).
[4] I. Rubinstein and L. Shtilman, J. Chem. Soc. Farad. Trans. 2 **75**, 231 (1979).
[5] J. A. Manzanares, W. D. Murphy, S. Mafe, and H. Reiss, J. Phys. Chem. **97**, 8524 (1993).
[6] M. B. Andersen, M. van Soestbergen, A. Mani, H. Bruus, P. M. Biesheuvel, and M. Z. Bazant, Phys. Rev. Lett. **109**, 108301 (2012).
[7] Y. I. Kharkats, J. Electroanal. Chem. **105**, 97 (1979).
[8] C. P. Nielsen and H. Bruus, Phys. Rev. E **89**, 042405 (2014).
[9] I. Rubinshtein, B. Zaltzman, J. Pretz, and C. Linder, Russ. J. Electrochem. **38**, 853 (2002).
[10] B. Zaltzman and I. Rubinstein, J. Fluid. Mech. **579**, 173 (2007).
[11] C. L. Druzgalski, M. B. Andersen, and A. Mani, Phys. Fluids **25**, 110804 (2013).
[12] S. M. Davidson, M. B. Andersen, and A. Mani, Phys. Rev. Lett. **112**, 128302 (2014).
[13] S. J. Kim, Y.-C. Wang, J. H. Lee, H. Jang, and J. Han, Phys. Rev. Lett. **99**, 044501 (2007).
[14] S. J. Kim, L. D. Li, and J. Han, Langmuir **25**, 7759 (2009).
[15] A. Mani and M. Z. Bazant, Phys. Rev. E **84**, 061504 (2011).
[16] A. Mani, T. A. Zangle, and J. G. Santiago, Langmuir **25**, 3898 (2009).
[17] T. A. Zangle, A. Mani, and J. G. Santiago, Langmuir **25**, 3909 (2009).
[18] D. Linden and T. B. Reddy, *Handbook of Batteries* (McGraw–Hill, New York, 2002).
[19] C. Tanner, K. Fung, and A. Virkar, J. Electrochem. Soc. **144**, 21 (1997).
[20] A. V. Virkar, J. Chen, C. W. Tanner, and J.-W. Kim, Solid State Ion. **131**, 189 (2000).
[21] A. ElMekawy, H. M. Hegab, X. Dominguez-Benetton, and D. Pant, Bioresource Technol. **142**, 672 (2013).
[22] S. J. Kim, S. H. Ko, K. H. Kang, and J. Han, Nat. Nanotechnol. **5**, 297 (2010).
[23] Y.-C. Wang, A. L. Stevens, and J. Han, Anal. Chem. **77**, 4293 (2005).
[24] R. Kwak, S. J. Kim, and J. Han, Anal. Chem. **83**, 7348 (2011).
[25] S. H. Ko, Y.-A. Song, S. J. Kim, M. Kim, J. Han, and K. H. Kang, Lab Chip **12**, 4472 (2012).
[26] E. V. Dydek, B. Zaltzman, I. Rubinstein, D. S. Deng, A. Mani, and M. Z. Bazant, Phys. Rev. Lett. **107**, 118301 (2011).
[27] E. V. Dydek and M. Z. Bazant, AIChE J. **59**, 3539 (2013).
[28] A. Yaroshchuk, Adv. Colloid Interface Sci. **168**, 278 (2011).
[29] A. Yaroshchuk, E. Zholkovskiy, S. Pogodin, and V. Baulin, Langmuir **27**, 11710 (2011).
[30] I. Rubinstein and B. Zaltzman, J. Fluid Mech. **728**, 239 (2013).
[31] S. H. Behrens and D. G. Grier, J. Chem. Phys. **115**, 6716 (2001).
[32] K. G. H. Janssen, H. T. Hoang, J. Floris, J. de Vries, N. R. Tas, J. C. T. Eijkel, and T. Hankemeier, Anal. Chem. **80**, 8095 (2008).
[33] M. B. Andersen, J. Frey, S. Pennathur, and H. Bruus, J. Colloid Interface Sci. **353**, 301 (2011).
[34] K. L. Jensen, J. T. Kristensen, A. M. Crumrine, M. B. Andersen, H. Bruus, and S. Pennathur, Phys. Rev. E **83**, 056307 (2011).
[35] F. G. Donnan, J. Membr. Sci. **100**, 45 (1995).
[36] L. D. Landau and E. M. Lifshitz, *Statistical Physics*, 3rd ed., Vol. 1(Elsevier, Amsterdam, 1980).
[37] A. J. Bard, G. Inzelt, and F. Scholz, *Electrochemical Dictionary*, 2nd ed. (Springer, Berlin, 2012).
[38] K. Oldham and J. Myland, *Fundamentals of Electrochemical Science* (Elsevier, Amsterdam, 1993).
[39] M. M. Gregersen, M. B. Andersen, G. Soni, C. Meinhart, and H. Bruus, Phys. Rev. E **79**, 066316 (2009).
[40] See Supplemental Material at http://link.aps.org/supplemental/10.1103/PhysRevE.90.043020 for additional I-V characteristics for $\alpha = 0.01$ and $\alpha = 0.1$.
[41] E. Zholkovskij, J. Masliyah, and J. Czarnecki, Anal. Chem. **75**, 901 (2003).
[42] E. Zholkovskij and J. Masliyah, Anal. Chem. **76**, 2708 (2004).
[43] S. Griffiths and R. Nilson, Anal. Chem. **72**, 4767 (2000).

Appendix G

Paper submitted to Phys Rev E

Title: Morphological instability during steady electrodeposition at overlimiting currents

Authors: Christoffer P. Nielsen and Henrik Bruus.

Reference: Submitted to Physical Review E

Morphological instability during steady electrodeposition at overlimiting currents

Christoffer P. Nielsen and Henrik Bruus
Department of Physics, Technical University of Denmark,
*DTU Physics Building 309, DK-2800 Kongens Lyngby, Denmark**
(Dated: 24 August 2015)
Resubmitted to Phys. Rev. E

We present a linear stability analysis of a planar metal electrode during steady electrodeposition. We extend the previous work of Sundstrom and Bark by accounting for the extended space-charge density, which develops at the cathode once the applied voltage exceeds a few thermal voltages. In accordance with Chazalviel's conjecture, the extended space-charge region is found to greatly affect the morphological stability of the electrode. To supplement the numerical solution of the stability problem, we have derived analytical expressions valid in the limit of low and high voltage, respectively.

I. INTRODUCTION

One of the most interesting aspects of systems, involving transport between matter in different phases, is their tendency to become morphologically unstable and develop ramified growth patterns. Well known examples include snow flake formation and dendritic growth during metal solidification [1, 2]. A particularly interesting and challenging growth problem is encountered in electrodeposition from an electrolyte onto an electrode [3–11]. Whereas snow flake formation and solidification are mainly driven by diffusion of water vapour and heat, respectively [1, 2], electrodeposition is driven by electromigration in addition to diffusion [12, 13]. For this reason, the electrodeposition rate can be driven to exceed the diffusion limit, at which point the system enters a nonlinear regime not encountered in the purely diffusion-driven systems. One of the features of this nonlinear regime is the development of a nonequilibrium space-charge region, which extends from the cathode into the electrolyte [12, 14–16]. This extended space-charge region significantly affects the transport in the system, and it is a central component in the well known electroosmotic instability [17–19]. Already in 1990, Chazalviel realized that the extended space-charge region is crucial to the understanding of ramified growth during electrodeposition [12]. Nevertheless, there has been very little work which actually takes this effect into account.

In this paper we investigate the morphological stability of the cathode during electrodeposition in both the linear and the nonlinear regime. We follow the approach of Sundstrom and Bark [20], and investigate steady electrodeposition in a system composed of an electrolyte sandwiched between two, initially planar, metal electrodes. We solve the stability problem numerically and find that the higher the applied voltage difference is, the more unstable the electrode surface becomes. Also, the most unstable wavelength becomes smaller as the voltage bias is increased. In the numerical solution we employ the widely used Butler–Volmer reaction expression with constant charge-transfer coefficients. Apart from the extensive use of this model in the literature, the main reason for choosing it here, is its conceptual simplicity and reliance on only a few reaction parameters from which, allowing for a basic understanding of the system. Also, while the model may not describe reaction kinetics as well as some more elaborate models, it nevertheless correctly captures the exponential dependence on overpotential, which is an almost universal feature in reaction models [21, 22].

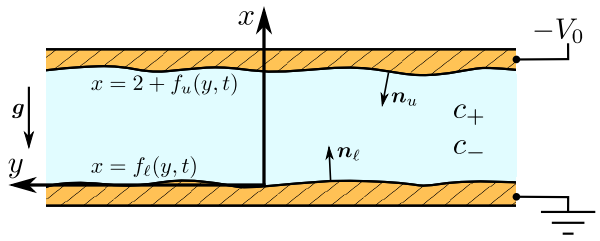

FIG. 1. (Color online) Sketch of the studied system with lower and upper electrode surfaces at $x = f_\ell(y,t)$ and $x = 2 + f_u(y,t)$, respectively. The coordinates are given relative to the moving frame of reference, following the mean rate of deposition on the electrode surfaces. The coordinates are also normalized by half the electrode spacing L.

In addition to solving the stability problem numerically, we derive analytical expressions for the perturbation growth rate, valid in the low and high voltage limit, respectively. In deriving these expressions, we make use of an accurate analytical model for the extended space-charge region, which we presented in a recent paper [16]. While our numerical results are restricted to the standard Butler–Volmer model, our analytical models cover a more general class of reaction models, including e.g. Marcus kinetics and Butler–Volmer–Frumkin kinetics.

II. MODEL SYSTEM

Following Sundstrom and Bark [20], we consider a binary electrolyte trapped between two co-planar metal electrodes at $x = 0$ and $x = 2L$. The electrolyte has initial concentration c_0 and is assumed symmetric with

* chnie@fysik.dtu.dk and bruus@fysik.dtu.dk

valence Z. The coordinate system is moving in the negative x-direction with velocity U, which is the rate of deposited layer growth and thus related to the average deposition rate on the electrodes. We consider the dilute solution limit, in which the effect of the moving coordinate system is negligible everywhere except in the surface evolution equation. A sketch of the system is shown in Fig. 1.

In the analysis, we investigate the stability of the electrodes under y-dependent perturbations along the x-direction. However, our analysis is general and applies to perturbations along any direction in the yz plane.

III. GOVERNING EQUATIONS

The current densities of either ion are given as

$$2\boldsymbol{J}_\pm = -c_\pm \boldsymbol{\nabla}\mu_\pm, \tag{1a}$$
$$\mu_\pm = \ln(c_\pm) \pm Z\phi, \tag{1b}$$

where we have non-dimensionalized the currents $\boldsymbol{J}_\pm$ by the limiting currents $2D_\pm c_0/L$, the electrochemical potentials $\mu_\pm$ by $k_\mathrm{B}T$, the electric potential ϕ by the thermal voltage $V_\mathrm{T} = k_\mathrm{B}T/e$, the coordinates by half the electrode spacing L, and the concentrations $c_\pm$ by the initial concentration c_0. Normalizing the time by the diffusion time $t_0 = L^2/(2D_+)$, the non-dimensionalized ion-conservation equations become

$$\frac{D_+}{D_\pm}\partial_t c_\pm = -\boldsymbol{\nabla}\cdot\boldsymbol{J}_\pm. \tag{2}$$

At the electrodes, the current of anions vanishes, while the current of cations is given by a reaction expression

$$\boldsymbol{n}_p\cdot\boldsymbol{J}_- = 0, \tag{3a}$$
$$\boldsymbol{n}_p\cdot\boldsymbol{J}_+ = -R_p, \tag{3b}$$

where R_p is the reaction rate at the lower and upper electrode, respectively, as indicated by the subscript $p = \ell, u$. We model the reaction rates R_u and R_ℓ using a reaction expression of the general form

$$R_p = K_0\left[c_+ e^{-\bar\gamma\kappa+\alpha_\mathrm{c}(\phi,c_+)Z(\phi+V_p)} - e^{-\bar\gamma\kappa-\alpha_\mathrm{a}(\phi,c_+)Z(\phi+V_p)}\right]. \tag{4}$$

Here, K_0 is the dimensionless version of the dimensionfull rate constant k_0 for the electrode reaction,

$$K_0 = \frac{k_0}{2D_+c_0/L}, \tag{5}$$

V_p is the normalized electrode potential, κ is the normalized curvature of the surface, and $\bar\gamma$ is the non-dimensionalized version of the dimensionfull surface energy γ,

$$\bar\gamma = \frac{a^3\gamma}{k_\mathrm{B}TL}. \tag{6}$$

We allow the cathodic and anodic charge-transfer coefficients α_c and α_a to vary with the potential ϕ and the cation concentration c_+. In this way, Eq. (4) represents a wide range of reaction models from classical Butler–Volmer kinetics to Marcus kinetics and Butler–Volmer–Frumkin kinetics [20–22]. In agreement with most realistic reaction models, we do impose one restriction on the charge transfer coefficients, namely that they vary slowly as a function of ϕ and $\ln(c_+)$,

$$\partial_\phi\left\{\alpha_\mathrm{c}(\phi,c_+)\phi\right\} \approx \alpha_\mathrm{c}(\phi,c_+), \tag{7}$$
$$\partial_{\ln(c_+)}\left\{\alpha_\mathrm{c}(\phi,c_+)\ln(c_+)\right\} \approx \alpha_\mathrm{c}(\phi,c_+). \tag{8}$$

The electrostatic part of the problem is governed by the Poisson equation,

$$2\bar\lambda_\mathrm{D}^2\nabla^2\phi = -\rho = -Zc_+ + Zc_-, \tag{9}$$

where the non-dimensional Debye length $\bar\lambda_\mathrm{D}$ is given as

$$\bar\lambda_\mathrm{D} = \frac{\lambda_\mathrm{D}}{L}, \quad \text{with} \quad \lambda_\mathrm{D} = \sqrt{\frac{k_\mathrm{B}T\epsilon_\mathrm{w}}{2e^2c_0}}. \tag{10}$$

For simplicity, and to be in accordance with most previous work, we choose not to explicitly model the Debye layers adjoining the electrodes. Instead, we apply the boundary conditions (3) just outside the Debye layer. Following Ref. [23] we implement the boundary condition

$$\boldsymbol{n}_u\cdot\boldsymbol{\nabla}c_+ = 0, \tag{11}$$

at the upper electrode, to indicate the minimum in c_+ at the outer edge of the Debye layer. We note that the Debye layers can be included implicitly by including the Frumkin correction to the reaction model. This correction can be implemented by an appropriate choice of the charge-transfer coefficients [22]. Together with Eq. (3b), condition (11) corresponds to ascribing the entire current into the upper electrode to electromigration.

Finally, since the anions can not enter or leave the system the total number of anions is conserved,

$$\int_\Omega \left(c_- - 1\right)\,\mathrm{d}V = 0. \tag{12}$$

We introduce functions $x = f_p(y)$ describing the position of the upper and lower electrode u and ℓ. The time evolution of f_p is determined by the single-ion volume a^3 and the current into the electrode,

$$\left(\partial_t f_\ell - U\right)\boldsymbol{e}_x\cdot\boldsymbol{n}_\ell = -a^3c_0\boldsymbol{n}_\ell\cdot\boldsymbol{J}_+, \quad \text{Anode}, \tag{13a}$$
$$\left(\partial_t f_u - U\right)\boldsymbol{e}_x\cdot\boldsymbol{n}_u = -a^3c_0\boldsymbol{n}_u\cdot\boldsymbol{J}_+, \quad \text{Cathode}. \tag{13b}$$

Here, the filling factor a^3c_0 is much less than unity, since we are dealing with dilute solutions. The normalized velocity U of the coordinate system accounts for the mean current into or out of the electrodes, and $\partial_t f_p$ accounts for local deviations from the mean current.

The curvature κ and the normal vectors are related to the surface function f_p by

$$\boldsymbol{n}_\ell = \frac{\boldsymbol{e}_x - \boldsymbol{e}_y \partial_y f_\ell}{\sqrt{1+(\partial_y f_\ell)^2}}, \quad \boldsymbol{n}_u = \frac{-\boldsymbol{e}_x + \boldsymbol{e}_y \partial_y f_u}{\sqrt{1+(\partial_y f_u)^2}}, \tag{14a}$$

$$\kappa_\ell = \frac{\partial_y^2 f_\ell}{\sqrt{1+(\partial_y f_\ell)^2}}, \quad \kappa_u = -\frac{\partial_y^2 f_u}{\sqrt{1+(\partial_y f_u)^2}}. \tag{14b}$$

In defining the above equations and boundary conditions, we have chosen slightly different normalizations than in Ref. [20], the main difference being that we allow for a non-zero space charge density.

IV. PERTURBATION

The stability of the electrodes is investigated using linear perturbation theory. That is, we impose a small perturbation on a steady-state base state, and investigate how the perturbation evolves. The base state is identified by a superscript "0" and the first-order perturbation by superscript "1",

$$f_p(y,t) \approx f_p^1(y,t), \tag{15a}$$

$$c_\pm(x,y,t) \approx c_\pm^0(x) + c_\pm^1(x,y,t), \tag{15b}$$

$$\phi(x,y,t) \approx \phi^0(x) + \phi^1(x,y,t). \tag{15c}$$

In first-order perturbation theory, we substitute the second-order factor $\sqrt{1+(\partial_y f_p)^2}$ in Eq. (14) by unity,

$$\boldsymbol{n}_\ell \approx \boldsymbol{e}_x - \boldsymbol{e}_y \partial_y f_\ell^1, \qquad \boldsymbol{n}_u \approx -\boldsymbol{e}_x + \boldsymbol{e}_y \partial_y f_u^1, \tag{16a}$$

$$\kappa_\ell \approx \partial_y^2 f_\ell^1, \qquad \kappa_u \approx -\partial_y^2 f_u^1. \tag{16b}$$

To find the field values at the perturbed surface, we Taylor expand to first order and obtain

$$\phi(f_\ell^1, y, t) \approx \phi^0(0) + \partial_x\phi|_0 f_\ell^1(y,t) + \phi^1(0,y,t), \tag{17a}$$

$$\begin{aligned}\boldsymbol{\nabla}\phi(f_\ell^1, y, t) &\approx \partial_y\phi^1|_0 \boldsymbol{e}_y \\ &\quad + \left(\partial_x\phi^0|_0 + \partial_x^2\phi^0|_0 f_\ell^1 + \partial_x\phi^1|_0\right)\boldsymbol{e}_x.\end{aligned} \tag{17b}$$

Similar expressions apply for $c_\pm$ and at the upper electrode. Evaluating the reaction rate at the lower electrode and expanding to first order, we find

$$R_\ell \approx R_\ell^0 + R_\ell^1, \tag{18a}$$

$$\frac{R_\ell^0}{K_0} = c_+^0 e^{\alpha_c Z(\phi^0+V_\ell)} - e^{-\alpha_a Z(\phi^0+V_\ell)}, \tag{18b}$$

$$\begin{aligned}\frac{R_\ell^1}{K_0} &= e^{\alpha_c Z(\phi^0+V_\ell)}\Big[c_+^1 + \partial_x c_+^0 f_\ell^1 \\ &\quad + c_+^0(\alpha_a+\alpha_c)Z\big[\phi^1 + \partial_x\phi^0 f_\ell^1\big]\Big] \\ &\quad + \frac{R_\ell^0}{K_0}\Big[-\bar{\gamma}\partial_y^2 f_\ell^1 - \alpha_a Z\big[\phi^1 + \partial_x\phi^0 f_\ell^1\big]\Big],\end{aligned} \tag{18c}$$

where all fields are evaluated at $x=0$, and the expression for R_ℓ^0 was used to simplify the expression for R_ℓ^1. Since the charge-transfer coefficients vary slowly with ϕ and $\ln(c_+)$, we have neglected their first order contributions. Similar expressions apply at the upper electrode.

Hence, the full zeroth-order problem becomes

$$0 = -\partial_x J_\pm^0, \tag{19a}$$

$$2J_\pm^0 = -\partial_x c_\pm^0 \mp Z c_\pm^0 \partial_x\phi^0, \tag{19b}$$

$$2\bar{\lambda}_D^2 \partial_x^2\phi^0 = -Z(c_+^0 - c_-^0) = -\rho^0, \tag{19c}$$

with the following boundary conditions and constraints

$$J_-^0(0) = 0, \qquad J_-^0(2) = 0, \tag{20a}$$

$$J_+^0(0) = -R_\ell^0, \qquad J_+^0(2) = R_u^0, \tag{20b}$$

$$\int_0^2 \left(c_-^0 - 1\right)\,\mathrm{d}x = 0, \qquad \partial_x c_+^0(2) = 0, \tag{20c}$$

and the mean growth velocity U derived from Eq. (13),

$$U = a^3 c_0 J_+^0. \tag{21}$$

Similarly, the first-order problem is given by

$$\frac{D_+}{D_\pm}\partial_t c_\pm^1 = -\boldsymbol{\nabla}\cdot\boldsymbol{J}_\pm^1, \tag{22a}$$

$$2\boldsymbol{J}_\pm^1 = -\boldsymbol{\nabla}c_\pm^1 \mp Z c_\pm^0 \boldsymbol{\nabla}\phi^1 \mp Z c_\pm^1 \boldsymbol{\nabla}\phi^0, \tag{22b}$$

$$2\bar{\lambda}_D^2\nabla^2\phi^1 = -Z(c_+^1 - Z c_-^1), \tag{22c}$$

and the boundary conditions,

$$\boldsymbol{e}_x\cdot\boldsymbol{J}_-^1(2) = 0, \qquad \boldsymbol{e}_x\cdot\boldsymbol{J}_-^1(0) = 0, \tag{23a}$$

$$\boldsymbol{e}_x\cdot\boldsymbol{J}_+^1(2) = R_u^1, \quad \boldsymbol{e}_x\cdot\boldsymbol{J}_+^1(0) = -R_\ell^1, \tag{23b}$$

$$\partial_x^2 c_+^0(2) f_u^1 + \partial_x c_+^1(2) = 0, \tag{23c}$$

together with the first-order electrode growth rates $\partial_t f_\ell^1$ and $\partial_t f_u^1$ derived from Eq. (13),

$$\partial_t f_\ell^1 = a^3 c_0 R_\ell^1, \qquad \partial_t f_u^1 = -a^3 c_0 R_u^1. \tag{24}$$

To find the eigenmodes, we make the following harmonic ansatz for the first-order fields,

$$c_\pm^1(x,y,t) = c_\pm^*(x) e^{\Gamma t + iky}, \tag{25a}$$

$$\phi^1(x,y,t) = \phi^*(x) e^{\Gamma t + iky}, \tag{25b}$$

$$f_p^1(y,t) = F_p e^{\Gamma t + iky}, \tag{25c}$$

where Γ is the nondimensional growth rate of the perturbation, and k is the wavenumber of the transverse eigenmode. For convenience we also define

$$R_p^1 = R_p^* e^{\Gamma t + iky}. \tag{25d}$$

With this ansatz, the first-order bulk equations become

$$\begin{aligned}2\frac{D_+}{D_\pm}\Gamma c_\pm^* &= -k^2(c_\pm^* \pm Z c_\pm^0 \phi^*) \\ &\quad + \partial_x\Big\{\partial_x c_\pm^* \pm Z c_\pm^* \partial_x\phi^0 \pm Z c_\pm^0 \partial_x\phi^*\Big\}\end{aligned} \tag{26a}$$

$$2\bar{\lambda}_D^2(\partial_x^2\phi^* - k^2\phi^*) = -Z(c_+^* - c_-^*), \tag{26b}$$

and the first-order reaction rate at the lower electrode is

$$\frac{R_\ell^*}{K_0} = e^{\alpha_c Z(\phi^0+V_\ell)}\Big[c_+^* + \partial_x c_+^0 F_\ell + c_+^0(\alpha_a+\alpha_c)Z\big[\phi^* + \partial_x\phi^0 F_\ell\big]\Big] + \frac{R_\ell^0}{K_0}\Big[-\bar{\gamma}k^2F_\ell - \alpha_a Z\big[\phi^* + \partial_x\phi^0 F_\ell\big]\Big]. \quad (27)$$

Inserting the ansatz in the growth equations (24) yields

$$\Gamma F_\ell = a^3 c_0 R_\ell^*, \qquad \Gamma F_u = -a^3 c_0 R_u^*. \quad (28)$$

V. ANALYTICAL RESULTS

For large wavenumbers, $k \gtrsim 1$, we can neglect f_ℓ and the left hand side in Eq. (26a). Analytical expressions for the growth rate can then be obtained in the limit of overlimiting and underlimiting current, respectively. In Appendices A and B we find that the growth rate can be expressed as

$$\Gamma = a^3 c_0 k J^0 \frac{\xi - \bar{\gamma}k^2}{\xi + k}. \quad (29)$$

Here, in the linear underlimiting regime, ξ is given as

$$\xi = (1+\alpha_a+\alpha_c)K_0 e^{\alpha_c Z(\phi^0+V_u)} - \alpha_a\frac{J^0}{c_+^0}, \quad (30)$$

$$c_+^0 = 1 - J^0, \quad \text{Linear case}, \quad (31)$$

while in the nonlinear overlimiting regime ξ is

$$\xi = 2(\alpha_a+\alpha_c)K_0 e^{\alpha_c Z(\phi^0+V_u)} - \alpha_a\frac{2J^0}{c_+^0}, \quad (32a)$$

$$c_+^0 \approx \frac{\bar{\lambda}_D}{Z}\sqrt{\frac{2J^0}{1-\frac{1}{J^0}}}, \quad \text{Nonlinear case}. \quad (32b)$$

The factors $K_0 e^{\alpha_c Z(\phi^0+V_u)}$ are found by solving the zero order reaction expression,

$$J^0 = R_u^0 = K_0\left[c_+^0 e^{\alpha_c Z(\phi^0+V_u)} - e^{-\alpha_a Z(\phi^0+V_u)}\right]. \quad (33)$$

The charge-transfer coefficients α_c and α_a may depend on ϕ^0 and c_+^0, so there is no general solution to Eq. (33). In the limit $K_0 \ll 1$ the deposition term in Eq. (33) dominates, and we simply have

$$K_0 e^{\alpha_c Z(\phi^0+V_u)} = \frac{J^0}{c_+^0}. \quad (34)$$

In that limit ξ becomes

$$\xi = (1+\alpha_c)\frac{J^0}{c_+^0}, \quad \text{Linear case}, \quad (35)$$

$$\xi = 2\alpha_c\frac{J^0}{c_+^0}, \quad \text{Nonlinear case}. \quad (36)$$

In the case of simple Butler–Volmer kinetics with constant charge transfer coefficients $\alpha_c = \alpha_a = \frac{1}{2}$, it is also possible to obtain simple solutions to Eq. (33). In that case we find

$$\xi = \frac{J^0}{c_+^0}\left[\frac{1}{2} + \sqrt{1+4\left(\frac{K_0}{J^0}\right)^2 c_+^0}\right], \text{ Linear}, \quad (37)$$

$$\xi = \frac{J^0}{c_+^0}\sqrt{1+4\left(\frac{K_0}{J^0}\right)^2 c_+^0}, \quad \text{Nonlinear}. \quad (38)$$

The critical wavenumber k_c, where the perturbation is marginally stable, is found to be

$$k_c = \sqrt{\frac{\xi}{\bar{\gamma}}}, \quad (39a)$$

and the wavenumber k_{max}, at which the growth rate is maximum, is given as

$$k_{max} = \frac{\xi}{2}\left[\left(\frac{2-\xi\bar{\gamma}+2\sqrt{1-\xi\bar{\gamma}}}{\xi\bar{\gamma}}\right)^{1/3} + \left(\frac{2-\xi\bar{\gamma}+2\sqrt{1-\xi\bar{\gamma}}}{\xi\bar{\gamma}}\right)^{-1/3} - 1\right]. \quad (39b)$$

We note that the analytical model takes the zeroth-order current density J^0 as input variable through ξ. If one wants the results as a function of the potential drop instead, a model of the system's current-voltage characteristic is needed. For simplicity, we just use the numerically calculated current-voltage characteristic in the following.

To compute the results without reference to a numerical solution, an analytical model for the system's current-voltage characteristic is required. Such a model can be found in our previous work [16]. To obtain the total voltage drop over the system, the interfacial voltages from Eq. (18b) should also be taken into account.

TABLE I. Fixed parameter values used in the numerics.

Parameter	Symbol	Value
Cation diffusivity[24]	D_+	$0.714\times10^{-9}\,\mathrm{m^2\,s^{-1}}$
Anion diffusivity[24]	D_-	$1.065\times10^{-9}\,\mathrm{m^2\,s^{-1}}$
Ion valence	Z	2
Surface energy	γ	$1.85\ \mathrm{J\,m^{-2}}$
Temperature	T	300 K
Permittivity of water	ϵ_w	$6.90\times10^{-10}\,\mathrm{F\,m^{-1}}$
Charge-transfer coefficients	α_c, α_a	$\frac{1}{2}$
Reaction constant[a]	k_0	$9.4\times10^{19}\,\mathrm{m^{-2}\,s^{-1}}$
Diameter of a copper atom[b]	a	0.228 nm

[a] Calculated using the exchange current $I_0 = 30\ \mathrm{A\,m^{-2}}$ from Ref. [25] and $k_0 = I_0/(Ze)$.
[b] The cube root of the volume per atom in solid copper [24].

VI. NUMERICAL SOLUTION

The numerical simulations are carried out in the commercially available finite element software COMSOL MULTIPHYSICS ver. 4.3a. Following our previous work [16, 23, 26], the zeroth- and first-order problems are rewritten in weak form and implemented in the mathematics module of COMSOL. In the first-order problem we set the parameter F_u to unity, meaning that the magnitude of the remaining first-order fields are given relative to the amplitude of the upper electrode perturbation. We choose to model the reaction using simple Butler–Volmer kinetics with $\alpha_c = \alpha_a = \frac{1}{2}$. To limit the parameter space, we choose fixed, physically reasonable values for the parameters listed in Table I. The values are chosen to correspond to copper electrodes in a copper sulfate solution. We note that the surface tension is quite difficult to determine experimentally, and most measurements are carried out at temperatures around 1000 °C [27, 28]. *Ab initio* calculations can give some impression of the behaviour at lower temperatures [29], but these can hardly stand alone. Extrapolating the linear fit of Ref. [27] down to 0 K yields surface tension values close to those obtained from *ab initio* calculations in Ref. [29]. This makes it somewhat plausible to apply the model from Ref. [27] in the region of interest around 300 K. This yields a copper-gas surface energy of 1.92 J/m^2. The contact angle at the copper-water interface is very small [30], so finding the copper-water surface energy is just a matter of subtracting the surface energy of water from that of copper. The resulting surface energy is $\gamma \approx 1.85$ J/m^2, as listed in Table I.

These choices leave us with three free parameters, which are the bias voltage V_0, the electrolyte concentration c_0, and the system length L.

The solution procedure is as follows: First, the zeroth-order problem is solved for a given set of parameters. Then the first-order problem is solved for a range of wavenumbers k. For each k value, the corresponding growth rate Γ and perturbation amplitude of the lower electrode, F_ℓ, are obtained.

In Fig. 2, the zeroth-order cation concentrations c_+^0 and space-charge density ρ^0 are shown for $c_0 = 10$ mM, $L = 10$ µm and varying bias voltage V_0. It is seen, that when the bias voltage exceeds $V_0 \simeq 12$, local electroneutrality is violated near the cathode. For $V_0 = 30$ the nonequilibrium space-charge region extends far $(0.04L)$ into the electrolyte.

A. Results

For plotting purposes we introduce the dimensionfull perturbation wavelength $\lambda = 2\pi L/k$. In Fig. 3, the growth rate Γ is plotted versus λ for $V_0 = 30$, $c_0 = 10$ mM, and $L = 10$ µm. Visible in the figure is a stable region for wavelengths smaller than the critical wavelength $\lambda_c = 51$ nm, and an unstable region for larger

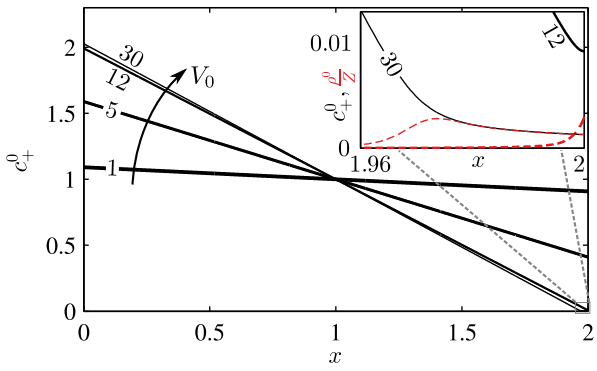

FIG. 2. (Color online) Zeroth-order cation concentrations c_+^0 shown in full (black) lines and zeroth-order charge densities ρ^0/Z shown in dashed (red) lines. The inset shows the fields close to the electrode. In the simulation the parameter values $c_0 = 10$ mM, $L = 10$ µm, and $V_0 = \{1, 5, 12, 30\}$ were used.

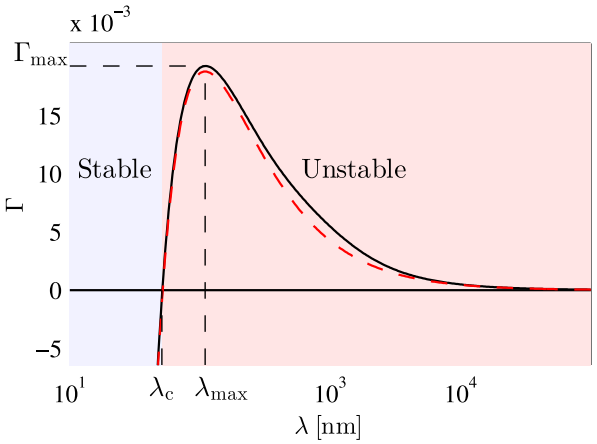

FIG. 3. (Color online) The growth rate Γ plotted versus the perturbation wavelength λ for $V_0 = 30$, $c_0 = 10$ mM, and $L = 10$ µm. The full (black) line shows the growth rate obtained from numerical simulations, and the dashed (red) line shows the growth rate according to the analytical model Eq. (29). For perturbation wavelengths smaller than the critical wavelength $\lambda_c = 51$ nm the system is stable and for larger wavelengths it is unstable. At the most unstable wavelength $\lambda_{max} = 110$ nm the growth rate is $\Gamma_{max} = 0.0193$.

wavelengths. The most unstable wavelength we denote λ_{max}, and the corresponding growth rate we denote Γ_{max}.

To enable a more compact representation of the data, we introduce a gray-scale contour plot of the magnitude of Γ, as illustrated in Fig. 4. Here, Γ is plotted versus the wavelength λ for $V_0 = \{5,\ 10,\ 15,\ 20,\ 25,\ 30\}$. The gray scale in the λ-V_0 plane is created by projecting the Γ values from the above curves onto the plane. The solid (blue) line in the $(\lambda,\ V_0)$-plane marks the crest of the hill, thus representing the most unstable wavelength for each value of V_0.

In Fig. 5, we make use of the contour plots to show results for twelve sets of (c_0, L)-values. In each contour plot, Γ is normalized by its maximum value, which is

given above each plot. Shown in thick lines are $\lambda_{\max}$ in bright (yellow) and λ_c in black. The corresponding analytical results are shown in dashed (blue) and dotted (green) lines, respectively. The thin black lines show contours, where Γ equals $\{0.01, 0.2, 0.7\}$ times the maximum value. There is a clear tendency in all of the panels that the growth rate Γ increases rapidly with V_0, and the most unstable wavelength decreases as V_0 increases. Across the panels, the maximum growth rate is seen to increase for increasing c_0 and increasing L. Also, the most unstable wavelength $\lambda_{\max}$ and the critical wavelength λ_c become smaller as c_0 increases and as L decreases.

A common feature seen in all of the panels, is the kink in the V_0-versus-$\lambda_{\max}$ and V_0-versus-λ_c lines. At this kink, the slope of the lines changes markedly. The kink is located at the voltage, where the current reaches the limiting current, and it thus signifies that there is a qualitatively different behavior for over- and underlimiting current. This qualitative difference between the two regimes is in accordance with the analytical models. We also see that the kink voltage changes with c_0 and L. Specifically, it increases with c_0 and decreases with L. The main reason for this behavior is easily understood with reference to the zeroth-order Butler-Volmer reaction expression (18b). Setting the current in the system to the limiting current $J_+^0 = 1$, the reaction rates at the electrodes become

$$\boldsymbol{e}_x \cdot \boldsymbol{n}_p = -K_0 \left[c_+ e^{\alpha_c Z(\phi+V_p)} - e^{-\alpha_a Z(\phi+V_p)} \right]. \quad (40)$$

At the cathode, the first term in the bracket dominates, and at the anode the other. Therefore, both potential drops over the electrode interfaces scale as

$$\Delta V \sim -\ln(K_0) = \ln\left(\frac{2D_+ c_0}{L}\right) - \ln(k_0), \quad (41)$$

which increases monotonically with increasing c_0/L. As a consequence, the total potential drop at the limiting current also increases with increasing c_0/L, just as observed in Fig. 5.

In addition to the instability growth rate Γ, which gives a time scale for the development of instabilities, it is useful to have a measure for the characteristic instability length scale. For instance, we would like to estimate the thickness of the deposited layer, when instabilities start to develop. We define this instability length scale as the product of the zeroth-order growth rate Eq. (21) and the instability time scale at the most unstable wavelength

$$L_\Gamma = L\frac{a^3 c_0 J_+^0}{\Gamma_{\max}}, \quad (42)$$

where the pre-factor L ensures a dimensionfull expression. In Fig. 6, we plot the instability length L_Γ versus applied voltage V_0 for $L = 100$ µm and varying c_0. The most unstable wavelength $\lambda_{\max}$ is also plotted in the same figure (dashed lines). It is seen that L_Γ decreases as V_0 increases, but for small voltages L_Γ is largest for high concentrations, while the opposite is true for high voltages. The reason for this reversal is that the interfacial voltage drops are largest for large c_0. At small voltages the bulk driving force in the systems with large c_0 is therefore small, and this causes the system to be less unstable than the low c_0 systems. We also see that $\lambda_{\max}$ scales in the same way as L_Γ. While the reason for this is not immediately obvious, it is seen to follow from the analytical expressions. Inserting Eq. (29) in Eq. (42) yields

$$L_\Gamma = \frac{\lambda_{\max}}{2\pi}\frac{\xi + \frac{2\pi L}{\lambda_{\max}}}{\xi - \bar{\gamma}\left(\frac{2\pi L}{\lambda_{\max}}\right)^2}, \quad (43)$$

which confirms the approximate scaling between L_Γ and $\lambda_{\max}$. The connection between L_Γ and $\lambda_{\max}$ implies that $\lambda_{\max}$ sets the scale, not only for the variations in the horizontal direction, but also for variations in the vertical direction. We might therefore expect that the ramified electrodeposits, emerging at much longer times than $\Gamma_{\max}^{-1}$, have a universal length scale roughly set by $\lambda_{\max}$.

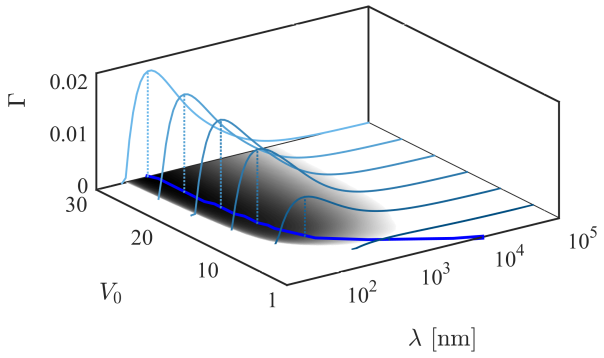

FIG. 4. (Color online) The growth rate Γ plotted versus the perturbation wavelength λ and voltage V_0 for $c_0 = 10$ mM, and $L = 10$ µm. The (cyan) space curves are plots of Γ versus λ for $V_0 = \{5, 10, 15, 20, 25, 30\}$. The shade of the in plane contour plot is based on the logarithm of Γ, which is why there are no contours in the low λ limit where Γ is negative. The thick (blue) in plane line marks the crest of the hill, i.e. it marks the most unstable wavelength for each value of V_0.

VII. DISCUSSION

The main feature, which sets our work apart from previous stability analyses of electrodeposition, is the inclusion of the overlimiting regime. Presumably, this regime has so far been avoided due to the non-linearities arising at overlimiting current, which necessitate a more complicated treatment. However, the overlimiting regime is highly relevant for ramified growth problems [7, 8]. As seen in Fig. 5, the instability growth rate increases markedly in the overlimiting regime, and there is also a change in qualitative behavior between the two regimes. Of course, the conclusions we reach, based on our model,

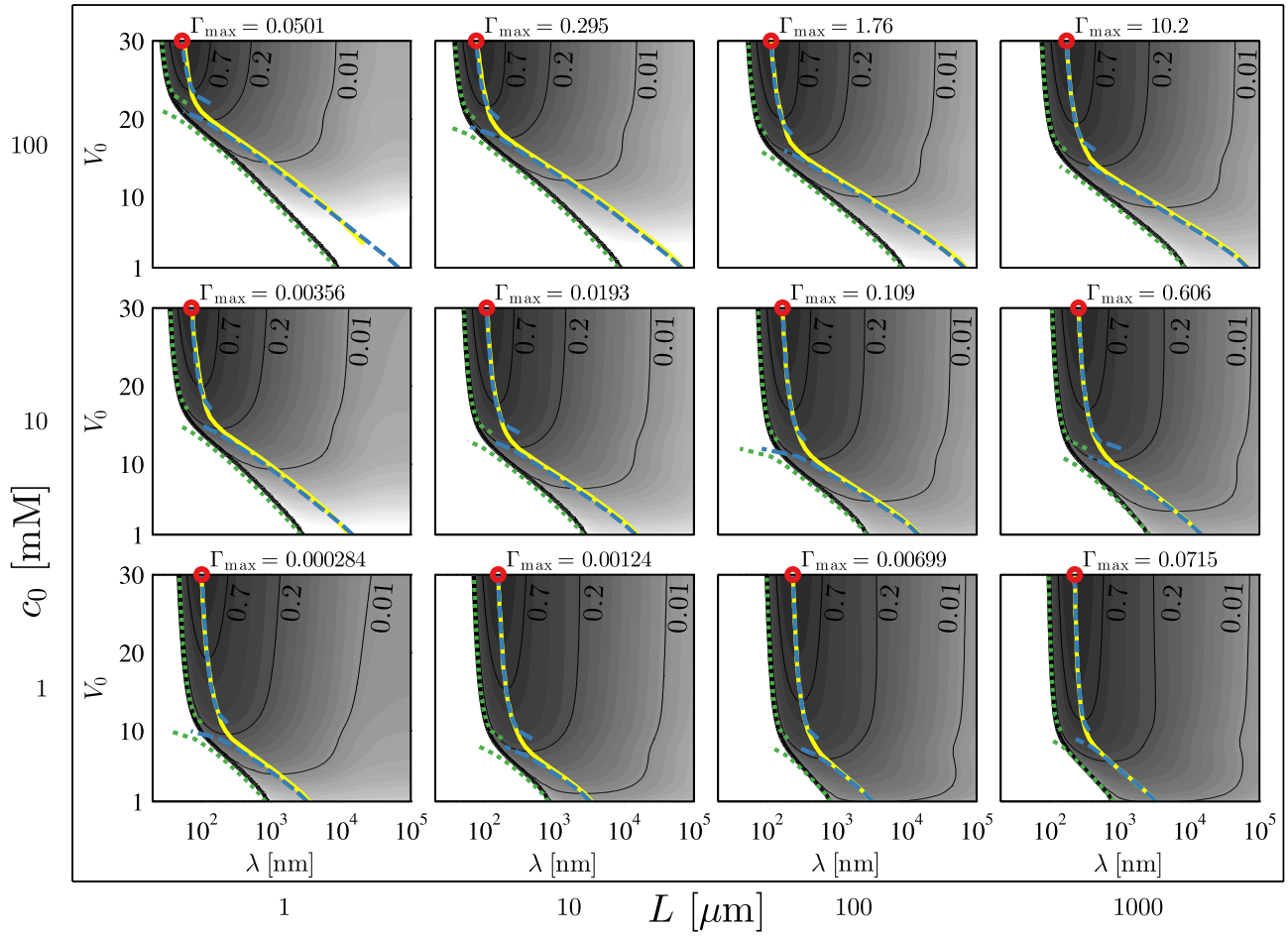

FIG. 5. (Color online) Contour plots of Γ plotted versus wavelength λ and voltage V_0 for $c_0 = \{1\text{ mM}, 10\text{ mM}, 100\text{ mM}\}$ and $L = \{1\text{ µm}, 10\text{ µm}, 100\text{ µm}, 1\text{ mm}\}$. In each plot, Γ is normalized by its maximum value, and the contours are logarithmically spaced. The maximum value $\Gamma_{\max}$ of Γ is given on top of each plot, and the point where the maximum value is attained is indicated with a dark (red) circle. The three thin black lines in each plot indicate contours where Γ equals 0.01, 0.2, and 0.7 times $\Gamma_{\max}$. The thick bright (yellow) line marks $\lambda_{\max}$ for each value of V_0, and the dashed (blue) lines mark the two corresponding analytical limits. The thick black line marks λ_c for each value of V_0, and the dotted (green) lines mark the two corresponding analytical limits.

are only strictly valid for planar electrodes. It does, however, seem reasonable to expect that the most unstable wavelength $\lambda_{\max}$ is comparable to the characteristic dimensions encountered in a ramified growth experiment. Our analysis can thus be used to rationalize experimental results. In this regard, our analytical models are particularly useful, since they allow for easy computation of the key quantities for other systems than the one treated here.

Perhaps the most important application of the stability analysis, is as a means of validating more elaborate numerical models of ramified growth. A model of ramified growth must necessarily deal with a moving interface and this, as well as other complications, make for highly complex numerical models. To validate such models it is very useful to have a comparatively simple model, like the present one, to benchmark against in the relevant limit. Indeed, this was what originally motivated us to treat the stability problem.

An obvious shortcoming of the given analysis, is the restriction to a steady-state zeroth-order solution. The principal reason for this choice is that it makes for a simpler problem. Furthermore, the numerical ramified growth model, to which we wish to compare our model, is at present also restricted to quasi-steady state. In time, we wish to extend both models to the fully transient regime.

There is, however, some physical justification for making the steady-state assumption. As seen in Fig. 5, the growth rate Γ is considerably smaller than unity in a large part of the investigated parameter space. The time it takes the system to reach steady state is given by the diffusive time, which in our normalization has the value one. Thus, as long as Γ is much smaller than unity, the system reaches steady state long before any instabilities build up. In this case it is therefore justified to assume

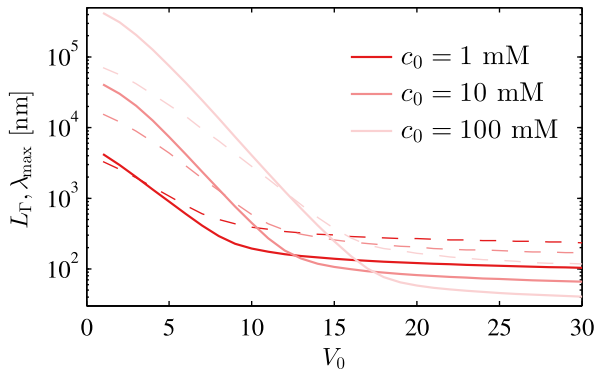

FIG. 6. (Color online) The instability length scale L_Γ (full line) and most unstable wavelength $\lambda_{\max}$ (dashed line) plotted versus bias voltage V_0. The concentration varies between the values $c_0 = \{1\text{ mM}, 10\text{ mM}, 100\text{ mM}\}$ and the length $L = 100$ µm was used.

steady state. It should be noted that in this argument we make the reasonable assumption that the true growth rate in the transient regime does not significantly exceed the steady-state value.

In the numerical model we employ the widely used Butler–Volmer model with equal cathodic and anodic charge-transfer coefficients. The analytical model is however not restricted to this particular reaction model. In deriving the analytical results we only required that the charge-transfer coefficients vary slowly with the interfacial potential drop and the cation concentration. Thus, we expect the analytical model to apply equally well to Marcus kinetics and Butler–Volmer kinetics with asymmetric charge-transfer coefficients. Also, the effects of an electric double layer can be included implicitly by applying the Frumkin correction.

In future work, it would of course be interesting to extend the implicit general modeling of the electric double layers to explicit and more specific schemes, such as those presented in Refs. [31–34]. Also, it would be relevant to study the influence of advection on the morphological stability, in particular the effect of electroosmotic instabilities [17–19].

Finally, we hope that our results may inspire experimentalists in the field to analyze electrodeposition experiments in terms of our theoretical framework.

VIII. CONCLUSION

We have successfully solved the stability problem in the under- and overlimiting regime for the case of a copper sulfate solution trapped between two copper electrodes. In addition to the numerical solution of this particular problem, we have derived analytical solutions valid in either the overlimiting or the underlimiting limit. The behavior in the overlimiting regime differs qualitatively from the behavior in the underlimiting regime, and we find that the electrode becomes increasingly unstable as the current is increased above the limiting current. The stability analysis, and in particular the analytical limits, are valuable both for rationalizing experimental results and for validating more elaborate numerical models of ramified growth.

Appendix A: The electroneutral limit

In the limit where the electrolyte is locally electroneutral and the time derivatives in the first-order transport problem are negligible, analytical solutions to the problem can be obtained. Setting the point of zero electrostatic potential at $x = 1$, it is easily found that

$$c = c_+ = c_- = e^{Z\phi}. \tag{A1}$$

It follows that $c = e^{Z(\phi^0+\phi^1)} \approx e^{Z\phi^0} + e^{Z\phi^0} Z\phi^1$, and thus

$$c^0 = e^{Z\phi^0} \quad \text{and} \quad c^1 = e^{Z\phi^0} Z\phi^1. \tag{A2}$$

Solving the zeroth-order problem yields

$$c^0 = 1 - J^0(x-1), \quad Z\phi^0 = \ln(1 - J^0(x-1)). \tag{A3}$$

Using the electroneutrality assumption in Eq. (26a) we find

$$0 = \partial_x^2 c^* - k^2 c^*. \tag{A4}$$

This equation has two solutions, but as long as the perturbation wavelength is considerably smaller than the electrode spacing, the solution which increases with x is dominant

$$c^* \approx C e^{k(x-2)}, \tag{A5}$$

where C is a constant to be determined. From Eq. (A2) we then find

$$\phi^* = \frac{1}{Z}\frac{c^*}{c^0} = \frac{C}{Z}\frac{e^{k(x-2)}}{1 - J^0(x-1)}. \tag{A6}$$

At the upper electrode, $x = 2$, the first-order reaction rate is (we set $F_u = 1$)

$$\frac{R_u^*}{K_0} = e^{\alpha_c Z(\phi^0+V_u)}\Big[c^* + \partial_x c^0 + c^0(\alpha_a + \alpha_c)Z\big(\phi^* + \partial_x\phi^0\big)\Big] + \frac{R_u^0}{K_0}\Big[\bar{\gamma}k^2 - \alpha_a Z\big(\phi^* + \partial_x\phi^0\big)\Big]. \tag{A7}$$

Evaluating the fields at $x = 2$, this expression becomes

$$\frac{R_u^*}{K_0} = (1 + \alpha_a + \alpha_c)(C - J^0)e^{\alpha_c Z(\phi^0+V_u)} + \frac{J^0}{K_0}\left[\bar{\gamma}k^2 - \alpha_a\frac{C - J^0}{1 - J^0}\right]. \tag{A8}$$

The first-order current into the upper electrode is $J^* = -\partial_x c^* = -kC$, meaning that

$$-kC = R_u^* = (1+\alpha_\mathrm{a}+\alpha_\mathrm{c})(C-J^0)K_0 e^{\alpha_\mathrm{c} Z(\phi^0+V_u)} + J^0\bar{\gamma}k^2 - \alpha_\mathrm{a} J_0 \frac{C-J^0}{1-J^0}, \tag{A9}$$

and solving for C, we obtain

$$C = J^0 \frac{(1+\alpha_\mathrm{a}+\alpha_\mathrm{c})K_0 e^{\alpha_\mathrm{c} Z(\phi^0+V_u)} - \bar{\gamma}k^2 - \alpha_\mathrm{a}\frac{J^0}{1-J^0}}{(1+\alpha_\mathrm{a}+\alpha_\mathrm{c})K_0 e^{\alpha_\mathrm{c} Z(\phi^0+V_u)} + k - \alpha_\mathrm{a}\frac{J^0}{1-J^0}}. \tag{A10}$$

The growth rate can be expressed as

$$\Gamma = -a^3 c_0 J^* = a^3 c_0 k C, \tag{A11}$$

so we have

$$\Gamma = a^3 c_0 k J^0 \frac{\xi - \bar{\gamma}k^2}{\xi + k}, \tag{A12}$$

with the parameter ξ given as

$$\xi = (1+\alpha_\mathrm{a}+\alpha_\mathrm{c})K_0 e^{\alpha_\mathrm{c} Z(\phi^0+V_u)} - \alpha_\mathrm{a}\frac{J^0}{1-J^0}. \tag{A13}$$

To test whether the time derivatives in the first-order problem really are negligible, we compare the time derivative term $2\Gamma c^*$ with the transverse diffusion term $k^2 c^*$. Since Eq. (A12) implies $\Gamma \leq a^3 c_0 k J^0$, our assumption is justified if

$$2a^3 c_0 J^0 \ll k. \tag{A14}$$

Consequently, because $a^3 c_0 \ll 1$ for dilute systems and J^0 is of order unity, it is justified to neglect the time derivative, unless the perturbation wavelength is much larger than the electrode spacing.

The critical wavenumber k_c is found by setting the nominator in Eq. (A12) equal to zero,

$$k_\mathrm{c} = \sqrt{\frac{\xi}{\bar{\gamma}}}. \tag{A15}$$

To find the wavenumber k_max, at which Γ attains its maximum Γ_max, we set the derivative of Γ equal to zero and solve for k,

$$k_\mathrm{max} = \frac{\xi}{2}\left[\left(\frac{2-\xi\bar{\gamma}+2\sqrt{1-\xi\bar{\gamma}}}{\xi\bar{\gamma}}\right)^{1/3} + \left(\frac{2-\xi\bar{\gamma}+2\sqrt{1-\xi\bar{\gamma}}}{\xi\bar{\gamma}}\right)^{-1/3} - 1\right], \tag{A16}$$

with the asymptotic solutions,

$$k_\mathrm{max} \approx \begin{cases} \left(\frac{\xi}{3\bar{\gamma}}\right)^{1/2}, & \text{for } \bar{\gamma}\xi \gg 1, \\ \left(\frac{\xi^2}{2\bar{\gamma}}\right)^{1/3} - \frac{\xi}{2}, & \text{for } \bar{\gamma}\xi \ll 1. \end{cases} \tag{A17}$$

Appendix B: The strongly non-linear limit

In the limit where the driving force is very large, some of the terms in Eqs. (26a) and (26b) become dominant, which makes an analytical solution of the problem possible.

If the system is strongly driven, the field gradients are large close to the upper electrode, and this makes the electrode surface much more unstable. It follows that a larger k value is needed for the surface tension to stabilize the system, so the most unstable value of k will be larger than for less driven systems. In the strongly driven limit, we might therefore expect that Eq. (26b) largely is a balance between $\partial_x^2\phi^*$ and $k^2\phi^*$ in the region of interest. This leads us to making the ansatz

$$\phi^* = \Phi e^{k(x-2)}, \tag{B1}$$

where Φ is a constant. We now consider Eq. (26a) for the cation concentration, neglecting the left hand side

$$0 = -\partial_x\Big\{ -\partial_x c_+^* - Z c_+^* \partial_x\phi^0 - Z c_+^0 \partial_x\phi^* \Big\} - k^2(c_+^* + Z c_+^0 \phi^*). \tag{B2}$$

We assume that the terms $\partial_x c_+^*$ and $Z c_+^* \partial_x\phi^0$ are negligible compared to $Z c_+^0 \partial_x\phi^*$ and insert the ansatz Eq. (B1)

$$0 \approx Z\partial_x c_+^0 k\phi^* + Z c_+^0 k^2\phi^* - k^2(c_+^* + Z c_+^0\phi^*) \tag{B3}$$

$$\approx Z\partial_x c_+^0 k\phi^* - k^2 c_+^*, \tag{B4}$$

implying that

$$c_+^* \approx \frac{Z}{k}\partial_x c_+^0 \phi^*. \tag{B5}$$

To test the assumptions leading to this result, we need expressions for c_+^0, $\partial_x c_+^0$ and $\partial_x\phi^0$. From Ref. [16] we have such expressions, and in the extended space-charge region (ESC) they take the simple forms

$$c_+^0(x) \approx \sqrt{2}\frac{\bar{\lambda}_\mathrm{D}}{Z}\sqrt{J^0}\left[x - 1 - \frac{1}{J^0}\right]^{-1/2}, \tag{B6}$$

$$\partial_x c_+^0(x) \approx -\frac{\sqrt{2}}{2}\frac{\bar{\lambda}_\mathrm{D}}{Z}\sqrt{J^0}\left[x - 1 - \frac{1}{J^0}\right]^{-3/2}, \tag{B7}$$

$$\partial_x\phi^0(x) \approx -\frac{\sqrt{2}}{\bar{\lambda}_\mathrm{D}}\sqrt{J^0}\left[x - 1 - \frac{1}{J^0}\right]^{1/2}. \tag{B8}$$

The width of the ESC is given as $L_\mathrm{ESC} = 1 - 1/J^0$, so in the region close to the electrode, compared to the width of the ESC, the fields can be written as

$$c_+^0(x) \approx \sqrt{2}\frac{\bar{\lambda}_\mathrm{D}}{Z}\sqrt{J^0}L_\mathrm{ESC}^{-1/2}, \tag{B9}$$

$$\partial_x c_+^0(x) \approx -\frac{c_+^0}{2L_\mathrm{ESC}}, \tag{B10}$$

$$\partial_x\phi^0(x) \approx -\frac{Z c_+^0}{\bar{\lambda}_\mathrm{D}^2}L_\mathrm{ESC}. \tag{B11}$$

Evaluating $\partial_x c_+^*$ we find

$$\partial_x c_+^* \approx \frac{Z}{k}\frac{3c_+^0}{4L_{\mathrm{ESC}}^2}\phi^* - Z\frac{c_+^0}{2L_{\mathrm{ESC}}}\phi^*, \tag{B12}$$

which is seen to be much smaller than $Zc_+^0\partial_x\phi^*$ if

$$2k \gg \frac{1}{L_{\mathrm{ESC}}}, \tag{B13}$$

that is, if the perturbation wavelength satisfies

$$\bar{\lambda} \ll 4\pi L_{\mathrm{ESC}}. \tag{B14}$$

Similarly, we find that $Zc_+^*\partial_x\phi^0$ is much smaller than $Zc_+^0\partial_x\phi^*$ if

$$\bar{\lambda}^2 \ll \frac{8\pi^2}{Z^2}\frac{\bar{\lambda}_{\mathrm{D}}^2}{c_+^0(2)}. \tag{B15}$$

Finally, the ansatz Eq. (B1) is justified if $2\bar{\lambda}_{\mathrm{D}}^2 k^2\phi^* \gg Zc_+^*$, which is equivalent to

$$\bar{\lambda}^3 \ll \frac{32\pi^3}{Z^2}\frac{\bar{\lambda}_{\mathrm{D}}^2}{c_+^0(2)}L_{\mathrm{ESC}}. \tag{B16}$$

This last requirement is seen to follow if the two first requirements Eqs. (B14) and (B15) are fulfilled.

In the strongly driven regime, where Eqs. (B14) and (B15) are satisfied, the first-order current is approximately

$$2J_+^* \approx -Zc_+^0\partial_x\phi^* = -Zkc_+^0\Phi, \tag{B17}$$

at the upper electrode. The zeroth-order diffusive contribution is also very small at the upper electrode, meaning that we can simplify Eq. (A7)

$$\begin{aligned} R_u^* &\approx K_0 e^{\alpha_{\mathrm{c}}Z(\phi^0+V_u)}c_+^0(\alpha_{\mathrm{a}}+\alpha_{\mathrm{c}})Z\big(\phi^*+\partial_x\phi^0\big) \\ &\quad + R_u^0\Big[\bar{\gamma}k^2 - \alpha_{\mathrm{a}}Z\big(\phi^*+\partial_x\phi^0\big)\Big] \qquad \text{(B18)} \\ &\approx K_0 e^{\alpha_{\mathrm{c}}Z(\phi^0+V_u)}(\alpha_{\mathrm{a}}+\alpha_{\mathrm{c}})\big(c_+^0 Z\Phi - 2J^0\big) \\ &\quad + R_u^0\left[\bar{\gamma}k^2 - \alpha_{\mathrm{a}}\left(Z\Phi - \frac{2J^0}{c_+^0}\right)\right]. \qquad \text{(B19)} \end{aligned}$$

Inserting $R_u^* = J_+^* \approx -\frac{1}{2}Zkc_+^0\Phi$ we find

$$\frac{Z}{2}kc_+^0\Phi = kJ^0\frac{2(\alpha_{\mathrm{a}}+\alpha_{\mathrm{c}})K_0 e^{\alpha_{\mathrm{c}}Z(\phi^0+V_u)} - \bar{\gamma}k^2 - \alpha_{\mathrm{a}}\frac{2J^0}{c_+^0}}{2(\alpha_{\mathrm{a}}+\alpha_{\mathrm{c}})K_0 e^{\alpha_{\mathrm{c}}Z(\phi^0+V_u)} + k - \alpha_{\mathrm{a}}\frac{2J^0}{c_+^0}}, \tag{B20}$$

and since $\Gamma = -a^3c_0J_+^*$,

$$\Gamma = a^3c_0kJ^0\frac{\xi - \bar{\gamma}k^2}{\xi + k}, \tag{B21}$$

with

$$\xi = 2(\alpha_{\mathrm{a}}+\alpha_{\mathrm{c}})K_0 e^{\alpha_{\mathrm{c}}Z(\phi^0+V_u)} - \alpha_{\mathrm{a}}\frac{2J^0}{c_+^0}. \tag{B22}$$

Like in the electroneutral limit, neglecting the time derivative in the first-order problem is justified, unless the perturbation wavelength is much larger than the electrode spacing. The expressions (A15) and (A16) are also valid for the strongly nonlinear limit, if we use the nonlinear expression for ξ.

[1] G. Libbrecht, Rep Prog Phys **68**, 855 (2005).
[2] R. Trivedi and W. Kurz, Int Mater Rev **39**, 49 (1994).
[3] R. M. Brady and R. C. Ball, Nature **309**, 225 (1984).
[4] N. Nikolic, K. Popov, L. Pavlovic, and M. Pavlovic, Surf Coat Technol **201**, 560 (2006).
[5] G. Kahanda and M. Tomkiewicz, J electrochem soc **136**, 1497 (1989).
[6] C. Leger, J. Elezgaray, and F. Argoul, Phys Rev E **61**, 5452 (2000).
[7] G. Gonzalez, M. Rosso, and E. Chassaing, Phys Rev E **78**, 011601 (2008).
[8] J.-H. Han, E. Khoo, P. Bai, and M. Bazant, Sci. Rep. **4**, 7056 (2014).
[9] P. Trigueros, J. Claret, F. Mas, and F. Sagues, J Electroanal Chem **312**, 219 (1991).
[10] O. Devos, C. Gabrielli, L. Beitone, C. Mace, E. Ostermann, and H. Perrot, J. Electroanal. Chem **606**, 75 (2007).
[11] K. Nishikawa, E. Chassaing, and M. Rosso, J Electrochem Soc **160**, D183 (2013).
[12] J.-N. Chazalviel, Phys. Rev. A **42**, 7355 (1990).
[13] M. Rosso, Electrochim. Acta **53**, 250 (2007).
[14] W. H. Smyrl and J. Newman, Trans Faraday Soc **63**, 207 (1967).
[15] M. Rosso, J.-N. Chazalviel, and E. Chassaing, J Electroanal Chem **587**, 323 (2006).
[16] C. P. Nielsen and H. Bruus, Phys Rev E **89**, 042405 (2014).
[17] I. Rubinstein and B. Zaltzman, Phys Rev E **62**, 2238 (2000).
[18] S. M. Rubinstein, G. Manukyan, A. Staicu, I. Rubinstein, B. Zaltzman, R. G. H. Lammertink, F. Mugele, and M. Wessling, Phys Rev Lett **101**, 236101 (2008).
[19] C. L. Druzgalski, M. B. Andersen, and A. Mani, Phys Fluids **25**, 110804 (2013).
[20] L. Sundstrom and F. Bark, Electrochim Acta **40**, 599 (1995).
[21] M. Z. Bazant, Acc. Chem. Res. **46**, 1144 (2013).
[22] M. van Soestbergen, Russ J Electrochem **48**, 570 (2012).
[23] C. P. Nielsen and H. Bruus, Phys Rev E **90**, 043020 (2014).
[24] D. R. Lide, *CRC Handbook of Chemistry and Physics*, 91st ed., edited by W. M. Haynes, (Internet Version 2011) (CRC Press/Taylor and Francis, Boca Raton, FL, 2010).

[25] D. R. Turner and G. R. Johnson, J Electrochem Soc **109**, 798 (1962).
[26] M. M. Gregersen, M. B. Andersen, G. Soni, C. Meinhart, and H. Bruus, Phys Rev E **79**, 066316 (2009).
[27] H. Udin, A. J. Shaler, and J. Wulff, Trans. AIME **185**, 186 (1949).
[28] V. K. Kumikov and K. B. Khokonov, J. Appl. Phys. **54**, 1346 (1983).
[29] H. L. Skriver and R. N. M, Phys rev B **46**, 7157 (1992).
[30] D. J. Trevoy and H. Johnson, J. Phys. Chem. **62**, 833 (1958).
[31] L. H. Olesen, M. Z. Bazant, and H. Bruus, Phys Rev E **82**, 011501 (2010).
[32] P. M. Biesheuvel, R. Zhao, S. Porada, and A. van der Wal, J Colloid Interface Sci **360**, 239 (2011).
[33] T. R. Ferguson and M. Z. Bazant, J Electrochem Soc **159**, A1967 (2012).
[34] M. A. Quiroga, K.-H. Xue, T.-K. Nguyen, M. Tulodziecki, H. Huang, and A. A. Franco, J Electrochem Soc **161**, E3302 (2014).

Appendix H

Paper submitted to Phys Rev E

Title: A sharp-interface model of electrodeposition and ramified growth

Authors: Christoffer P. Nielsen and Henrik Bruus.

Reference: Submitted to Physical Review E

A sharp-interface model of electrodeposition and ramified growth

Christoffer P. Nielsen and Henrik Bruus
Department of Physics, Technical University of Denmark,
*DTU Physics Building 309, DK-2800 Kongens Lyngby, Denmark**
(Dated: 27 August 2015)
Resubmitted to Phys. Rev. E

We present a sharp-interface model of two-dimensional ramified growth during quasi-steady electrodeposition. Our model differs from previous modeling methods in that it includes the important effects of extended space-charge regions and nonlinear electrode reactions. The electrokinetics is described by a continuum model, but the discrete nature of the ions is taken into account by adding a random noise term to the electrode current. The model is validated by comparing its behavior in the initial stage with the predictions of a linear stability analysis. The main limitations of the model are the restriction to two dimensions and the assumption of quasi-steady transport.

I. INTRODUCTION

Electrodeposition is a technologically important process with diverse applications and implications, e.g. for battery technology, electroplating, and production of metal powders and microstructures [1–11]. For well over a century it has, however, been known that the layer deposited during electrodeposition is prone to morphological instabilities, leading to ramified growth of the electrode surface. Over the years, a large number of experimental, theoretical, and numerical studies have been devoted to increasing the understanding of this ramified growth regime [12–20]. Big contributions to our understanding of the growth process have come from diffusion-limited aggregation (DLA) models [21, 22] and, more recently, phase-field models similar to those which have successfully been applied to solidification problems [23–29]. However, while both of these approaches capture parts of the essential behavior of ramified growth, they have some fundamental shortcomings when applied to the electrodeposition problem.

The first of these shortcomings has to do with the ion transport in the system. Typically, the electrolyte contains a cation of the electrode metal which can both deposit on the electrodes and be emitted from the electrodes. The anion, on the other hand, is blocked by the electrodes. The electrodes thus act as ion-selective elements, and for this reason the system exhibits concentration polarization when a voltage is applied. In 1967, Smyrl and Newman showed [30] that in systems exhibiting concentration polarization, the linear ambipolar diffusion equation breaks down when the applied voltage exceeds a few thermal voltages. At higher voltages a non-equilibrium extended space-charge region develops next to the cathode, causing the transport properties of the system to change dramatically. It seems apparent that this change in transport properties must also lead to a change in electrode growth behavior. Indeed, this point was argued by Chazalviel already in his 1990 paper [12]. Now, the issue with DLA and phase-field models is that neither of these methods account for non-zero space-charge densities. It is therefore only reasonable to apply these methods in the linear regime, where the applied voltage is smaller than a few thermal voltages.

The other shortcoming of DLA and phase-field methods is their treatment of the electrode-electrolyte interface. It is well known in electrochemistry that electrodeposition occurs with a certain reaction rate, which is dependent on the electrode overpotential and typically modeled using a Butler–Volmer type expression [31, 32]. Thus, since the established reaction models are only defined for sharp interfaces, they cannot be properly implemented in DLA methods or in phase-field methods.

There have been attempts to include finite space-charge densities in phase-field models, but the resulting models are only practical for 1D systems because they require an extremely dense meshing of the computational domain [23, 24, 33]. Attempts at including electrode reactions suffer from similar problems, as the proposed models are sensitive to the width of the interface region and to the interpolation function used in the interface region [26, 34]. See Appendix A for a short discussion of this point.

To circumvent the shortcomings of the established models we pursue a different solution strategy in this paper. Rather than defining the interface via a smoothly varying time-dependent parameter as in the phase-field models, we employ a sharp-interface model, in which the interface is moved for each discrete time step. Using a sharp-interface model has the distinct advantage that electrode reactions are easily implemented as boundary conditions. Likewise, it is fairly straightforward to account for non-zero space charge densities in a sharp-interface model, see for instance our previous work Refs. [35, 36].

Like most previous models, our sharp-interface model of electrodeposition models the electrode growth in two dimensions. There have been some experiments in which ramified growth is confined to a single plane and is effectually two dimensional [17, 37–39]. However, for most systems ramified growth occurs in all three dimensions. There will obviously be some discrepancy between our 2D results and the 3D reality, but we are hopeful that our 2D model does in fact capture much of the essential

* chnie@fysik.dtu.dk and bruus@fysik.dtu.dk

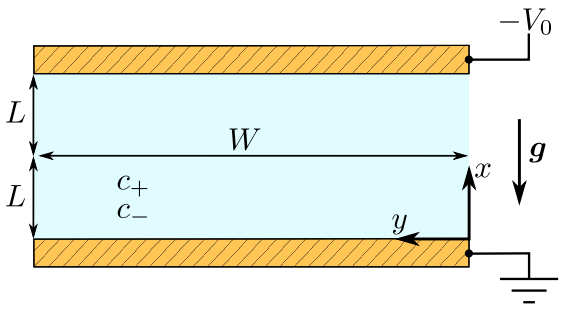

FIG. 1. (Color online) Sketch of the initial geometry of the system. Two co-planar metal electrodes of width W are placed a distance of $2L$ apart. The gap between them is filled by an electrolyte with cation concentration c_+ and anion concentration c_-. A voltage difference of V_0 is applied between the electrodes.

behavior.

At this stage, our sharp-interface model is only applicable once the initial transients in the concentration distribution have died out. In its current form the model is therefore mainly suitable for small systems, in which the diffusive time scale is reasonably small. We aim at removing this limitation in future work.

II. MODEL SYSTEM

The model system consists of two initially flat parallel metal electrodes of width W placed a distance of $2L$ apart. The system is very thin in the third dimension, so that the transport and growth can be modeled as quasi two-dimensional. In the space between the electrodes is a binary symmetric electrolyte of concentration c_0, in which the cation is identical to the electrode material. The electrodes can thus act as both sources and sinks for the cation, whereas the anion can neither enter nor leave the system. A voltage difference V_0 (in units of the thermal voltage $V_\mathrm{T} = k_\mathrm{B}T/e$) is applied between the two electrodes, driving cations towards the top electrode and anions toward the bottom electrode. A sketch of the system is shown in Fig. 1.

By depositing onto the top electrode we ensure that the ion concentration increases from top to bottom, so we do not have to take the possibility of gravitational convection into account. Since the system is very thin, a similar convection suppression can be obtained by simply placing the 2D sample horizontally. To limit the complexity of the treatment, we also disregard any electroosmotic motion, which may arise in the system. We note, however, that the sharp-interface model would be well suited to investigate the effects of electroosmosis, since the space charge density is an integral part of the model.

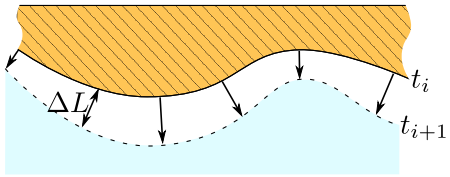

FIG. 2. (Color online) Sketch of the electrode growth. The electrode surface at time t_i is indicated with a full line. In the time step $t_{i+1} - t_i$ an amount of material ΔL, which may vary with position, is deposited on the electrode. On basis of the deposited material the geometry at time t_{i+1} is created (indicated with a dashed line).

III. SOLUTION METHOD

The basic idea in our solution method is to solve the transport-reaction problem for each time step, and then use the calculated currents to find the amount of material deposited at each point on the electrode. Based on this deposition rate the geometry is updated, and the transport-reaction problem is solved for a new time step, as illustrated in Fig. 2.

The major difficulty in employing this method is that when the geometry is updated the computational domain is also remeshed, so there is no straightforward way of continuing from the old solution of the transport-reaction problem. One way of getting around this issue is to separate the time scales in the problem. More to the point, we assume that the growth of the electrode happens so slowly, compared to the transport time scales, that the transport problem always is in quasi steady-state. By treating the transport-reaction problem as being in steady state in each time step, a solution can be computed without reference to solutions at previous time steps. Note, that although the transport is modeled as quasi steady, the model is not Laplacian, since we account for deviations from electroneutrality occurring at overlimiting current.

Obviously, the quasi steady-state assumption is flawed in the initial time after a voltage is applied to the system, as the application of a voltage gives rise to some transients in the transport problem. However, after the initial transients have died out the assumption is quite reasonable, except for the case of very concentrated electrolytes. To see that, we consider the thickness ΔL of the electrode growth in a time interval Δt,

$$\Delta L = a^3 \Delta t J_+, \tag{1}$$

where a^3 is the volume of a metal atom in the solid phase and J_+ is the current density of metal ions entering the electrode. The current density is on the order of the limiting current $2c_0D_+/L$, so the time scale associated with an electrode growth of ΔL is

$$\Delta t = \frac{\Delta L}{a^3 J_+} \sim \frac{L\Delta L}{2D_+c_0a^3}. \tag{2}$$

On the other hand, the transport time scale $t_{\mathrm{diff}}^{\Delta L}$ associated with the distance ΔL is

$$t_{\mathrm{diff}}^{\Delta L} \sim \frac{\Delta L^2}{2D_+}. \tag{3}$$

The ratio of the transport time scale to the growth time scale is thus

$$\frac{t_{\mathrm{diff}}^{\Delta L}}{\Delta t} \sim \frac{\Delta L}{L} c_0 a^3, \tag{4}$$

which is indeed very much smaller than unity.

As mentioned above, our model does not apply to the initial time after the voltage is applied. To estimate how this impacts our results, we make a comparison of the important time scales. The time it takes for the transients to die out is given by the diffusion time,

$$t_{\mathrm{diff}}^{L} = \frac{L^2}{2D_+}. \tag{5}$$

The growth rate of the most unstable harmonic perturbation to the electrode surface we denote $\Gamma_{\max}$ (see Ref. [40]), and from this we obtain an instability time scale,

$$t_{\mathrm{inst}} \sim \frac{1}{\Gamma_{\max}}. \tag{6}$$

It is apparent that if

$$t_{\mathrm{diff}}^{L} \lesssim t_{\mathrm{inst}}, \tag{7}$$

then nothing interesting happens to the electrode surface in the time it takes the transients to disappear. In this case our quasi-steady approach is therefore justified.

Even if $t_{\mathrm{diff}}^{L} \gg t_{\mathrm{inst}}$ our approach may be justified. If the total deposition time is much larger than t_{diff}^{L}, then what happens in the time before the transients die out is largely unimportant for the growth patterns observed in the end. Thus, though the quasi-steady assumption seems restrictive, it actually allows us to treat a fairly broad range of systems.

IV. GOVERNING EQUATIONS

A. Bulk equations

The ion-current densities in the system are given as

$$\boldsymbol{J}_{\pm} = -D_{\pm} c_0 c_{\pm} \boldsymbol{\nabla} \mu_{\pm}, \tag{8a}$$
$$\mu_{\pm} = \ln(c_{\pm}) + z_{\pm}\phi, \tag{8b}$$

where $D_{\pm}$ are the diffusivities of either ion, c_0 is the initial ion concentration, $c_{\pm}$ are the concentrations of either ion normalized by c_0, $\mu_{\pm}$ are the electrochemical potentials normalized by the thermal energy $k_{\mathrm{B}}T$, and ϕ is the electrostatic potential normalized by the thermal voltage $V_{\mathrm{T}} = k_{\mathrm{B}}T/e$. In steady state the Nernst–Planck equations take the form

$$0 = -\boldsymbol{\nabla} \cdot \boldsymbol{J}_{\pm}. \tag{9}$$

The electrostatic part of the problem is governed by the Poisson equation,

$$2\lambda_{\mathrm{D}}^2 \nabla^2 \phi = -\rho = -z_+ c_+ - z_- c_-, \tag{10}$$

where the Debye length λ_{D} is given as

$$\lambda_{\mathrm{D}} = \sqrt{\frac{k_{\mathrm{B}} T \epsilon_{\mathrm{w}}}{2e^2 c_0}}. \tag{11}$$

At the electrodes the anion flux vanishes,

$$\boldsymbol{n} \cdot \boldsymbol{J}_- = 0, \tag{12}$$

and the cation flux is given by a reaction expression

$$\boldsymbol{n} \cdot \boldsymbol{J}_+ = -R. \tag{13}$$

Rather than explicitly modeling the quasi-equilibrium Debye layers at the electrodes, we follow Ref. [36] and implement a condition of vanishing cation gradient at the cathode,

$$\boldsymbol{n} \cdot \boldsymbol{\nabla} c_+ = 0. \tag{14}$$

The last degree of freedom is removed by requiring global conservation of anions,

$$\int_{\Omega} \left(c_- - 1\right) \mathrm{d}V = 0. \tag{15}$$

B. Reaction expression

We model the reaction rate using the standard Butler–Volmer expression [14],

$$R = k_0 \left[c_+ e^{-\bar{\gamma}\kappa + \alpha Z(\phi+V)} - e^{-\bar{\gamma}\kappa - (1-\alpha) Z(\phi+V)} \right], \tag{16}$$

where k_0 is the rate constant of the reaction, V is the non-dimensionalized electrode potential, κ is the surface curvature, α is the charge-transfer coefficient, and $\bar{\gamma}$ is given in terms of the surface energy γ,

$$\bar{\gamma} = \frac{a^3 \gamma}{k_{\mathrm{B}} T}. \tag{17}$$

Here, a^3 is the volume occupied by one atom in the solid phase. $\bar{\gamma}\kappa$ is thus a measure of the energy per atom relative to the thermal energy.

In Appendix A we discuss how the sharp-interface reaction model Eq. (16) relates to typical phase-field reaction models.

V. NUMERICAL STABILITY

Due to the surface energy term in the reaction expression, the surface is prone to numerical instability. In an attempt to reach the energetically favorable surface shape, the solver will sequentially overshoot and undershoot the correct solution. The fundamental issue we are facing is that the problem at hand is numerically stiff. As long as we are using an explicit time-integration method we are therefore likely to encounter numerical instabilities.

A. Updating the interface position

The straightforward way of updating the position $\boldsymbol{r}$ of the interface is to use the explicit Euler method,

$$\boldsymbol{r}(t+\Delta t) = \boldsymbol{r}(t) + \boldsymbol{n}a^3\Delta t R(t), \tag{18}$$

where $R(t)$ is the (position dependent) reaction rate at time t. To avoid numerical instabilities, we should instead use the implicit Euler method,

$$\boldsymbol{r}(t+\Delta t) = \boldsymbol{r}(t) + \boldsymbol{n}a^3\Delta t R(t+\Delta t), \tag{19}$$

where the reaction rate is evaluated at the endpoint instead of at the initial point. This is however easier said than done. $R(t+\Delta t)$ depends on $\boldsymbol{r}(t+\Delta t)$ as well as on the concentration and potential distribution at $t+\Delta t$. Even worse, through the curvature $R(t+\Delta t)$ also depends on the spatial derivatives of $\boldsymbol{r}(t+\Delta t)$.

The way forward is to exploit that only part of the physics give rise to numerical instabilities. It is therefore sufficient to evaluate the problematic surface energy at $t+\Delta t$ and evaluate the remaining terms at t. For our purposes we can therefore make the approximation

$$R(t+\Delta t) \approx R\big(t, \kappa(t+\Delta t)\big), \tag{20}$$

where κ is the curvature. This does still make for a quite complicated nonlinear PDE, but we are getting closer to something tractable. The difference in curvature between t and $t+\Delta t$ is small (otherwise we are taking too big time steps), so we can approximate

$$R\big(t, \kappa(t+\Delta t)\big) \approx R\big(t, \kappa(t)\big) + R'\big(t, \kappa(t)\big)\Delta\kappa, \tag{21}$$

where R' denotes R differentiated with respect to κ and $\Delta\kappa = \kappa(t+\Delta t) - \kappa(t)$. The curvature can be written as

$$\kappa = \frac{\partial\theta}{\partial s}, \tag{22}$$

where θ is the tangential angle of the interface and s is the arc length along the interface. We therefore have

$$\Delta\kappa = \kappa(t+\Delta t) - \kappa(t) = \frac{\partial\theta_2}{\partial s_2} - \frac{\partial\theta_1}{\partial s_1}, \tag{23}$$

where we have adopted the shorthand notation 1 and 2 for time t and $t+\Delta t$, respectively. The arc lengths s_1 and s_2 will obviously differ for any nonzero displacement, but this is a small effect compared to the angle difference. As an approximation we therefore use $s_2 \approx s_1$ and obtain

$$\Delta\kappa \approx \frac{\partial(\theta_2 - \theta_1)}{\partial s_1}. \tag{24}$$

The tangential angle is a function of the surface parametrization,

$$\tan(\theta_1) = \frac{\partial y_1}{\partial x_1}. \tag{25}$$

For small displacements we can approximate

$$\begin{aligned}\tan(\theta_2) &= \frac{\partial y_2}{\partial x_2} = \frac{\partial(y_1+\Delta y)}{\partial(x_1+\Delta x)} \\ &\approx \tan(\theta_1) + \frac{\partial\Delta y}{\partial x_1} - \tan(\theta_1)\frac{\partial\Delta x}{\partial x_1}.\end{aligned} \tag{26}$$

The difference in tangential angles can then be written

$$\begin{aligned}\theta_2 - \theta_1 &= \arctan\left[\tan(\theta_1) + \frac{\partial\Delta y}{\partial x_1} - \tan(\theta_1)\frac{\partial\Delta x}{\partial x_1}\right] - \theta_1 \\ &\approx \frac{1}{1+\tan^2(\theta_1)}\left[\frac{\partial\Delta y}{\partial x_1} - \tan(\theta_1)\frac{\partial\Delta x}{\partial x_1}\right].\end{aligned} \tag{27}$$

Returning to the implicit Euler method Eq. (19), we project it onto the normal vector to obtain

$$\begin{aligned}\Delta L &= a^3\Delta t R(t+\Delta t) \\ &\approx a^3\Delta t\left[R\big(t,\kappa(t)\big) + R'\big(t,\kappa(t)\big)\Delta\kappa\right],\end{aligned} \tag{28}$$

where $\Delta L = \boldsymbol{n}\cdot\big[\boldsymbol{r}(t+\Delta t) - \boldsymbol{r}(t)\big]$. The increments in the x and y directions are related to ΔL via

$$\Delta x = n_x\Delta L, \quad \Delta y = n_y\Delta L. \tag{29}$$

Inserting these in Eq. (27) and writing out the curvature difference $\Delta\kappa$, we obtain a linear PDE for the displacement ΔL

$$\begin{aligned}&\frac{\Delta L - a^3\Delta t R\big(t,\kappa(t)\big)}{a^3\Delta t R'\big(t,\kappa(t)\big)} \\ &\qquad = \Delta\kappa = \frac{\partial}{\partial s_1}\left\{\frac{n_y - n_x\tan(\theta_1)}{1+\tan^2(\theta_1)}\frac{\partial\Delta L}{\partial x_1}\right\}.\end{aligned} \tag{30}$$

In the limit $\Delta\kappa = 0$ this equation reduces to the original forward Euler method (18).

B. Correction for the curvature

In the previous derivation, we did not take into account that the local curvature slightly changes the relation between amount of deposited material and surface displacement ΔL. The deposited area in an angle segment $d\theta$ can

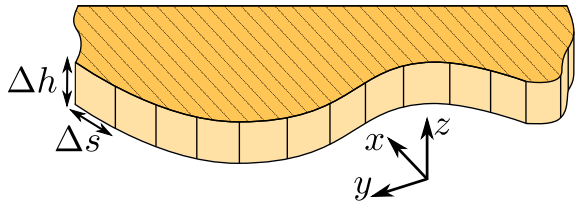

FIG. 3. (Color online) Three-dimensional extension of our two-dimensional model. The electrode interface can vary in the xy-plane according to the calculated ion-currents, but it has a fixed depth Δh in the z-direction. The interface is also divided into a number of bins of width Δs in the xy-plane. Each bin thus has the area $\Delta h \Delta s$.

be calculated as

$$\begin{aligned} dA &= \frac{d\theta}{2\pi}\left[\pi\left(\frac{1}{\kappa}+\Delta L\right)^2 - \pi\frac{1}{\kappa^2}\right] \\ &= \frac{d\theta}{2}\left[\Delta L^2 + 2\frac{\Delta L}{\kappa}\right]. \end{aligned} \tag{31}$$

The line segment ds is related to the angle segment as $ds = d\theta/\kappa$. This means that

$$\begin{aligned} a^3\Delta t R(t+\Delta t) = \frac{dA}{ds} &= \frac{\kappa}{2}\left[\Delta L^2 + 2\frac{\Delta L}{\kappa}\right] \\ &= \Delta L + \frac{\kappa}{2}\Delta L^2. \end{aligned} \tag{32}$$

Using this expression in Eq. (28) yields the slightly nonlinear PDE, with the term $\frac{1}{2}\kappa\Delta L^2$,

$$\begin{aligned} &\frac{\Delta L + \frac{\kappa}{2}\Delta L^2 - a^3\Delta t R\big(t,\kappa(t)\big)}{a^3\Delta t R'\big(t,\kappa(t)\big)} \\ &\qquad = \frac{\partial}{\partial s_1}\left\{\frac{n_y - n_x\tan(\theta_1)}{1+\tan^2(\theta_1)}\frac{\partial \Delta L}{\partial x_1}\right\}, \end{aligned} \tag{33}$$

in place of Eq. (30).

VI. NOISE

An important part of the problem is the noise in the system, since the noise is what triggers the morphological instability and leads to formation of dendrites. Exactly how the noise should be defined is however a matter of some uncertainty. Most previous work uses a thermal white noise term with a small, but seemingly arbitrary amplitude. In this work we use a slightly different approach, in which we assume that the noise is entirely attributed to shot noise.

As it turns out, this approach requires us to be more specific about how our 2D model is related to the three-dimensional reality. In Fig. 3 a sketch of the three-dimensional electrode is shown. The electrode interface is free to vary in the xy-plane, but has a fixed depth Δh in the z-direction. Obviously, most real electrodeposits will have a more complicated behavior in the z-direction, but for electrodeposits grown in a planar confined geometry this is actually a reasonable description.

Solving the transport-reaction problem yields the current density at each point along the electrode surface, that is the average number of ions arriving per surface area per time. The mean number Q of ions arriving in an electrode section of size $\Delta h \Delta s$ in a time interval Δt is thus

$$Q = J_+ \Delta h \Delta s \Delta t. \tag{34}$$

Since the ions are discrete entities, the actual number of arriving ions will, however, fluctuate randomly around the mean Q with some spread σ. We assume that within the time interval Δt, the arrival of each ion is statistically uncorrelated with the arrival of each other ion. It can then be shown that, as long as $Q \gtrsim 10$, the number of arriving ions follow a normal distribution with mean Q and standard deviation

$$\sigma = \sqrt{Q}. \tag{35}$$

This corresponds to an extra random current density

$$J_{\text{rand}} = \frac{\sqrt{Q}}{\Delta h \Delta s \Delta t} q_{\text{rand}} = \sqrt{\frac{J_+}{\Delta h \Delta s \Delta t}}\, q_{\text{rand}}, \tag{36}$$

where q_{rand} is a random number taken from a normal distribution with mean 0 and standard deviation 1. This in turn corresponds to a random electrode growth of

$$\Delta L_{\text{rand}} = a^3\sqrt{\frac{J_+\Delta t}{\Delta h \Delta s}}\, q_{\text{rand}}. \tag{37}$$

Now, there is something slightly weird about this expression for the random growth: it seems that the random growth becomes larger the smaller the bin size Δs is. However, as the bin size becomes smaller the weight of that bin in the overall behavior is also reduced. The net effect is that the bin size Δs does not matter for the random growth, see Appendix B for a more thorough treatment.

The bin depth Δh, on the other hand, does matter for the random growth. Since our model is not concerned with what happens in the z-direction, we simply have to choose a physically reasonable value of Δh, and accept that our choice will have some impact on the simulations. This is a price we pay for applying a 2D model to a 3D phenomenon.

VII. NUMERICAL SOLUTION

To solve the electrodeposition problem we use the commercially available finite element software COMSOL Multiphysics ver. 4.3a together with MATLAB ver. 2013b. Following our previous work [35, 36, 41], the governing equations and boundary conditions Eqs. (8a),

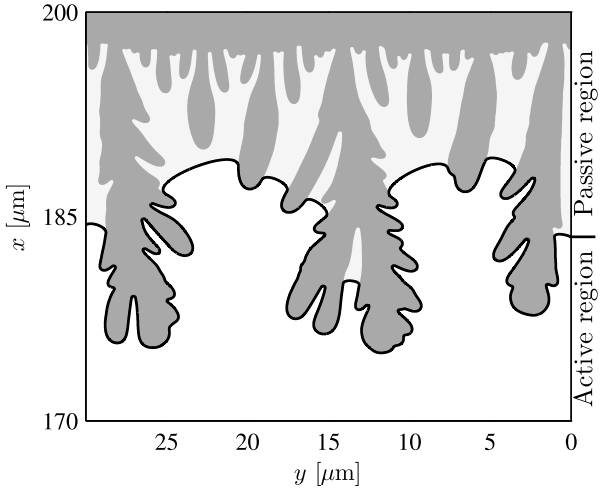

FIG. 4. Example of the simplifying cutting procedure. The reduced interface (thick black line) divides the domain into an active region (white) and a passive region (light gray). The dark gray area shows the real cathode. The example is taken from a simulation with $c_0 = 1$ mM and $V_0 = 10$ after deposition for 31 hours and 28 minutes.

(8b), (9), (10), (12), (13), (14), (15), (16), and (33) are rewritten in weak form and implemented in the mathematics module of COMSOL. For each time step the following steps are carried out: First, a list of points defining the current electrode surface is loaded into COMSOL, and the surface is created using a cubic spline interpolation between the given points. The computational domain is meshed using a mesh size of Δs at the electrode surface, a mesh size of l in a small region next to the electrode, and a much coarser mesh in the remainder of the domain. Next, the curvature of the surface is calculated at each point. The solution from the previous time step is then interpolated onto the new grid, to provide a good initial guess for the transport-reaction problem. Then the transport-reaction problem is solved. Based on the solution to the transport-reaction problem the electrode growth ΔL is calculated by solving Eq. (33) on the electrode boundary. At each mesh point a small random contribution $\Delta L_{\text{rand}} = a^3 \Delta t J_{\text{rand}}$ is then added to ΔL. Finally, the new x and y positions are calculated by adding $n_x(\Delta L + \Delta L_{\text{rand}})$ and $n_y(\Delta L + \Delta L_{\text{rand}})$ to the old x and y positions.

The new x and y positions are exported to MATLAB. In MATLAB any inconsistencies arising from the electrode growth are resolved. If, for instance, the electrode surface intersects on itself, the points closest to each other at the intersection position are merged and any intermediate points are discarded. This corresponds to creating a hollow region in the electrode which is no longer in contact with the remaining electrolyte. The points are then interpolated so that they are evenly spaced, and exported to COMSOL so that the entire procedure can be repeated for a new time step.

The simulations are run on a standard work station with two 2.67 GHz Intel Xeon processors and 48 GB RAM. The electrodeposits shown in Section VIII typically take 2 days to run.

TABLE I. Fixed parameter values used in the simulations.

Parameter	Symbol	Value
Cation diffusivity [42]	D_+	$0.714 \times 10^{-9}\text{m}^2/\text{s}$
Anion diffusivity [42]	D_-	$1.065 \times 10^{-9}\text{m}^2/\text{s}$
Ion valence	Z	2
Surface energy	γ	$1.85\ \text{J/m}^2$
Temperature	T	300 K
Permittivity of water	ϵ_{w}	$6.90 \times 10^{-10}\text{F/m}$
Charge-transfer coefficient	α	0.5
Reaction constant[a]	k_0	$9.4 \times 10^{19}\text{m}^{-2}\text{s}^{-1}$
Diameter of a copper atom[b]	a	0.228 nm

[a] Calculated using the exchange current $I_0 = 30\ \text{A/m}^2$ from Ref. [43] and $k_0 = I_0/(Ze)$.
[b] The cubic root of the volume per atom in solid copper [42].

A. Reduction of the computational domain

At the cathode the mesh is much finer than in the remainder of the domain. The number of mesh points, and hence the computation time, therefore roughly scales with the length of the electrolyte-cathode interface. This has the unfortunate consequence that the computation time for each time step increases drastically, when branching structures emerge at the cathode. To lower the computation time we exploit the fact that the vast majority of the current enters near the tips of the dendritic structures. The parts of the cathode which are not near the tips can therefore be left fixed in time and thus removed from the simulation, without changing the results appreciably. This part of the domain is denoted the passive region. In regions where the current density is less than 0.001 times the maximum value, we thus substitute the real, ramified electrode with a smooth line connecting the parts of the electrode with larger currents. The procedure is carried out in such a way that the real electrode surface can always be recovered from the reduced surface. For a few select examples we have verified that the results are virtually unchanged by this simplifying procedure. One of these examples is shown in Appendix C. In Fig. 4 is shown an example electrode surface together with the reduced surface. It is seen that the length of the electrolyte-cathode interface is heavily reduced by excluding parts of the electrode from the computation.

B. Parameter values

To limit the parameter space we choose fixed, physically reasonable values for the parameters listed in Table I. The values are chosen to correspond to copper

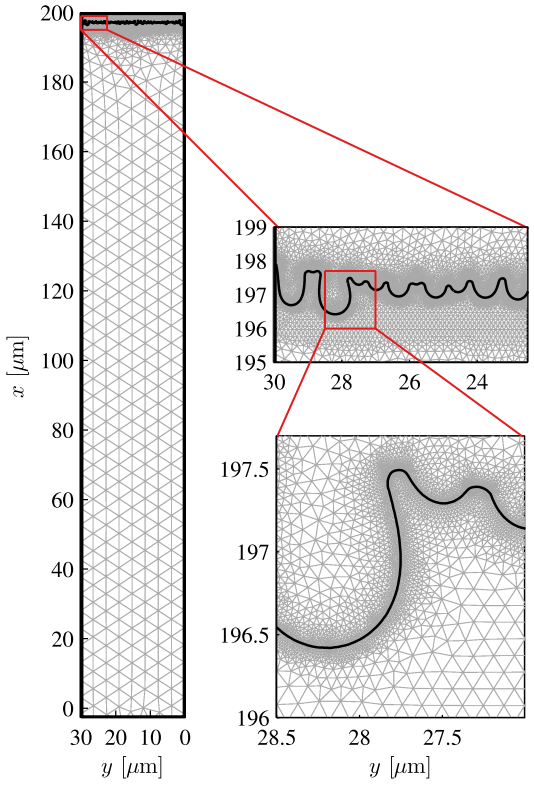

FIG. 5. (Color online) Example of domain meshing at varying magnification. The example is taken from a simulation with $c_0 = 1$ mM and $V_0 = 10$ after deposition for 7 hours and 50 minutes. The wiggly black line is the cathode surface. The light gray lines are the mesh boundaries and the dark (red) lines show the sections that are magnified. The mesh elements above the cathode surface are only used for storing the solution between time steps.

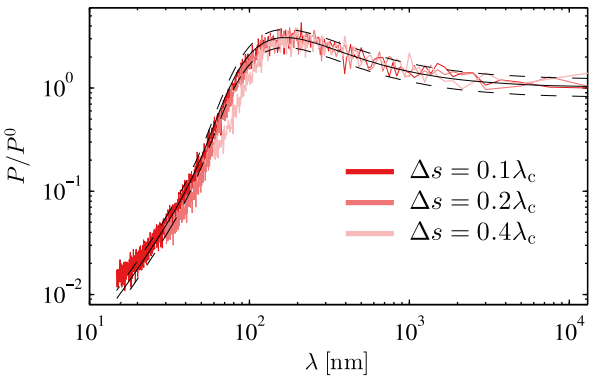

FIG. 6. (Color online) Power spectra averaged over 50 runs for three different mesh sizes, $\Delta s = \{0.1\lambda_c, 0.2\lambda_c, 0.4\lambda_c\}$. In each run we used $M = 100$ time steps of $\Delta t = 0.64$ s and the parameter values $c_0 = 10$ mM, $L = 100$ µm, and $V_0 = 30$. The full black line shows the analytical result and the dashed black lines show the analytical standard error on the mean. The result for $\Delta s = 0.1\lambda_c$ is shown in dark (red), the result for $\Delta s = 0.2\lambda_c$ is shown in medium (red), and the result for $\Delta s = 0.4\lambda_c$ is shown in bright (red).

electrodes in a copper sulfate solution, see Ref. [40] for details.

In Ref. [40] we calculate the critical wavelength λ_c, i.e. the smallest unstable perturbation wavelength, for a range of parameters. See Appendix D for a brief outline of the results of the stability analysis. We expect the critical wavelength to be the smallest feature in the problem, so we choose the mesh size accordingly. We set the mesh size at the electrode to $\Delta s = 0.1\lambda_c$, since our investigations, see Section VII C, show that this is a suitable resolution. We also require that the mesh size does not exceed 0.1 times the local radius of curvature. In the bulk part of the system we use a relatively coarse triangular mesh with mesh size $W/6$. Close to the cathode, in a region $l = 0.5$ µm from the electrode surface, we use a triangular mesh with mesh size $l/4$. See Fig. 5 for a meshing example.

We choose a fixed value for the bin depth $\Delta h = 0.2\lambda_c$. In accordance with the analysis in Appendix B, the time step Δt is chosen so that it is always smaller than $0.5/\Gamma_{\max}$. In addition, the time step is chosen so that at each point on the cathode, the growth during the time step is smaller than the local radius of curvature.

We fix the length L to 100 µm. According to the timescale analysis in Section III and the instability growth rates found in Ref. [40], the quasi-steady state approximation is valid for $L = 100$ µm. The width W of the system is set to $W = 200\lambda_c$, rounded to the nearest micrometer. This makes for a system that is broad enough to exhibit interesting growth patterns, while having a reasonable computation time. The growth is somewhat affected by the symmetry boundaries at $y = 0$ and $y = W$, especially at later times.

These choices leave us with two free parameters, which are the bias voltage V_0 and the electrolyte concentration c_0. We solve the system for $c_0 = \{1 \text{ mM}, 10 \text{ mM}, 100 \text{ mM}\}$ and $V_0 = \{10, 20, 30\}$.

C. Validation

The random nature of the phenomena we are investigating poses obvious challenges when it comes to validating the numerical simulations. The individual steps in the computation can be, and have been, thoroughly tested and validated, but testing whether the aggregate behavior after many time steps is correct is a much taller order. At some level, we simply have to trust that, if the individual steps are working correctly, then the aggregate behavior is also correct. To support this view, there is one test we can make of the aggregate behavior in the very earliest part of the simulation.

In the early stages of the simulation the electrode surface is deformed so little, that the linear stability analysis from [40] should still be valid. We thus have an analytical expression for the wavelength-dependent growth rate Γ, which we can compare with the growth rates found in the numerical simulations. In Appendix B we calcu-

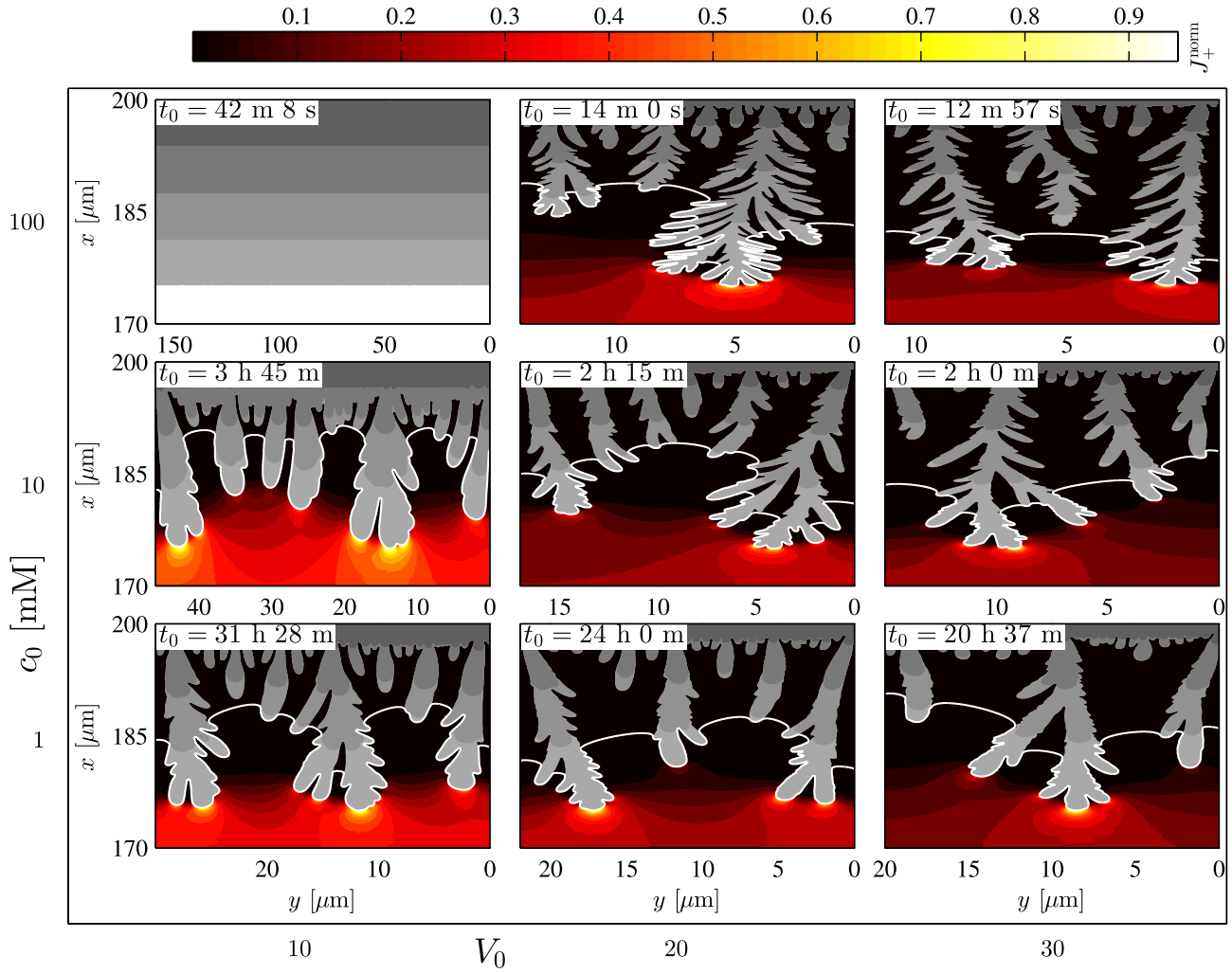

FIG. 7. (Color online) Electrodeposits in the V_0-c_0 plane obtained for $L = 100$ µm, $c_0 = \{1\text{ mM}, 10\text{ mM}, 100\text{ mM}\}$ and $V_0 = \{10, 20, 30\}$. The aspect ratio varies between the panels, since the width W of the simulated region is always set to $200\lambda_c$. The gray area has different shades corresponding to times t_0 (light), $0.75t_0$ (darker), $0.5t_0$ (darker yet), $0.25t_0$ (darkest). The white line indicates the reduced surface at time t_0. The contours in the liquid represent the relative magnitude of the cation current.

late an expression for the average power spectrum of the cathode interface after deposition for a time $t_{\rm tot}$, given the type of noise described in Section VI,

$$\langle P_n \rangle = a^6 \frac{J_+}{2\Delta h W \Gamma_n} \left[e^{2\Gamma_n t_{\rm tot}} - 1 \right], \tag{38}$$

where Γ_n is the growth rate of the n'th wavelength $\lambda_n = W/n$ component in the noise spectrum. We also find the standard deviation $\mathrm{SD}(P_n)$ of the power spectrum

$$\mathrm{SD}(P_n) \approx \sqrt{2}\langle P_n \rangle. \tag{39}$$

Because the standard deviation of P_n is so large compared to the mean value, it is necessary to average over many runs before a meaningful comparison with Eq. (38) can be made. Averaging the power spectrum over 50 simulations brings the standard error on the mean down to 20 percent times the mean value, at which point a reasonable comparison can be made. In Fig. 6 the power spectrum averaged over 50 runs is shown for three different mesh sizes, $\Delta s = \{0.1\lambda_c, 0.2\lambda_c, 0.4\lambda_c\}$. In each run we used $M = 100$ time steps of $\Delta t = 0.64$ s and the parameter values $c_0 = 10$ mM, $L = 100$ µm, and $V_0 = 30$. The chosen step size corresponds to $0.01/\Gamma_{\rm max}$. The analytical result (38) is also shown together with the standard error on the mean. The power spectra are normalized with the power P^0 obtained for $\Gamma = 0$,

$$P^0 = a^6 \frac{J_+ t_{\rm tot}}{\Delta h W}. \tag{40}$$

It is seen that for $\Delta s = 0.4\lambda_c$ some of the power in the small wavelength components is filtered out. As the mesh size is decreased to $\Delta s = 0.2\lambda_c$ and $\Delta s = 0.1\lambda_c$ the low wavelength components are represented increasingly well.

In the above treatment, the time step was chosen very small compared to the instability time scale, $\Delta t = 0.01/\Gamma_{\max}$. This was done to approach the limit of continuous time, and thus enable the best possible comparison with the analytical theory. Such a short time step is, however, impractical for the much longer simulations in the remainder of the paper. In those simulations we use time steps as large as $\Delta t = 0.5/\Gamma_{\max}$. Due to the coarser time resolution employed in the remaining simulations, we expect their power spectrum to deviate somewhat from the almost ideal behavior seen in Fig. 6.

VIII. RESULTS

We let the simulations run until the cathode has grown 25 µm. The time t_0 it takes to reach this point varies greatly with the parameters, mainly because the limiting current scales with c_0. In Fig. 7 the cathode surfaces are shown along with heat plots showing the relative magnitude of the current density at the last time step. The white line shows the position of the reduced interface at the last time step, and the gray area shows the actual position and shape of the cathode. The gray electrodeposits have different shades corresponding to $0.25t_0$, $0.5t_0$, $0.75t_0$, and t_0. The heat plot shows the value of J_+^{norm}, which is the magnitude of the cation current density normalized with its maximum value. In each panel J_+^{norm} thus varies from 0 to 1.

To investigate the reproducibility of the results we have repeated the simulation of the $c_0 = 1$ mM, $V_0 = 10$ system two times. All three electrodeposits are seen in Fig. 8. The electrodeposits are clearly different from one another, as expected for a random process, but they are also seen to share some general features. These shared features are most easily appreciated by comparing the electrodeposits in Fig. 8 to the electrodeposits in Fig. 7. It is seen that the electrodeposits in Fig. 8 are much more similar to each other, than to any of the remaining electrodeposits in Fig. 7. Thus, the results are reproducible in the sense, that the random electrodeposits have some general features that are determined by the parameter values.

When interpreting the plots in Fig. 7, we should be mindful that the aspect ratio is not the same in each panel. The reason for this is that the vertical axis has the same length, 30 µm, in each panel, while the length of the horizontal axis, W, varies between panels. In Fig. 9 we show adapted versions of the panels from Fig. 7. The subfigures in Fig. 9 are created by repeatedly mirroring the subfigures from Fig. 7 until their horizontal length is 100 µm. Obviously, the resulting extended cathodes are somewhat artificial, since we have imposed some symmetries, which would not be present in a simulation of a system with $W = 100$ µm. Nevertheless, we find the subfigures in Fig. 9 useful, since they give a rough impression of the appearance of wider systems and allow for easier comparison of length scales between panels.

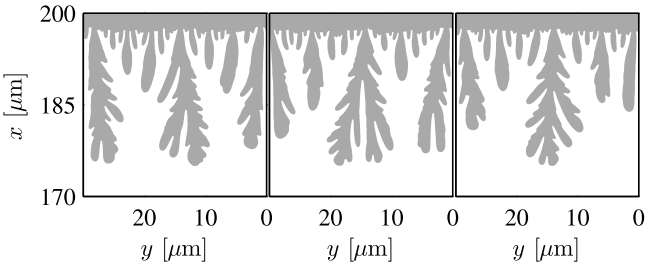

FIG. 8. Three simulations of electrodeposits using the same parameter values $L = 100$ µm, $c_0 = 1$ mM, and $V_0 = 10$. The electrodeposits are clearly different from one another, but they do share some general features.

A. Rationalizing the cathode morphologies

The cathode morphologies observed in Fig. 7 and Fig. 9 are a function of several factors, some of which we attempt to outline below. First, we consider the time t_0 it takes before part of the cathode reaches $x = 175$ µm. As seen from Eq. (1), this time is mainly a function of the limiting current. This explains the approximately inverse scaling with c_0. The current density also increases with V_0, which is why the time t_0 decreases slightly as V_0 increases. Finally, the time t_0 scales with the filling factor. This is the reason why t_0 is much larger in the upper left panel of Fig. 7, than in either of the two other top row panels.

It is apparent from the lack of ramified growth, that the cathode in the upper left panel in Fig. 7 is considerably more stable than the other systems in the leftmost column. To explain this variation in stability, we refer to Fig. 6 in Ref. [40]. There it is shown that the instability length scale is on the order of 50 µm for $c_0 = 100$ mM at $V_0 = 10$, while it is considerably lower for $c_0 = 10$ mM and $c_0 = 1$ mM. Fig. 6 in Ref. [40] also shows that for $V_0 > 18$ the instability length scale decreases in size as the concentration increases. The same tendency is observed in Fig. 9.

From the subfigures in Fig. 9 it appears that there is a connection between the thickness δ_{inst} of the layer deposited before the instabilities develop (the base layer between 200 µm and the onset of the ramification), and the characteristic length scale δ_{char} of the ramified electrodeposits (the fineness of the ramification). For example, the top-right subfigure has a thin base layer and a fine ramification (δ_{inst} and δ_{char} are both small), while the middle-left subfigure has a thick base layer and a coarse ramification (δ_{inst} and δ_{char} are both large). In lack of a full theory for this behavior, a tentative explanation may be found in our recent stability study of the electrode deposition [40]. There we found that the base-layer thickness, defined as the instability length scale L_Γ of an initially flat deposition layer, scales approximately linearly with the most unstable wavelength $\lambda_{\max}$ for a perturbation in deposition thickness along the surface. If these initial instabilities are developed into the final

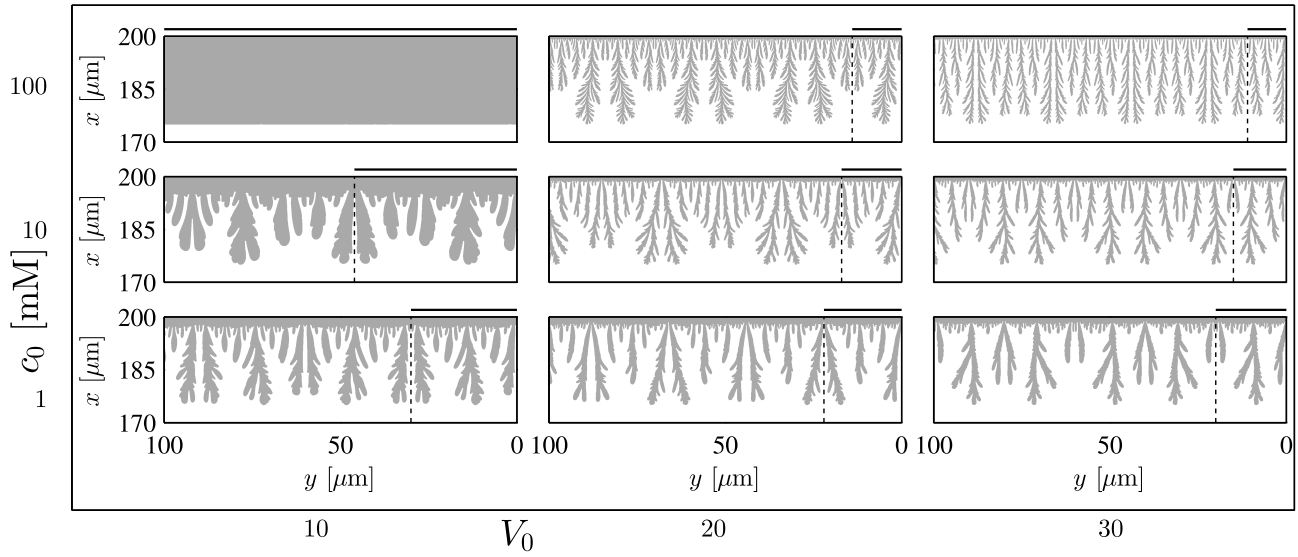

FIG. 9. The electrodeposits in the V_0-c_0 plane extended to an equal width of 100 µm by mirror-repetition of the original part from Fig. 7 (marked by the horizontal black line) between 0 µm and the first mirror-axis (vertical dashed line). Here, in contrast to Fig. 7, the aspect ratio is constant across the panels.

ramified electrodeposit, we are led to the assertion that δ_{inst} and δ_{char} might be linearly correlated. To test this assertion, we first plot the thickness δ_{inst} versus $\lambda_{\max}$

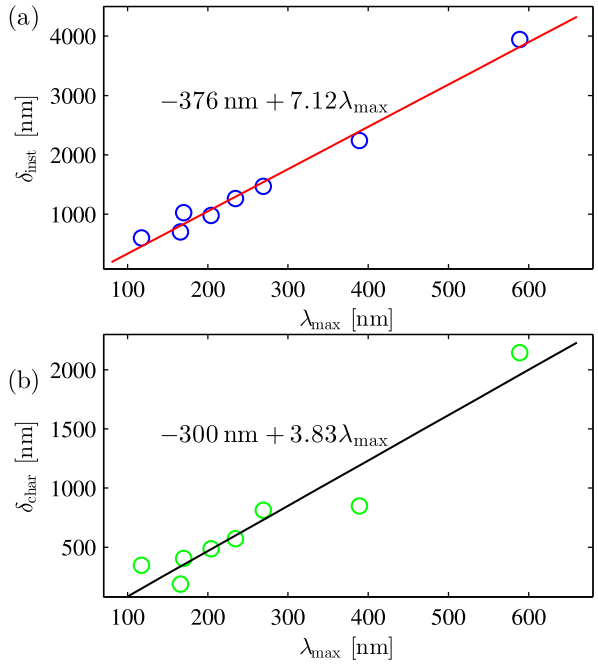

FIG. 10. (Color online) (a): The instability length scale δ_{inst} obtained from the simulations, plotted versus the most unstable wavelength $\lambda_{\max}$. Also, a linear fit highlighting the roughly linear dependence is shown. (b): The characteristic length scale δ_{char} obtained from the simulations, plotted versus the most unstable wavelength $\lambda_{\max}$. Also, a linear fit highlighting the roughly linear dependence is shown.

and observe the outcome. We exclude the system with $c_0 = 100$ mM and $V_0 = 10$, since instabilities have not yet developed in this system. The resulting plot is seen in Fig. 10(a) together with a linear fit. Although there is a good amount of scatter around the linear fit, it is seen to capture the general trend reasonably well.

We then make a similar plot with the characteristic length scale δ_{char} of the ramified electrodeposits on the y-axis. To extract δ_{char}, we follow the approach in Ref. [44] and calculate the so-called Minkowski dimension of each electrodeposit. In doing this we only consider the part of the electrodeposit lying between 170 µm and 190 µm, and as before we exclude the system with $c_0 = 100$ mM and $V_0 = 10$. In this work we are actually not interested in the Minkowski dimension itself, but rather in a partial result that follows from the analysis. In a range of length scales the electrodeposits appear roughly fractal, but below a certain length scale the electrodeposits are locally smooth. The length scale at which this transition occurs, can be extracted from the analysis, and we use this length as the characteristic length scale δ_{char} of the electrodeposit, for details see Appendix E. In Fig. 10(b) we plot δ_{char} versus $\lambda_{\max}$, together with a linear fit of the data. While the plot suggests that δ_{char} and $\lambda_{\max}$ are linearly correlated to some degree, this is a more tenuous correlation than the one between δ_{inst} and $\lambda_{\max}$.

Evidently, $\lambda_{\max}$ plays an important role for the morphology of the electrodeposits. However, δ_{inst} and δ_{char} alone are not sufficient to characterize the electrodeposits. As seen in the top row of Fig. 9, the characteristic length scale δ_{char} varies very little between $V_0 = 20$ and $V_0 = 30$. Yet, the morphology still changes appreciably. The reason for this change in morphology is probably that the gradient in electrochemical potential increases

near the cathode as the bias voltage is increased. The larger the electrochemical gradient is, the more the system will favor deposition at the most protruding parts of the electrodeposits. For large voltages we therefore expect long and narrow electrodeposits, whereas we expect dense branching electrodeposits for low voltages.

IX. DISCUSSION

Our model improves on existing models in three important ways: it can treat systems at overlimiting current including the extended space-charge region, it allows for a proper reaction boundary condition, and it can be tested against results from sharp-interface stability analyses. Our model is, however, not without issues of its own. Perhaps the most apparent of these is the quasi-steady-state assumption. This assumption limits the applicability of the model to short systems, in which the diffusion time is small compared to the deposition time, as discussed in Section III. In principle the phase-field models are superior to our model in this aspect, since they do not have this limitation. However, it is not of practical relevance, as all of the published phase-field simulations are for systems so short that the quasi-steady-state assumption is valid anyway [25–27].

It is well known, that the strong electric fields at the dendrite tips give rise to electroosmotic velocity fields in the system [45–47]. To simplify the treatment and bring out the essential physics of electrodeposition, we have chosen not to include fluid dynamics and advection in our model. However, it is straightforward to include these effects, see for instance our previous work [36].

One of the main advantages the sharp-interface model has over the phase-field models, is that it allows for the implementation of proper reaction boundary conditions. The standard Butler–Volmer model used in this paper is a first step towards realistic reaction boundary conditions. As elaborated by Bazant in Ref. [32], there are other reaction models, such as Marcus kinetics, which might better describe the electrode reactions. Also, the standard Butler–Volmer model has the contentious assumption that the overpotential is the total potential drop over both the electrode-electrolyte interface and the Debye layer. A more realistic approach might be to model the Debye layer explicitly or include the Frumkin correction to the Butler–Volmer model [48]. Furthermore, a proper reaction expression should take the crystal structure of the material into account. There are simple ways of implementing crystal anisotropy in the surface tension term, see for instance Refs. [27, 49], but again, to keep the model simple we have chosen not to include anisotropy at the present stage. Any of the above mentioned reaction models can be easily implemented in the framework of the sharp-interface model, and as such the specific Butler–Volmer model used in this work does not constitute a fundamental limitation.

More broadly, our sharp-interface model includes, or allows for the easy inclusion of, most effects that are important for electrodeposition in 2D. A natural next step is therefore to see how our results compare to experimental electrodeposits. Unfortunately, most such experimental data are viewed at the millimeter or centimeter scale, whereas our simulation results are at the micrometer scale. In one paper, Ref. [4], the electrodeposits are probed at the micrometer scale, but the results do not make for the best comparison, since the morphology of their electrodeposits was a result of adding a surface active molecule. We hope that as more experimental results become available, it will be possible to perform rigorous tests of our model.

X. CONCLUSION

We have developed a sharp-interface model of electrodeposition, which improves on existing models in a number of ways. Unlike earlier models, our model is able to handle sharp-interface boundary conditions, like the Butler–Volmer boundary condition, and it readily deals with regions with non-zero space-charge densities. A further advantage is that our model handles the physical problem in much the same way as done in various linear stability analyses. We can thus obtain a partial validation of our model by comparing its predictions with those of a linear stability analysis. As of now, the main weakness of our model is that it assumes quasi-steady state in the transport equations. For the systems studied in this paper this is a reasonable assumption, since the diffusion time is small compared to the instability time. In future work we want to extend the model to the transient regime, so that larger systems can be treated as well.

The main aim of this paper has been to establish the sharp-interface method, but we have also included a study of the simulated electrodeposits. An interesting observation is, that there seems to be a linear correlation between the characteristic length scale of the electrodeposits and the size of the most unstable wavelength. This exemplifies a promising application of our sharp-interface model, namely as a tool to develop a more quantitative understanding of electrodeposits and their morphology.

ACKNOWLEDGMENTS

We thank Edwin Khoo and Prof. Martin Z. Bazant for valuable discussions of electrode reactions and the growth mechanisms.

Appendix A: Phase-field models of reaction kinetics

An important feature of the presented electrodeposition model is that it allows for a proper nonlinear reaction model at the electrode interface. The reaction

model Eq. (16) is equivalent to the expression [32]

$$R = i_0 \left[e^{-\alpha n \eta_\mathrm{t}} - e^{(1-\alpha) n \eta_\mathrm{t}} \right], \tag{A1}$$

$$i_0 = k_0 c_+^{1-\alpha} e^{-\bar{\gamma}\kappa}, \tag{A2}$$

where i_0 is the exchange current density, n is the number or electrons participating in the reaction, and we introduced the total overpotential η_t (normalized by the thermal voltage V_T).

In phase-field models a phase-field parameter $\xi \in [0; 1]$ is used to distinguish between the solid phase ($\xi = 1$) and the aqueous phase ($\xi = 0$). In the interface region the phase-field parameter ξ varies smoothly between 0 and 1. To determine the dynamics of the system a free energy $F[\xi, c_i, \phi]$ (or grand free energy $\Omega[\xi, \mu_i, \phi]$) is introduced, which, as a function of ξ, interpolates between the free energy of a pure electrolyte and the free energy of a pure electrode. Using a variational approach the ion-currents can be found from the free energies,

$$\boldsymbol{J}_i = -D_i c_i \boldsymbol{\nabla} \frac{\delta F}{\delta c_i}, \tag{A3}$$

and together with the relevant conservation equations this defines the ion-transport problem.

The fundamental assumption in phase-field models of reaction kinetics is, that a similar variational approach can be used to define the overpotential as a local field quantity,

$$\eta[\xi, c_i, \phi] \propto \frac{\delta F}{\delta \xi}, \quad \text{or} \quad \eta[\xi, \mu_i, \phi] \propto \frac{\delta \Omega}{\delta \xi}, \tag{A4}$$

where we have omitted the proportionality constants. The total overpotential η_t is defined as the integral of the local overpotential η over the interface region,

$$\eta_\mathrm{t} = \frac{1}{\delta} \int \eta[\xi, c_i, \phi] \, \mathrm{d}x, \tag{A5}$$

where δ is the width of the interface region and we have assumed the system to be one-dimensional. The phase-field parameter ξ is then assumed to evolve according to the Butler–Volmer like expression

$$\partial_t \xi \propto \left[e^{-\alpha n \eta[\xi, c_i, \phi]} - e^{(1-\alpha) n \eta[\xi, c_i, \phi]} \right], \tag{A6}$$

where, again, we omitted the proportionality constant. The current into the electrode corresponds to the phase-field growth rate $\partial_t \xi$ integrated over the interface region,

$$\begin{aligned} I &\propto \int \partial_t \xi \, \mathrm{d}x \\ &\propto \int \left[e^{-\alpha n \eta[\xi, c_i, \phi]} - e^{(1-\alpha) n \eta[\xi, c_i, \phi]} \right] \mathrm{d}x. \end{aligned} \tag{A7}$$

Superficially, this expression looks fairly similar to the Butler–Volmer model Eq. (A1). However, in general the two expressions are not identical. The reason for this is that the total overpotential occurring in Eq. (A1) is the integral over the local overpotential occurring in Eq. (A7). Thus, Eq. (A1) and Eq. (A7) yield identical results if, and only if, the local overpotential η has a form which makes it indifferent to the order in which integration and exponentiation are performed. Although this condition is satisfied for small or constant overpotentials, there is no way of guaranteeing it in general. Consequently, we expect Eq. (A7) to differ from Eq. (A1) in most cases.

Another issue with the phase-field models of reaction kinetics is, that the connection between the electric potential ϕ and the total overpotential η_t is not apparent. From Ref. [32] we expect that

$$\eta_\mathrm{t} = \Delta\phi - \Delta\phi_\mathrm{eq}, \tag{A8}$$

where $\Delta\phi$ is the potential difference across the electrode interface, and $\Delta\phi_\mathrm{eq}$ is the potential difference in equilibrium. However, there does not seem to be any guarantee that this is true for phase-field reaction kinetics. In general, since most phase-field models of electrodeposition lack a simple sharp-interface limit [34], it is difficult to relate the parameters in a phase-field reaction model to those in the corresponding sharp-interface model.

The above objections to the phase-field reaction models do not necessarily mean that those models are wrong. After all, the Butler–Volmer model or similar nonlinear reaction models are by no means exact, so it is entirely possible that phase-field reaction models approximate the true reaction kinetics equally well. However, in lack of convincing reasons to believe that this is the case, the various sharp-interface reaction models remain the preferable way of modeling electrode reactions.

Appendix B: Initial growth

In the initial part of the simulation the electrode is so flat that the linear stability analysis from Ref. [40] gives a good description of the growth. We parameterize the cathode position as

$$x = X(t) + f(y, t), \tag{B1}$$

where $f(y, t)$ is the y-dependent deviation from the mean electrode position $X(t)$. According to the linear stability analysis each mode grows exponentially in time with the growth factor Γ. After a time t an initial perturbation,

$$f(y, 0) = \sum_{n=1}^{N} a_n e^{i k_n y}, \tag{B2}$$

has therefore evolved to

$$f(y, t) = \sum_{n=1}^{N} a_n e^{\Gamma_n t} e^{i k_n y}. \tag{B3}$$

We note that some of the growth rates Γ_n can be negative. In our simulation we add new perturbations with

small time intervals, which we, for the purpose of this analysis, assume to be evenly spaced. After M time intervals Δt the surface is therefore described by

$$f(y, M\Delta t) = \sum_{m=0}^{M}\sum_{n=1}^{N} a_{nm} e^{\Gamma_n (M-m)\Delta t} e^{ik_n y}. \tag{B4}$$

We are interested in the average power of each mode

$$\langle P_n \rangle = \left\langle \left| \sum_{m=0}^{M} a_{nm} e^{\Gamma_n (M-m)\Delta t} \right|^2 \right\rangle. \tag{B5}$$

The coefficients are random and uncorrelated with zero mean. On average the cross-terms in the sum therefore cancel and we can simplify,

$$\begin{aligned}\langle P_n \rangle &= \left\langle \sum_{m=0}^{M} |a_{nm}|^2 e^{2\Gamma_n (M-m)\Delta t} \right\rangle \\ &= \langle |a_n|^2 \rangle \sum_{m=0}^{M} e^{2\Gamma_n (M-m)\Delta t} \\ &= \langle |a_n|^2 \rangle \frac{e^{2\Gamma_n (M+1)\Delta t} - 1}{e^{2\Gamma_n \Delta t} - 1}.\end{aligned} \tag{B6}$$

The variance of the power is given as

$$\mathrm{Var}(P_n) = \langle P_n^2 \rangle - \langle P_n \rangle^2. \tag{B7}$$

The first of these terms is

$$\begin{aligned}\langle P_n^2 \rangle &= \left\langle \left(\left| \sum_{m=0}^{M} a_{nm} e^{\Gamma_n (M-m)\Delta t} \right|^2 \right)^2 \right\rangle \\ &= e^{4\Gamma_n M \Delta t} \left\langle \left(\left| \sum_{m=0}^{M} a_{nm} q^m \right|^2 \right)^2 \right\rangle,\end{aligned} \tag{B8}$$

where $q = e^{-\Gamma_n \Delta t}$. Writing out the absolute value

$$\langle P_n^2 \rangle = e^{4\Gamma_n M \Delta t} \left\langle \left(\sum_{m'=0}^{M}\sum_{m=0}^{M} a_{nm} a_{nm'}^* q^{m+m'} \right)^2 \right\rangle, \tag{B9}$$

where superscript $*$ denotes complex conjugation. Because the coefficients are uncorrelated with mean 0, only the terms including $|a_{nm}|^2 |a_{nm'}|^2$ survive in the average of the square,

$$\begin{aligned}\langle P_n^2 \rangle &= e^{4\Gamma_n M \Delta t} \left\langle \frac{1}{2} \sum_{m'=0}^{M}\sum_{m=0}^{M} 6 |a_{nm}|^2 |a_{nm'}|^2 q^{2(m+m')} \right\rangle \\ &= 3 e^{4\Gamma_n M \Delta t} \sum_{m'=0}^{M}\sum_{m=0}^{M} \left\langle |a_{nm}|^2 |a_{nm'}|^2 \right\rangle q^{2(m+m')}.\end{aligned} \tag{B10}$$

Here, the factor of six comes from the binomial coefficient and the factor of a half takes into account that the double sum counts each combination twice. Now, there are two possibilities; either $m \neq m'$ or $m = m'$. In the first case $|a_{nm}|^2$ and $|a_{nm'}|^2$ are uncorrelated, meaning that

$$\left\langle |a_{nm}|^2 |a_{nm'}|^2 \right\rangle = \left\langle |a_n|^2 \right\rangle^2. \tag{B11}$$

Whereas if $m = m'$, then

$$\left\langle |a_{nm}|^2 |a_{nm'}|^2 \right\rangle = \left\langle |a_n|^4 \right\rangle. \tag{B12}$$

This means that

$$\begin{aligned}\langle P_n^2 \rangle &= 3 e^{4\Gamma_n M \Delta t} \left\langle |a_n|^2 \right\rangle^2 \sum_{m' \neq m}^{M}\sum_{m=0}^{M} q^{2(m+m')} \\ &\quad + 3 e^{4\Gamma_n M \Delta t} \left\langle |a_n|^4 \right\rangle \sum_{m=0}^{M} q^{4m} \\ &= 3 e^{4\Gamma_n M \Delta t} \left\langle |a_n|^2 \right\rangle^2 \sum_{m'=0}^{M}\sum_{m=0}^{M} q^{2(m+m')} \\ &\quad + 3 e^{4\Gamma_n M \Delta t} \left(\left\langle |a_n|^4 \right\rangle - \left\langle |a_n|^2 \right\rangle^2 \right) \sum_{m=0}^{M} q^{4m} \\ &= 3 \langle P_n \rangle^2 \\ &\quad + 3 e^{4\Gamma_n M \Delta t} \left(\left\langle |a_n|^4 \right\rangle - \left\langle |a_n|^2 \right\rangle^2 \right) \frac{q^{4(M+1)} - 1}{q^4 - 1}.\end{aligned} \tag{B13}$$

The variance of the power is thus given as

$$\mathrm{Var}(P_n) = 2\langle P_n \rangle^2 + \left(\left\langle |a_n|^4 \right\rangle - \left\langle |a_n|^2 \right\rangle^2 \right) \frac{e^{4\Gamma_n (M+1)\Delta t} - 1}{e^{4\Gamma_n \Delta t} - 1}. \tag{B14}$$

If $\Gamma_n \Delta t \ll 1$ we can expand the denominators of $\langle P_n \rangle^2$ and the last term. We find that they scale as $4(\Gamma_n \Delta t)^2$ and $4\Gamma_n \Delta t$, respectively. In the limit $\Gamma_n \Delta t \ll 1$ the first term thus dominates over the second, so to a good approximation we have

$$\mathrm{Var}(P_n) \approx 2\langle P_n \rangle^2, \tag{B15}$$

$$\mathrm{SD}(P_n) \approx \sqrt{2}\langle P_n \rangle. \tag{B16}$$

In the simulations the surface perturbations have the form

$$f(y, 0) = \sum_{n=1}^{N} b_n h(y - n\Delta y), \tag{B17}$$

where,

$$h(y) = \begin{cases} 1, & 0 \leq y \leq \Delta s, \\ 0, & \text{else.} \end{cases} \tag{B18}$$

We take the absolute square of $f(y, 0)$ given as both Eq. (B2) and Eq. (B17), and integrate over the domain

to obtain

$$\int_0^W |f(y,0)|^2 \, \mathrm{d}y = \sum_{n=1}^{N} |b_n|^2 \int_0^W |h(y - n\Delta y)|^2 \, \mathrm{d}y$$
$$= \Delta s \sum_{n=1}^{N} |b_n|^2, \tag{B19}$$
$$\int_0^W |f(y,0)|^2 \, \mathrm{d}y = \sum_{n=1}^{N} |a_n|^2 \int_0^W |e^{ik_n y}|^2 \, \mathrm{d}y$$
$$= W \sum_{n=1}^{N} |a_n|^2. \tag{B20}$$

The mean square of b_n is thus related to the mean square of a_n as

$$\langle |a_n|^2 \rangle = \frac{\Delta s}{W} \langle |b_n|^2 \rangle = \frac{1}{N} \langle |b_n|^2 \rangle. \tag{B21}$$

From Eq. (37) we have that

$$\langle |b_n|^2 \rangle = a^6 \frac{J_+ \Delta t}{\Delta h \Delta s}. \tag{B22}$$

Inserting in Eq. (B6) we find

$$\langle P_n \rangle = \frac{1}{N} a^6 \frac{J_+ \Delta t}{\Delta h \Delta s} \frac{e^{2\Gamma_n (M+1)\Delta t} - 1}{e^{2\Gamma_n \Delta t} - 1} \tag{B23}$$
$$= a^6 \frac{J_+ \Delta t}{\Delta h W} \frac{e^{2\Gamma_n (t_{\mathrm{tot}} + \Delta t)} - 1}{e^{2\Gamma_n \Delta t} - 1}, \tag{B24}$$

which is seen to be independent of the bin size Δs. We also introduced the total time $t_{\mathrm{tot}} = M\Delta t$. In a consistent scheme the power spectrum should of course only depend on the total time, and not on the size Δt of the time steps. For small values of $\Gamma_n \Delta t$ we can expand the denominator and neglect the Δt in the nominator,

$$\langle P_n \rangle \approx a^6 \frac{J_+}{2\Delta h W \Gamma_n} \left[e^{2\Gamma_n t_{\mathrm{tot}}} - 1 \right]. \tag{B25}$$

So, as long as $2\Gamma_n \Delta t \ll 1$ the power spectrum does not depend on the size of the time step.

For larger values of $2\Gamma_n \Delta t$ the power spectrum does depend on the size of the time step. However, as long as $2\Gamma_n \Delta t \lesssim 1$, we do not expect the overall morphology of the electrode to have a significant dependence on the time step.

Appendix C: Test of the domain reduction

In the numerical simulations we exploit the fact, that the electrode growth mainly occurs near the dendrite tips. This allows us to remove part of the domain (the passive region) from the simulations. To verify that we do not significantly affect the growth, by rendering part of the domain passive, we have carried out a simulation without a passive region. The gray domain in Fig. 11 indicates the electrode after deposition for 30 hours and 22 minutes in a system with $c_0 = 10$ mM and $V_0 = 10$. The black line indicates the electrode interface after deposition for 24 hours and 2 minutes. It is seen that a big part of the domain is virtually unchanged between the two times. It would therefore not have changed the results appreciably if we had rendered part of the domain passive.

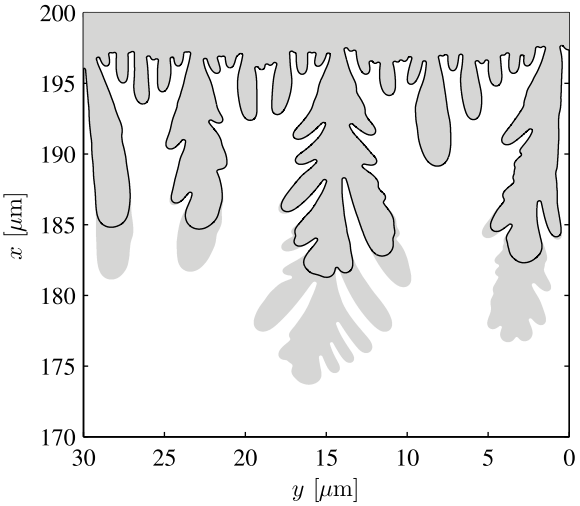

FIG. 11. Electrode interface at two different time steps for $c_0 = 1$ mM and $V_0 = 10$. In this simulation no part of the domain was rendered passive at any time. The gray area indicates the electrode after 30 hours and 22 minutes, and the black lines indicates the electrode interface after 24 hours and 2 minutes. In the upper part of the domain the electrode interface is virtually unchanged between the two times.

Appendix D: Stability analysis

In Ref. [40] we investigated the stability of the electrode interfaces under perturbations of varying wavelengths. We found numerical and analytical result for the instability growth rate, Γ, the critical wavelength λ_{c}, and the most unstable wavelength λ_{max}. In Fig. 12 the instability growth rate Γ is plotted versus perturbation wavelength for $c_0 = 10$ mM, $L = 100$ µm, $V_0 = 30$. The critical wavelength λ_{c} and the most unstable wavelength λ_{max} are indicated in the plot. In Fig. 13 we plot λ_{c} and λ_{max} versus V_0 for $c_0 = \{1 \text{ mM}, 10 \text{ mM}, 100 \text{ mM}\}$ and $L = 100$ µm.

Appendix E: Characteristic length scale

To find the characteristic length scale δ_{char} of the ramified electrodeposits we follow Ref. [44] and use the box-counting method to calculate the Minkowski dimension of the deposit perimeter. As a first step in calculating the Minkowski dimension, we place a square grid with

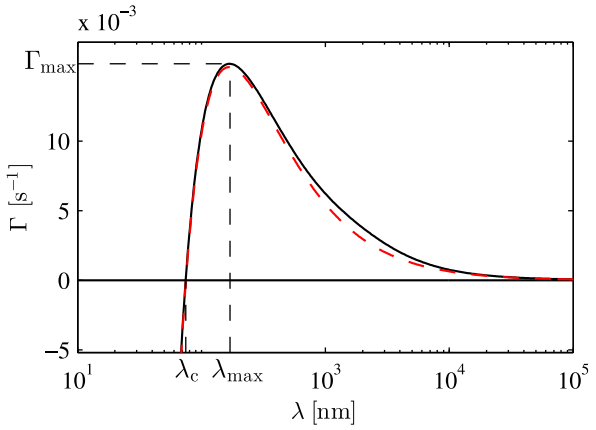

FIG. 12. (Color online) The instability growth rate Γ plotted versus perturbation wavelength λ. The full (black) line is the numerical result and the dashed (red) line is the analytical result. The critical wavelength λ_c and the most unstable wavelength λ_{max} are indicated in the figure. The parameter values used in the model are those in Table I as well as $c_0 = 10$ mM, $L = 100$ µm and $V_0 = 30$.

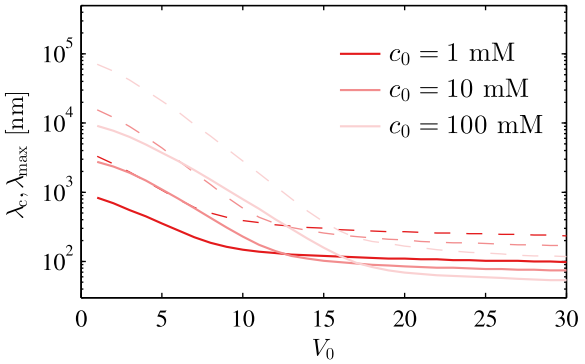

FIG. 13. (Color online) The critical wavelength λ_c (full) and the most unstable wavelength λ_{max} (dashed) plotted versus V_0. In addition to the values listed in Table I the used parameter values are $L = 100$ µm and $c_0 = \{1\text{ mM}, 10\text{ mM}, 100\text{ mM}\}$.

side length ϵ over each deposit, and count the number $N(\epsilon)$ of boxes it takes to completely cover the perimeter of the part of the deposit lying between $x = 170$ µm and $x = 190$ µm. An example is shown in Fig. 14.

For a proper fractal geometry, the Minkowski dimension is defined as

$$\delta_M = -\lim_{\epsilon \to 0} \frac{\ln\left[N(\epsilon)\right]}{\ln(\epsilon)}. \qquad \text{(E1)}$$

The electrodeposits we are investigating are not fractal at all length scales, but in a range of length scales, we can calculate an approximate Minkowski dimension as the negative slope in a $\ln\left[N(\epsilon)\right]$ vs $\ln(\epsilon)$ plot. In Fig. 15 such a plot is seen, together with linear fits in each of the two approximately linear regions. The Minkowski dimension at small ϵ is nearly unity, indicating that the deposit perimeter is locally smooth at this length scale.

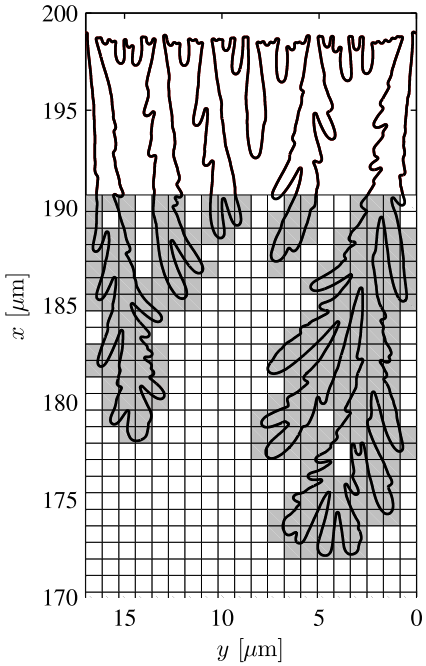

FIG. 14. Illustration of the box-counting method leading to the Minkowski dimension for the electrodeposit obtained for $c_0 = 10$ mM and $V_0 = 20$. The boxes that cover part of the deposit perimeter are shown in gray and the remaining boxes are shown in white. In this example the grid size is $\epsilon = 0.85$ µm and the number of boxes it takes to cover the perimeter is $N(\epsilon) = 234$.

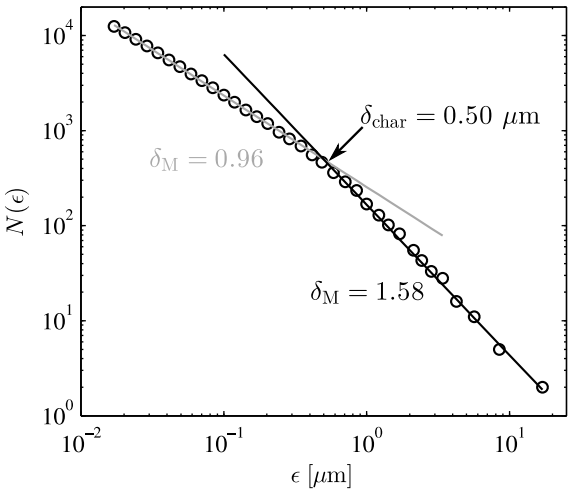

FIG. 15. The number $N(\epsilon)$ of boxes it takes to cover the electrodeposit plotted vs the box side length ϵ. A linear fit is shown in each of the two approximately linear regions, and the Minkowski dimension in each region is indicated. The crossing point between the linear fits is marked by an arrow, and the characteristic dimensions $\delta_{char} = 0.50$ µm is calculated based on this crossing point.

For larger values of ϵ the Minkowski dimension deviates from unity, because the deposit is approximately fractal in this size range. At the transition point between these

two regions is the smallest length scale, which is related to the morphology of the electrodeposit. This length scale we denote the characteristic length δ_{char}. Technically, we define δ_{char} as the point where the linear fits from each region cross each other, as indicated in Fig. 15.

[1] V. Fleury, W. Watters, L. Allam, and T. Devers, Nature **416**, 716 (2002).
[2] M. Rosso, Electrochim. Acta **53**, 250 (2007).
[3] J. W. Gallaway, A. M. Gaikwad, B. Hertzberg, C. K. Erdonmez, Y.-C. K. Chen-Wiegart, L. A. Sviridov, K. Evans-Lutterodt, J. Wang, S. Banerjee, and D. A. Steingart, J. Electrochem. Soc. **161**, A275 (2014).
[4] T.-H. Lin, C.-W. Lin, H.-H. Liu, J.-T. Sheu, and W.-H. Hung, Chem. Commun. **47**, 2044 (2011).
[5] M. Park, X. Zhang, M. Chung, G. B. Less, and A. M. Sastry, J. Power Sources **195**, 7904 (2010).
[6] B. Scrosati and J. Garche, *Journal of Power Sources*, J. Power Sources **195**, 2419 (2010).
[7] J. M. Tarascon and M. Armand, Nature , (2001).
[8] M. Winter and R. J. Brodd, Chem. Rev. **104**, 4245 (2004).
[9] J.-H. Han, E. Khoo, P. Bai, and M. Bazant, Sci. Rep. **4**, 7056 (2014).
[10] H.-C. Shin, J. Dong, and M. Liu, Adv mater **15**, 1610 (2003).
[11] O. Devos, C. Gabrielli, L. Beitone, C. Mace, E. Ostermann, and H. Perrot, J. Electroanal. Chem **606**, 75 (2007).
[12] J.-N. Chazalviel, Phys. Rev. A **42**, 7355 (1990).
[13] M. Z. Bazant, Phys. Rev. E **52**, 1903 (1995).
[14] L. Sundstrom and F. Bark, Electrochim Acta **40**, 599 (1995).
[15] G. Gonzalez, M. Rosso, and E. Chassaing, Phys Rev E **78**, 011601 (2008).
[16] K. Nishikawa, E. Chassaing, and M. Rosso, J Electrochem Soc **160**, D183 (2013).
[17] P. Trigueros, J. Claret, F. Mas, and F. Sagues, J Electroanal Chem **312**, 219 (1991).
[18] G. Kahanda and M. Tomkiewicz, J electrochem soc **136**, 1497 (1989).
[19] N. Nikolic, K. Popov, L. Pavlovic, and M. Pavlovic, Surf Coat Technol **201**, 560 (2006).
[20] C. Lambert, P. Lauque, J.-L. Seguin, G. Albinet, M. Bendahan, J.-M. Debierre, and P. Knauth, ChemPhysChem **3**, 107 (2002).
[21] T. A. Witten and L. M. Sander, Phys Rev B **27**, 5686 (1983).
[22] T. A. Witten and L. M. Sander, Phys Rev Lett **47**, 1400 (1981).
[23] J. E. Guyer, W. J. Boettinger, J. A. Warren, and G. B. McFadden, Phys Rev E **69**, 021603 (2004).
[24] J. E. Guyer, W. J. Boettinger, J. A. Warren, and G. B. McFadden, Phys Rev E **69**, 021604 (2004).
[25] Y. Shibuta, Y. Okajima, and T. Suzuki, Sci technol adv mater **8**, 511 (2007).
[26] L. Liang and L. Chen, Appl Phys Lett **105**, 263903 (2014).
[27] D. A. Cogswell, Phys rev E **92**, 011301 (2015).
[28] D. Ely, A. Jana, and R. E. Garcia, J. Power Sources **272**, 581 (2014).
[29] D. A. Cogswell and M. Z. Bazant, ACS Nano **6**, 2215 (2012).
[30] W. H. Smyrl and J. Newman, Trans Faraday Soc **63**, 207 (1967).
[31] J. Dukovic, IBM J. Res. Develop. **34**, 693 (1990).
[32] M. Z. Bazant, Acc. Chem. Res. **46**, 1144 (2013).
[33] J. Deng, G. J. Wagner, and R. P. Muller, J Electrochem Soc **160**, A487 (2013).
[34] L. Liang, Y. Qi, F. Xue, S. Bhattacharya, S. J. Harris, and L. Q. Chen, Phys Rev E **86**, 051609 (2012).
[35] C. P. Nielsen and H. Bruus, Phys Rev E **89**, 042405 (2014).
[36] C. P. Nielsen and H. Bruus, Phys Rev E **90**, 043020 (2014).
[37] V. Fleury and D. Barkey, Europhys lett **36**, 253 (1996).
[38] C. Leger, L. Servant, J. L. Bruneel, and F. Argoul, Physica A **263**, 305 (1999).
[39] C. Leger, J. Elezgaray, and F. Argoul, Phys Rev E **61**, 5452 (2000).
[40] C. P. Nielsen and H. Bruus, Arxiv **arXiv:1505.07571** (2015).
[41] M. M. Gregersen, M. B. Andersen, G. Soni, C. Meinhart, and H. Bruus, Phys Rev E **79**, 066316 (2009).
[42] D. R. Lide, *CRC Handbook of Chemistry and Physics*, 91st ed., edited by W. M. Haynes, (Internet Version 2011) (CRC Press/Taylor and Francis, Boca Raton, FL, 2010).
[43] D. R. Turner and G. R. Johnson, J Electrochem Soc **109**, 798 (1962).
[44] A. Genau, A. Freedman, and L. Ratke, J. Chryst. Growth **363**, 49 (2013).
[45] V. Fleury, J.-N. Chazalviel, and M. Rosso, Phys Rev Lett **68**, 2492 (1992).
[46] V. Fleury, J. Kaufman, and B. Hibbert, Phys rev E **48**, 3831 (1993).
[47] J. M. Huth, H. L. Swinney, W. D. McCormick, A. Kuhn, and F. Argoul, Phys Rev E **51**, 3444 (1995).
[48] M. van Soestbergen, Russ J Electrochem **48**, 570 (2012).
[49] R. Kobayashi, Physica D **63**, 410 (1993).

Bibliography

[1] S. Alizadeh and A. Mani, *Computational modeling of electrokinetic transport in random networks of micro-pores and nano-pores*, 67th Annual Meeting of the APS Division of Fluid Dynamics, 2014.

[2] M. B. Andersen, H. Bruus, J. P. Bardhan, and S. Pennathur, *Streaming current and wall dissolution over 48 h in silica nanochannels*, J Colloid Interface Sci **360** (2011), 262–271.

[3] M. B. Andersen, J. Frey, S. Pennathur, and H. Bruus, *Surface-dependent chemical equilibrium constants and capacitances in bare and 3-cyanopropyldimethylchlorosilane coated silica nanochannels*, J Colloid Interface Sci **353** (2011), 301–310.

[4] M. B. Andersen, D. M. Rogers, J. Mai, B. Schudel, A. V. Hatch, S. B. Rempe, and A. Mani, *Spatiotemporal ph dynamics in concentration polarization near ion-selective membranes*, LANGMUIR **30** (2014), no. 26, 7902–7912.

[5] M. B. Andersen, M. van Soestbergen, A. Mani, H. Bruus, P. M. Biesheuvel, and M. Z. Bazant, *Current-induced membrane discharge*, Phys Rev Lett **109** (2012), no. 10, 108301.

[6] A. J. Bard, G. Inzelt, and F. Scholz, *Electrochemical dictionary*, 2nd ed., Springer, 2012.

[7] M. Z. Bazant, *Theory of chemical kinetics and charge transfer based on nonequilibrium thermodynamics*, Acc. Chem. Res. **46** (2013), no. 5, 1144–1160.

[8] M. Z Bazant, K. T. Chu, and B. J. Bayly, *Current-Voltage relations for electrochemical thin films*, SIAM J Appl Math **65** (2005), no. 5, 1463–1484.

[9] S. H. Behrens and D. G. Grier, *The charge of glass and silica surfaces*, J Chem Phys **115** (2001), no. 14, 6716–6721.

[10] P. M. Biesheuvel, M. van Soestbergen, and M. Z. Bazant, *Imposed currents in galvanic cells*, Electrochim Acta **54** (2009), no. 21, 4857–4871.

[11] M. Block and J. A. Kitchener, *Polarization phenomena in commercial ion-exchange membranes*, J. Electrochem. Soc. **113** (1966), no. 9, 947–953.

[12] S.C Brenner and L. R. Scott, *The mathematical theory of finite element methods*, Springer, 1994.

[13] H. Bruus, *Theoretical microfluidics*, Oxford master series in physics, no. 18, Oxford University Press, Oxford, 2008.

[14] J.-N. Chazalviel, *Electrochememical aspects of the generation of ramified metallic electrodeposits*, Phys. Rev. A **42** (1990), no. 12, 7355–7367.

[15] I. Cho, G. Y. Sung, and S. J. Kim, *Overlimiting current through ion concentration polarization layer: hydrodynamic convection effects*, Nanoscale **6** (2014), 4620–4626.

[16] K. T. Chu and M. Z. Bazant, *Electrochemical thin films at and above the classical limiting current*, SIAM J Appl Math **65** (2005), no. 5, 1485.

[17] D. A. Cogswell, *Quantitative phase-field modeling of dendritic electrodeposition*, Phys rev E **92** (2015), 011301.

[18] COMSOL AB, *Comsol multiphysics reference guide*, 2012, Version 4.3a.

[19] C.-O. Danielsson, A. Dahlkild, A. Velin, and M. Behm, *A model for the enhanced water dissociation on monopolar membranes*, Electrochim Acta **54** (2009), no. 11, 2983–2991.

[20] S. M. Davidson, M. B. Andersen, and A. Mani, *Chaotic induced-charge electro-osmosis*, Phys Rev Lett **112** (2014), 128302.

[21] D. Deng, W. Aouad, W. A. Braff, S. Schlumpberger, M. E. Suss, and M. Z. Bazant, *Water purification by shock electrodialysis: Deionization, filtration, separation, and disinfection*, Desalination **357** (2015), 77–83.

[22] D. Deng, E. V. Dydek, J.-H. Han, S. Schlumpberger, A. Mani, B. Zaltzman, and M. Z. Bazant, *Overlimiting current and shock electrodialysis in porous media*, Langmuir **29** (2013), 16167–16177.

[23] J. Deng, G. J. Wagner, and R. P. Muller, *Phase field modeling of solid electrolyte interface formation in lithium ion batteries*, J electrochem soc **160** (2013), no. 3, A487–A496.

[24] O. Devos, C. Gabrielli, L. Beitone, C. Mace, E. Ostermann, and H. Perrot, *Growth of electrolytic copper dendrites. i: Current transients and optical observation*, J. Electroanal. Chem **606** (2007), 75–84.

[25] C. L. Druzgalski, M. B. Andersen, and A. Mani, *Direct numerical simulation of electroconvective instability and hydrodynamic chaos near an ion-selective surface*, Phys Fluids **25** (2013), no. 11, 110804.

[26] E. V. Dydek and M. Z. Bazant, *Nonlinear dynamics of ion concentration polarization in porous media: The leaky membrane model*, AIChE J **59** (2013), 3539–3555.

[27] E. V. Dydek, B. Zaltzman, I. Rubinstein, D. S. Deng, A. Mani, and M. Z. Bazant, *Overlimiting current in a microchannel*, Phys Rev Lett **107** (2011), no. 11, 118301.

[28] A. Elattar, A. Elmidaoui, N. Pismenskaia, C. Gavach, and G. Pourcelly, *Comparison of transport properties of monovalent anions through anion-exchange membranes*, J Membr Sci **143** (1998), no. 1-2, 249–261.

[29] J. Elezgaray, C. Leger, and F. Argoul, *Linear stability analysis of unsteady galvanostatic electrodeposition in the two-dimensional diffusion-limited regime*, J electrochem soc **145** (1998), no. 6, 2016–2024.

[30] A. ElMekawy, H. M. Hegab, X. Dominguez-Benetton, and D. Pant, *Internal resistance of microfluidic microbial fuel cell: Challenges and potential opportunities*, Bioresource Technol **142** (2013), no. 0, 672 – 682.

[31] D.R. Ely, A Jana, and R. E. Garcia, *Phase field kinetics of lithium electrodeposits*, J. Power Sources **272** (2014), 581–594.

[32] Vinodkumar Etacheri, Rotem Marom, Ran Elazari, Gregory Salitra, and Doron Aurbach, *Challenges in the development of advanced Li-ion batteries: a review*, Energy Environ Sci **4** (2011), no. 9, 3243–3262 (English).

[33] V. Fleury and D. Barkey, *Runaway growth in two-dimensional electrodeposition*, Europhys lett **36** (1996), no. 4, 253–258.

[34] V. Fleury, J.-N. Chazalviel, and M. Rosso, *Theory and experimental evidence of electroconvection around electrochemical deposits*, Phys Rev Lett **68** (1992), no. 16, 2492–2495.

[35] V. Fleury, J. Kaufman, and B. Hibbert, *Evolution of the space-charge layer during electrochemical deposition with convection*, Phys rev E **48** (1993), no. 5, 3831–3840.

[36] V. Fleury, W. A. Watters, L. Allam, and T. Devers, *Rapid electroplating of insulators*, Nature **416** (2002), 716–719.

[37] J. W. Gallaway, A. M. Gaikwad, B. Hertzberg, C. K. Erdonmez, Y.-C. K. Chen-Wiegart, L. A. Sviridov, K. Evans-Lutterodt, J. Wang, S. Banerjee, and D. A. Steingart, *An in situ synchrotron study of zinc anode planarization by a bismuth additive*, J. Electrochem. Soc. **161** (2014), no. 3, A275–A284.

[38] A. L. Genau, A. C. Freedman, and L. Ratke, *Effect of solidification conditions on fractal dimension of dendrites*, J. Chryst. Growth **363** (2013), 49–54.

[39] G. Gonzalez, M. Rosso, and E. Chassaing, *Transition between two dendritic growth mechnisms in electrodeposition*, Phys Rev E **78** (2008), 011601.

[40] S. K. Griffiths and R. H. Nilson, *Electroosmotic fluid motion and late-time solute transport for large zeta potentials*, Anal Chem **72** (2000), no. 20, 4767–4777 (English).

[41] J. E. Guyer, W. J. Boettinger, J. A. Warren, and G. B. McFadden, *Phase field modeling of electrochemistry. i. equilibrium*, Phys Rev E **69** (2004), 021603.

[42] ———, *Phase field modeling of electrochemistry. ii. kinetics*, Phys Rev E **69** (2004), 021604.

[43] M. Haataja, D. J. Srolovitz, and A. B. Bocarsly, *Morphological stability during electrodeposition - i. steady states and stability analysis*, J electrochem soc **150** (2003), no. 10, C699–C707.

[44] J.-H. Han and M. Z. Bazant, *Shock electrodeposition in charged porous media*, arXiv:1505.05604 [physics.chem-ph] (2015).

[45] J.-H. Han, E. Khoo, P. Bai, and M.Z. Bazant, *Over-limiting current and control of dendritic growth by surface conduction in nanopores*, Sci. Rep. **4** (2014), 7056.

[46] C. Heitner-Wirguin, *Recent advances in perfluorinated ionomer membranes: structure, properties and applications*, J Membr Sci **120** (1996), no. 1, 1–33.

[47] J M Huth, H L Swinney, W D McCormick, A Kuhn, and F Argoul, *Role of convection in thin-layer electrodeposition*, Phys Rev E **51** (1995), no. 4, 3444–3458.

[48] K. G. H. Janssen, H. T. Hoang, J. Floris, J. de Vries, N. R. Tas, J. C. T. Eijkel, and T. Hankemeier, *Solution titration by wall deprotonation during capillary filling of silicon oxide nanochannels*, Anal Chem **80** (2008), no. 21, 8095–8101.

[49] K. L. Jensen, J. T. Kristensen, A. M. Crumrine, M. B. Andersen, H. Bruus, and S. Pennathur, *Hydronium-dominated ion transport in carbon-dioxide-saturated electrolytes at low salt concentrations in nanochannels*, Phys Rev E **83** (2011), no. 5, 056307.

[50] L. Jialin, W. Yazhen, Y. Changying, L. Guangdou, and S. Hong, *Membrane catalytic deprotonation effects*, J Membr Sci **147** (1998), no. 2, 247–256.

[51] G. L. M. K. S. Kahanda and M. Tomkiewicz, *Morphological evolution in zinc electrodeposition*, J electrochem soc **136** (1989), no. 5, 1497–1502.

[52] A. Karma and W.-J. Rappel, *Quantitative phase-field modeling of dendritic growth in two and three dimensions*, Phys rev E **57** (1998), no. 4, 4323–4349.

[53] A. S. Khair, *Concentration polarization and second-kind electrokinetic instability at an ion-selective surface admitting normal flow*, Phys Fluids **23** (2011), 072003.

[54] Y. I. Kharkats, *Theory of the exaltation effect and the effect of correlation exaltation of migration current*, J Electroanal Chem **105** (1979), no. 1, 97–114.

[55] Y. I. Kharkats and A. V. Sokirko, *Theory of the effect of migration current exaltation taking into account dissociation-recombination reactions*, J Electroanal Chem **303** (1991), no. 1, 27–44.

[56] P. Kim, S. J. Kim, J. Han, and K. Y. Suh, *Stabilization of ion concentration polarization using a heterogeneous nanoporous junction*, Nano Lett. **10** (2010), 16–23.

[57] S. J. Kim, S. H. Ko, K. H. Kang, and J. Han, *Direct seawater desalination by ion concentration polarization*, Nat Nanotechnol **5** (2010), no. 4, 297–301.

[58] S. J. Kim, L. D. Li, and J. Han, *Amplified electrokinetic response by concentration polarization near nanofluidic channel*, Langmuir **25** (2009), no. 13, 7759–7765.

[59] S. J. Kim, Y.-C. Wang, J. H. Lee, H. Jang, and J. Han, *Concentration polarization and nonlinear electrokinetic flow near a nanofluidic channel*, Phys Rev Lett **99** (2007), no. 4, 044501.

[60] S.H. Ko, Y.-A. Song, S. J. Kim, M. Kim, J. Han, and K. H. Kang, *Nanofluidic preconcentration device in a straight microchannel using ion concentration polarization*, Lab Chip **12** (2012), no. 21, 4472–4482 (English).

[61] R. Kobayashi, *Modeling and numerical simulations of dendritic crystal growth*, Physica D **63** (1993), 410–423.

[62] V. K. Kumikov and K. B. Khokonov, *On the measurement of surface free energy and surface tension of solid metals*, J. Appl. Phys. **54** (1983), 1346.

[63] R. Kwak, S. J. Kim, and J. Han, *Continuous-flow biomolecule and cell concentrator by ion concentration polarization*, Anal Chem **83** (2011), no. 19, 7348–7355 (English).

[64] L. D. Landau and E. M. Lifshitz, *Statistical physics*, 3rd ed., vol. 1, Elsevier, 1980.

[65] C. Leger, J. Elezgaray, and F. Argoul, *Internal structure of dense electrodeposits*, Phys Rev E **61** (2000), no. 5, 5452–5463.

[66] C. Leger, L. Servant, J. L. Bruneel, and F. Argoul, *Growth patterns in electrodeposition*, Physica A **263** (1999), 305–314.

[67] L. Liang and L. Q. Chen, *Nonlinear phase field model for electrodeposition in electrochemical systems*, Appl Phys Lett **105** (2014), 263903.

[68] L. Liang, Y. Qi, F. Xue, S. Bhattacharya, S. J. Harris, and L. Q. Chen, *Nonlinear phase-field model for electrode-electrolyte interface evolution*, Phys Rev E **86** (2012), 051609.

[69] D. R. Lide, *CRC handbook of chemistry and physics*, 91st ed., (Internet Version 2011), CRC Press/Taylor and Francis, Boca Raton, FL, 2010.

[70] T.-H. Lin, C.-W. Lin, H.-H. Liu, J.-T. Sheu, and W.-H. Hung, *Potential-controlled electrodeposition of gold dendrites in the presence of cysteine*, Chem. Commun. **47** (2011), no. 7, 2044–2046.

[71] D. Linden and T. B. Reddy, *Handbook of batteries*, McGraw-Hill, 2002.

[72] J. S. Mackie and P. Meares, *The sorption of electrolytes by a cation-exchange resin membrane*, Proceedings of the Royal Society of London **232** (1955), 485–498.

[73] P. Malek, J. M. Ortiz, B. S. Richards, and A. I. Schaefer, *Electrodialytic removal of NaCl from water: Impacts of using pulsed electric potential on ion transport and water dissociation phenomena*, J Membr Sci **435** (2013), 99–109 (English).

[74] A. Mani and M. Z. Bazant, *Deionization shocks in microstructures*, Phys Rev E **84** (2011), no. 6, –.

[75] A. Mani, T. A. Zangle, and J. G. Santiago, *On the propagation of concentration polarization from Microchannel-Nanochannel interfaces part i: Analytical model and characteristic analysis*, Langmuir **25** (2009), no. 6, 3898–3908.

[76] R. A. Marcus, *On the theory of electrontransfer reactions. vi. unified treatment for homogeneous and electrode reactions*, J chem phys **43** (1965), no. 2, 679–701.

[77] K. A. Mauritz and R. B. Moore, *State of understanding of nafion*, Chem Rev **104** (2004), 4535–4586.

[78] V. Mavrov, W. Pusch, O. Kominek, and S. Wheelwright, *Concentration polarization and water splitting at electrodialysis membranes*, Desalination **91** (1993), 225–252.

[79] S. Nam, I. Cho, J. Heo, G. Lim, M. Z. Bazant, D. J. Moon, G. Y. Sung, and S. J. Kim, *Experimental verification of overlimiting current by surface conduction and electro-osmotic flow in microchannels*, Phys Rev lett **114** (2015), 114501.

[80] J. Newman, *The polarized diffuse double layer*, Trans Faraday Soc **61** (1965), 2229–2237.

[81] ———, *Current distribution on a rotating disk below the limiting current*, J electrochem soc **113** (1966), no. 12, 1235–1241.

[82] C. P. Nielsen and H Bruus, *Concentration polarization, surface currents, and bulk advection in a microchannel*, Phys Rev E **90** (2014), 043020.

[83] C. P. Nielsen and H. Bruus, *Transport-limited water splitting at ion-selective interfaces during concentration polarization*, Phys Rev E **89** (2014), 042405.

[84] C. P. Nielsen and H Bruus, *Morphological instability during steady electrodeposition at overlimiting currents*, Arxiv **arXiv:1505.07571** (2015).

[85] ———, *A sharp-interface model of electrodeposition and ramified growth*, Arxiv **arXiv:1507.01040** (2015).

[86] N. D. Nikolic, K. I. Popov, L. J. Pavlovic, and M. G. Pavlovic, *Morphologies of copper deposits obtained by the electrodeposition at high overpotentials*, Surf Coat Technol **201** (2006), 560–566.

[87] V. Nikonenko, V. Zabolotsky, C. Larchet, B. Auclair, and G. Pourcelly, *Mathematical description of ion transport in membrane systems*, **147** (2002), no. 1, 369–374.

[88] V. V. Nikonenko, A. V. Kovalenko, M. K. Urtenov, N. D. Pismenskaya, J. Han, P. Sistat, and G. Pourcelly, *Desalination at overlimiting currents: State-of-the-art and perspectives*, Desalination **342** (2014), no. 0, 85 – 106, Special Issue: Electromembrane Processes for Desalination.

[89] V. V. Nikonenko, N. D. Pismenskaya, E. I. Belova, P. Sistat, P. Huguet, G. Pourcelly, and C. Larchet, *Intensive current transfer in membrane systems: Modelling, mechanisms and application in electrodialysis*, Adv Colloid Interface Sci **160** (2010), no. 1-2, 101–123.

[90] V. V. Nikonenko, N. D. Pismenskaya, and E. I. Volodina, *Rate of generation of ions H+ and OH- at the ion-exchange membrane/dilute solution interface as a function of the current density*, Russ J Electrochem **41** (2005), no. 11, 1205–1210.

[91] K. Nishikawa, E. Chassaing, and M. Rosso, *Evolution of the morphology og electrodeposited copper at the early stage of dendritic growth*, J Electrochem Soc **160** (2013), no. 4, D183–D187.

[92] K. Oldham and J. Myland, *Fundamentals of electrochemical science*, Elsevier, 1993.

[93] L. H. Olesen, *Computational fluid dynamics in microfluidic systems*, Master's thesis, Technical University of Denmark, 2003.

[94] L. H. Olesen, M. Z. Bazant, and H. Bruus, *Strongly nonlinear dynamics of electrolytes in large ac voltages*, Phys Rev E **82** (2010), no. 1, 011501.

[95] M. Park, X. Zhang, M. Chung, G. B. Less, and A. M. Sastry, *A review of conduction phenomena in li-ion batteries*, J. Power Sources **195** (2010), no. 24, 7904–7929.

[96] M. Rosso, *Electrodeposition from a binary eleectrolyte: new developments and applications*, Electrochim. Acta **53** (2007), 250–256.

[97] I. Rubinstein, *A diffusional model of 'water splitting' in electrodialysis*, J Phys Chem **81** (1977), no. 14, 1431–1436.

[98] I. Rubinstein and L. Shtilman, *Voltage against current curves of cation exchange membranes*, J Chem Soc, Faraday Trans 2 **75** (1979), 231.

[99] I. Rubinstein and B. Zaltzman, *Electro-osmotically induced convection at a permselective membrane*, Phys Rev E **62** (2000), no. 2, 2238.

[100] I. Rubinstein and B. Zaltzman, *Electro-osmotic slip of the second kind and instability in concentration polarization at electrodialysis membranes*, Math. Models Methods Appl. Sci. **11** (2001), no. 2, 263–300.

[101] ———, *Electroconvective instability in concentration polarization and nonequilibrium electro-osmotic slip*, Phys rev E **72** (2005), 011505.

[102] ———, *Electro-convective versus electroosmotic instability in concentration polarization*, **134-135** (2007), 190–200.

[103] ———, *Convective diffusive mixing in concentration polarization: from taylor dispersion to surface convection*, J Fluid Mech **728** (2013), 239–278 (English).

[104] S. M. Rubinstein, G. Manukyan, A. Staicu, I. Rubinstein, B. Zaltzman, R. G. H. Lammertink, F. Mugele, and M. Wessling, *Direct observation of a nonequilibrium Electro-Osmotic instability*, Phys Rev Lett **101** (2008), no. 23, 236101.

[105] B. Scrosati and J. Garche, *Lithium batteries: Status, prospects and future*, J. Power Sources **195** (2010), no. 9, 2419–2430.

[106] Y. Shibuta, Y. Okajima, and T. Suzuki, *Phase-field modeling for electrodeposition process*, Sci technol adv mater **8** (2007), 511–518.

[107] H.-C. Shin, J. Dong, and M. Liu, *Nanoporous structures prepared by an electrochemical deposition process*, Adv mater **15** (2003), no. 19, 1610–1614.

[108] R. Simons, *The origin and elimination of water splitting in ion exchange membranes during water demineralisation by electrodialysis*, Desalination **28** (1979), no. 1, 41–42.

[109] ———, *Strong electric field effects on proton transfer between membrane-bound amines and water*, Nature **280** (1979), no. 5725, 824–826.

[110] ———, *Electric field effects on proton transfer between ionizable groups and water in ion exchange membranes*, Electrochim Acta **29** (1984), no. 2, 151–158.

[111] ———, *Water splitting in ion exchange membranes*, Electrochim Acta **30** (1985), no. 3, 275–282.

[112] H. L. Skriver and Rosengaard N. M., *Surface energy and work function of elemental metals*, Phys rev B **46** (1992), no. 11, 7157.

[113] W. H. Smyrl and J. Newman, *Double layer structure at the limiting current*, Trans Faraday Soc **63** (1967), 207–216.

[114] A. A. Sonin and G. Grossman, *Ion transport through layered ion exchange membranes*, J Phys Chem **76** (1972), no. 26, 3996–4006.

[115] L. G. Sundstrom and F. H. Bark, *On morphological instability during electrodeposition with a stagnant binary electrolyte*, Electrochim Acta **40** (1995), no. 5, 599–614.

[116] Y. Tanaka, *Water dissociation reaction generated in an ion exchange membrane*, J Membr Sci **350** (2010), no. 1-2, 347–360.

[117] Y. Tanaka and M. Seno, *Concentration polarization and water dissociation in ion-exchange membrane electrodialysis. mechanism of water dissociation*, J Chem Soc, Faraday Trans 1 **82** (1986), 2065–2077.

[118] Y. Tanaka, H. Uchino, and M. Murakami, *Continuous ion-exchange membrane electrodialysis of mother liquid discharged from a salt-manufacturing plant and transport of Cl- ions and SO42- ions*, Membr Water Treat **3** (2012), no. 1, 63–76 (English).

[119] C. W. Tanner, K. Z. Fung, and A. V. Virkar, *The effect of porous composite electrode structure on solid oxide fuel cell performance .1. theoretical analysis*, J Electrochem Soc **144** (1997), no. 1, 21–30 (English).

[120] J. M. Tarascon and M. Armand, *Issues and challenges facing rechargeable lithium batteries*, Nature (2001), –.

[121] D. J. Trevoy and H. Johnson, *The water wettability of metal surfaces*, J. Phys. Chem. **62** (1958), no. 7, 833.

[122] P. P. Trigueros, J. Claret, F. Mas, and F. Sagues, *Pattern morphologies in zinc electrodeposition*, J Electroanal Chem **312** (1991), 219–235.

[123] D. R. Turner and G. R. Johnson, *The effect of some addition agents on the kinetics of copper electrodeposition from a sulfate solution. 1. cathode potential-current density relation*, J Electrochem Soc **109** (1962), no. 9, 798–804.

[124] H. Udin, A. J. Shaler, and J. Wulff, *Surface tension of solid copper*, Trans. AIME **185** (1949), 186.

[125] M. Urtenov, E. V. Kirillova, N. M. Seidova, and V. V. Nikonenko, *Decoupling of the nernst-planck and poisson equations. application to a membrane system at overlimiting currents*, J Phys Chem B **111** (2007), 14208–14222.

[126] M. van Soestbergen, *Frumkin-butler-volmer theory and mass transfer in electrochemical cells*, Russ J Electrochem **48** (2012), no. 6, 570–579.

[127] A. V. Virkar, J. Chen, C. W. Tanner, and J.-W. Kim, *The role of electrode microstructure on activation and concentration polarizations in solid oxide fuel cells*, Solid State Ionics **131** (2000), 189 – 198.

[128] Y.-C. Wang, A. L. Stevens, and J. Han, *Million-fold preconcentration of proteins and peptides by nanofluidic filter*, Anal Chem **77** (2005), no. 14, 4293–4299.

[129] M. Winter and R. J. Brodd, *What are batteries, fuel cells, and supercapacitors?*, Chem. Rev. **104** (2004), no. 10, 4245–4270.

[130] T. A. Witten and L. M. Sander, *Diffusion-limited aggregation, a kinetic critical phenomenon*, Phys Rev Lett **47** (1981), no. 19, 1400–1403.

[131] ———, *Diffusion-limited aggregation*, Phys Rev B **27** (1983), no. 9, 5686–5697.

[132] T. Xu, *Ion exchange membranes: State of their development and perspective*, J Membr Sci **263** (2005), no. 1–2, 1–29.

[133] E. Yariv, *Asymptotic current-voltage relations for currents exceeding the diffusion limit*, Phys Rev E **80** (2009), no. 5, 051201.

[134] E. Yariv, *Improved current-voltage approximations for currents exceeding the diffusion limit*, SIAM J Appl Math **71** (2011), no. 6, 2131–2150.

[135] A. Yaroshchuk, *Transport properties of long straight nano-channels in electrolyte solutions: A systematic approach*, Adv Colloid Interface Sci **168** (2011), 278–291.

[136] ———, *Over-limiting currents and deionization "shocks" in current-induced polarization: Local-equilibrium analysis*, Adv Colloid Interface Sci **183-184** (2012), 68–81.

[137] ———, *What makes a nano-channel? a limiting-current criterion*, Microfluid Nanofluidics **12** (2012), no. 1-4, 615–624.

[138] A. Yaroshchuk, Y. Boiko, and A. Makovetskiy, *Ion-rejection, electrokinetic and electrochemical properties of a nanoporous track-etched membrane and their interpretation by means of space charge model*, LANGMUIR **25** (2009), no. 16, 9605–9614.

[139] A. Yaroshchuk, E. Zholkovskiy, S. Pogodin, and V. Baulin, *Coupled concentration polarization and electroosmotic circulation near micro/nanointerfaces: Taylor-aris model of hydrodynamic dispersion and limits of its applicability*, Langmuir **27** (2011), no. 18, 11710–11721 (English).

[140] V. I. Zabolotskii, V. V. Nikonenko, N. M. Korzhenko, R. R. Seidov, and M. K. Urtenov, *Mass transfer of salt ions in an electromembrane system with violated electroneutrality in the diffusion layer: The effect of a heterolytic dissociation of water*, Russ J Electrochem **38** (2002), no. 8, 810–818.

[141] V. I. Zabolotsky, V. V. Nikonenko, N. D. Pismenskaya, E. V. Laktionov, M. K. Urtenov, H. Strathmann, M. Wessling, and G. H. Koops, *Coupled transport phenomena in overlimiting current electrodialysis*, Sep Purif Technol **14** (1998), no. 1, 255–267.

[142] T. A. Zangle, A. Mani, and J. G. Santiago, *On the propagation of concentration polarization from Microchannel-Nanochannel interfaces part II: numerical and experimental study*, Langmuir **25** (2009), no. 6, 3909–3916.

[143] Y. Zeng, R. B. Smith, P. Bai, and M. Z. Bazant, *Simple formula for marcus-hush-chidsey kinetics*, J electroanal chem **735** (2014), 77–83.

[144] E. K. Zholkovskij and J. H. Masliyah, *Hydrodynamic dispersion due to combined pressure-driven and electroosmotic flow through microchannels with a thin double layer*, Anal Chem **76** (2004), no. 10, 2708–2718 (English).

[145] E. K. Zholkovskij, J. H. Masliyah, and J. Czarnecki, *Electroosmotic dispersion in microchannels with a thin double layer*, Anal Chem **75** (2003), no. 4, 901–909 (English).